Thesis for the Degree of Ph. D.

Search for New Physics Phenomena in Mono-Lepton Final States in pp Collisions at $\sqrt{s} = 13$ TeV with CMS detector at LHC

Department of Physics, Major in Particle Physics

The Graduate School

Lee JeongEun

December 2017

The Graduate School

Kyungpook National University

Search for New Physics Phenomena in Mono-Lepton Final States in pp Collisions at $\sqrt{s} = 13$ TeV with CMS detector at LHC

Lee JeongEun

Department of Physics, Major in Particle Physics
The Graduate School

Supervised by Professor Kim DongHee

Approved as a qualified thesis of Lee Jeongeun
for the degree of Ph.D. by the Evaluation Committee

December 2017

Chairman	Prof. Moon Chang-Seong
	Prof. Kim Minsuk
	Prof. Oh Youngdo
	Prof. Yang Un-Ki
	Prof. Kim DongHee

The Graduate School Council
Kyungpook National University

Contents

List of Figures

List of Tables

Chapter 1

Introduction

"What the new discovery in high energy physics mean?"
They indicate the range of exciting opportunities that may be expected.
More exciting still is the certain knowledge that nature's possibilities are not limited by our imagination. We must remember that the knowledge and art we gain today are our legacy to posterity. This is what civilization is all about. Individual names may soon be forgotten, but the aspiration and achievements of an age, and of a nation, will forever be remembered.

— Benjamin W. Lee, 1976

The most fundamental questions for the human being are about the origin of the world and about what exists fundamentally. These questions could be understood as questions about the nature of the universe. Over the centuries, people have sought to answer them and from at least the 5th century BC, come to realize that the matter of world is composed of fundamental building blocks, so-called elementary particles. In the 19th century, John Dalton introduced the atomic theory that proposed atoms could no longer be divided or destroyed. This atom has since then denoted the smallest particle but physicists soon realized that atoms are not elementary particles of nature. The early 20th century, Ernest Rutherford postulated the structure of the atom by alpha particle scattering experiment, that atom consists of the positively charged nucleus and negatively charged electrons and the model was superseded by the Bohr atomic model, which incorporated the quantum mechanics. Throughout the latter half of the 20th century, the theories and experimental discoveries of many physicists have resulted in a remarkable insight into the fundamental understandings of the smallest constituents of matter and their interactions. The variety of particles were observed, refer to "particle zoo", in collisions of particles from increasingly high-energy beams. Many physicists around the world have been devoted themselves to find new particles and categorize them in order to find the patterns of how fundamental building blocks of the universe interact. With a great deal of effort, the Standard Model has become

established in the early 1970s and this model has been verified through many particle physics experimental results. To these days, the most widely accepted theory of elementary particle physics is the Standard Model (SM). It successfully describes the three of the four known fundamental forces in the universe, the electromagnetic, weak, and strong forces except for gravitational force, as well as it is classifying all known elementary particles, quarks, and leptons, which are the constituents of matter. The formulation of this model was finalized by the experimental confirmation of the existence of quarks. As the power and energy of particle accelerator increased, all particles predicted by the SM were discovered. In addition, it has predicted the existence of the W and Z boson (1983) [1,2] with high accuracy, all of which were discovered with various properties of weak neutral currents. And the discovery of the top quark (1995) [3,4], the tau neutrino (2000) [5], and the "Higgs boson" (2012) [6,7] have increased the credibility of the Standard Model. Although the Standard Model has been demonstrated huge successes in providing experimental predictions, in a strict sense, it is an incomplete theory. There is some experimental evidence which cannot be explained until today, such as Dark matter, baryon asymmetry, neutrino oscillations and their mass problem, hierarchy problems and so on, which strongly suggest the existence of new physics Beyond the Standard Model (BSM). Furthermore, SM does not incorporate the gravitation and the unification gravity and other forces. Hence the LHC and its experiments have the main goal to test the proposed BSM theories and search for new phenomena not detected yet. At the collider experiment like LHC, the typical approach for searches is theory driven. In other words, the experimentalist investigated the real data for promising signatures predicted by a certain theoretical physics model. To distinguish the signal events from already known processes (Standard Model Background processes), special strategies of event selection criteria are developed and utilized.
In this thesis, the promising signature is mono-lepton (electron or muon) and missing energy in the final state and we search for new physics phenomena with this signatures. Since the discovery of the SM W boson, experiments have scrutinized closely this signature for evidence of BSM. Neither searches by the D0 [8] and CDF [9] experiment at Tevatron, nor searches performed previously CMS [10,11,12] and ATLAS [13,14,15] experiment at LHC, have not yet found evidence for such a new particle. The present analysis improves upon the discovery potential of its predecessors based on the increased statistics. The analyzed data are proton-proton collision data from an integrated luminosity of 35.9 ± 0.9 fb^{-1} at a center-of-mass energy of $\sqrt{s} = 13\,\text{TeV}$, collected by the CMS detector at CERN's Large Hadron Collider(LHC) during 2016.

In this thesis is structured as follows. This introductory chapter is followed by the theoretical motivation for this search in the Chapter 2. The physics theories, SM as well as BSM models predicting signatures with mono-lepton are described in this Chapter. Chapter 3 contains the experimental apparatus: LHC accelerator and CMS detector at CERN. Chapter 4 provides Data and Monte Carlo (MC) simulation samples for this search. MC simulated signal processes and SM background processes are summarized and applications of crucial corrections for the signal and the main background are explained. Also, a study of QCD background estimation for the data-driven method is also described in this Chapter. Afterwards, the reconstruction, identification of particle candidates and Trigger used in the experimental analysis are explained in Chapter 5. And the strategy for event selection and its relevant efficiency and scale factor are presented in this Chapter. The systematic uncertainties of the background and signal samples are described in Chapter 6. In Chapter 7, the statistical method for limit calculation is explained and the result with the limits on the cross section times branching ratio and its mass is described in Chapter 8. These results are re-interpreted in terms of 3 different new physics models as described in Chapter 2. Finally, the conclusion and outlook to the future sensitivity of the lepton and missing transverse energy final states are in Chapter 9.

Chapter 2

Theoretical Motivation

2.1 The Standard Model

The Standard Model (SM) of particle physics is theoretically based on the Glashow-Salam-Weinberg model of electro-weak interaction and Quantum Chromodynamics (QCD, strong interaction). The introduction to the SM can be found in [16, 17, 18, 19, 20]. It is a robust theoretical framework described by a local gauge theory of relativistic quantum fields theory (QFT), which has been validated through a wide range of the experimental phenomena with high accuracy so far. The underlying SM symmetry group is given as follows,

$$\mathrm{SU(3)_C \times SU(2)_L \times U(1)_Y} \tag{2.1}$$

Where $\mathrm{SU(3)_C}$ symmetry describes the color degree of freedom (C) of the theory of quarks, strong interaction (QCD) and the rest term describes the unification of weak and electromagnetic interactions with charges of weak iso-spin ($\mathrm{T_3}$) and electric charge (Q), respectively. $\mathrm{SU(2)_L}$ symmetry is for the weak interaction acting on only left-handed fermions (L) and $\mathrm{U(1)_Y}$ symmetry is for electromagnetic interaction with quantum number hypercharge (Y), which is formed by T_3 and Q via Gell-Mann-Nishijima formula:

$$\mathrm{Q = T_3 + \frac{Y}{2}} \tag{2.2}$$

The SM contains spin-$\frac{1}{2}$ fermions, spin-1 gauge bosons and the spin-0 Higgs boson. All matter in the universe is described by the fermions, composed of quarks and leptons, which are organized into 3 generations each. Till today, total six quarks and six leptons have been observed and they are arranged into three Generations (or families). Basically, each generation corresponds to heavier replicas (identical quantum numbers) of its preceding generation. The quark generations include an up-type quark (u, c, and t) with electric charge $+\frac{2}{3}$ and a down-type quark (d, s, and b) with electric charge $-\frac{1}{3}$ and quarks carry color charge. The lepton generations contain a negative charged (q = -1) lepton (e, μ, and τ) and an associated electrically neutral (q = 0) neutrino (ν_e, ν_μ, and ν_τ) and all color-neutral. These quarks and leptons are described in Table 2.1 with their electric charge and mass. All of these quarks and leptons are allocated a quantum number weak iso-spin T_3. While left-handed fermions are organized as weak iso-spin doublets within one generation with weak iso-spin $T_3 = \frac{1}{2}$, right-handed fermions are weak isospin singlets with $T_3 = 0$. They have their carbon-copy called anti-particle, which has opposite electric charge and opposite lepton flavor quantum numbers for leptons. Interactions between SM particles are mediated by the exchange of force-carrier,

quark			lepton		
Flavor	Charge	Mass (MeV/c^2)	Flavor	Charge	Mass (MeV/c^2)
u	$+2/3$	$1.8 \sim 2.8$	ν_e	0	$< 225 \times 10^{-6}$(CL = 95%)
d	$-1/3$	$4.3 \sim 5.2$	e^-	-1	0.511
c	$+2/3$	$(1.25 \sim 1.31) \times 10^3$	ν_μ	0	< 0.19(CL = 90%)
s	$-1/3$	$92 \sim 104$	μ^-	-1	105.7
t	$+2/3$	$(172.5 \pm 173.7) \times 10^3$	ν_τ	0	< 18.2(CL = 95%)
b	$-1/3$	$(4.15 \sim 4.22) \times 10^3$	τ	-1	1777.1

Table 2.1: All fermions (quarks and leptons, Spin $= \frac{1}{2}$) in the Standard Model with their electric charge and mass. Each values taken from the latest Particle Data Group (PDG) [21].(Neutrino masses are not finally determined yet, upper limits of the mass was given.

integer spin-1 gauge bosons. The gauge bosons and the allowed interactions arise from gauge symmetries associated with the corresponding gauge groups. There are four gauge bosons that mediate the interactions between the Standard Model particles. All bosonic particles in the SM are listed in Table 2.2,

Boson (Spin)	Charge	Mass (GeV/c^2)	Discovered
γ (S=1)	$< 1 \times 10^{-35} e$	$< 1 \times 10^{-27}$	Photoelectric effect 1905 [22]
g (S=1)	0	0	DESY PETRA 1979 [23, 24]
W (S=1)	± 1	80.385 ± 0.015	CERN UA1/2 1983 [1]
Z (S=1)	0	91.1876 ± 0.0021	CERN UA1/2 1983 [2]
H (S=0)	0	125.09 ± 0.24	CERN LHC 2012 [6, 7]

Table 2.2: Gauge (Spin $\neq 0$) and Scalar (Spin $= 0$) Higgs bosons in the Standard Model with their properties according to the latest PDG [21].

Strong Interaction

The interaction that binds quarks together to form hadrons (like proton) is the strong interaction. This strong interaction governing all colored particles is described theoretically by QCD and mediated via eight massless gluons (g) carrying color charge. The evidence of the existence of gluons was discovered at the PETRA collider in three jets events, where one jet originateds from a radiated gluon. The quantum number color charge has 3 representations (RGB = red, green and blue) and historically, it first brought in a process of understanding the discovery of Δ^{++} (uuu) baryon, causing the contradiction to the Pauli principle. Each gluon carries a color charge themselves, a linear combination of a color and anti-color states. Thus, gluons also couple to other gluons. This leads to a growth of the effective coupling strength of the strong force (α_s) at the small energy scale of the interaction (Q^2), contrary to the QED. That means that the stored potential energy in gluon between two colored particles increases in proportion to the distances between two colored particles. At very close distances, the strong coupling strength is quite small and the colored particles act like free particles, resulting in a phenomenon called "asymptotic freedom". The quarks inside the proton at the Large Hadron Collider environment (large momentum transfer or small distance) behave as free particles. The asymptotic freedom is connected with the effect of quark confinement at large distances, describing that colored particles never appear alone and only exist in neutral-color bound states, denoted as hadrons. The hadrons are formed by the hadronization process with two different types, consisted of $q - \bar{q}$ pair (called meson) and of three quarks (called baryon). Exceptionally, the top quark differs from other quarks in the SM because the lifetime is too short that it decays before starting the hadronization process.

Electroweak Interaction

Electroweak interactions are a unification of the electromagnetic and weak interactions. The electromagnetic force is carried by an electrically neutral and massless photon (γ) described by quantum electromagnetic dynamics (QED) and it interacts with all electrically charged particles and has an infinite range. The weak interaction is mediated by two $W^{\pm}$ bosons (charged current) as well as the Z^0 boson (neutral current). Unlike massless photon, W and Z bosons have large masses, thus they have a very short lifetime and limited range. They were discovered by UA1 and UA2 experiments at CERN in 1983. Before the discoveries of W and Z boson, the β-Decays by Wu experiment in 1957 firstly observed that the parity is violated in weak interactions. While weak charged currents (W boson) exclusively couple to left-handed fermions and right-handed anti-fermions, the neutral current (Z boson) couples to both left, right-handed fermions, but different strengths depending on flavor and handness[1]. Since then, the various experiments have confirmed that the weak interaction violates parity (P) and charge-conjugation (C) symmetry, but the fundamental origin in nature is not known yet. The coupling of the Z boson to both handness is explained by the unification of electroweak interaction, described by Glashow-Weinberg-

[1]The handness is determined as the projection operators $P_L = \frac{1}{2}(1 - \gamma_5)$, $P_R = \frac{1}{2}(1 + \gamma_5)$

Salam (GSW) model. The coupling to left handed fermions is stronger than right-handed fermions. While this asymmetry is quite small for chargeed lepton, the down-type quarks are relatively strong, and up-type quarks are in between. Flavor-changing only occurs in a charged weak current, for example, charged leptons can be transformed to their corresponding neutrinos by exchanging W bosons (only possible within the same generation in lepton). Quarks interacting with W boson can be transformed into a different quark generation, which was observed experimentally so-called quark mixing between flavors and CP violation in Kaon decays. The transition relation (probabilities) are experimentally measured and given by the Cabibbo-Kobayashi-Maskawa matrix (CKM matrix).

The electroweak unification theory described by the $\mathrm{SU(2)_L \times U(1)_Y}$ symmetry group. The $\mathrm{W^0}$ and $\mathrm{W^\pm}$ bosons ($\mathrm{W}_{\mu=0,1,2}$) are three new spin-1 massless field that arise from the $\mathrm{SU(2)_L}$ group and the $\mathrm{B^0}$ boson is another massless field associated with weak hypercharge (Y) to preserve the $\mathrm{U(1)_Y}$ group. Form this unification, the neutral current Z boson and photon are generated by rotating the representations of the gauge bosons $\mathrm{W^0}$ and $\mathrm{B^0}$ by the Weinberg angle or electroweak mixing angle θ_W.

$$\begin{bmatrix} \mathrm{W}^3_\mu \\ \mathrm{B}_\mu \end{bmatrix} = \begin{bmatrix} \cos\theta_\mathrm{W} & \sin\theta_\mathrm{W} \\ -\sin\theta_\mathrm{W} & \cos\theta_\mathrm{W} \end{bmatrix} \begin{bmatrix} \mathrm{Z}_\mu \\ \mathrm{A}_\mu \end{bmatrix} \tag{2.3}$$

The bosonic field $\mathrm{W^\pm}$, $\mathrm{Z^0}$ and photon (A_μ) corresponding to the observed mass eigenstates are fomed as linear combinations,

$$\begin{aligned} \mathrm{W^\pm} &= \frac{1}{\sqrt{2}}(\mathrm{W_1 \mp iW_2}) \\ \mathrm{A} &= \cos\theta_\mathrm{W} \cdot \mathrm{B} + \sin\theta_\mathrm{W} \cdot \mathrm{W_0} \\ \mathrm{Z} &= -\sin\theta_\mathrm{W} \cdot \mathrm{B} + \cos\theta_\mathrm{W} \cdot \mathrm{W_0} \end{aligned} \tag{2.4}$$

$$\cos\theta_\mathrm{W} = \frac{\mathrm{g}}{\sqrt{\mathrm{g}^2 + \mathrm{g}'^2}}, \sin\theta_\mathrm{W} = \frac{\mathrm{g}'}{\sqrt{\mathrm{g}^2 + \mathrm{g}^{2\prime}}} = 0.215 \tag{2.5}$$

Where the Weinberg angle (θ_W) is not theoretically predicted that can be measured with high precision from weak decay rates. It was given by the coupling strengths. The g and g′ parameters are the coupling strength of the W and B interaction respectively. The relation between Q, $\mathrm{T_3}$, and Y is given as Equation 2.2 and the coupling strengths of the electromagnetic force (e) is given,

$$\mathrm{e} = \mathrm{g}\sin\theta_\mathrm{W} = \mathrm{g}'\cos\theta_\mathrm{W} \tag{2.6}$$

The Higgs Mechanism

The electroweak in SM can be invariant under local gauge symmetry by predicting “massless” $\mathrm{W_{1,2,3}, B}$ bosons and fermions. This local gauge invariance cannot be maintained if the mass term of gauge boson or fermion is added. However, experimentally it is well known that the W and Z bosons have large masses (only the photon is massless boson). Furthermore some of SM scattering cross sections, for example, WW-scattering ($\sigma(\mathrm{WW} \rightarrow \mathrm{ZZ})$ increased as energy increased. This energy dependence indicates that the electroweak model has a problem with violating unitary at high energy and is non-renormalizable. To account for this problem, SM requires the inclusion of the concept of Spontaneous Symmetry Breaking (SSB) via the Higgs mechanism and a new fundamental scalar field, the Higgs boson is introduced. The Higgs mechanism spontaneously breaks the electroweak symmetry ($\mathrm{SU(2)_L \times U(1)_Y}$) without spoiling the gauge invariance of Lagrangian. To spontaneously break the symmetry, a new complex scalar field, so-called Higgs field Φ_H, which is a doublet under the $\mathrm{SU(2)_L}$ and contains a charged and neutral component $\Phi_\mathrm{H}^+, \Phi_\mathrm{H}^0$ is postulated with $\mathrm{T_3} = \pm\frac{1}{2}$ and $\mathrm{Y} = \frac{1}{2}$ respectively to keep the photon to be a massless boson.

$$\Phi_H = \begin{bmatrix} \Phi^+ \\ \Phi^0 \end{bmatrix} = \frac{1}{\sqrt{2}} \begin{bmatrix} \Phi_1 + i\Phi_2 \\ \Phi_3 + i\Phi_4 \end{bmatrix} \tag{2.7}$$

This Higgs field couples to gauge bosons ($\mathcal{L}_\mathrm{Higgs}$) as well as to the fermion by including Yukawa interaction ($\mathcal{L}_\mathrm{Yukawa}$). The square of the covariant derivative ($\mathrm{D}_\mu\Phi$) associated to $\mathrm{SU(2)_L \times U(1)_Y}$,

$$\begin{aligned} \mathcal{L}_\mathrm{Higgs} &= (\mathrm{D}^\mu\Phi)^\dagger(\mathrm{D}_\mu\Phi) - \mathrm{V}(\Phi) \\ \mathrm{D}_\mu\Phi &= \big(\partial_\mu + \mathrm{ig}\frac{1}{2}\vec{\mathrm{T}}\cdot\vec{\mathrm{W}}_\mu + \mathrm{i}\frac{1}{2}\mathrm{g}'\mathrm{Y}\mathrm{B}_\mu\big)\Phi \end{aligned} \tag{2.8}$$

$$\mathcal{L}_\mathrm{Yukawa} = \bar{\psi}\Phi_\mathrm{i}\mathrm{C_i}\psi + \mathrm{h.c.}(\mathrm{i} = 1, 2) \tag{2.9}$$

where the matrix $\mathrm{C_i}$ contains the masses of the fermion, which corresponds to the coupling strength to the scalar Higgs field. Furthermore, renormalizability and gauge invariance require a particular structure of the minimum of the scalar Higgs potential $\mathrm{V}(\Phi_\mathrm{H})$ that will spontaneously break the symmetry,

$$\mathrm{V}(\Phi) = \mu^2\Phi^\dagger\Phi + \lambda\big(\Phi^\dagger\Phi\big)^2, \quad \text{with } \mu^2 < 0 \tag{2.10}$$

The Higgs potential has two free parameters μ and λ. When these parameters are set to the negative μ^2 and the positive λ, the potential will not converge to $\Phi_\mathrm{H} = 0$ and there is an infinite number of non-zero minimum energy of degenrate states satisfying as follows,

$$\Phi^\dagger\Phi =<\Phi>= -\frac{\mu^2}{2\lambda} = \frac{v^2}{2}, \quad \text{where } v = \sqrt{\frac{-\mu^2}{\lambda}} \sim 246\,\mathrm{GeV} \tag{2.11}$$

Thus, the symmetry of the potential is spontaneously broken by the choice of a specific ground state, denoted as the Higgs vacuum expectation value (VEV v[2].)

[2]VEV of Higgs field is given as $\mathrm{v} = (\sqrt{2}\mathrm{G_F})^{-1/2} = 2\mathrm{M_W/g} \sim 246\,\mathrm{GeV}$. g is the weak isospin coupling and $\mathrm{G_F}$ is the Fermi coupling constant which was precisely estimated by the muon lifetime measurement. [25]

which set the electroweak energy scale. In the view of early universe after big bang, at the very early status of the universe with very high energies and temperature ($\gg$ v), the $V(\Phi)$ has a degenerate state with minimum energy $<\Phi>=0$ and the SM is gauge invariant under $SU(2)_L \times U(1)_Y$, while when the universe cooling down to energy below the electroweak energy scale ($\ll$ v), the $V(\Phi)$ is no longer stay at zero and obtains a non-zero VEV with minimum energy in Equation 2.11 and the SM symmetry will spontaneously break. To give a possible solution of $SU(2)_L \times U(1)_Y$ symmetry breaking and maintain the SM invariant under the $U(1)_{EM}$ symmetry, the charged Higgs field Φ^+ is zero(leads to massless photon) then the neutral Higgs field contains v and a scalar field h(x).

$$\Phi(x) = \frac{1}{\sqrt{2}} \begin{bmatrix} 0 \\ v + h(x) \end{bmatrix} \tag{2.12}$$

The massless Goldston boson arising in broken symmetry is absorbed as longitudinal degree of freedom of the W and Z bosons. In the process of replacing Higgs field Φ with Φ (Equation 2.13) in Equation 2.8, the mass terms arise. The W and Z bosons gain large mass and interactions with the Higgs field through the kinetic term $(D^\mu \Phi D_\mu \Phi)$. The electroweak gauge bosons and their masses are defined as follows:

$$\begin{aligned}
W^{\pm}_\mu &\equiv \frac{1}{\sqrt{2}}(W^1_\mu \mp iW^2_\mu) \quad \text{with mass } M_W = \frac{gv}{2} \\
Z^0_\mu &\equiv \frac{1}{\sqrt{g^2+g'^2}}(gW^3_\mu - g'B_\mu) \quad \text{with mass } M_Z = \frac{v}{2}\sqrt{g^2+g'^2} \\
A_\mu &\equiv \frac{1}{\sqrt{g^2+g'^2}}(g'W^3_\mu + gB_\mu) \quad \text{with mass } M_\gamma = 0 \\
\cos\theta_W &= \frac{M_W}{M_Z}
\end{aligned} \tag{2.13}$$

A new scalar Higgs boson also acquires mass through its self interaction in the Higgs potential $(V(\Phi))$. Its mass is given by $v\sqrt{2\lambda}$, which is not able to predict in theory. In 2012, the Higgs boson was finally discovered by CMS and ATLAS experiment at the LHC and its mass was measured $M_H = 125.09 \pm 0.21(\text{Stat.}) \pm 0.11(\text{Syst.})$ GeV [26]. Lastly, The interaction of the fermions with the Higgs field generates the mass terms and to couplings to the Higgs field c_f so-called Yukawa couplings, which are proportional to the fermion mass, m_f ($\mathcal{L}_{\text{Yukawa}}$). The fermion masses can be expressed as $m_f = vc_f/\sqrt{2}$. Yukawa couplings are not able to predict in theory. All masses of fermions are measured in the experiment over many years. A summary of all elementary particles of Standard Model and of symmetry breaking are given in Figure 2.1.

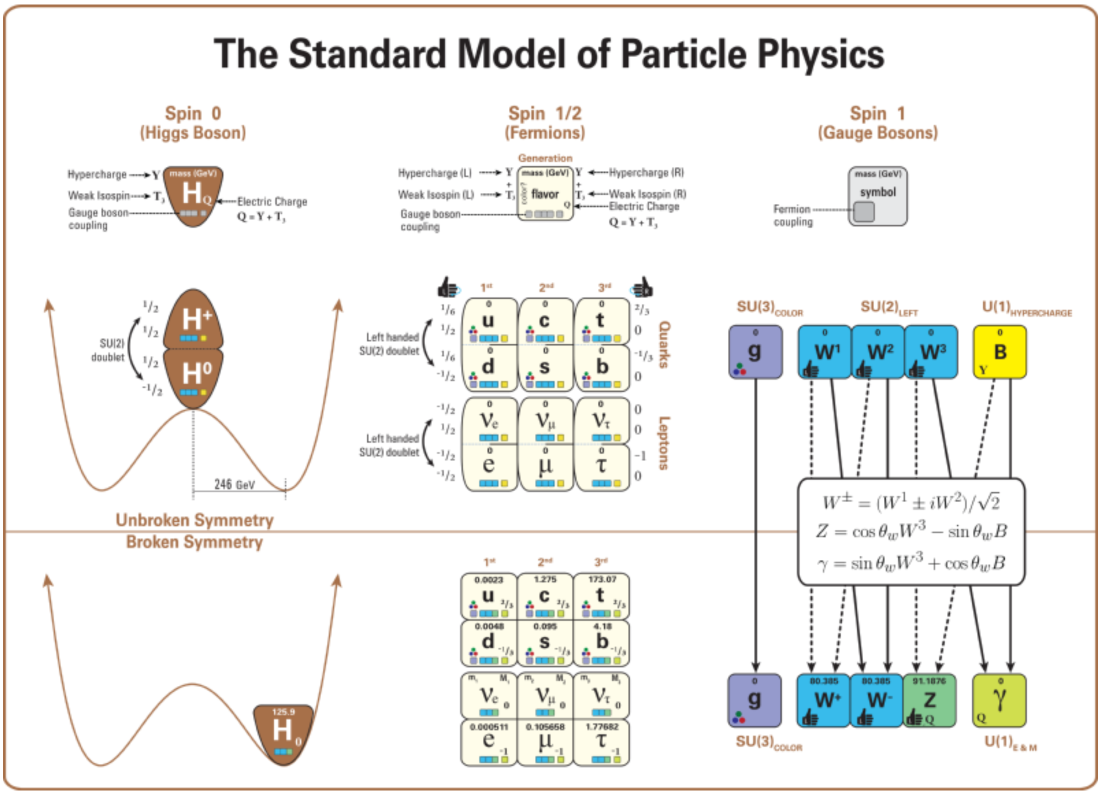

Figure 2.1: The diagram shows the elementary particles of the Standard Model: the Higgs boson (left), the three generations of quarks and leptons (middle), and the gauge bosons (right) with their names, masses, spins, charges, chiralities, and interactions with the strong, weak and electromagnetic forces. It also depicts the crucial role of the Higgs boson in electroweak symmetry breaking and shows how the properties of the various particles differ in the (high-energy) symmetric phase (top) and the (low-energy) broken-symmetry phase (bottom). This figure made by Latham Boyle.

2.2 Limitations of the Standard Model

The Standard model has provided an elegant theoretical framework and successful description for strong and electroweak interactions, which could be approximately valid till grand unification energy scale (GUT scale, $\Lambda_{\mathrm{GUT}} \sim 10^{16}\,\mathrm{GeV}$) or even up to the Planck scale ($\Lambda_{\mathrm{P}} \sim 10^{19}\,\mathrm{GeV}$). Despite the tremendous success of accurately predicting the physics phenomena of the SM, there is still no solution to the fundamental question and cannot properly explain the natural principle of being discovered experimentally in nature. The limitations of the SM up to date are described in this Section. Many questions of these limitations naturally led to the advent of new physics models. The physics beyond the Standard Model (BSM) has been proposed on the basis of various theoretical forms of modification of the SM in ways enough to be matched with existing data, predict the non-SM output of next-generation experiments addressing those deficiencies of SM [27, 28]. In this respect, the LHC is an excellent place to search for new physics evidence with huge data at a unique high energy scale in particle physics, 13 TeV.
There are various parts which are not explained in the SM model. Firstly, there are some physics phenomena in nature that the Standard Model can not properly explain.

Gravity:
The most familiar force in our life, however, it is very difficult challenges to fit gravity comfortably into Standard Model framework (not renormalizable). The SM cannot yet account for the gravity, which is based on Einstein's general theory of relativity. This reflects the fact that general relativity theory and QFT in SM have different origins of aspect and structures. If there is a beautiful unified theory (Quantum Gravity), then the SM can be extended to contain a particle to mediate the gravitational interaction, "graviton". Although it was very difficult to experimentally discover this graviton, a lot of experiments have been performed to get information about the nature of it and to set experimental limits. According to astronomical observations of the kinematics of galaxies, graviton might have non-zero mass [29]. Until today, the most stringent upper bound of $6 \times 10^{-23}\,\mathrm{eV/c^2}$ on the mass of graviton have set (from weak gravitational lensing data [30]). Also recently the first direct detection of cosmic gravitational waves was reported in 2015 by the LIGO and Virgo Collaboration [31](Their result is an upper bound of $1.2 \times 10^{-22}\,\mathrm{eV/c^2}$).

Dark matter and dark energy:
The SM of cosmology declares that the total mass-energy of the universe contains 5% ordinary matter which is made up of particles in the SM, while 27% is dark matter and rest 68% is dark energy. The existence of dark matter is confirmed by

significant astrophysical observational evidence like the measurements of rotation curve of the galaxy, gravitational lensing effects determining the galaxy clusters, the temperature distribution of hot gas in galaxies and clusters, and the pattern of anisotropies detected in the cosmic microwave background (CMB) [32,33]. The dark matter behaves like the matter, but only interacts with gravity and weak force and the dark energy is a constant energy density of the vacuum. This dark energy was incompatible with vacuum energy of the SM, resulting in a mismatch of 120 order of magnitude and the SM still does not have good dark matter candidates satisfying the whole measured density.

Neutrino Masses and Oscillations:
In the SM, neutrinos are massless particles, however, the various experiments with solar (Sudbury neutrino observatory [34]) atmospheric (Super-Kamiokande [35]) reactor (RENO [36] and Daya Bay [37]) and accelerator neutrinos (OPERA [38]) have observed neutrino oscillations with spontaneously flavor changing, which is caused by non-zero masses. These experimental observations provide the mass differences between the different flavors and imply the existence of 3 neutrinos mixing in the vacuum. The mass term of the neutrinos can be set to the SM by hand, but these bring new theoretical problems of origins of masses. Some questions of why neutrinos have extraordinarily small mass terms and how neutrinos masses arise are not answered yet.
These lead to modification of SM, which proposes the Majorana mass for left-handed neutrinos or proposes right-handed neutrinos that interact with the left-handed neutrinos and Higgs field like the rest of the fermions.

Matter-antimatter asymmetry:
At present, the universe consists mostly of baryonic matter (atomic matter), but the SM tells that matter and antimatter should have been produced in equal amounts at the big bang. In the SM there is still no mechanism adequately describing the origin of the matter remains, known as Baryonic asymmetry problem. Several possible explanations have been provided. One of them is the CP violation which occurs as a complex phase in the quark mixing CKM matrix of the weak interaction in the SM. Similarly, there may be a non-zero CP-violating phase in the neutrino mixing matrix, though this is not measured yet. To compatible with given limits on the baryon number violation, the amount of CP violation in the SM is insufficient to account for the observed baryon asymmetry of the universe, thus approaches of BSM are required.

Experimentally there is also some evidence that is different from the Standard Model expectation, although most of them have been unfolded to be statistical fluctuations or experimental errors as more data has been accumulated. Whereas, any new BSM physics would necessarily first appear experimentally as a statistically significant difference between the theoretical prediction and an experiment. Experiments are usually well tailored to be more sensitive to experimental results that can distinguish the SM from theoretical alternatives. Some of the most notable examples include the following.

Proton radius puzzle:
The SM precisely predicts the atomic radius size of hydrogen (a proton-electron system) and muonic hydrogen (a proton-muon system). However, the measurement of the atomic radius of muonic hydrogen is different from SM prediction within 4 % accuracy. Despite the clear statistical significance of the result and a lack of any identified source of experimental error, physicists are hesitant to describe these as contradicting the SM due to the absence of motivated theories that could well explain this discrepancy [39, 40].

Anomalous magnetic dipole moment of muon:
The experimentally measured value of muon's anomalous magnetic dipole moment (muon g-2) is significantly different from the SM prediction by 3.5 standard deviations [41, 42] and it is compelling evidence of BSM and also represents a crucial constraint of new physics theories such as supersymmetry or extra dimensions.

Moreover, there are some crucial theoretical limitations of SM in the following. It contains many free parameters and some features are implemented in an ad hoc way. These unnatural properties have motivated to look for more fundamental theories with fewer parameters.

Hierarchy problem and free parameters:
One of the most serious theoretical issues of SM is the large hierarchy of different scales(EW scale 10^2 GeV to Plank scale 10^{19} GeV) in high energy physics. As explained earlier, the particles of the SM obtain their masses through the spontaneous symmetry breaking mediated by the Higgs boson. The mass of the Higgs boson gets some very large quantum loop corrections due to the presence of virtual particles. These corrections are much larger than the actual mass of the Higgs boson, therefore extremely cancelations of the quantum corrections must be required to fix the Higgs mass, denoted as the fine-tuning or naturalness problem. Many theorists want to avoid these unnatural high level of fine-tunning. Additionally, the SM depends on 19 free parameters whose values are set by experiment, but the origin of them is unknown. The large differences in the SM fermion masses(ν 2 GeV to t 173 GeV) are not explained.

Quantum triviality:
The quantum triviality suggests that it may not be possible to create a consistent quantum field theory involving elementary scalar Higgs particles. Theoreti-

cal proofs evidencing triviality of the scalar field theory have appeared, but the nature of the quantum field theories interacting with it remains an open question.

Strong CP problem:
According to QCD, the SM could contain a violation of CP symmetry term in the strong interaction. However, no violation has been observed in experiments, implying that the coefficient of this term is close to zero. This fine tuning is regarded as unnatural.

2.3 Beyond the Standard Model

These limitations of standard model have motivated to the building the Beyond the Standard Model (BSM). The most general ways to build new models is extending the gauge structures of the SM, which is inspired by Grand Unified Theories (GUT) theories seeking the unification of the fundamental forces of nature with an unique coupling (except gravity[3]). The various GUT theories have been developed, but commonly all of them have features that unification is achieved by extending the SM symmetry group into a larger GUT symmetry group and the energy scale at which the unified symmetry is broken is called the GUT scale. (The SM symmetry group is $\mathrm{SU(3)_C \times SU(2)_L \times U(1)_Y}$)
For instance, the minimal extension of the electroweak sector, which contains new heavy gauge bosons W′ and Z′, manifests a gauge structure of $\mathrm{SU(2)_1 \times SU(2)_2 \times U(1)_X}$ that ultimately breaks to $\mathrm{U(1)_{EM}}$, commonly called G(221) models [43, 44]. In G(221) models, the symmetry is spontaneously broken in two steps, assigning mass to the new W′ and Z′ bosons and to the W and Z bosons [45].
There are various models depending on the patterns of symmetry breaking : left-right(LR) [46,47,48,49], leptophobic(LP), hadrophobic(HP), fermiophobic(FP) [50, 51, 52], un-unified(UU) [53] and non-universal(NU) [54, 55] models (summarized in Table 2.3).

- Breaking Pattern I (BP1, the LR, LP, HP and FP models):
  $\mathrm{SU(2)_1}$ is identified with $\mathrm{SU(2)_L}$ of the SM. The first stage of symmetry breaking is $\mathrm{SU(2)_2 \times U(1)_X \Rightarrow U(1)_Y}$, bringing about heavy gauge bosons W′ and Z′ at the TeV scale, whereas the second stage of symmetry breaking $\mathrm{SU(2)_L \times U(1)_Y \Rightarrow U(1)_{EM}}$ occurs at the electroweak scale.

- Breaking Pattern II (BP2, the UU and NU models):
  $\mathrm{U(1)_X}$ is identified with $\mathrm{U(1)_Y}$ of the SM. The first stage of symmetry breaking is $\mathrm{SU(2)_1 \times SU(2)_2 \Rightarrow SU(2)_L}$ takes place at the TeV scale, while

[3]Unifying gravity with the other three forces would provide a Theory of Everything (TOE; Quantum Gravity∈TOE). GUTs are often seen as an intermediate step towards a TOE.

the second stage of symmetry breaking is $SU(2)_L \times U(1)_Y \Rightarrow U(1)_{EM}$ occurs at the electroweak scale.

	Breaking Pattern I	Breaking Pattern II
Starting Point	$SU(2)_1 = SU(2)_L$	$U(1)_X = U(1)_Y$
First Stage	$SU(2)_2 \times U(1)_X \Rightarrow U(1)_Y$	$SU(2)_1 \times SU(2)_2 \Rightarrow SU(2)_L$
Second Stage	$SU(2)_L \times U(1)_Y \Rightarrow U(1)_{EM}$	$SU(2)_L \times U(1)_Y \Rightarrow U(1)_{em}$

Table 2.3: The two different symmetry breaking patterns and the two different stages of breaking in G(221) models.

In the following, the description of how our main interest, new physics with mono-lepton signature, can be derived and behaves in these different breaking patterns of G(221) model.

Breaking Pattern 1 (LR model) : The parity violation in weak interaction has been detected by several experiments with high precision, but its origin in nature is unexplained by it. Because of this incompleteness, and with symmetry percepts, many extensions of the SM predict that the Left-Right(LR) symmetry in weak interactions is restored at higher energy scales. One of the simplest way to obtain the LR symmetry model is the addition of a $SU(2)_R$ gauge group by replacing the singlets of right-handed fermions to doublets, resulting in the existence of new gauge bosons W' and right-handed neutrino, ν_R. therefore the electroweak symmetry group in the SM($SU(2)_L \times U(1)_Y$) is extended($SU(2)R \times SU(2)_L \times U(1)_{BL}$, and assume that the symmetry breaking happens twice as follows :

$$SU(2)_R \times SU(2)_L \times U(1)_{BL} \xrightarrow{\Phi} SU(2)_L \times U(1)_Y \xrightarrow{H} U(1)_{EM} \tag{2.14}$$

where B-L means baryon and lepton number respectively, and Φ (in first stage breaking) and H (in second stage breaking) scalar fields play a role in assigning mass to the new gauge bosons and SM gauge bosons respectively (More detailed in [43]). With assuming the left-right mixing angle(ζ) to be zero, $W_L^\pm$ and new $W_R^\pm$ in this model indicate the SM gauge $W^\pm$ boson and the new $W'^\pm$ gauge boson respectively, that couple with Left/Right handed fermions. By current observation, mass of the W_R might be much heavier than the mass of the W_L. The W_R with the mass at the TeV scale could be produced via s-channel at the LHC and it may potentially observe $W_R \rightarrow \ell_R \nu_R$ (ℓ = e,μ and τ) signature in case $m_{\nu_R} < m_{W_R}$). Basically, coupling with only right-handed fermion may not occur a large amount of signal, however, the nature of right-handed neutrino is still unknown and it has no constraint on mass as long as it does not couple with SM particles. If it exists with large mass (but lighter than W_R), then it will detect with mono-lepton signature in the detector (ex. ν_R is undetected in the detector, or decay into invisible particles or decays outside the detectors). In this model, the lower bounds on the mass of this W′ boson was set to 0.269 TeV.

Otherwise in case of $m_{W_R} < m_{\nu_R}$, leptonic channel is not allowed anymore but other final states are also possible to search for a W_R, like $W' \to qq'$, $W' \to WZ/WH$.

Breaking Pattern 2 (UU model) : In this model, the W′ boson couples with left handed fermions, therefore it directly decays to a lepton and the SM neutrino and the interference effect between W_{SM} and W′ is occured. Its symmetry breaking pattern is as follows.

$$SU(2)_{L_1} \times SU(2)_{L_2} \times U(1)_Y \xrightarrow{\Phi} SU(2)_L \times U(1)_Y \xrightarrow{H} U(1)_{EM} \tag{2.15}$$

This $W' \to \ell_{L,SM} + \nu_{\ell,SM}$ processes are produced at the LHC with mono-lepton signature. In this model, the lower bounds on the mass of new charged heavy gauge boson W′ was set to 2.474 TeV, thus lepton and neutrino are expected to be very energetic also in LR model.
Theoretically, not only for these two models, many other BSM theories predict W′ boson or other new physics which is detectable from the mono-lepton signature.(See following Section 2.3.2,2.3.3). In virtue of its very clean signature in the detectors than other hadronic channels, this can be the frontrunner to announce the discovery of new physics. It is important to remark that if this signature is discovered, we can not guarantee which theory corresponds to it, thus further studies on its properties and other possible decay modes will be necessary to distinguish between different theories.
The charge assignments of the SM fermions in these models are described in Table 2.4.

Model	$SU(2)_1$	$SU(2)_2$	$U(1)_X$
Left-right (LR)	$\binom{u_L}{d_L}$, $\binom{\nu_L}{e_L}$	$\binom{u_R}{d_R}$, $\binom{\nu_R}{e_R}$	$\frac{1}{6}$ for quarks, $-\frac{1}{2}$ for leptons
Un-unified (UU)	$\binom{u_L}{d_L}$	$\binom{\nu_L}{e_L}$	Y_{SM} for all fermions

Table 2.4: The charge assignments of the SM fermions in the G(221) gauge groups. Unless otherwise specified, the fermion doublet represents three generations of SM fermions.

2.3.1 Sequential Standard Model W′

Many BSM models had predicted W′ bosons as stated in the previous section. In experimental point of view, it is reasonable to set one specific approach in which

the generic properties of many different models are utilized without depending on their specific assumptions and details. This specific approach is derived in a general framework from the "reference model" by Altarelli [56] and called the benchmark model evaluating the discovery potential. Traditionlly in collider experiments, the benchmark signal model used for the $W' \to \ell\nu$ search corresponds to the Sequential Standard Model (SSM).
In the SSM, the new gauge boson W' is supposed to be a heavy carbon-copy of

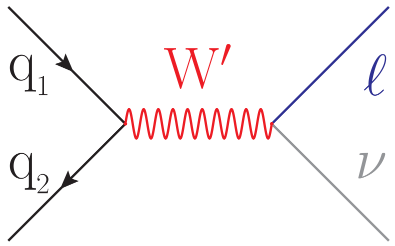

Figure 2.2: The feynman diagram of production and decay of an W' in SSM or W^{n}_{KK} in split-UED model.

the SM W and has the equal couplings to fermions as SM W. The masses of W' is the only parameter in this model. The couplings to the SM W/Z/H are highly model dependent and in SSM they assumed to be suppressed and this results in a moderate decay width of the W'. If the new gauge bosons and the SM ones belong to different gauge groups, vertices of the $W' \to WZ$ (or $Z' \to ZZ$) is forbidden. It can only happen after symmetry breaking due to the mixing of the gauge group eigenstates to mass eigenstates. These vertices are suppressed by a factor of the order of $(m_W/m_{W'})^2$. If the mass of the W' is heavy enough($m_{W'} \gg$180 GeV), the process $W' \to t\bar{b}$ allowed. The modified full width of the W' (the sum of the individual decay widths for all available fermion pairs) boson and branching ratio (for leptonic decay channel) are described as follows:

$$\Gamma_{W'} = \begin{cases} \frac{m_{W'}}{m_W}\Gamma_W & \text{for } m_{W'} \ll 180\,\text{GeV} \\ \frac{4}{3}\frac{m_{W'}}{m_W}\Gamma_W & \text{for } m_{W'} \gg 180\,\text{GeV} \end{cases}$$

Where m_W and Γ_W are the mass(80.385 GeV) and total width(2.085 GeV) of the SM W boson respectively. The factor 4/3 comes from the additional decay channel into $t\bar{b}$.
The number of decay channels of the W' boson is:

$$\Sigma N_{decay} = \begin{cases} 9 & \text{for } m_{W'} \ll 180\,\text{GeV} \\ 12 & \text{for } m_{W'} \gg 180\,\text{GeV} \end{cases} \tag{2.16}$$

$$\mathcal{B}(\mathrm{W}' \to \ell\nu) = \frac{\Gamma_{\mathrm{W}'\to\ell\nu}}{\Gamma_{\mathrm{W}'_{\mathrm{Total}}}} = \begin{cases} \frac{1}{9} \sim 11.1\% & \text{for } \mathrm{m_{W'}} \ll 180\,\mathrm{GeV} \\ \frac{1}{12} \sim 8.3\% & \text{for } \mathrm{m_{W'}} \gg 180\,\mathrm{GeV} \end{cases} \tag{2.17}$$

The branching ratio for the $\ell\nu$ channel($\ell = \mathrm{e}, \mu$, and τ) is 8.3 %. A formulation of the Lagrangian term for the interaction of a W'^{+} coupling to fermions is given as follows:

$$\begin{gathered} \frac{\mathrm{W}'^{+}_{\mu}}{2\sqrt{2}}[\bar{\mathrm{u}}_{\mathrm{i}}(\mathrm{C}^{\mathrm{R}}_{\mathrm{q_{ij}}}\mathrm{P_R} + \mathrm{C}^{\mathrm{L}}_{\mathrm{q_{ij}}}\mathrm{P_L})\gamma^{\mu}\mathrm{d_j} + \bar{\nu}_{\mathrm{i}}(\mathrm{C}^{\mathrm{R}}_{\ell_{\mathrm{ij}}}\mathrm{P_R} + \mathrm{C}^{\mathrm{L}}_{\ell_{\mathrm{ij}}}\mathrm{P_L})\gamma^{\mu}\mathrm{e_j} \\ \mathrm{P_R} = 1 + \gamma^5/2 \text{ and } \mathrm{P_L} = 1 - \gamma^5/2 \text{ , } \mathrm{P_R} + \mathrm{P_L} = 1 \\ \text{where } \gamma^5 = \mathrm{i}\gamma^0\gamma^1\gamma^2\gamma^3 \end{gathered} \tag{2.18}$$

where i = 1,2,3 refers to generation of fermions and $\bar{\mathrm{u}}, \mathrm{d}, \mathrm{e}$ and $\bar{\nu}$ indicate mass eigenstate basis of the fermions in SM. The $\mathrm{C}^{\mathrm{R/L}}$ is coupling strength of the W'^{+} to the right/left-handed fermions, and the $\mathrm{P_{R/L}}$ is the chirality projector operation for the Right/Left component.
In case of a non-zero $\mathrm{C^R}$, ν_{R} is expected and this correspond to Breaking Pattern1 (BP1), while if the $\mathrm{C}^{\mathrm{L}}_{\mathrm{q_{ij}}} = \mathrm{gV_{CKM_{ij}}}$, $\mathrm{C}^{\mathrm{L}}_{\ell} = \mathrm{g}$ and $\mathrm{C^R} = 0$, this would correspond to Breaking Pattern2 (BP2) in the section 2.3.

In this thesis, the interference effects with the SM W does not be considered. (SSM W′ without interference) There are other types of theories that could be verified with the same or similar signature. Among many of new physics theory, two attractive BSM models will be introduced in the next section.

2.3.2 Split Universal Extra Dimension model

The leptonic($\ell\nu$) channel in this study could be interpreted by the universal extra dimensions (UED) framework with bulk mass fermions, denoted as split-UED [57,58,59,60,61]. This model is based on a TeV scale extra-dimension, where all of SM fields is assumed to the zero Kaluza-Klein(KK) mode of scalar, fermion, and gauge fields that propagate on a space-time in 5 dimensions $\mathcal{M}_4 \times \mathrm{X}$, where $\mathcal{M}_4$ is 4-dimensional Minkowski space and X is a compact flat space of extra dimension(s). In this extra dimensions, zero mode fermions can be given when the extra dimensional space is in the interval $\mathrm{X} \in [-\mathrm{L}, \mathrm{L}] = [-\pi\mathrm{R}, \pi\mathrm{R}]$, where R is the compactification radius determining the size of compact fifth dimension.
All fermions and gauge bosons of SM are propagated to their KK excitations, for example $\mathrm{q_n}, \ell_{\mathrm{n}}, \nu_{\mathrm{n}}, \gamma_{\mathrm{n}}, \mathrm{W_n}, \mathrm{Z_n}$, and $\mathrm{g_n}$ (n stands for the n-th KK excitation mode) with a mass gap of the order of the 1/R. For simplicity, we use $\mathrm{W_n} = \mathrm{W^n_{KK}}$, the n-th KK excited W boson, which is interesting in this study.

$$\mathrm{m}^2_{\mathrm{W^n_{KK}}} \equiv \mathrm{m}^2_{\mathrm{n}} = \mathrm{m}^2_{\mathrm{W}} + \left(\frac{\mathrm{n}}{\mathrm{R}}\right)^2 \tag{2.19}$$

It shows that the larger radius R gives smaller KK mass.

$$g_n = g^{SM}\mathcal{F}_n(\pi\mu R) \tag{2.20}$$

$$\mathcal{F}_n(x) = \begin{cases} 0 & \text{if } n = 2m+1 \\ \frac{x^2[-1+(-1)^m e^{2x}](\coth x - 1)}{\sqrt{2(1+\delta_{m0}(x^2+m^2\pi^2/4)}} & \text{if } n = 2m \end{cases} \tag{2.21}$$

Where μ is the bulk mass parameter in 5 dimensions of the fermion field determine the mass of KK fermions, with the UED parameter space [1/R, μ]. In this model, we assume a non-zero value for μ[4] and g_n is the coupling of the W^n_{KK} to fermions and defined as a modification of the SM coupling g^{SM} of the W boson. The $\mathcal{F}_{n=2m}$ seems to be approaching $(-1)^m\sqrt{2}$ when x goes to ∞. One of the noticeable features of the UED model is the KK-parity conservation. As the Eq 2.21 show, the coupling of KK-odd modes(n=1,3,5$\cdots$) of W^n_{KK} is zero(not couple with fermions), in consequence of KK-parity conservation. Furthermore, there is no expected sensitivity for n$\geq$4 modes at the LHC environment, therefore $W^{n=2}_{KK} \to \ell\nu$ is only considerable. The final state is kinematically equal to the SSM W′-like decay.(see Fig. 2.2).

2.3.3 R-Parity Violation SUSY model

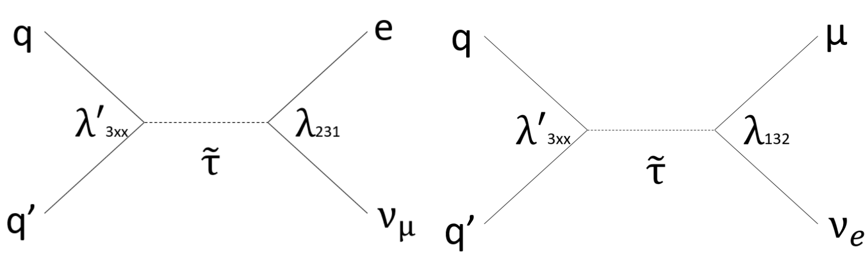

Figure 2.3: A stau ($\tilde{\tau}$) acts as a mediator with corresponding λ couplings for the decay which are different for the final states. For electrons it is λ_{231} (letf) and muons λ_{132} (right).

A further reinterpretation is performed with the R-parity violation supersymmetry (RPV SUSY) model [62,63]. The R-parity (R_p) is a discrete multiplicative symmetry and it is defined as follows :

$$R_p = (-1)^{3B+L+2S}$$
$$R_p = +1 \text{ for SM particle, } R_p = -1 \text{ for superpartner.} \tag{2.22}$$

[4]The production cross section of the W^n_{KK} production times the branching fraction of SM fermions goes to 0 as μ goes to 0.

Where B, L, and S denote the baryon number, lepton number, and spin of a particle, respectively. This R_p is conserved in Minimal Supersymmetric Standard Model (MSSM) and because all initial states at collider experiments are R_p even, superpartners should be only produced in pairs and Lightest Supersymmetric Particle (LSP), a potential dark matter candidnate, is stable and escapes detection. However, there is no strong theoretical argument that R-parity must be conserved thus it is mandatory to experimentally search for both possibilities. If R-parity violation is allowed, lepton or baryon number can be violated and supersymmetric particles including LSP can decay to non-supersymmetric particles and the single production of supersymmetric particles can be possible. In RPV SUSY model, the additional RPV term apper in the superpotential as follows :

$$\begin{aligned} W &= W_{MSSM} + W_{\not{R}_p} \\ W_{\not{R}_p} &= \lambda_{ijk} L_i L_j \bar{E}_k + \lambda'_{ijk} L_i Q_j \bar{D}_k + \lambda''_{ijk} \bar{U}_i \bar{D}_j \bar{D}_k . \end{aligned} \tag{2.23}$$

Here $i, j = 1, 2, 3$ are generation indicies ($1 = e$, $2 = \mu$, $3 = \tau$) and a summation is implied. L_i and Q_i are $SU(2)_L$ left-handed doublet superfields of lepton and quark, $\bar{E}_j(\bar{D}_j, \bar{U}_j)$ are $SU(2)_L$ right-handed singlet superfields of the charged lepton (down and up-type quark). λ, λ', and λ'' are Yukawa couplings and λ_{ijk} and λ''_{ijk} are anti-symmetric for interchanging of i and j [5]. The first ($LL\bar{E}$) and second ($LQ\bar{D}$) term violate lepton number and the third ($\bar{U}\bar{D}\bar{D}$) term violates baryon number. This model can assume that a supersymmetric particle such as scalar lepton($\tilde{\ell}$) as a mediator and its subsequent lepton-flavor violating decay to one charged lepton and a neutrino. For the mono-lepton search,the cases where a scalar tau lepton($\tilde{\tau}$) decays to an $e + \nu_\mu$ or $\mu + \nu_e$ are selected. The coupling on the production side is a version of λ'_{3XX}, which is the coupling to the third generation, the $\tilde{\tau}$, while the decay to $e + \nu_\mu$ is governed by λ_{231} and by λ_{132} for the $\mu + \nu_e$ final state (See one example in Equation 2.24).

$$\begin{aligned} &\text{If , } \lambda_{231} L_{i=2} L_{j=3} \bar{E}_{k=1} = \binom{\nu_\mu}{\mu}_L \binom{\tilde{\nu_\tau}}{\tilde{\tau}}_L (e_R) \\ &\tilde{\nu_\tau} \rightarrow e^\pm \mu^\mp \quad \text{ and } \tilde{\tau} \rightarrow e\nu_\mu \text{ possible.} \end{aligned} \tag{2.24}$$

Feynman diagrams are depicted in the Fig. 2.3 for the two decay channels are considered. The production cross section is dependent on these two couplings (λ', λ) and the mass of scalar lepton($\tilde{\tau}$).

[5]The combination (ijk) can be (121), (131), (122), (132), (232), (123), (133), and (233).

Chapter 3

Experimental Apparatus

3.1 Overview

The Large Hadron Collider (LHC) [64, 65], located 100 meters underground in a 26.7-kilometer long circular tunnel at the European Organization for Nuclear Research (CERN) Laboratory on the Swiss-French border in Geneva Switzerland, provides the world's highest energy proton-proton collisions. The underground tunnel was previously used for Large Electron Positron Collider (LEP) experiments [66] from 1989 until 2000 and after then it was taken apart to build the LHC. The LHC first started up on 10 September 2008 and remains the latest addition to CERN's accelerator. It designed to provide proton-proton collisions at center of mass energies $\sqrt{s}$ of up to 14 TeV. In the LHC, four elaborate detectors are installed at each collision points to carry various physics goals: CMS, ATLAS, LHCb, and ALICE. In this Chapter, the LHC is briefly described followed by the detailed description of the CMS detector and its components.

3.2 The Accelerator: Large Hadron Collider

The LHC accelerator is designed to collide two counter-rotating proton beams with a maximal center-of-mass energy ($\sqrt{s}$) of 14 TeV (7 TeV per each beam) and a peak luminosity of $\mathcal{L} = 10^{34}\,\mathrm{cm^{-2}s^{-1}}$. An overview of the LHC is shown in Figure 3.1. It can also provide heavy Pb ions collision with an energy of 2.76 TeV per nucleon and a peak instantaneous luminosity of $10^{27}\,\mathrm{cm^{-2}s^{-1}}$. Proton beams are confined around the accelerator ring which is kept at ultra-high vacuum state by a strong magnetic field maintained by 1232 dipole electromagnets, 392 focusing quadrupole magnets, and 3700 multipole magnets. These electromagnets coil's niobium-titanium (NbTi) wires must be kept at a temperature of 1.9 K (−271.3°C) colder than the 2.7 K of outer space in order to reach a superconduction state. The cryogenic system with a closed circuit of 120 tonnes of liquid-helium cools 36,000 tonnes of the magnet and all of the magnets on LHC produce a magnetic field of 8.33 Tesla to keep particle beams on the course around the ring. The LHC machine accelerates two high-energy proton beams to 99.9999991% of the speed of light in opposite directions in separate beam pipes and smashes them together up to 600 million times every second at four interaction points (IP) on the ring.

There are four gigantic detectors surrounding each of these collision points: CMS, ATLAS, LHCb, and ALICE. Each experiment at the LHC using these detectors serves a distinct purpose. CMS (Compact Muon Solenoid) [67] and ATLAS (A Toroidal LHC ApparatuS) [68] are general-purpose detectors designed to investigate a broad spectrum of particle physics ranging from precision measurement of the Standard Model particle (including the Higgs boson) to searching possible new physics like extra-dimension and dark matter. LHCb (LHC Beauty experiment) [69] is designed to make the exquisite measurement of B mesons to study the subtle differences between matter and antimatter also CP violation and rare decays of heavy quarks. ALICE (A Large Ion Collider Experiment) [70] is designed for Pb-Pb collisions and its main aim is to detect the quark gluon plasma. In addition, there are three small experiments called LHCf (LHC Forward experiment) [71] and TOTEM (TOTal Elastic and diffractive cross section Measurement) [72], which focus on forward particles to test theories of ultra high-energy cosmic rays atmospheric shower development and MoEDAL (Monopole and Exotics Detector at the LHC) [73] to search for a hypothetical particle called the magnetic monopole . The Figure 3.1 shows the locations of these official LHC experiments.

Operation of LHC at 13 TeV

The LHC had started its first research run so-called 'Run 1' from March 2010 to early 2013 at a 3.5 to 4 TeV per beam (7 to 8 TeV total). In 2012, given this data CMS and ATLAS were able to announce the discovery of the Higgs boson on 4th July. Afterwards, to prepare the machine for next running at almost double the energy of Run1, LHC shut down on 14 Feb 2013 and took a long technical stop(LS1) for upgrades for 2 years. During LS1, one principal activity is the opening of all magnet interconnects, the measurement of the resistance of all splices in the cables that carry the current between the main dipole and quadrupole magnets, and the repair of any non-conformities. The LHC had restarted its second 3 year (2015-2018) run so called 'Run2', reaching 6.5 TeV per beam (13 TeV total) in early 2015. (The long term LHC schedule can be founded in [74]) In 2015, LHC delivered peak luminosity in the order of $4.4 \times 10^{33}\,\mathrm{cm^{-2}s^{-1}}$ to CMS and ATLAS with an integrated luminosity of $4\,\mathrm{fb^{-1}}$. In 2016, beam intensity and

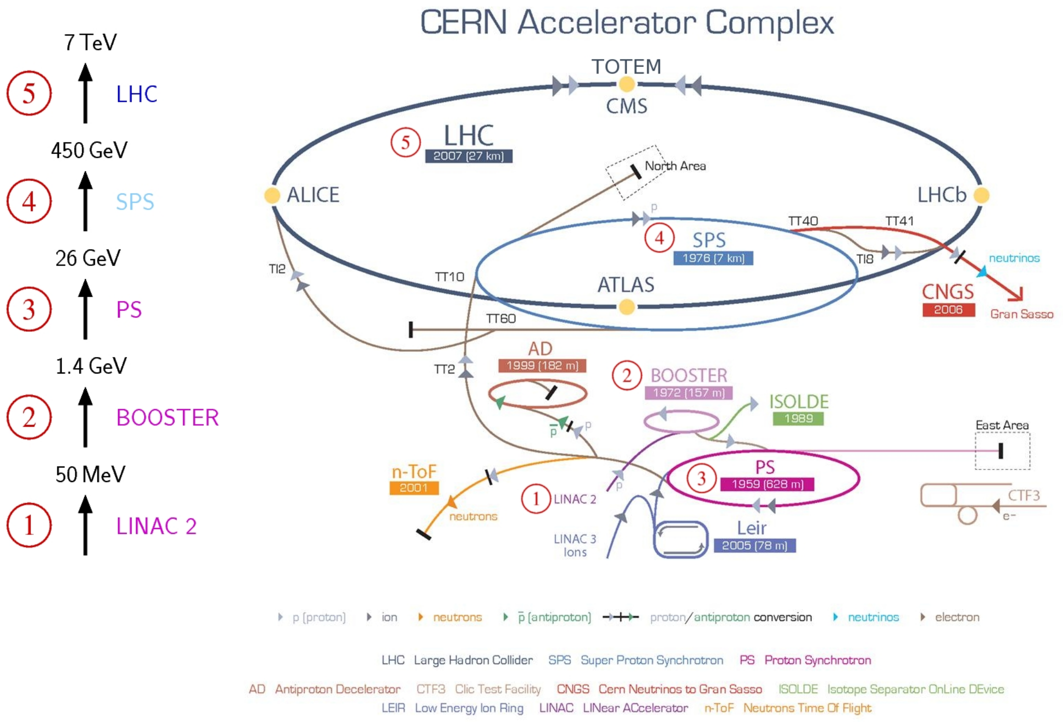

Figure 3.1: The picture of the LHC accelerator chain. Protons start to travel at the linear accelerator LINAC2 and then follow 3 circular accelerators: Booster, Proton Synchrotron(PS), and Super Proton Synchrotron(SPS). The proton injection energy at the LHC is 450 GeV and they accelerated up to 6.5 TeV before the collisions.

the number of bunches were increased and a final integrated luminosity reached 40 fb^{-1} for CMS and ATLAS. The luminosity at the LHC is defined as follows :

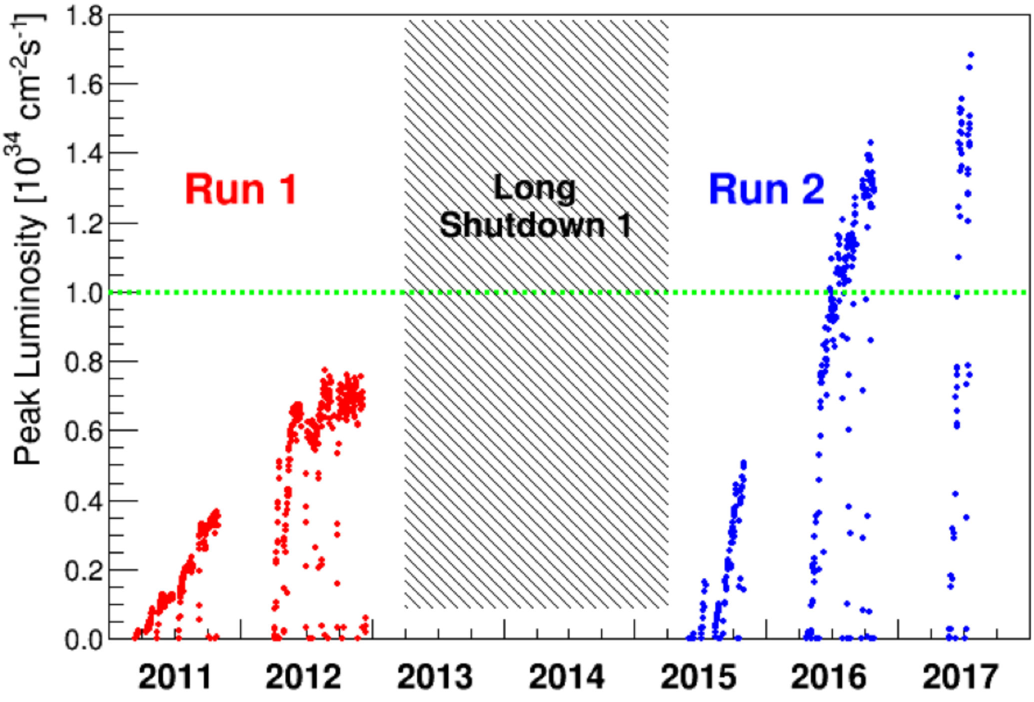

Figure 3.2: Evolution of the LHC peak luminosity over the past seven years. The green dotted line is the LHC design luminosity.

$$L = \frac{\gamma f_{rev} n_b N_p^2}{4\pi \epsilon_n \beta^*} \tag{3.1}$$

where γ is the Relativistic Lorentz factor, f_{rev} is the revolution, k_B is the number of bunches, N_p is the number of protons bunch, ϵ_n is the normalized transverse emittance, β^* is the betatron function at the IP, and F is the reduction factor due to the crossing angle. The target energy of each proton beam is 7 TeV and the designed luminosity of 10^{34} $cm^{-2}s^{-1}$ leads to about one billion proton-proton interactions per second.

The LHC parameters relevant for the operation of CMS experiment and their values of Run2 (2015 and 2016) are listed in Table 3.1. The result in this thesis is based on Run2 13 TeV pp collision data collected by CMS detector in 2016.

Parameter	Designed	2015	2016	description
$\sqrt{s}$	14	13	13	[TeV]
Luminosity(L)	10^{34}	5.3×10^{33}	1.1×10^{34}	Peak luminosity[$\mathrm{cm^{-2}\,s^{-1}}$]
n_b	2808	2376	2736	Num of colliding bunches
N_p	1.15×10^{11}	1.1×10^{11}	1.18×10^{11}	Num of protons/bunch (at start)
f_{rev}	11245	11245	11245	Revolution frequency [Hz]
γ_r	6930	6930	6930	Relativistic Lorentz factor (E/m)
ϵ_n	3.75	2.5	3.5	Emittance into Stable Beams [μ m]
β^*	0.55	0.8	0.4	β^* function at IP [m]
$\sigma_{x=y}$	17.25	19.81	14.21	Transverse beam size at IP [μ m]
σ_z	7.55	7.87	7.87	Longitudinal bunch length [cm]
Pile-up		21	40	Peak mean pu (inelastic $\sigma = 80\,\mathrm{mb}$)

Table 3.1: The machine parameter relevant to the LHC beam and their typical value of designed 14 TeV operation and of Run2 in 2015 and 2016 at 13 TeV . Detailed description of these parameter are documented in [64]. All values are taken from [75].

Introduction to LHC physics

The LHC has established to collide stable beam at a center of mass energy of 13 TeV and produce the particles. The different physics processes have different probabilities and these probabilities are referred to as cross sections. At a given center of mass energy, the cross sections for the various processes are constant. In Figure 3.2, a summary of cross section measurements of each SM process are well displayed. For the discovery of new particles with extremely small cross section, it is important to increase production rate of the events of interest. The total number of events of a certain process, N_p, produced in a certain period of time, dt at a particle accelerator is given as:

$$N_p = \sigma_p \int \mathcal{L} dt \tag{3.2}$$

Where σ_p is the cross section[1] and corresponds to the effective area for a given process to occur at a $\mathcal{L}$, the instantaneous luminosity. To increase event rate, the $\mathcal{L}$ is required to be as high as possible. It depends on the number of particles in each proton beam and on the size of overlap of both beams at the collision point (in Equation 3.1, Table 3.1). Thus maximizing the instantaneous luminosity over a long time represents a technological challenge for the accelerator. In 2016 at 13 TeV, finally LHC surpassed its maximum peak value at the design instantaneous luminosity of $\mathcal{L} = 10^{34}\,\mathrm{cm^{-2}\,s^{-1}}$. The integrated luminosity (L) is the integral of $\mathcal{L}$ over time, $L = \int \mathcal{L} dt$. This is the total amount of collisions delivered by the LHC. In the real world, recording all the luminosity delivered by the LHC

[1] unit Barn, $1\,\mathrm{b} = 10^{-28}\,\mathrm{m}^2$

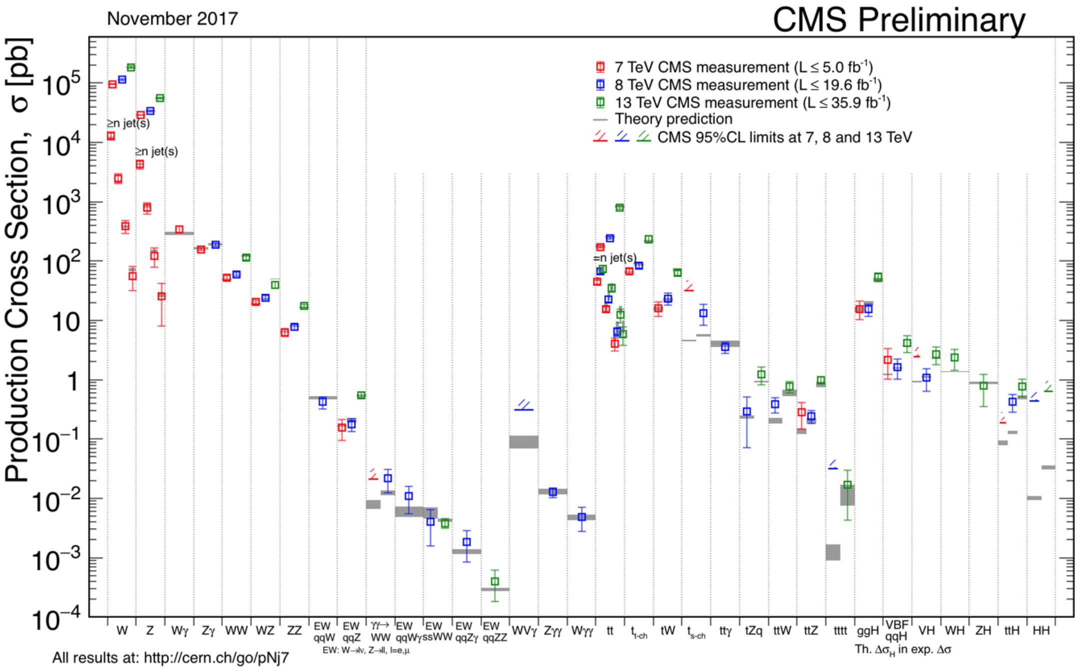

Figure 3.3: Summary of the cross section measurements of Standard Model processes at different $\sqrt{s} = 7$ (red), 8 (blue), 13 (green) TeV, compared to the theoretical predictions (gray). This figure demonstrates that the measurements are surprisingly in agreement with SM predictions.

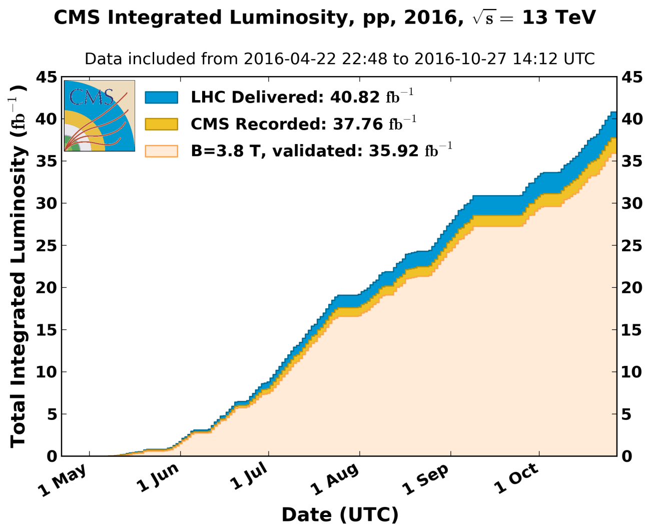

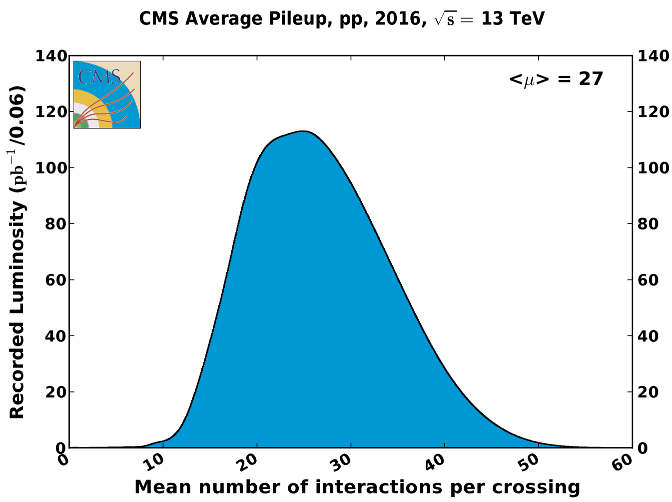

Figure 3.4: The plot on the top shows the cumulative curves for the luminosity delivered by LHC (azure), recorded by CMS (orange) and certified as good for physics analysis during stable beams (light orange). The luminosity validated for physics analysis corresponds to data recorded with all detectors and reconstructed physics objects showing good performance. The plot on the bottom shows the average number of interaciton per bunch crossing denoted as pileup in 2016 at 13 TeV.

is a complicated. In 2016, the overall uncertainty in the measured integrated luminosity recorded by the CMS experiment is estimated to be 2.5% [76]. The LHC Run 2 program has delivered approximately delivered 40.82 fb^{-1} and the CMS detector recorded 92.5 % (37.8 fb^{-1}) of proton-proton collisions to the CMS and ATLAS experiments. Prior to physics analysis, all data should go through stringent certification procedure that ensures that only those with the highest possible quality are used. The total amount of luminosity certified for analysis is **35.9** fb^{-1} at 13 TeV in this study. A summary of the delivered and recorded luminosities in 2016 Run2 is shown in Figure 3.4-top.

Pileup

At the hadron collider experiment like LHC, the proton beam is bunched not continuous. Every time bunches crossing each other, more than one proton-proton interaction occurs (See Figure 3.5) and these multiple interactions are known as pileup (PU). This specifically refers to cases where there are other (background) collisions somewhere within a timing window around the signal collision. CMS experiment has to observed the decay products of various particles produced in these collisions and then determines which collision interactions produced which particles. In 2016 Run2, the average number of interaciton per bunch crossing is $<\mu>= 27$ (See Figure 3.4-bottom). The probability of having $\mu = \mathrm{n_{pu}}$ depends only on the total inelastic pp cross section (σ_{pp}) as follows :

$$\mathrm{P}(\mathrm{n_{pu}}) = \frac{(\mathcal{L}\cdot\sigma)^{\mathrm{n_{pu}}}}{\mathrm{n_{pu}}!}\cdot \mathrm{e}^{-(\mathcal{L}\cdot\sigma)} \tag{3.3}$$

The pileup is sensitive to the instantaneous luminosity per bunch crossing (Equation 3.1). By raising luminosity to collect more data, this leads to an increase in the number of proton-proton collisions per bunch crossing and PU. The measurement of the luminosity is based on the pixel tracker and has been calibrated by means of a dedicated analysis of Van der Meer scans. Details can be found in [76]. The inelastic pp cross section, σ_{inel}, is used in the estimation of PU and is thus important to properly control the contribution of PU in pp collision events at LHC[2]. In 2016 the total $\sigma_{\mathrm{inel}} \sim 69.2$ mb at 13 TeV. (More on PU for this analysis will be described in Section 5.4).

Parton distribution functions

In hadronic collision, the initial scattering occurs between constituents that are not elementary. This is the key feature of LHC phenomenology. At first order,

[2] In CMS the total σ_{inel} is measred by hadron forward calorimeter HF ($+3.0 < \eta < +5.2$) and CASTOR ($-6.6 < \eta < -3.0$).

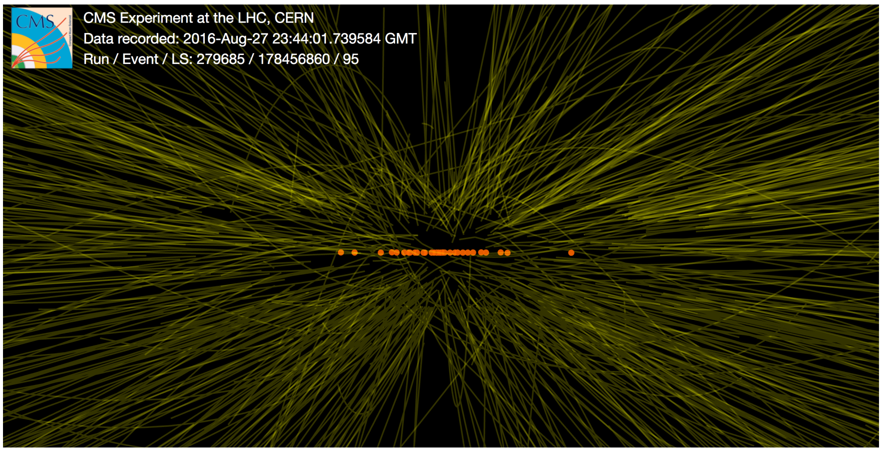

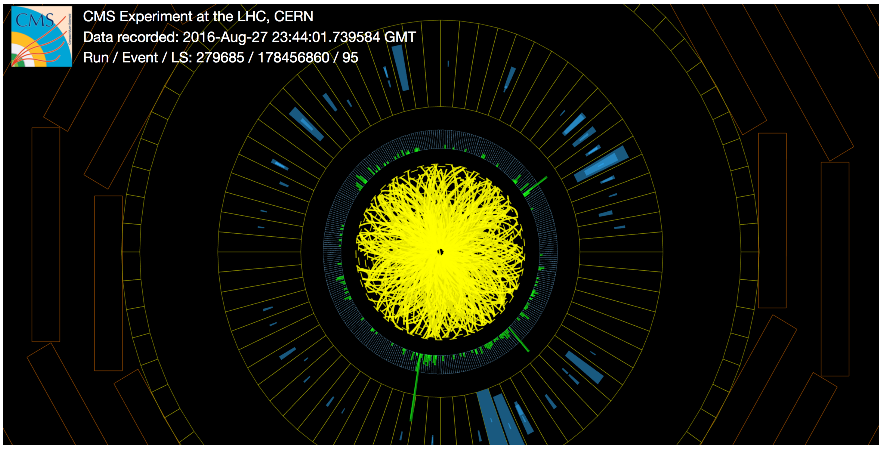

Figure 3.5: The CMS Rho-Z (top) view of reconstructed vertices (orange circles) in one beam crossing, obtained from a specific proton-proton collision run at 13 TeV in 2016. (A high-pileup event with 30 reconstructed vertices.) The bottom one is for the CMS Rho-Phi view. These event displays are taken from [77].

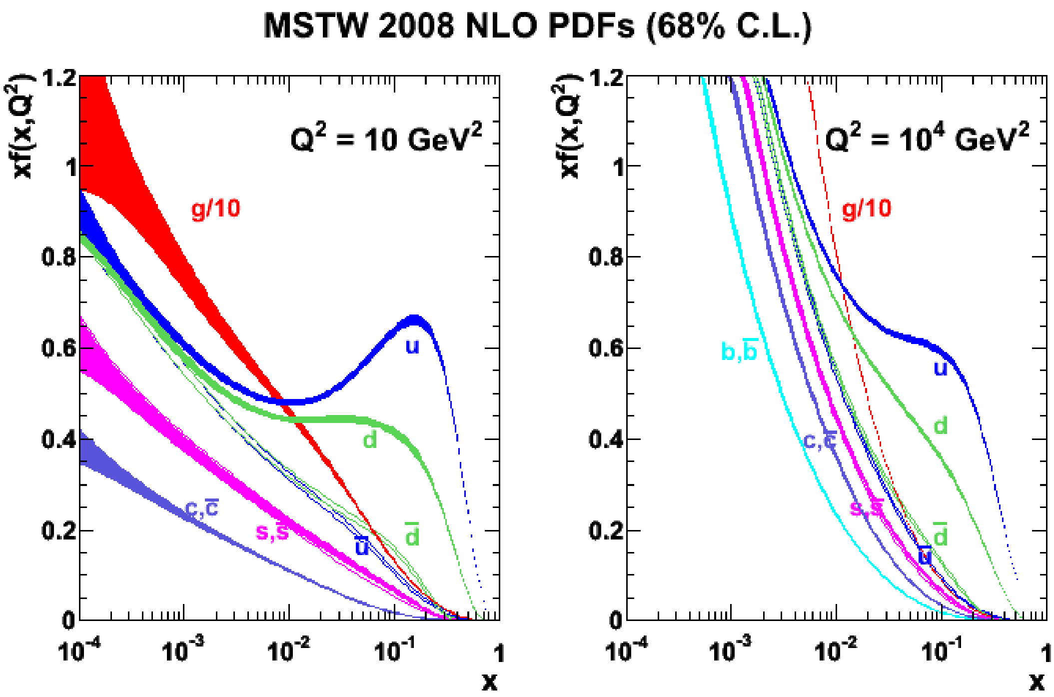

Figure 3.6: The Parton distribution function for each parton determination from the MSTW [78] group using deep inelastic scattering energy scale $Q^2 = 10\,\mathrm{GeV}^2$ (left) and its evolution to the LHC energy scale $Q^2 = 10^4\,\mathrm{GeV}^2$ (right)with the DGLAP evolution equation [79].

only one parton[3] from each proton participates to the collision, and the energy scale of the interaction vertex of a proton proton collision, Q^2, is defined with respect to the fraction of momentum along the beam axis, x, carried by the two partons i and j that participate to the interaction: $Q^2 = \hat{s} = x_i x_j s$, where $\hat{s}$ is defined as an effective center of mass energy of the collisions, differ from the center of mass energy s.
For each type of parton in the proton i (= u, d, s, c, b, g, and t) the Parton Distribution Function (PDF), $f_i(x, Q^2)$, defined as the probability density function for finding a particle with a certain longitudinal momentum fraction, x, carried by the parton at a given energy scale Q^2. The structure of hadrons is studied in deep inelastic collisions of leptons and hadrons. Here, the momentum of the lepton before and after the collision, gives the transferred four-momentum $q(Q^2 = -q^2)$. The proton is made of three valence quark (uud) and the remaining sea quarks.

[3] Parton is a constituent of the hadron and subsequently referred to as quarks and gluons.

Total sum (=probability) of the fractions x for each parton must add up to 1.

$$\sum_{i=\mathrm{u,d,s}\cdots} \int_0^1 dx x f_i(x, \mathrm{Q}^2) = 1$$
$$\int_0^1 dx(f_\mathrm{u}(x) - f_{\bar{\mathrm{u}}}(x)) = 2 \ , \ \int_0^1 dx(f_\mathrm{d}(x) - f_{\bar{\mathrm{d}}}(x)) = 1 \quad \text{for valence quarks}$$
$$\int_0^1 dx(f_\mathrm{s}(x) - f_{\bar{\mathrm{s}}}(x)) = 0 \ , \ f_\mathrm{c,b}(x) = f_{\bar{\mathrm{c}},\bar{\mathrm{b}}}(x) \quad \text{for sea quarks} \tag{3.4}$$

Many PDF groups use different methodologies and data samples to evaluate the $f_i(x, \mathrm{Q}^2)$ in their own PDF fits. These lead to the irreducible systematic uncertainties for the production cross section. This will be described in section 6. The PDFs can be interpreted as the probability to define a parton carrying the momentum fraction x given a momentum transfer. They are used in a hadron collider to compute the cross section of any process, $\sigma_{\mathrm{i,j}\rightarrow\mathrm{X}}(\mathrm{s}, \mathrm{Q}^2)$ is given as follows:

$$\sigma_{\mathrm{i,j}\rightarrow\mathrm{X}}(\mathrm{s}, \mathrm{Q}^2) = \sigma_{i,j} \int_{x_{min}}^1 dx_1 dx_2 f_i(x, \mathrm{Q}^2) f_j(x, \mathrm{Q}^2) \hat{\sigma}_{\mathrm{i,j}\rightarrow\mathrm{X}}(x_1 x_2 s, \mathrm{Q}^2) \tag{3.5}$$

Where $\hat{\sigma}_{\mathrm{i,j}\rightarrow\mathrm{X}}(x_1 x_2 s, \mathrm{Q}^2)$ term is the partonic cross section. Radiative corrections from initial state emissions are absorbed into PDFs and separated from the partonic cross section calculation. This procedure introduces a factorization scale (μ_F) in the calculation and it can be set to the energy scale for the process, $\mu_\mathrm{F} = \mathrm{Q}^2$.
It is important that PDFs are the empirical fuction so they cannot be determined only from theory. It needs to be calculated using input from experimental measurements carried out at different energy scales. Once PDFs are determined at a given scale, they are recomputed at any other energy scale by using the DGLAP evolution equation [79]. They have been obtained as a result of a QCD fit using data collected from many different experiments (HERA, Tevatron, and LHC). For example, most of the PDF measurements were done at the Deep Inelastic Scattering (DIS) scale of $\mathrm{Q}^2 \sim 10\ \mathrm{GeV}^2$ and extracted PDFs are extrapolated to the LHC physics scale $\mathrm{Q}^2 \sim 10^4\,\mathrm{GeV}^2(\sim \mathrm{M}_\mathrm{Z}^2)$. The Figure 3.2 show the PDF determination from the MSTW group using DIS data on the left and its evolution to the LHC scale with the DGLAP evolution equation on the right. One of the main effects of evolution to the LHC scale is the enhancement of gluon and sea quark PDFs at low x. Different measurements allow constraining different PDF at different x.

The Hard Parton Scattering

The scattering processes at high energy hadron colliders can be classified as hard or soft. QCD is the underlying theory for all such processes, but the approach is different for these two cases. The hard scattering is referred as proton-proton interactions that involve the creation of a hard process and the "hard" means the large momentum transfer Q^2, either a creation of a system of large mass. Therefore the production rates and event properties can be predicted with some precision using perturbative QCD. Otherwise, for the soft processes, the rates and properties are dominated by non-perturbative QCD effects. For the hard parton scattering for a certain process $\mathrm{i,j} \to \mathrm{X}$, the partons i and j are directly involved in the interaction carrying a longitudinal momentum fraction x_i and x_j, respectively. By the convenient Feynman formalism, the partonic cross section is computed by the phase-space integral of the corresponding squared matrix element $|\mathcal{M}_{\mathrm{i,j}\to\mathrm{X}}|^2$. The matrix element is defined as the infinitie sum of over all the possible ways to perform the process :

$$\begin{aligned} \mathcal{M}_{\mathrm{i,j}\to\mathrm{X}} &= \sum_{i}^{\infty} \mathcal{F}^{(i)}_{\mathrm{i,j}\to\mathrm{X}} \\ \mathcal{M}_{\mathrm{i,j}\to\mathrm{X}} &= \mathcal{F}^{0}_{\mathrm{i,j}\to\mathrm{X}}(\mathrm{g_s^{qcd} g^{em} g'^{ew}}) + \sum_{\mathrm{n=0}}^{\mathrm{n'}} \mathcal{F}^{\mathrm{corr.}}_{\mathrm{i,j}\to\mathrm{X}}(\mathrm{g_s^{qcd+n} g^{em} g'^{ew}}) \end{aligned} \tag{3.6}$$

Each term in this expansion, $\mathcal{F}^{(i)}_{\mathrm{i,j}\to\mathrm{X}}$, corresponds to one allowed Feynman diagram computed using the Feynman rules. The subset of the lowest order Feynman diagrams is so-called Leading Order (LO) and is denoted as $\mathcal{F}^{(0)}_{\mathrm{i,j}\to\mathrm{X}}(\mathrm{g_s^{qcd} g^{em} g'^{ew}})$, where $\mathrm{g_s^{qcd}}$ is the minimum number of QCD interacting vertices with strong coupling constant, and $\mathrm{g^{em} g^{ew}}$ is the minimum number of electromagnetic or electroweak vertices with their coupling constant.

The Leading Order cross section prediction correspons to the term up to n = 0, QCD Next-to-leading order (NLO) cross section includes up to n =1, and Next-to-next-to leading order(NNLO) includes up to n=2 $\cdots$. When the presence of QCD interacting vertices increased by n, coupling constant expanded with the powers of $\alpha_\mathrm{s}(= \mathrm{g_s^2}/4\pi)$ as follows :

$$\hat{\sigma} = \sigma^{\mathrm{Born}}(1 + \frac{\alpha_\mathrm{s}}{2\pi}\sigma^{(1)} + \left(\frac{\alpha_\mathrm{s}}{2\pi}\right)^2 \sigma^{(2)} + \left(\frac{\alpha_\mathrm{s}}{2\pi}\right)^3 \sigma^{(3)} + \cdots \tag{3.7}$$

The EW correction with higher number of EW vertices that involve W, Z, H or γ is also possible to consider. In general the effect of the NLO EW corrections is quiet small since at the LHC energy scale, $\mathrm{g_s^2} \sim \mathrm{g'}$. However when the invariant mass of the process ($\mathrm{Q^2} \sim \mathrm{M_X^2}$) is larger enough ($\mathrm{Q} \gg \mathrm{M_{W/Z}}$), electroweak correction are dominated by large negative Sudakov corrections of $\mathrm{g'log^2 Q/M_W^2}$, that could enhance the EW correction at high masses. In some cases, these enhanced EW

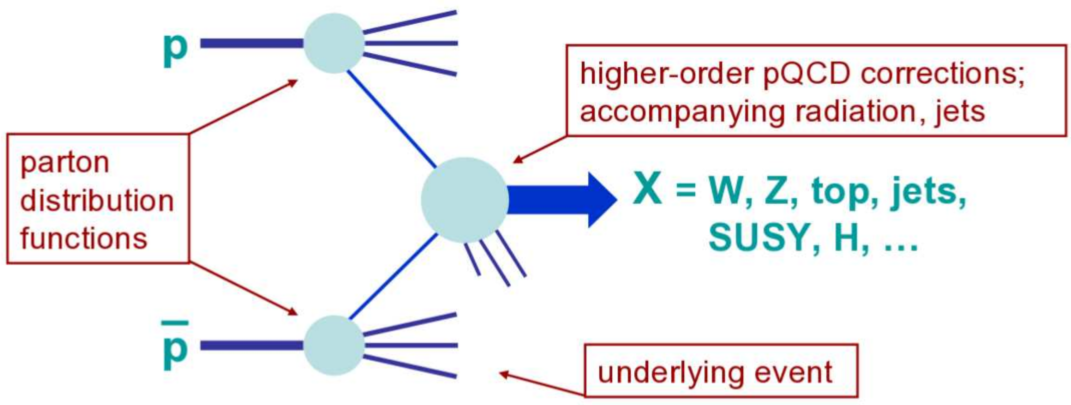

Figure 3.7: A schematic representation of a proton-proton collision in LHC.

corrections affect the background in searches of new massive particles.
Thus, though the LO calculations provide the fastest and simplest calculation, in order to achieve the precise theoretical predictions and reduce the uncertainties for production cross sections, higher-order correction terms need to be considered. In this thesis, NNLO QCD correction and NLO EW corrections are considered (Section 4.3.1).

The Underlying Event

The Figure 3.7 shows a process in the proton proton collision at the LHC. Here, the underlying event (UE) refers to the additional activity produced in soft scattering, together with the remnants of the beam hadrons. At sufficiently high energy (at the LHC), the several hard parton scattering processes between other incoming partons, so-called multiple parton interactions (MPI). The UE is mostly derived from the hadronization of the partons that did not take part in the hard scattering and potential MPI. To describe the UE, one has to resort to models which are typically implemented in event generators. Due to the theoretical complexity of describing the UE activity, current generators rely on phenomenological models and constrain their parameters using collision data. The calibration of the UE activity with data is referred as the tuning of the generator so-called CMS Underlying Event Tune Pythia8 Monash Version1 (CUETP8M1) [80, 81]. For the effects of the UE and of MPI, theoretical uncertainty can be estimated by comparing the results obtained with different event generators.

3.3 The detector: Compact Muon Solenoid

The Compact Muon Solenoid (CMS) is a multi-purpose detector designed to identifies particles and measure their properties such as momentum and energy. It has a broad physics programming ranging from studying the Standard Model including the Higgs boson to search for signatures of new physics. Especially, the detection of physics beyond the Standard Model such as searching for new massive vector bosons, extra dimensions and dark matter becoming more crucial goal after the discovery of a Higgs boson in 2012. The CMS detector has a cylindrical structure which is 21.6 meters long, 15 meters in diameter and it is built around a huge solenoid magnet. This cylindrical coil of superconducting cables generates a magnetic field of 4 tesla. The field is confined by a steel yoke that forms the bulk of the detectors 14,000-tonne weight. To exploit the different interaction properties of particles, CMS is made up of different layers. From the innermost part of the outer part, the CMS detector consists of 5 components. Each component is optimized to detect and measure specific particles as shown in Figure 3.8. The central feature of the CMS apparatus is a superconducting solenoid of 6 m

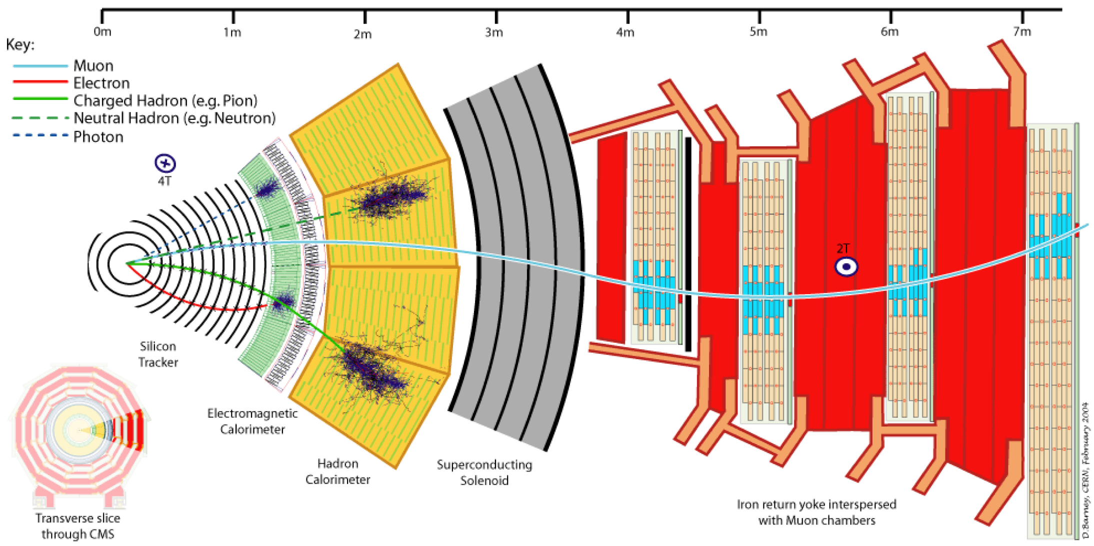

Figure 3.8: A schematic view of the specific particle interactions in a transverse plane of the CMS detector, from interaction point region to the muon deteector.

internal diameter, providing a magnetic field of 3.8 T. Within the solenoid, the volume is a silicon pixel and strip tracker, a lead tungstate crystal electromagnetic calorimeter (ECAL), and a brass and scintillator hadron calorimeter (HCAL), each composed of a barrel and two endcap sections. Forward calorimeters extend the pseudorapidity coverage provided by the barrel and endcap detectors. Muons are detected in gas-ionization chambers embedded in the steel flux-return yoke outside the solenoid. A picture of the CMS detector is shown in Figure 3.9

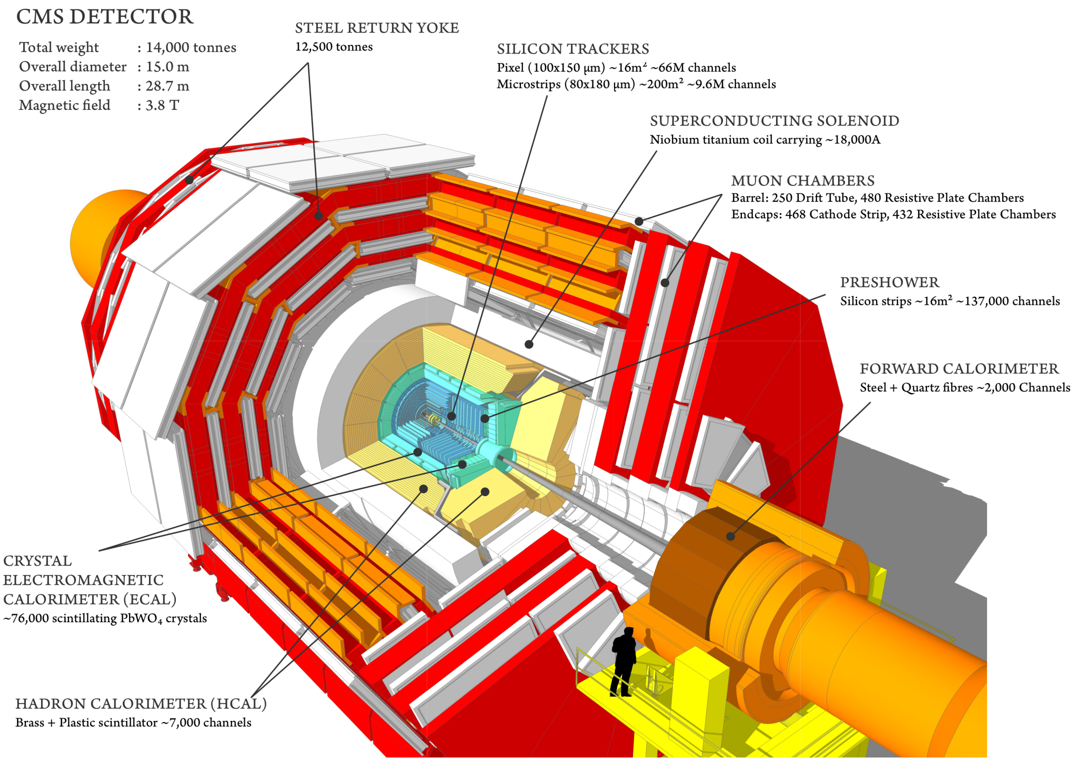

Figure 3.9: The overview of the CMS detector. This picture is taken from [82].

- Layer 1 Tracker: entirely made of silicon, it tracks the charged particles that curve in the magnetic field thus providing a measurement of the momentum of the particle.

- Layer 2 Electromagnetic Calorimeter (ECAL): it measures with high accuracy the energies of electrons and photons. Electromagnetic showers are initiated by the impinging electrons and photons that develop inside the calorimeter producing scintillation light, which is detected, in proportion to the particles energy.

- Layer 3 Hadronic Calorimeter (HCAL): it measures the energy of hadrons, i.e. particles made up of quarks and gluons (protons, neutrons, pions, and kaons) which penetrate more than electrons and photons due to their different properties of interaction with matter.

- Layer 4 Superconducting solenoid: a huge magnet to generate the 4 T magnetic field.

- Layer 5 Muon chambers and return yoke: muons are charged particles just like electrons and positrons, but 200 times more massive. They can penetrate several meters of iron without interacting, and thats why they cannot be detected by the ECAL but they need a specific detector. Muon chambers are the gas detector that allows the identification of the muons and the measurement of their momenta, interleaved with magnet coils (return yoke) that guide the magnetic field.

In next section, before describing details of sub detector layers, the coordinate system and popularly used variables have to be explained first.

3.3.1 The Coordinate system and important Variables

The reference frame for the LHC is a right-handed cartesian coordinate system, whose origin is decided to the interaction point, with the x-axis pointing towards the LHC center, the z-axis being defined along the proton beam line and the y-axis upward. This coordinate system is shown in Figure 3.10). In the CMS detector, the conventional coordinates triplet system (z, ϕ, η) is commonly used. z is the distance from the z-axis, ϕ is the azimuthal angle in the transverse plane and η is the pseudo-rapidity defined as Equation 3.8. This η quantity has a property that it transforms additively under a Lorentz boost along the z-axis It is particularly useful in hadron collider, where interactions rarely have their center of mass frame coincident with the detector rest frame and measure for highly energetic and relativistic particles.

$$\eta = -\ln[\tan(\frac{\theta}{2})] \tag{3.8}$$

Where θ is the polar angle $(0 < \phi < \pi)$ measured with respect to the z-axis and it is odd about $\theta = 90°(\eta(\theta) = -\eta(180° - \theta))$.
For example, $\theta = 0, \pi/2, \pi$ leads to $\eta = \infty, 0, -\infty$. The negative sign makes η positive when points to the same direction as the magnetic field. The angle between 2 objects (η_1, ϕ_1) and (η_2, ϕ_2) is often used, being $\Delta\text{R} = \sqrt{\Delta\eta^2 + \Delta\phi^2}$

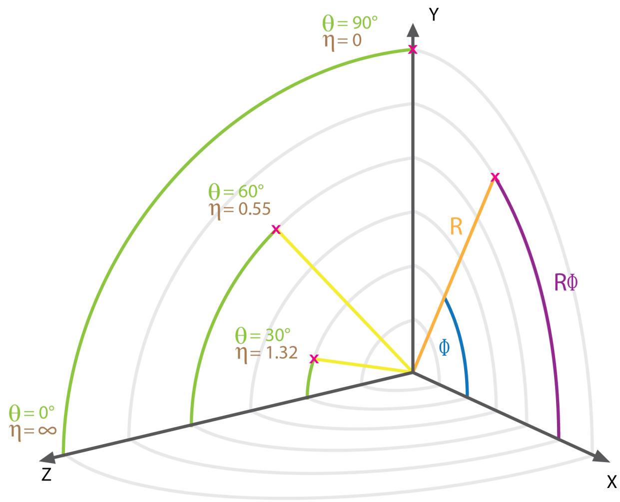

Figure 3.10: The coordinate system of the CMS detector. The beam direction is parallel to the z direction.

$(\Delta\eta = \eta_1 - \eta_2, \Delta\phi = \phi_1 - \phi_2)$.
In addition, the so-called "transverse variables" $\mathrm{E_T}, \mathrm{p_T}, \vec{\mathrm{p}}_\mathrm{T}^\mathrm{miss}, \mathrm{E_T^{miss}}$ and $\mathrm{M_T}$ are often used. The transverse energy $\mathrm{E_T}$ in place of the scalar energy E, and the transverse momentum $\mathrm{p_T}$ in place of the scalar momentum p. These variables are defined as the projection of the energy and momentum onto the transverse plane for the proton beam direction.

$$\mathrm{E_T} = \mathrm{E}\sin\theta \text{ and } \mathrm{p_T} = \mathrm{p}\sin\theta \tag{3.9}$$

Interesting and rare processes, such as new electroweak boson, are marked by particles with high transverse momenta, referred to as "high-$\mathrm{p_T}$"physics. The missing transverse momentum vector $\vec{\mathrm{p}}_\mathrm{T}^\mathrm{miss}$ also defined as the projection onto the plane perpendicular to the beam axis of the negative vector sum of the momenta of all particles produced in an event.

$$\vec{\mathrm{p}}_\mathrm{T}^\mathrm{miss} = -\sum_\mathrm{i} \mathrm{p_T} \cdot \hat{\mathrm{n}}_\mathrm{i} \tag{3.10}$$

Its magnitude is referred to as $\mathrm{p_T^{miss}}$ or $\mathrm{E_T^{miss}}$. Because of momentum conservation in each direction, the transverse momentum of protons was zero before the collision, the magnitude of $\mathrm{p_T}$ to be also zero. Therefore $\vec{\mathrm{p}}_\mathrm{T}^\mathrm{miss}$ is an imbalance in the transverse momentum that must have been carried by invisible particles (neutrino or some other invisible, stable, non-interacting, as yet undiscovered particles). In this thesis, we select events with a very high $\mathrm{p_T}$ charged lepton and large missing transverse energy ($\mathrm{E_T^{miss}}$). The remaining one, the transverse mass $\mathrm{M_T}$, is a key variable in this analysis.

Suppose that we consider a single heavy particle of mass M produced in association with visible particles (1, ℓ) and invisible particle (2, ν), assumed to come from a two-body decay. It is impossible to measure z-components of invisible particle, the mass of the parent particle can be constrained with the quantity M_T defined as follows :

$$\begin{aligned} M_T &\equiv \sqrt{[E_{T,1} + E_{T,2}]^2 - [\vec{p}_{T,1} + \vec{p}_{T,2}]^2} \\ &= \sqrt{m_1^2 + m_2^2 + 2[E_{T,1}E_{T,2} - \vec{p}_{T,1} \cdot \vec{p}_{T,2}]} \end{aligned} \tag{3.11}$$

$$M_T \equiv \sqrt{2p_{T,1}E_{T,2}^{miss}(1 - \cos[\Delta\phi(\vec{p}_{T,1}, \vec{p}_{T,2}^{miss})])} \tag{3.12}$$

Where $\vec{p}_{T,2} = \vec{p}_T^{miss}$ and $\Delta\phi(\vec{p}_{T,1}, \vec{p}_{T,2}^{miss})$ is the difference in azimuthal angle between 2 decaying particles.

3.3.2 Tracker System

The Tracker is a closest sub-detector to the collision point of particle beams and it has a length of 5.8 m and a diameter of 2.5 m and provides a coverage up to $|\eta| < 2.5$. The purpose of the tracker system is measuring tracks of charged particles and quantifying their momentum in the small time interval between each bunch crossing (25 ns). To assign the momentum, tracker reconstructs particle's trajectories through a magnetic field. (the more curved the path, the less momentum the particle had.) In order to perform reconstruction of trajectories and momentum assignment to each bunch crossing, a high granularity for precision positions measurement and fast response are essential. These allow providing a good spatial and time resolution of the tracker. A scheme of the tracker is shown in Figure 3.11 and detailed descriptions and its performance result are provided in [83, 84, 85]. It is completely made of silicon, which is the best choice for tracking purposes in the LHC environment to cope with high energetic particle fluxes and damage of radiation. It consists of two sub detectors: an silicon pixel detector, at the core of the detector and dealing with the highest intensity of particles, and a silicon microstrip detectors that surround it.
The innermost pixel detector has 3 cylindrical barrel layers (BPIX) having active length of 53 cm with radius of 4.4, 7.3 and 10.2 cm, and 2 forward backward disks (FPIX) located at longitudinal position z of of ±34.5 and ±46.5 cm with radius from 4.8 cm to 14.4 cm. The BPIX consists of 48 million pixels covering a total area of 0.78 m^2 and the FPIX contains 18 million channels covering an area of 0.28 m^2. These pixelated detectors produce 3D measurements along the tracks of the charged particles with single hit spatial resolutions between 1020 μm, a fraction of the width of a human hair. The system facilitates efficient 3-hit coverage in the region of $|\eta| < 2.2$ and efficient two-hit coverage in the region of $|\eta| < 2.5$.

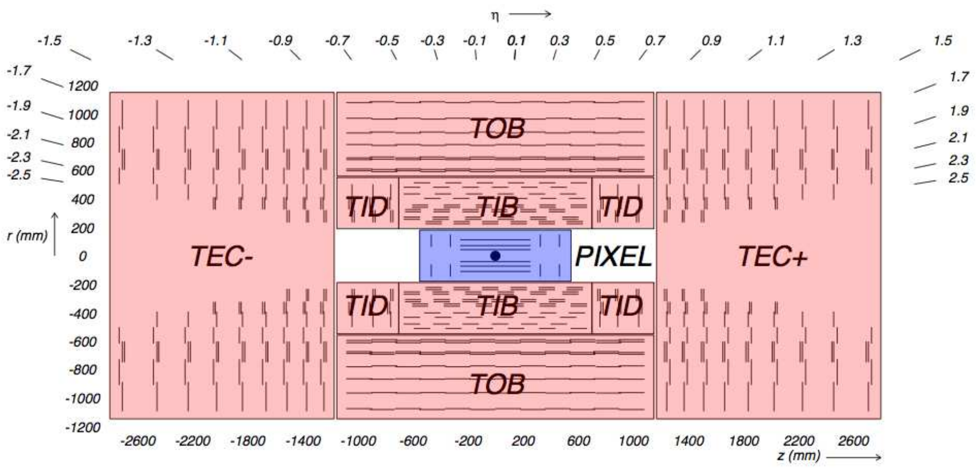

Figure 3.11: An r-z slice of the CMS Tracker. Each line indicates a detector module. This picture is taken from [67].

The silicon strip detector has 9.3 million active elements instrumenting a surface area of 198 m^2 and consists of 4 subsystems. The Tracker Inner Barrel (TIB) is composed of 4 barrel layers ($|z| < 60$ cm and $20 < r < 55$ cm) and the Tracker Inner Disks (TID) contains 3 disks at each edge ($60 < |z| < 118$ cm) with a spatial resolution of 13-38 μm. The TIB/TID provides up to 4 r-ϕ measurements on a particle's trajectory by using 320 μm thick silicon microstrip sensors, which have their strips placed parallel to the beam axis in barrels and placed radially in disks. These TIB/TID are surrounded by the Tracker Outer Barrel (TOB). The TOB consists of 6 barrel layers ($|z| < 118$ cm and $55 < r < 116$ cm) with 500 μm thick microstrip sensors and has a spatial resolution of 18-47 μm. Beyond z region of TOB, two Tracker EndCaps (TEC) are located ($124 < |z| < 280$ cm and $22.0 < r < 113.5$ cm). Each TEC is composed of 9 disks contained up to 7 rings of radial-strip detectors with 320 μm thick sensor in the inner 4 rings and 500 μm thick in the outer 3 rings. The inner two layers of the TIB and TOB, the inner two rings of the TID and TEC and the 5th ring of the TEC include a 2nd microstrip detector module that is mounted back-to-back at a stereo angle of 100 mrad and that enables a measurement of the orthogonal coordinate. Assuming fully efficient planes and not counting hits in stereo modules, there are from 8 to 14 high precision measurements of track impact points for $|\eta| < 2.4$. More detailed of the tracker system can be found in [86, 87].

3.3.3 Electromagnetic Calorimeter

The electromagnetic calorimeter (ECAL) is a compact, hermetic, homogeneous and fine-grained crystal based calorimeter, located just behind the tracker [88].

The purpose of ECAL is to measure the energy of electromagnetic shower with high resolution and to identify electrons/photon (covers $|\eta| < 3$). This system is composed of 61200 lead tungstate ($PbWO_4$) scintillating crystals installed in the barrel (EB) and of 7324 crystals in the 2 endcaps (EE). A 3-D sketch of the ECAL is shown in Figure 3.3.3. To improve photon identification capabilities, a

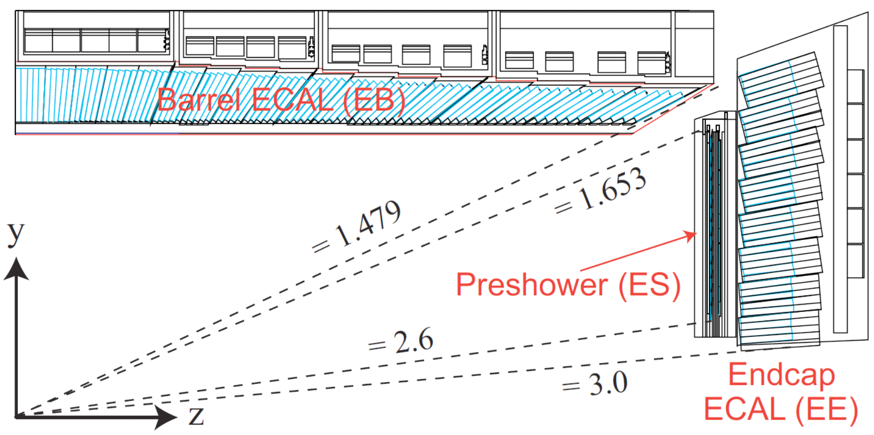

Figure 3.12: The Layout of the CMS ECAL, showing the barrel supermodules, the endcaps, and the pre-shower detectors. The ECAL barrel coverage is up to $|\eta| = 1.479$. the endcaps extend the coverage to $|\eta| = 3.0$. the pre-shower detector fiducial area is approximately $1.65 < |\eta| < 2.6$. This figure was taken from [67]

pre-shower detector (ES) is placed in front of the EE crystals, consists of lead absorbers fitted with silicon strip sensor. The decision of the $PbWO_4$ crystals for CMS ECAL came from many factors. The important features of these crystal are short radiation length ($X_0 = 0.89\,\text{cm}$), small Molière ardius ($R_M = 2.2\,\text{cm}$), high density ($\delta = 8.28\text{g/cm}^3$) and strong radiation tolerancy (10 Mrad). These advantages allow constructing a compact calorimeter with fine granularity. The crystals also have a fast response (emitting 80% of light within 25ns) but relatively low light yield ($30\,\gamma/$ MeV). To enhance this defect, the use of photodetectors (collect and amplify the scintillation light) with intrinsic gain which can be operated in the magnetic field is required. Therefore silicon Avalanche PhotoDiodes (APDs) are used as photodetectors in EB and Vacuum PhotoTriodes (VPTs) in the EE. The crystals and the APD are sensitive to temperature change, therefore the temperature stability (the goal is 0.1°C) and the photodetector gain are crucial for the accurate measurement of the energy deposited in the crystals.

The EB calorimeter is organized into 36 supermodules each including 1700 crystal. These crystals have a truncated pyramidal shape with a cross-section size of $2.2 \times 2.2\,\text{cm}^2$, a length of 23 cm which corresponds to $25.8X_0$ and they are mounted in a quasi-projective geometry (positioned slightly tilted $\sim 3°$ in both

ϕ and in η with respect to the primary interaction vertex) to minimize crystal gaps aligned to the particle trajectories. The EB covers the range of $|\eta| < 1.48$ and amounts to $8.14\,\mathrm{m}^3$, 67.4 ton in total.
The EE calorimeter consists of two dee-shaped sections, consisting of semi-circular aluminum plates arranged in units of 5×5 crystals, known as supercrystals. Each dee (EE) contains 3662 (7324) crystals and crystals are arranged in an x-y grid and tilted like EB ($2.86 \times 2.86 \times 22\,\mathrm{cm}^3$ at inner side, $3 \times 3 \times 22\,\mathrm{cm}^3$ at the outer side), covering $1.479 < |\eta| < 3.0$.
The ES detector, placed in front of the EE, is made of 2 layers of the lead absorber, 2 planes of silicon strip detectors, which installed behind lead disks. The total thickness of ES is 20 cm ($\sim 3\mathrm{X}_0$). To provide accurate position measurment (to identify and separate $\pi^0 - \gamma$), this detector has a much finer granularity than ECAL (4288 sensors, 137216 strips (0.2 cm wide)). Each silicon sensor measure $0.2 \times 6.1 \times 6.1\,\mathrm{cm}^3$ and divided into 32 strips, covering $1.65 < |\eta| < 2.6$. As in the tracker, the ES silicon sensors must be kept at a cold temperature ($\sim -10°\mathrm{C}$). However, the ECAL must be kept within precisely 0.1°C. Therefore, the ES must be cold on the inside but warm on the outside, achieved using both heating and cooling systems. In CMS, the energy resolution of the EB as a function of electron energy measured from beam tests has been measured as:

$$(\frac{\sigma}{E})^2 = (\frac{S}{\sqrt{E}})^2 + (\frac{N}{E})^2 + C^2 \tag{3.13}$$

where S (2.8%) is the stochastic term, N (12%) is the noise and C (0.3%) is the constant term. [89,90] The stochastic term comes from fluctuations in the shower containment as well as photostatistics. The noise term includes the contributions from electronics noise (important at low energy) and pileup energy (in case of a high luminosity environment). The constant term accounts for energy leakage and non-uniformity of light collections.

3.3.4 Hadronic Calorimeter

The CMS hadron calorimeter (HCAL) surrounds the electromagnetic calorimeter and acts in conjunction with it to measure the energies and directions particles (particularly for hadrons such as p, n, π and K) and provides hermetic coverage for measuring non-interacting particles missing transverse energy (such as ν). It also helps identification of e, γ, and μ by cooperating with ECAL and Muon detector. The hadrons are emitted as a tightly collimated spray with almost the same direction and energy as the parent quark or gluon, so-called "jets". The objects therefore actually observed are hadronic jets of ordinary particles. The determination of energy and direction of particle jets and of the missing transverse energy is important to form a signature for new particles (like W', Susy particles).

The HCAL is consist of four sections: the HCAL Barrel (HB), HCAL Endcap (HE), HCAL Outer (HO) and HCAL Forward (HF) sections. A layout of HCAL and the locations of each of these sub-sections are shown in Figure 3.13. The HB

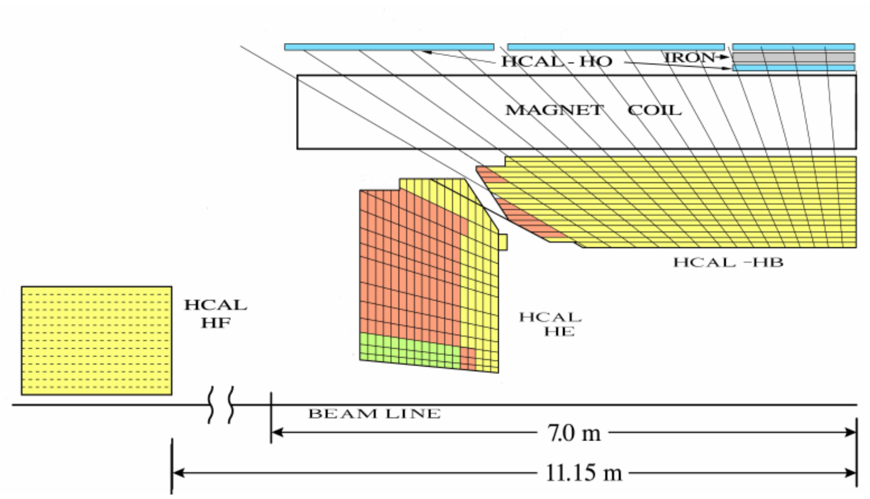

Figure 3.13: An r-Z schematic view of a quarter CMS detector showing the HCAL and its subsystems: HB, HE, HO and HF in CMS taken from [67]. The locations of the front-end electronics for the HB and HE calorimeters are indicated by FEE. The current depth segmentation of the HB and HE.

($|\eta| < 1.3$) and HE ($1.3 < |\eta| < 3.0$) are placed in between the ECAL and the magnet. The HO ($|\eta| < 1.3$) is located outside of the magnet, ensuring no energy leaks out the back of the HB undetected and the two HF ($2.5 < |\eta| < 5.0$) are positioned at either end of the CMS to identify forward jets, determine missing transverse energy, and measure the luminosity. A more detailed description of the detector and its performance is documented [91,92].
The HB and HE are sampling calorimeters made of alternating layers of the brass absorber and active tiles of plastic scintillator, fitted with pixels of silicon-photomultipliers (SiPM). The wave length shifting (WLS) fibers readout are embedded in this active plastic scintillator tiles and scintillating light captured in these WLS fibers which are fused to clear optical fibers for transport to the photo-transducers and front-end electronics (FEE). The HO, which functions as a tail-catcher for hadronic showers and is useful for muon identification, uses the same active material and WLS fibers as the HB and HE calorimeters but uses the steel return yoke and magnet material of CMS as the absorber.
The HB, HE and HO calorimeters were all originally fitted with hybrid photodiode (HPD) transducers however during LS1, they have been all replaced

with silicon-photomultipliers (SiPM). The SiPM is a multi-pixel Geiger-mode avalanche photodiode (APD) device which provides gains between 10^4 and 10^6 using an applied voltage less than 100 V. The signal-to-noise performance of the HPD was not sufficient to provide finer segmentation, nor were the particle-flow techniques, used to reconstruct jets of particles in the CMS. With the excellent signal-to-noise and improved gain of the SiPM, a segmentation with three depth segments in the HB and four to five in the HE become available and It gives better tracking of hadronic shower development which is important for particle-flow techniques and better management of the radiation damage which occurs in the high-η region (HE), reducing the response of the individual tiles. The longitudinal segmentation of the hadron calorimeter can provide shower profile information that is used to verify that electromagnetic particles identified in the ECAL. In particular, the segmentation suppresses the influence of pileup particles that contribute to the first layer of HCAL but not to deeper layers. The deepest segment of HCAL is not affected by the pileup particles so it can be useful for accurate identification of prompt muons and rejection of muons produced in the decay of hadrons in flight with isolation requirements that are robust against pileup.
The HF is a Cherenkov calorimeter based on a steel absorber and quartz fibers which run longitudinally through the absorber and collect Cherenkov light, primarily from the electromagnetic component of showers which develop in the calorimeter. The quartz fibers are inserted into the HF with a spacing of 5 mm and the fibers associated with a particular $\eta \times \phi$ region are bundled and the optical signal is converted to an electrical signal using a photomultiplier tube (PMT).

During 8 TeV operation of the detector in 2010, anomalous signals were identified which were associated with single muons or particle showers passing through the phototubes. These events produced anomalously large energy deposits which could be clearly identified in the low occupancy environment of initial operation. However, these anomalous signals become harder to remove as the luminosity increases, as topological requirements become more difficult to apply. The most powerful technique for removing these signals has been based on timing, as the signal from the energy deposit directly in the PMT arrives before the signal from the calorimeter which must pass through the quartz fibers. Similarly, other classes of anomalous signals produce pulses which are very long in time compared with the normal Cherenkov pulse. The phototubes were therefore replaced with multi-anode tubes to achieve the significant reduction of the rate of anomalous signals (though not suppress entirely) and availability to identify single-particle anomalous signals and even to recover the response for the channel rather than rejecting the energy deposit entirely. A TDC in the ADC chip is also upgraded, allowing the determination of pulse arrival times and pulse widths for signals.

3.3.5 Superconducting Solenoid Magnet

The high magnetic field is mandatory for the CMS detector. A large superconducting solenoid magnet, designed magnetic field of 4 T, provides substantial benefits not only for the muon tracking and inner tracking but also for electromagnetic calorimetry. This magnet allows the charge/mass ratio of particles to be determined from the curved track. The CMS began with the goal of having the strongest magnet possible because a higher strength field bends paths more and, combined with high-precision position measurements in the tracker and muon detectors, this allows accurate measurement of the momentum of even high-energy particles. Inside the solenoid, the real operating field was scaled down to 3.8 T instead of the full design strength in order to maximize longevity. The magnetic field is uniform inside the solenoid but complex in outshde (See Figure 3.14). Special features are NbTi winding consisted of 4 layers, mechanically reinforced

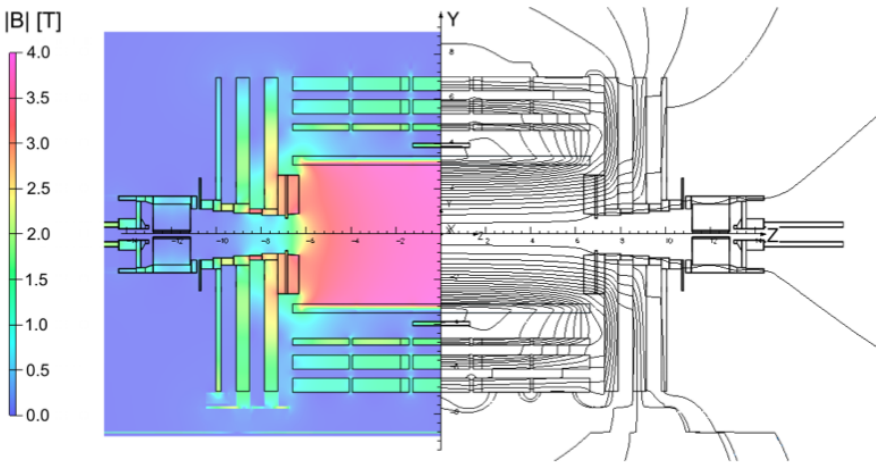

Figure 3.14: Field map of the CMS magnetic field measured by using cosmic rays. The intensity of the field is of 3.8 T inside the solenoid and typically 2 T outside the solenoid. This figure is taken from [67].

with aluminum alloy and Large dimension (6.2 m cold bore, 12.5 m length, 220 ton). The tracker, ECAL, and HCAL detectors fit inside the magnet coil and CMS muon detectors are interleaved with a 12 sided iron structure that surrounds the magnet coils and contains and guides the field. Outside of the magnet, the magnetic flux is returned to help the iron yoke whose total weight ~10000 ton. The return yoke is made up of three layers that reach out 14 m in diameter and also acts as a filter, allowing through only muons and weakly interacting particles such as neutrinos. More details will be described in next section.

3.3.6 Muon System

The main tasks of CMS muon detector are muon identification, accurate measurement of muon momentum and muon triggering. To achieve the goals, the muon detector, distributed to provide hermetic coverage of $0 < |\eta| < 2.4$, utilizes 3 different technologies all based on the gas-ionization process : The drift tubes (DT) in the barrel region ($0 < |\eta| < 1.3$), cathode strip chambers (CSC) in the endcap region ($0.9 < |\eta| < 2.4$), and resistive plate chambers (RPC) in both the barrel and endcap ($0 < |\eta| < 1.8$). The schematic layout of the CMS muon chambers is shown in Figure 3.15. In the barrel, the drift tube chambers consist of 12 sectors per wheel, each covering 30° along the ϕ coordinate. (total 5 wheels in barrel, named YB0, YB±1,2). Each ϕ-sector forms 4 stations, named MB1-MB4 at different radii surrounding the beam pipe and The DT basically consists of the drift cell ($42 \times 13\,\mathrm{mm}^2$) and gold-plated stainless-steel anode wire (50 μm diameter) at the center. Each station contains two super-layers (SL) that measure the position along CMS bending plane (rϕ) and one orthogonal SL that measure along the beam axis plane (rz), where each the SL is made of 4 staggered layers of parallel drift cells. (except for MB4, which has only an rϕ SL) The designed spatial resolution of the DTs is 100 μm along rϕ and 150 μm along rz.
In the endcaps, the magnetic field is non-uniform and strong and the level of the muon/background rates is relatively higher than barrel region. This condition motivates to using the Cathode Strip Chambers (CSC), which provides a fast response and high tolerance to the non-uniform magnetic field and as well as a fine segmentation. Each endcap consists of 4 CSC stations of the chamber, named ME1-ME4 fitted on the front of each endcap steel disks (made of 2-3 rings located at different radii). The CSC contains 6 layers that give an accurate position measurement in the bending rϕ plane and each layer contains 80 cathode strip, each of which delimits a ϕ from 2.2 to 4.7 mrad and projects to the beam line axis. The spatial resolution is $75 \sim 150\mu$m along rϕ and $1.9 \sim 6\,$mm in r. The important features of the DT and CSC devices are identifying bunch crossing in each collision and generating the muon and triggering on the p_T of muons with good efficiency, and the ability to reject background by using the means of timing discrimination. In addition, to provide an independent and robust triggering detector system, RPCs are installed in both the barrel and endcaps. The RPC system is a complementary system with good time resolution better than 3ns. 4 RPC stations (RB1-4) are installed in the barrel and the 3 stations (RE1-3) in the endcap. RPCs are the double-gap chamber, operated in avalanche mode and each gap has two 2 mm thick resistive Bakelite plates split to a 2 mm thick gas gap. When a charged particle goes through the RPC detector, this RPC ionizes the gas and avalanches generated by the high electric field then it creates a pattern of hits that contains information about the bending of the track and thus about the p_T of the muon. The parameters and properties of the muon subdetector systems are summarized in Table 3.2. More details of muon detector

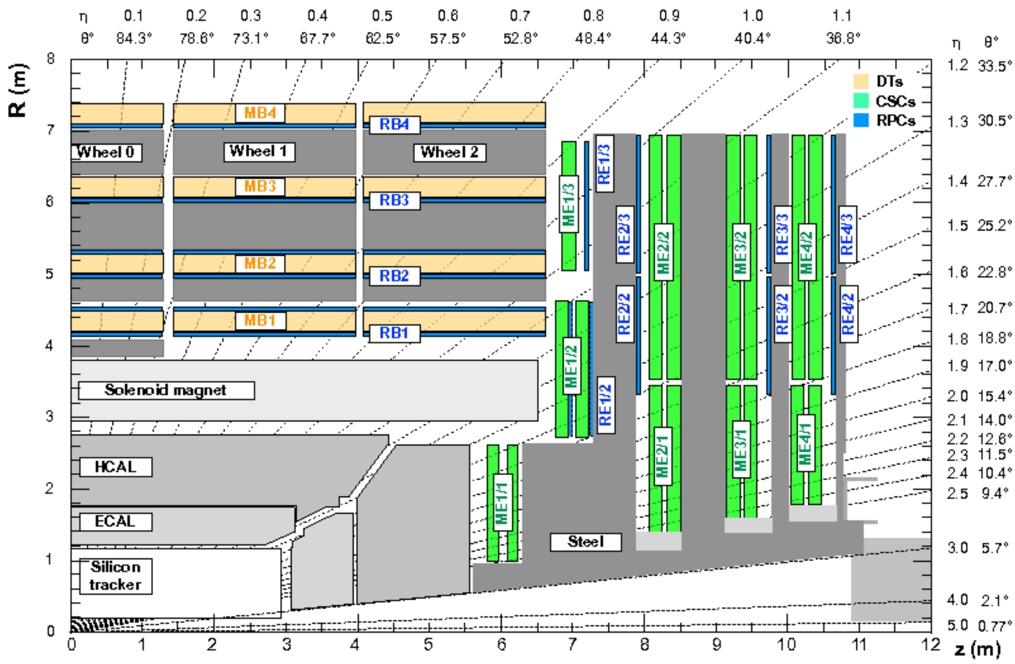

Figure 3.15: A rz cross section of a quadrant of the CMS full detector with the z-axis and radius (R). The interaction point is at (0, 0). The locations of the multiplex muon stations and the steel disks (dark gray) are shown. In the muon barrel, 4 drift tube stations (light orange) are displyed and in the endcap, the cathode strip chambers (green) are displayed. Resistive plate chambers (blue) are in both the barrel and the endcaps of CMS (This figure is taken from [93]).

Muon sub-detector	DT	CSC	RPC
$\|\eta\|$ range	0.0 - 1.2	0.9 - 2.4	0.0 - 1.9
Number of stations	4	4	4
Number of chambers	250	540	480(RB), 576(RE)
Number of layers/chamber	8(R-ϕ), 4(z)	6	2(RB1, RB2), 1(elsewhere)
Number of channels	172000	Strips: 266112 Anode channels: 210816	68136(RB) 55296(RE)
% of working channels	98.4%	99.0%	98.3%

Table 3.2: The parameters and properties of the muon subdetector systems in CMS during the 2016 data-taking period.

and its performance can be found in [94, 95, 96].

The muon detectors play an important role in the CMS L1 trigger system. The L1 muon trigger is formed from trigger primitives in DT or CSC or RPC hits forwarded from multiple chambers. The CSC and DT give candidate muon track segments through complicated local trigger hardware. The DT local trigger (muon barrel) and CSC local trigger (muon endcap) perform this task. In the RPC trigger, instead of using local trigger hardware, muon candidates are directly formed from the spatial and temporal coincidence of hits in multiple RPCs. The trigger track finder (TF) hardware collect the DT and CSC local trigger segments from each muon station and combines them to provide a muon track and a transverse momentum value. To construct muon candidates, TF requires at least 2 segments in 2 different stations. During LS1 period, several upgrades have been done in order to cope with the increased LHC luminosity. In particular, a new trigger system has been designed, to combine the trigger information from DT and RPC before of the reconstruction of muon tracks. The details about L1 trigger upgrade is discussed in next section.

3.3.7 Trigger and Data Acquisition

As stated in the LHC section, at the designed luminosity of $10^{34}\,\mathrm{cm}^{-2}s^{-1}$, the proton beams cross each other at a frequency of 40 MHz and each crossing results in an average of about 20 inelastic pp events per every 25 ns producing approximately 1 MB of zero suppressed data. The collision and overall data rates are much higher than the rate at which one can write data to mass storage by the limited archival capability. Therefore the Trigger and Data Acquisition (DAQ) system plays an essential role in the CMS experiment. The trigger is defined as the system that decides, in real-time, which subset of data is to be read-out by the detector and archived for offline analysis.

The important requirement of the trigger is the high background rejection, filtering with high efficiency signals of interest and affordable trigger algorithms for limited custom electronics and computing power. The DAQ system collects the data from the different parts of the detector, converts the data to a suitable format and saves it to permanent storage. This system must provide online service to keep the record of data-taking and detector conditions (like, run control system, data-flow monitoring, detector controls, etc.) and need to minimize dead-time and be robust against varying data-taking conditions and detector/electronics problems. The flexibility to record data in different configurations (such as commissioning, calibration, and physics data-taking) is also needed.

In CMS experiment, the Trigger and Data Acquisition System (TriDAS) is designed to select events with a maximum rate of $\mathcal{O}(10^2)$ Hz for archiving and offline analysis. For the trigger system, full selection task has been performed

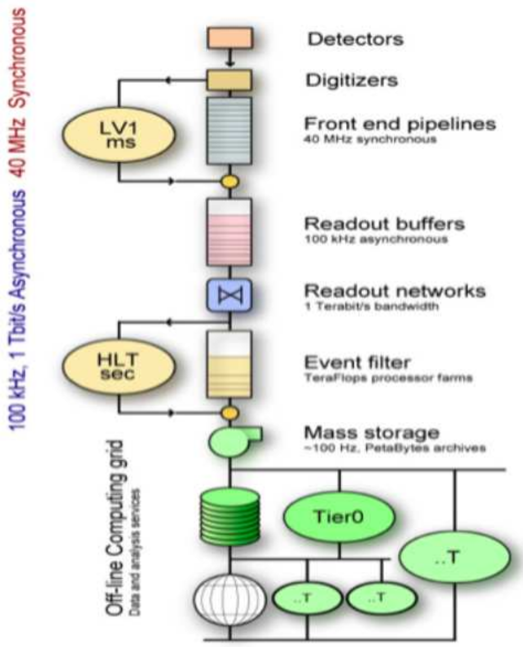

Figure 3.16: The CMS experiment has been designed with a 2-level trigger system. The first level is Level-1 Trigger and the second level is High-Level Trigger.

with a 2-level trigger system. (See Figure 3.16) The first level is implemented using custom-designed electronics. The second level is the so-called High-Level Trigger (HLT), a streamlined version of the CMS offline reconstruction software running on a computer farm. The Level-1 Trigger is designed to reduce the rate of events accepted for further processing to less than 100 kHz. The High-Level Trigger is designed to reduce the maximum L1 trigger rate of 100 kHz to a final output rate of 100 Hz. Each Trigger for Run2 is more described in the following section.

The CMS Level-1 Trigger upgrade for LHC Run2

In RunII, the bunch spacing has reduced to 25 ns and pile-up (the number of interactions per bunch crossing) has increased up to an average value of 50. This expects a huge increase in event rates. (e.g.- Single e/γ(18 GeV)and Double e/γ (13 and 7 GeV) will give a rate of 40 and 50 kHz respectively in Run II without upgrade, compared to 6 and 5 kHz in RunI) To maintain high signal efficiency and low physics thresholds, while maintaining the L1 rate below 100 kHz, the CMS L1 trigger system has been upgraded significantly in LS (2015). The new L1 system was commissioned with data in 2015 and it has been used successfully for full 2016 data taking period. More details about the design and the hardware of the trigger system and of the L1 upgrade can be found in [97, 98].

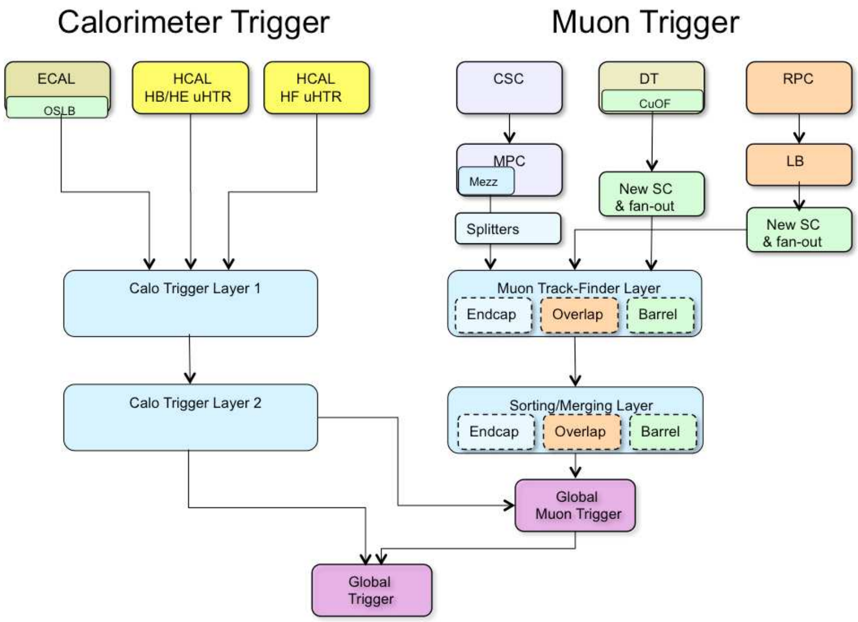

Figure 3.17: A schematics of the architecture of the upgraded L1 trigger system for RunII. The L1 Calorimeter Trigger (left) and the L1 Muon Trigger (right) receive input trigger primitives from different subdetectors, and their outputs are combined into the Micro Global Trigger (bottom) for the final trigger decision. The Muon Trigger also receives information from the Calorimeter trigger to calculate muon candidates isolation.

The upgraded system is split into two main parts: the L1 Calorimeter Trigger and the L1 Muon Trigger respectively. Their structure of the system is shown in Figure 3.17 The outputs of these two trigger system indicate different physics objects: electrons, photons (eγ cannot be distinguished at L1 due to the lack of track info), muons, tau leptons decays containing hadrons, jets, energy sums.
The L1 Calorimeter trigger receives information from the ECAL, HCAL and HF calorimeters, and utilize it to reconstruct e/γ, τ, and jet candidates, and to compute energy sums (scalar sum $\mathrm{H_T}$ and vector sums $\mathrm{E_T}$). The input is organized in Trigger Towers (TT), each corresponding to a region of approximately 0.087×0.087 of extension in η, ϕ in the central part of the detector. (In endcaps, they have a slightly more complex geometry.) The energies deposited in ECAL, HCAL, and HF at a specific position are encoded in each TT. The key technological development at RunII is that the implementation of the Time Multiplexed Trigger (TMT) [99] architecture, which lets a global view and full granularity of the calorimeters. In RunI, the calorimeter trigger had processed independently different detector regions, due to the limited access to the individual TT information, however, in RunII it can access the entire detector information at the TT granularity. The upgraded trigger is comprised of two processing layers and different hardware are used in two layers.

- The Layer-1 consists of 18 Calorimeter Trigger Processor cards (CTP7), designed for data sharing within a single crate and data formatting. Preprocessing is executed such as the sum of energies in ECAL and HCAL or the computation of the H/E ratio [99, 100].

- The Layer-2 consists of 9 Master Processor Virtex 7 cards (MP7), designed as generic stream-processing engines. The MP7 hosts all calorimeter algorithms that search particle candidates and global energy sums [101, 102].

As a consequence, the TMT remove the boundaries by streaming data from the single event into one FPGA and data distribution and algorithm implementation is physically separated in the Layer-1 and Layer-2 and can be optimized independently. More details about the algorithm and their performance can be found in [103, 104].
The L1 Muon Trigger receives information from the three muon sub-detectors with a different $|\eta|$ coverage and different space and time resolution capabilities. In Run I, muon trigger system had processed the information from each subdetector individually and combine the outputs a later stage, resulting in a robust muon track reconstruction and muon $\mathrm{p_T}$ assignment. The upgraded L1 Muon Trigger is designed to utilize the sub-detector redundancy at an earlier stage, thus improving the overall performance. For this reason, the upgraded system contains three different muon track finders, each covering different η regions.

- The Barrel Muon Track Finder (BMTF) receives information from DT and RPC detectors and covers the $|\eta| < 0.83$ region.
- The Endcap Muon Track Finder (EMTF) receives information from CSC and RPC in the region $|\eta| > 1.24$.
- The Overlap Muon Track Finder (OMTF) receives information from the all 3 sub-detectors in the intermediate region $0.83 < |\eta| < 1.24$.

In the BMTF case, the track bending angle information in each DT station allows implementing a road search extrapolation track finding: the hits in every station are extrapolated pair-wise to adjacent stations and matched together as the first step of track reconstruction and p_T assignment. 12 separate wedges of 30 each are processed in parallel. The number of hits and the quality of the match determines the quality of the reconstructed muon that can be used to control the trigger rate. DT and RPC information is combined in the TwinMUX system into super-primitives that are currently being commissioned. The increased precision in the super-primitives position and timing resulting from systems redundancy will further improve the algorithm performance.
In the OMTF and EMTF cases, a system latency of about 750 ns, higher background rates, and non-uniformities in the magnetic field impose the usage of a fast pattern-based track finding algorithm. This is implemented in the form of large look-up tables (LUTs) that convert specific hit patterns into p_T assignments. The number and topology of the hits are used to determine the quality of the reconstructed muon track. The OMTF uses a customized firmware to properly handle non-uniformities of the magnetic field in this region. The OMTF and the EMTF are currently receiving data from CSC directly, but a Concentration, Pre-Processing and Fan-out card (CPPF) is foreseen to combine CSC and RPC hits.
The Global Muon Trigger (μGMT) collects the output of these systems and then ranks the muons by transverse momentum and quality, removes the reconstruction duplicates across boundary regions, and sends the output muon collection to the μGT [105, 106]. The inputs from the Calorimeter Trigger can be provided to compute the isolation of muon candidates. The very different type of algorithms implemented in the three muon track finders results in the usage of a different hardware: MP7 cards are used to implement the BMTF track segment extrapolations as well as for TwinMux and μGMT, while Modular Track Finder cards (MTF7) [107], providing very large memories for LUTs, are used in OMTF and EMTF.
The micro Global Trigger (μGT) [108] collect objects information and combines their position, momentum, isolation, and quality to perform the final trigger decision. This μGT is implemented with 500 algorithms that are regularly updated with respect to the evolving running conditions and it is responsible for allowing

the event to be further scrutinized by the HLT. A details of the performance can be found in [109, 110].

The CMS High-Level Trigger and DAQ system

While Level-1 Trigger is instrumented by custom-designed hardware boards, the High-Level Trigger (HLT) is implemented in software running on a farm of commercial computers which includes about 16,000 CPU cores, and reduces the L1 output rate to the sustainable level for storage and physics analysis of about 1 kHz. The HLT software consists of a streamlined version of the offline reconstruction algorithms. it exploits the same sophisticated software used for offline reconstruction and analysis, optimized in order to comply with the strict time requirements of the online selection. The HLT menu in CMS has a modular structure, which is graphically depicted Figure 3.18. The menu is subdivided in paths (there are up to now more than 500 different HLT paths prepared for the data taking at Run2), each corresponding to a dedicated trigger (such as a prescaled single-electron trigger or a 3-jets-with-MET trigger). Each path consists of several steps (software modules), each module performing a well-defined task such as unpacking (raw to digi), reconstruction of physics objects (electrons, photons, muons, b-tagged jets, jets, MET, etc.), making intermediate decisions triggering more refined reconstructions in subsequent modules, or calculating the final decision for a trigger path. The modules within a path, either object producers or filters, are arranged in blocks of increased complexity, so that faster algorithms are run first and their products are filtered. if a filter fails, the rest of the path is skipped. There are other important features that differentiate the algorithms used at HLT to the ones used for the offline reconstructions, all meant to reduce the CPU time consumption at HLT. In general it is expected that all HLT trigger paths are run, even if the event is already accepted by a path. In case this turns out to be too time-consuming, a truncated mode of HLT operations should be foreseen where the HLT short-circuits after the first accept (and after the triggers needed to classify the event for a primary data set and output stream are computed) and does not run the rest of the triggers. Presumably, the triggers not run online could be run in the offline reconstruction step to compute all trigger bits (for events written out) in order to get a complete trigger picture allowing trigger efficiency studies. Each HLT trigger path must be seeded by one or more L1 trigger bit seeds. The first filter module in each HLT path is looking for a suitable L1 seed (consisting of L1 bits and L1 objects) as a starting point for that specific HLT trigger.

The data acquisition (DAQ) system of the CMS experiment assembles events at a rate of 100 kHz, transporting event data at an aggregate throughput of 100 GB/s to the high level trigger (HLT) farm. The HLT farm selects interesting events for storage and offline analysis at a rate of around 1 kHz. The DAQ sys-

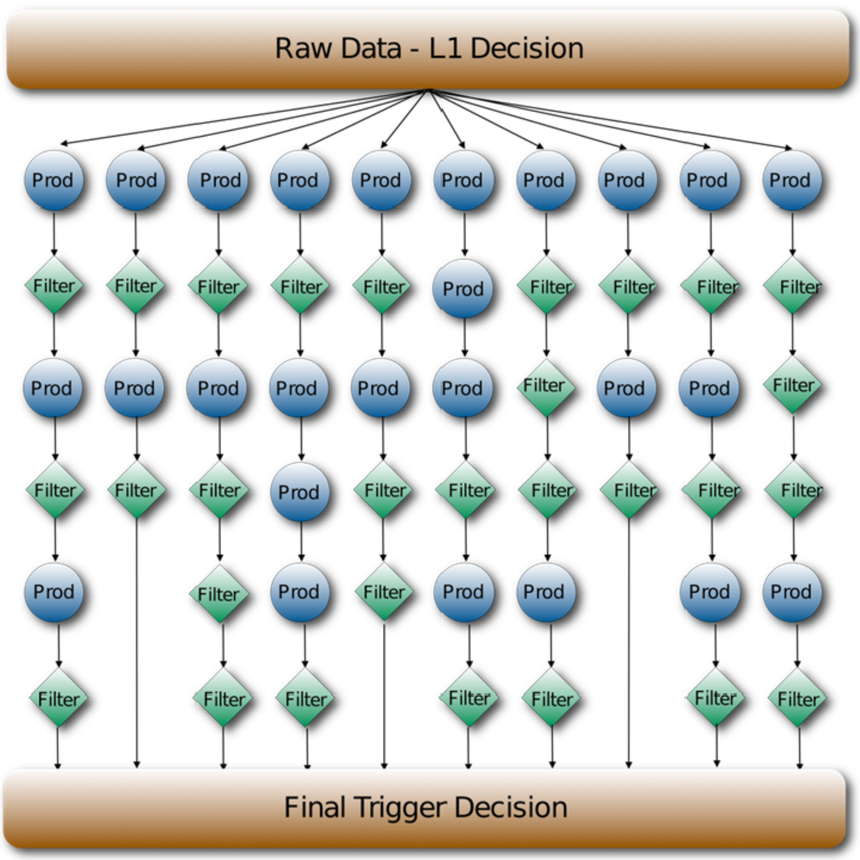

Figure 3.18: Schematic representation of a HLT menu in CMS and of the HLT paths in it. The final trigger decision is the logical OR of the decisions of the single paths.

tem has been redesigned during the accelerator long shutdown period (2013-14). There are two motivations. Firstly, the current compute nodes, networking, and storage infrastructure will have reached the end of their lifetime by the time the LHC restarts. Secondly, in order to handle higher LHC luminosities and event pileup, a number of sub-detectors will be upgraded, increasing the number of readout channels and replacing the off-detector readout electronics with a TCA implementation. The new DAQ architecture will take advantage of the latest developments in the computing industry. For data concentration, 10/40 Gb/s Ethernet technologies will be used, as well as an implementation of a reduced TCP/IP in FPGA for a reliable transport between custom electronics and commercial computing hardware. A Clos network based on 56 Gb/s FDR Infiniband has been chosen for the event builder with a throughput of about 4 Tb/s. The HLT processing is entirely file based. This allows the DAQ and HLT systems to be independent and to use the HLT software in the same way as for the offline processing. The fully built events are sent to the HLT with 1/10/40 Gb/s Ethernet via network file systems. Hierarchical collection of HLT accepted events and monitoring meta-data are stored into a global file system. Overall process of tne DAQ system is illustrated in Figure 3.19. The main parameter of the DAQ/HLT system in CMS for RunI and RunII system and for Phase II are listed in Table 3.3

	LHC RunI	LHC RunII	HL-LHC PhaseII upgrade	
$\sqrt{s}$	7-8 TeV	13 TeV	14 TeV	
Avg. Peak Pile-up/BX	35	50	140	200
Max. Level-1 accept rate	100 kHz	100 kHz	500 kHz	750 kHz
Designed Event Size	1 MB	1.5 MB	4.5 MB	5.0 MB
HLT accept rate	1 kHz	1 kHz	5 kHz	7.5 kHz
Designed Storage throughput	2 GB/s	3 GB/s	27 GB/s	42 GB/s

Table 3.3: The DAQ/HLT system parameter relevant to the 3 different times of LHC operation.

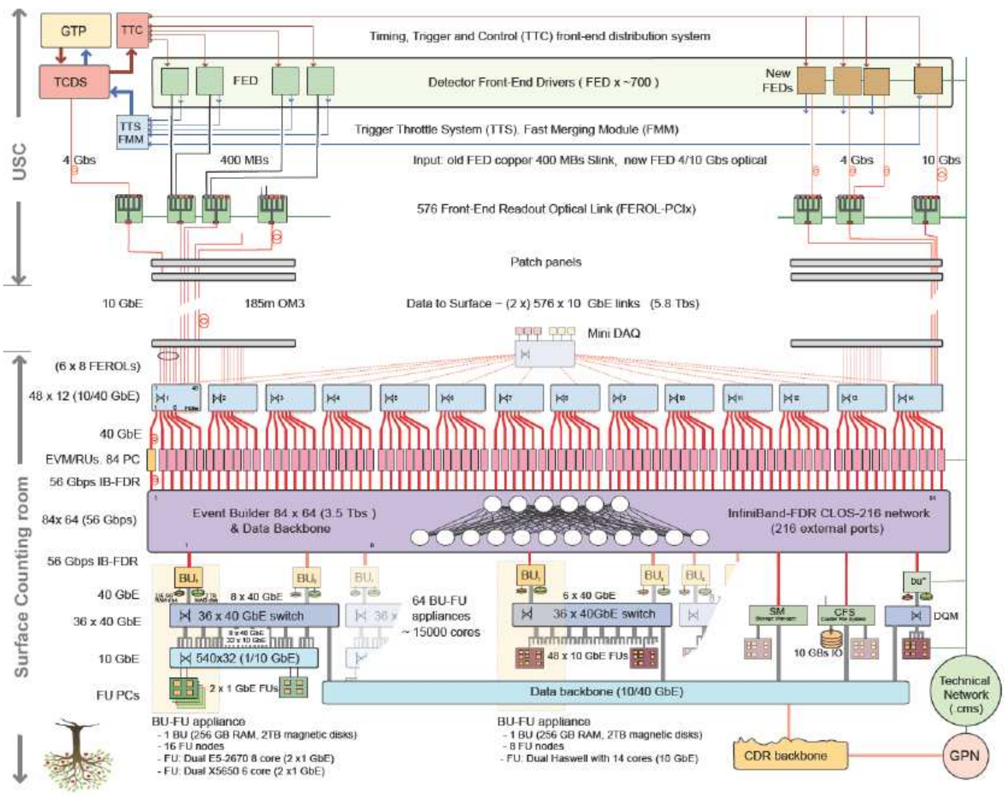

Figure 3.19: Over-all architecture of the new CMS DAQ system for Run-2 of the LHC. This picture is taken from [111].

Chapter 4

Data and MC Samples

4.1 Data Sample

This mono-lepton search analysis is performed by using the data sample recorded in CMS during 2016 LHC 13 TeV operation with the magnetic field at 3.8 T and a bunch crossing every 25 ns with increasing pileup during data taking. The standard `Golden JSON`[1] for 2016 run conditions is applied to ensure high data quality with good functioning of all sub-detectors. This file contains the good run list associated with the condition of magnetic field and activity of each detector component during data taking period and describe which luminosity sections in which runs are considered good and should be processed[2]. The used `JSON` file provided by the Data Certification (DC) group in CMS is as follows :

`Cert_271036-284044_13TeV_23Sep2016ReReco_Collisions16_JSON.txt`

The total luminosity measurement with this `Golden JSON` is based on `brilcalc`[3] and used command is as follows :

```
$ brilcalc lumi -b "STABLE BEAMS" -i JSON.txt --normtag normtag_DATACERT.json
```

The total integrated luminosity during 2016 stable proton beams is 35.867 fb^{-1}. (See Figure 4.1.) The data-taking run period was divided into eight run eras, denoted A, B, C, D, E, F, G, and H. Here we used from RunB to RunH because Run A data was taken at 0 Tesla, including commissioning run so not used. The datasets and corresponding run ranges and integrated luminosity from

[1] JSON stands for Java Script Object Notation. All certified good luminosity section files in JSON format can be found in https://cms-service-dqm.web.cern.ch/cms-service-dqm/CAF/certification/Collisions16/13TeV/.

[2] (ex) "273158": [[1, 1279]] = "good run number" : [[good lumi section range]]

[3] The `brilcalc` is a commandline toolkit for CMS Beam Radiation Instrumentation and Luminosity (BRIL).

certified data are listed in Table 4.1. The 2016 samples use the `80X ReReco`

Era	Golden Runs	L[fb^{-1}]	Dataset
RunB	273158-275376	5.79	/SingleElectron(Muon)/Run2016B-03Feb2017_ver2-v2
RunC	275657-276283	2.57	/SingleElectron(Muon)/Run2016C-03Feb2017_v1
RunD	276315-276811	4.25	/SingleElectron(Muon)/Run2016D-03Feb2017_v1
RunE	276831-277420	4.01	/SingleElectron(Muon)/Run2016E-03Feb2017_v1
RunF	277981-278808	3.10	/SingleElectron(Muon)/Run2016F-03Feb2017_v1
RunG	278820-280385	7.54	/SingleElectron(Muon)/Run2016G-03Feb2017_v1
RunH	281613-283685	8.61	/SingleElectron(Muon)/Run2016H-03Feb2017_ver2,3-v1

Table 4.1: Summary of the data taking periods with the corresponding Golden run ranges, integrated luminosity (L) and dataset names of single-electron and single-muon data streams collected by the CMS at $\sqrt{s} = 13$ TeV. These datasets is divided into the eight runs (Run A to H, A is 0 Tesla Run, not considered.) of the 2016 data aquisition periods.

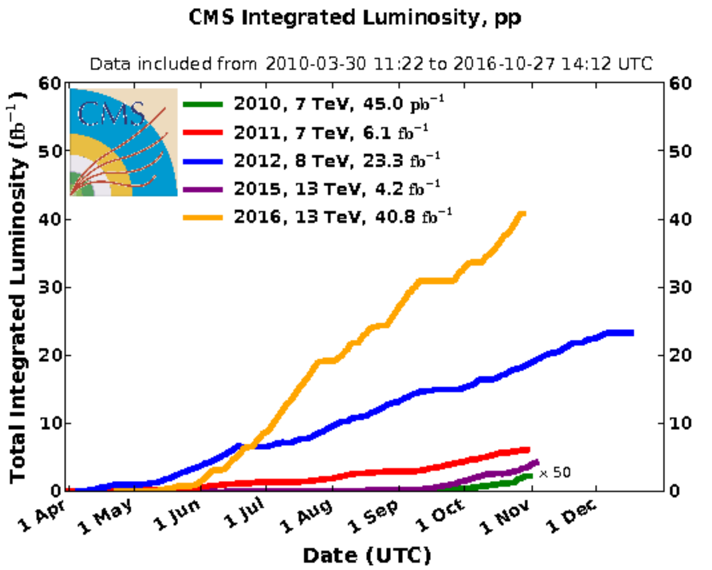

Figure 4.1: The cumulative luminosity delivered by the LHC to CMS during stable pp collisions beams in 2016 compared to previous data-taking years. The integrated luminosity achieved in 2016 far surpassed expectations. The final 2016 total of 40 fb^{-1} to CMS and ATLAS.

and `ReMiniAODv2`. We used these ReRecoed `ReMiniAODv2` datasets from RunB to RunH, produced with CMSSW_8_0_26_patch1. During 2016 run, data acuisition era B to G have been re-recoed in the `23Sep2016` (for 2016 ICHEP) and `03Feb2017` (for 2017 Moriond) re-reco pass. When CMS take real 2016 data, the

PromptReco datasets were firstly reconstructed, however in order to use the most up-to-date CMSSW for recent detector alignment, calibration constant and fixes for several issues, the ReReco datasets were re-reconstructed. The main re-reco features are listed as follows :

- Heavy Ionizing Particle (HIP) issue: also known as Analog Pipeline Voltage (APV) issue. The SiStrip dynamic inefficiencies, tracking mitigation is applied in the eras B to F
- ECAL Slew Rate issue: Underestimation of EcalRecHit energy at very high E_T egamma objects. It affects all data in the barrel. The energy of hit with gain switch and Cluster, egamma objects in the barrel are remade for the new RecHits.(See Appendix 9.)
- Fix Bad PF muon issue: MET tails is affected by bad PF muons. This bad event filtered out using MET Filters (See Section 5.5.1.)

This ReReco process brings the data from different periods in more homogeneous conditions. Essentially they are the conditions used for the data-taking during last period RunH. This analysis uses the single lepton triggers (electrons and muons) and all triggers are listed in Table 4.2.

Dataset	Trigger path	purpose
SingleElectron	HLT_Ele27_eta2p1_WPTight	measuring ϵ
	HLT_Ele115_CaloIdVT_GsfTrkIdT	
	HLT_Photon175	signal selection
SingleMuon	HLT_Mu50	
	HLT_TkMu50	

Table 4.2: High-Level Triggers used in mono-lepton analysis.

4.2 Signal Samples

As previously described in Section 2.3, many BSM scenarios predict new particles decaying with an experimental signature of a high p_T charged ℓ (electron/muon) and missing transverse energy, E_T^{miss} occurs in a number of different physics models. Four different physics interpretations are performed in this thesis and their information are summarized in Table. 4.3. For SSM W′ without interference effect, the simulation of signal samples ($W' \to \ell\nu$) is performed at leading order (LO) with PYTHIA 8.2.1.2 [112], with tune CUETP8M1 [80, 81], using the NNPDF2.3 [113] parton distribution functions (PDF). The considered boson masses range from 400 GeV to 6000 GeV, where the minimum mass is

Table 4.3: Overview of models considered, with the relevant model parameters and correction orders (The next-to-next-to leading order (NNLO) cross sections are in Table 4.4). These models are explained in Section 2.3.

Model name	Parameters	Generator	Order
Sequential standard model without W-W′ interference (SSM)	$M_{W'}$	PYTHIA	NNLO
SSM W′ with varying coupling strength	$g_{W'}/g_W$	MADGRAPH	LO
Split universal extra dimensions model (split-UED)	μ, R	PYTHIA	NNLO
RPV SUSY with scalar lepton mediator	λ, $m(\tilde{\ell})$	MADGRAPH	LO

determined by the trigger thresholds. Examples of transverse mass distribution from three different signal samples with $m_{W'} = 1.8, 3.8, \text{and} 5.8$ TeV are depicted in Figure 4.2 top-left. The transverse mass signature is a Jacobian peak, similar to that of the W boson, except at higher masses. With increasing the mass of W′ boson, the phase space for the production in pp collisions at 13 TeV decrease, because of constraint from the PDFs, resulting in an arising fraction produced off-shell at lower masses. A mass-dependent K-factor is used for the W′ signal, to correct for next-to-next-to-leading order (NNLO) QCD cross sections. The method and LO and NNLO cross section for the mass of W′ in $\sqrt{s}= 13$ TeV are described in Section 4.2.1.

The coupling strength of the W′ with respect to the SM W coupling, denoted $g_{W'}/g_W$ affects both the total cross section and the width of the Jacobian peak. For SSM W′ with varying coupling strength, the signal samples are simulated in LO with MADGRAPH 5(v1.5.11) [114]. The range of couplings $g_{W'}/g_W$ is from 10^{-2} to 3. These signals have each different width, besides a different cross section. Due to the relation between the coupling of a particle to its width and the resulting transverse mass distribution, an upper limit can be set on the coupling strength. The width is connected to the coupling constant via

$$\Gamma_{W'\to f\bar{f}} = M_{W'}\frac{g^2}{2\cdot 48\pi}\left(18 + 3F(\frac{M_t}{M_{W'}}, \frac{M_b}{M_{W'}})\right) \tag{4.1}$$

where $F(x_1, x_2)$ is a correction to the leading order cross section from NNLO calculations.
This behavior is considered when deriving mass limits as a function of the coupling strength, which will be shown in terms of $g_{W'}/g_W$ with 1 corresponding to SM-W like coupling strengths. To account for the varying width, the PYTHIA samples are reweighted to consider the proper width and the differences in reconstructed M_T shapes have the sensitivity for other coupling strength. On the top-right of Figure 4.2, a $m_{W'} = 2000$ GeV sample is reweighted to three different

$g_{W'}/g_W = 3, 1, 0.01$. It shows that the larger (smaller) coupling corresponds to the increases (decreases) of width.

For split-UED model, the signal samples are generated with PYTHIA 8.2.1.2 at LO and the mass dependent NNLO k-factors are from the SSM W′ signals are equally applied. The signal generated with the parameter 1/R from 200 GeV up to 3000 GeV and μ from 50 GeV up to 10000 GeV. From the Equation 2.19, the 1/R range corresponds to the $m_{W^2_{KK}}$ of the order of 400 GeV to 6000 GeV. The larger radius R of the extra dimension corresponds to smaller KK masses. The mass of KK fermions depends on the bulk mass parameter μ. Examples of transverse mass distribution from three different signal samples with $m_{W^2_{KK}} = 1.8, 3.8, \text{and} 5.8\,\text{TeV}$ are shown in Figure 4.2 bottom-left and these are similar to SSM W′ one.

For RPV SUSY model, the signal samples for a range of tau slepton masses, $m_{\tilde{\tau}}$ are generated with MADGRAPH 5 (v1.5.14) at LO. (higher order corrections are not considered yet.) Signal samples are simulated with the parameter $\lambda_{231}, \lambda_{132} \text{and} \lambda'_{3xx} = 0.05$ to 0.5 in terms of $m_{\tilde{\tau}} = 400$ GeV to 6000 GeV.

4.2.1 High-order correction for the W′ production

To have an accurate cross section for the signal, the high-order QCD corrections are applied with the K-factor in order to get NNLO cross section from LO. The K-factor is calculated in terms of the invariant mass of W′ boson, defined as follows:

$$\text{K-Factor} = \frac{\sigma(\text{NNLO})}{\sigma(\text{LO})} \tag{4.2}$$

To calculate the K-Factor, we used the public code called FEWZ [115] designed to make predictions for LHC observables with realistic acceptance cuts at NNLO in the strong coupling constant. The LO and NNLO cross section from CTEQ6L1 and MSTW2008 PDF, respectively are calculated in terms of various W′ mass points. MC signal samples for SSM $W' \to \ell\nu$ production at 13 TeV[4] are generated by PYTHIA8 from 400 to 5800 GeV of W′ mass. All MINIAOD samples for beam-crossing interval 25 ns scenario are produced with tune CUETP8M1 [80] frontier condition. The FEWZ code allows us to set the perturbative QCD order, value of the renormalization and factorization scales, the mass of the W′ boson, width of the W′ boson as well as PDF. To calculate the cross section in terms of W′ mass, the total width and the partial width of the leptonic decay of the W′ boson (Eq. 2.3.1) have been adjusted according to the mass of W′ boson. In order to

[4] /WprimeToLNu_M_400_TuneCUETP8M1_13TeV-pythia8/RunIISpring16MiniAODv2-PUMoriond17_80X_mcRun2_asymptotic_2016_TrancheIV_v6/MINIAOD

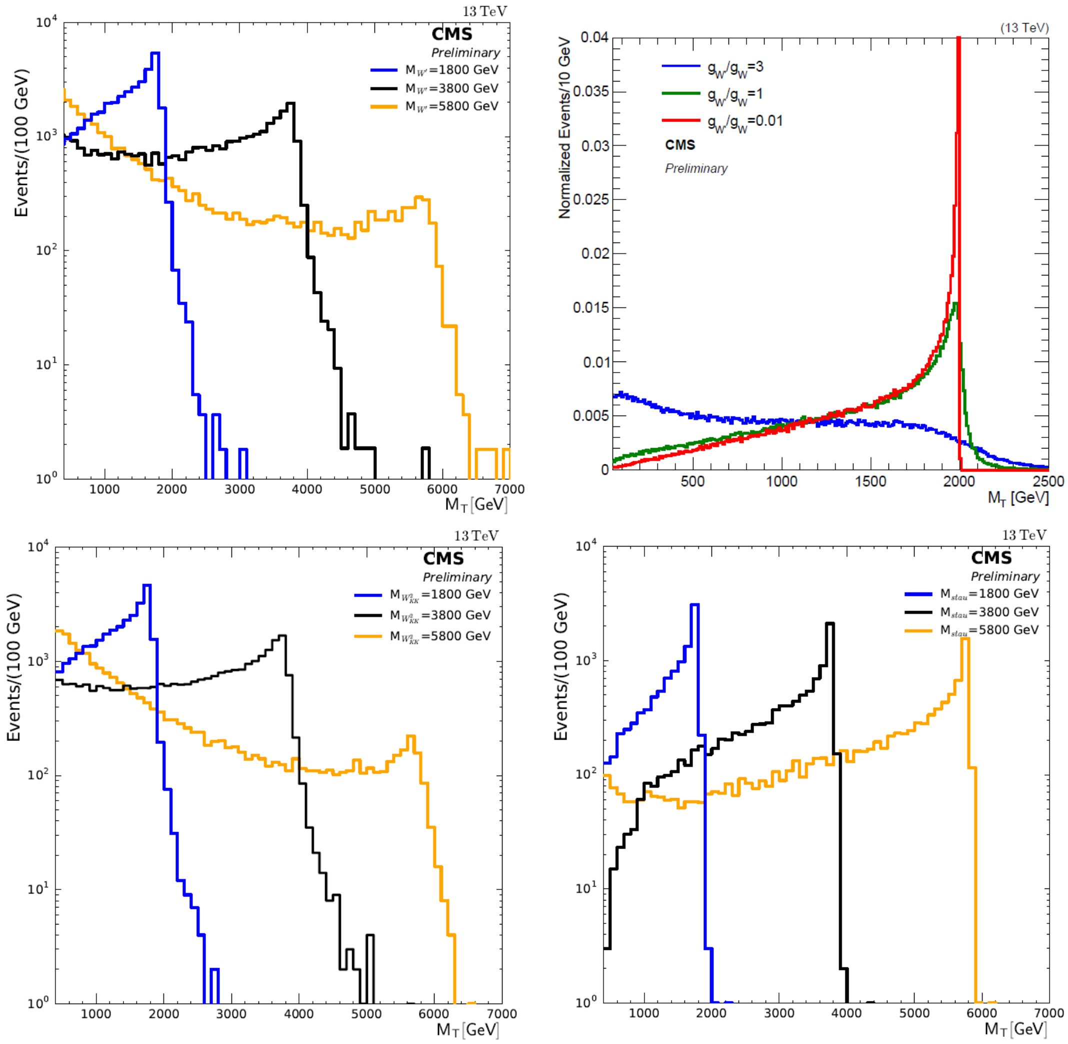

Figure 4.2: The M_T distribution for some signal samples: SSM W′ signals for different masses ($m_{W'}$) (top left), the change of the SSM W′ width with coupling strength for a boson of 2 TeV mass (top right), different masses for W^n_{KK} with KK excitation mode, n=2 (bottom left), and RPV SUSY with a scalar tau as a mediatior (bottom right).

apply the code FEWZ to CMS environment, the CMS default PDF, CTEQ6L1, has to be added to the code. The K-factor for 13 TeV center of mass energy varies from 1.146 to 1.343 depending on the mass points as shown in Table 4.4. The calculated K-factor has been applied to the LO cross section from 0.4 to 5.8 TeV of W′ mass using CTEQ6L1 which is default PDF set in PYTHIA. The Figure 4.3 shows both LO and NNLO cross section times branching fraction of W′ boson decaying to lepton and neutrino and K-factor for $\sqrt{s} = 13$ TeV.

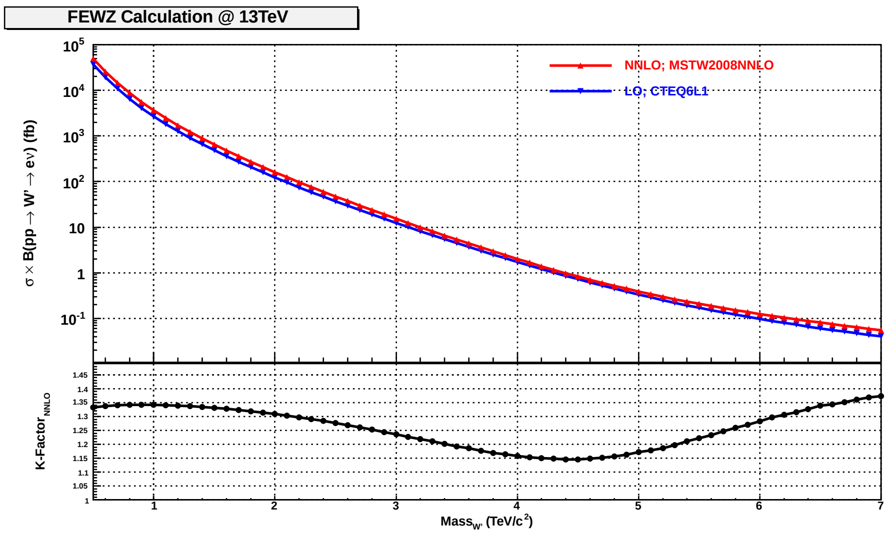

Figure 4.3: The LO and NNLO Cross section for $\sqrt{s} = 13$ TeV versus the mass of W′. The LO with blue line, the NNLO with red line and the K-factor with black line.

4.3 Standard Model Background Samples

The MC simulation of SM backgrounds in this analysis is described in this section. There are several MC background processes whose final state is identical to the signal or can be misidentified as the signal: $\mathrm{W} \to \ell\nu, \mathrm{t\bar{t}}, \mathrm{Drell-Yan} \to \ell\ell$, WW, WZ, and ZZ. The minor background gamma+jets (only for electron channel).

Searching for deviations from the steeply falling W boson transverse mass spectrum requires an accurate background estimate at very high $\mathrm{M_T}$ region. For the majority of background sources, the estimate is determined from MC simulation, based on samples with a large amount of event at high transverse mass. The dominant and main irreducible background is W$\to \ell\nu$ with $\ell = \mathrm{e}, \mu$ and τ. The primary source of background for all signals exists at the off-peak, high $\mathrm{M_T}$ tails

Table 4.4: Signal production cross sections (at LO and NNLO) times branching fraction, as well as the K-factor, for SSM W′ bosons decaying to lepton plus neutrino, at $\sqrt{s} = 13$ TeV.

W′ mass [TeV]	$\sigma_{\mathrm{LO}}\mathcal{B}$ (fb)	$\sigma_{\mathrm{NNLO}}\mathcal{B}$ (fb)	K-factor
0.4	84153	111394	1.324
0.6	19225	25718	1.338
0.8	6494	8717	1.342
1.0	2699.0	3623.5	1.343
1.2	1275.8	1708.9	1.340
1.4	657.28	877.23	1.335
1.6	360.15	478.18	1.328
1.8	206.47	272.38	1.319
2.0	122.55	160.43	1.309
2.2	74.726	96.957	1.298
2.4	46.584	59.813	1.284
2.6	29.560	37.510	1.269
2.8	19.035	23.852	1.253
3.0	12.412	15.348	1.237
3.2	8.1952	9.9844	1.218
3.4	5.4675	6.5682	1.201
3.6	3.6865	4.3708	1.186
3.8	2.5158	2.9432	1.170
4.0	1.7337	2.0092	1.159
4.2	1.2108	1.3926	1.150
4.4	8.5649×10^{-1}	9.8188×10^{-1}	1.146
4.6	6.1476×10^{-1}	7.0621×10^{-1}	1.149
4.8	4.4871×10^{-1}	5.1886×10^{-1}	1.156
5.0	3.3227×10^{-1}	3.8928×10^{-1}	1.172
5.2	2.5146×10^{-1}	2.9832×10^{-1}	1.186
5.4	1.9300×10^{-1}	2.3371×10^{-1}	1.211
5.6	1.5128×10^{-1}	1.8659×10^{-1}	1.233
5.8	1.2029×10^{-1}	1.5148×10^{-1}	1.259

of this W decays. The W→ $\tau\nu$ decay channel mostly contributes to the region of the lower transverse mass region relative to decays into the electron and muon channels, because of the momentum carried away by the two neutrinos from the tau decay.
To estimate the dominant W boson background, two different W→ $\ell\nu$ samples are used. An inclusive W sample generated at NLO with MADGRAPH 5_MCatNLO [116] describing the events with a W boson mass up to 100 GeV is used. And another several exclusive W samples covering high-mass region, from 100 GeV to 600 GeV, generated at LO with PYTHIA 8.2.1.2 [80,112] using tune CUETP8M1 and NNPDF2.3 PDF.
Drell-Yan (DY) process of dilepton (ℓ = e, μ) constitutes a background when one of the lepton escapes detection (outside the acceptance) or missing. High mass DY samples are generated with POWHEG at NLO, with parton showering and hadronization described by PYTHIA 8, using the CUETP8M1 tune and NNPDF3.0 PDFset.
The $t\bar{t}$ and single-top quark production are other sources of high-p_T leptons and E_T^{miss} and these are generated with POWHEG [117,118,119] in combination with PYTHIA, except for the s-channel of single top quark production, which generated with MADGRAPH5_MCatNLO prediction.
Contributions from dibosons are derived from inclusive sample (WW, ZZ), generated with PYTHIA with tune CUETP8M1 and the NNPDF2.3 LO PDF set and exclusive samples ($WW \to \ell\nu QQ, WW \to 4Q, WW \to \ell\ell\nu\nu$) generated with POWHEG. The inclusive samples are scaled to NLO, the exclusive samples are scaled to NNLO cross sections.
In the e+ν channel, a γ+jet process generated with MADGRAPH5_MLM [120] at LO, is used to estimate the effects of photons misidentified as electrons. The contribution of these background processes is estimated by MC simulation with particular generator [121]. In addition, the misidentified of jets as leptons is a possible source of background for this search. While the contribution of QCD multijet events to the muon channel is negligible, a small contribution to the electron channel remains event after tight selection. For the latter, the shape and normalization of the QCD multijet background are derived from the data using data-driven ABCD method, as will be described in Section 4.3.2.

The used MC simulated SM background samples, either in the mono-electron or muon final state or both, are summarized as follows :

- Offshell high mass W : The main irreducible background for the search, SM $W \to l\nu$ with $l = e, \mu, \tau$, and masses M(W) > 100, 200, 500, 1000, 2000, 3000, 4000, 5000 and 6000 GeV. 1 million events each mass and decay channel. Generated with PYTHIA 8.2.1.2 and tune CUETP8M1. A k-factor described in the next section is applied to the LO cross section.

- Low mass region of SM $W \to l\nu$ plus jets, from MADGRAPH 5_MCatNLO, inclusive sample.

- W+ jets (W$\rightarrow$ e/μ/$\tau + \nu$), inclusive and binned in HT: 100–200, 200–400, 400–600, 600–800, 800–1200, 1200–2500, >2500 GeV. Generator MADGRAPH 5_MCatNLO. A k-factor of 1.21 is applied to the LO cross section.

- Inclusive $t\bar{t}$, semileptonic or dileptonic decays ($t \rightarrow e/\mu/\tau$). Also single top generated inclusively in s-,t- and tW-channel. Generator POWHEG, except single top s-channel, which is MADGRAPH5_MCatNLO.

- High mass Drell-Yan samples ($Z/\gamma \rightarrow \ell\ell$) with $\ell = e, \mu, \tau$, with the following mass bins: 50–120, 120–200, 200–400, 400–800, 800–1400, 1400–2300, 2300–3500, 3500–4500, 4500–6000. 100k events per mass and decay channel point. Generator POWHEiG at NLO level.

- γ+ jets, binned in HT: 40–100, 100–200, 200–400, 400–600, >600 GeV, Generator MADGRAPH5_MLM.

- Dibosons WZ and ZZ inclusive sample. Generator PYTHIA 8 and NNPDF2.3 PDF on LO and a k-factor (2.0653 for WZ, 1.6011 for ZZ (NLO correction)) applied to cross section.

- WW exclusive sample (WW$\rightarrow$ lνQQ, WW$\rightarrow$ 4Q, WW$\rightarrow$ ll$\nu\nu$). Generator POWHEG, a k-factor (1.1486, 1.1443, 1.162 (NNLO correction)) applied to cross section.

In the Table 4.5, the generator and the order of cross sections for the different background samples used in this analysis are summarized. In order to improve data-MC agreement, several re-calibrating is need to be considered in the every MC simulations. All simulated event samples are normalized to the integrated luminosity of the recorded data using the given order of cross sections.(all for NNLO, exceptions are the diboson and QCD samples, for which the NLO and LO cross sections are used, respectively.)
The weighting factor of each individual background (also for the signal) simulation is considered as follows :

$$\begin{gathered} w_{\mathrm{bg}} = \mathrm{L}\frac{\mathrm{N_{bg}}}{\sigma_{\mathrm{bg}}} \cdot \mathrm{R(n_{pu})} \cdot \frac{\epsilon^{\mathrm{trigger}}_{\mathrm{Data}}}{\epsilon^{\mathrm{trigger}}_{\mathrm{MC}}} \cdot \frac{\epsilon^{\mathrm{selections}}_{\mathrm{Data}}}{\epsilon^{\mathrm{selections}}_{\mathrm{MC}}} \\ \frac{\epsilon^{\mathrm{trigger}}_{\mathrm{Data}}}{\epsilon^{\mathrm{trigger}}_{\mathrm{MC}}} = \mathrm{SF^{trigger}}, \frac{\epsilon^{\mathrm{selections}}_{\mathrm{Data}}}{\epsilon^{\mathrm{selections}}_{\mathrm{MC}}} = \mathrm{SF^{selections}} \end{gathered} \tag{4.3}$$

Where $\mathrm{N_{bg}}$ and σ_{bg} are the total number of generated events and the theoretical cross section, respectively. $\mathrm{R(n_{pu})}$ is the pileup rewieghting function that correct the number of reconstructed vertices in simulation to the one estimated in data. This will be more described in Section 5.4. The $\mathrm{SF_{trigg}}$ and $\mathrm{SF_{selections}}$ are scale

Table 4.5: Analyzed MC simulated samples for several background processes (L= μ, e τ), generator used and the order of cross sections times branching fractions.

	Background	Generator	Order	σ (pb)
W	WJetsToLNu	Madgraph	NNLO	61526.7
	WJetsToLNu HT-100To200	Madgraph	NLO	1627.45
	WJetsToLNu HT-200To400	Madgraph	NLO	435.237
	WJetsToLNu HT-400To600	Madgraph	NLO	59.1811
	WJetsToLNu HT-600To800	Madgraph	NLO	14.5805
	WJetsToLNu HT-800To1200	Madgraph	NLO	6.65621
	WJetsToLNu HT-1200To2500	Madgraph	NLO	1.60809
	WJetsToLNu HT-2500ToInf	Madgraph	NLO	0.0389136
W offshell	WToENu M-100 13TeV	PYTHIA 8	LO	163.15
	WToENu M-200	PYTHIA 8	LO	6.236
	WToENu M-500	PYTHIA 8	LO	0.2138
	WToENu M-1000	PYTHIA 8	LO	0.01281
	WToENu M-2000	PYTHIA 8	LO	5.56e-04
	WToENu M-3000	PYTHIA 8	LO	2.904e-05
	WToENu M-4000	PYTHIA 8	LO	3.31-06
	WToENu M-5000	PYTHIA 8	LO	2.7-07
	WToENu M-6000	PYTHIA 8	LO	1.5-08
	WToMuNu M-100	PYTHIA 8	LO	163.15
	WToMuNu M-200	PYTHIA 8	LO	6.236
	WToMuNu M-500	PYTHIA 8	LO	0.2138
	WToMuNu M-1000	PYTHIA 8	LO	0.01281
	WToMuNu M-2000	PYTHIA 8	LO	5.56e-04
	WToMuNu M-3000	PYTHIA 8	LO	2.904e-05
	WToMuNu M-4000	PYTHIA 8	LO	3.31-06
	WToMuNu M-5000	PYTHIA 8	LO	2.7-07
	WToMuNu M-6000	PYTHIA 8	LO	1.5e-08
	WToTauNu M-100	PYTHIA 8	LO	163.15
	WToTauNu M-200	PYTHIA 8	LO	6.236
	WToTauNu M-500	PYTHIA 8	LO	0.2138
	WToTauNu M-1000	PYTHIA 8	LO	0.01281
	WToTauNu M-2000	PYTHIA 8	LO	5.56e-04
	WToTauNu M-3000	PYTHIA 8	LO	2.904e-05
	WToTauNu M-4000	PYTHIA 8	LO	3.31-06
	WToTauNu M-5000	PYTHIA 8	LO	2.7-07
	WToTauNu M-6000	PYTHIA 8	LO	1.5e-08
$t\bar{t}$	single top s-channel 4f leptonDecays	aMC@NLO	NLO	3.36
	single top tW antitop 5f inclusiveDecays	POWHEG	NNLO	35.85
	single top tW top 5f inclusiveDecays	POWHEG	NNLO	35.85
	TTbar	PowHeg	NNLO	831.76
Drell Yan	ZToLL M_50_120	POWHEG	NLO	1975
	ZToLL M_120_200	POWHEG	NLO	19.3
	ZToLL M_200_400	POWHEG	NLO	2.73
	ZToLL M_400_800	POWHEG	NLO	0.241
	ZToLL M_800_1400	POWHEG	NLO	0.01678
	ZToLL M_1400_2300	POWHEG	NLO	0.0013
	ZToLL M_2300_3500	POWHEG	NLO	8.95e-05
	ZToLL M_3500_4500	POWHEG	NLO	4.13e-06
	ZToLL M_4500_6000	POWHEG	NLO	4.56e-07
	ZToLL M_6000_Inf	POWHEG	NLO	2.066e-08
γ+ jets	GJets HT-40To100	Madgraph	LO	20790.0
	GJets HT-100To200	Madgraph	LO	9238.0
	GJets HT-200To400	Madgraph	LO	2305.0
	GJets HT-400To600	Madgraph	LO	274.4
	GJets HT-600ToInf	Madgraph	LO	93.46
Diboson	WWToLNuQQ	POWHEG	NNLO	49.997
	WWTo4Q	POWHEG	NNLO	51.723
	WWTo2L2Nu	POWHEG	NNLO	12.178
	WZ 13TeV	PYTHIA 8	NLO	47.13
	ZZ 13TeV	PYTHIA 8	NLO	23.23

factors corresponds to the calibration of the trigger efficiencies and to the offline selections such as identification and isolation (Efficiencies and scale factors can be found in Section 5.3).

4.3.1 Higher-order corrections for the main background SM W

The main background, in particular at very high M_T where the signal is expected, is the irreducible off-shell SM W events. Therefore It is important to have an accurate description of the tail of the M_T distribution. W exclusive backgrounds are corrected for the K-factor depending on W mass to take into account QCD effects up to NNLO (two jets) and the photon-induced electroweak (EWK) effects up to NLO in the CMS acceptance. The differential cross section with Higher-order EWK and QCD corrections are evaluated binned in invariant mass ($M_{\ell\nu} = M_{inv}$) of SM W boson:

$$K(M_{inv}) = \frac{\Delta\sigma^{NLO}/\Delta M_{inv}}{\Delta\sigma^{LO}/\Delta M_{inv}} \tag{4.4}$$

The $\sqrt{s}$ =13 TeV NLO EWK corrections are computed by using the MCSANC [122] event generator and NNLO QCD corrections were derived from the FEWZ [115] program. (The strong coupling constant is set to $\alpha_s(M_Z) = 0.118$.) These QCD and EWK corrections can be combined with two apporaches : an additive (top equation) or a multiplicative (bottom equation) approach [123]:

$$\left[\frac{d\sigma}{d\mathcal{O}}\right]_{QCD\oplus EWK} = \left[\frac{d\sigma}{d\mathcal{O}}\right]_{QCD} + \left[\frac{d\sigma}{d\mathcal{O}}\right]_{EWK} - \left[\frac{d\sigma}{d\mathcal{O}}\right]_{LO} \tag{4.5}$$

$$\left[\frac{d\sigma}{d\mathcal{O}}\right]_{QCD\otimes EWK} = \left(\frac{\left[\frac{d\sigma}{d\mathcal{O}}\right]_{QCD}}{\left[\frac{d\sigma}{d\mathcal{O}}\right]_{LO}}\right) \times \left[\frac{d\sigma}{d\mathcal{O}}\right]_{EWK} \tag{4.6}$$

The additive approach assumes that the EWK corrections, except Final-state radiation (FSR), have an additive nature and are of the same order and need to be added for all orders of QCD, thus the relative fraction of higher-order EWK corrections for each order of QCD is changing. The factorized approach assumes that the higher order EWK corrections are the same for all orders of QCD, and thus can be determined based on LO QCD and then transferred to any order of QCD. Both approaches can be theoretically motivated and the correct combination would lie between these two approaches. The combination of both approaches was used to derive the K-factor with their spread as systematic uncertainty. Following the new recommendation of the LHC working group [123], the K-factor calculation is based on the additive combination and the difference to the factorized is used as uncertainty. The K-factors calculated with the background samples from Table 4.5, are a function of the invariant mass. The K-factor is maximal at low W masses and falls well below one for very high masses. It varies from 1.35 (1.3) for $m_W = 300$ GeV to 0.8 (0.7) for $m_W = 5$ TeV in the electron (muon) channel. (See Figure 4.4.) The differences between additive and multiplicative approach are larger in the muon channel since photon emission is not taken into account.

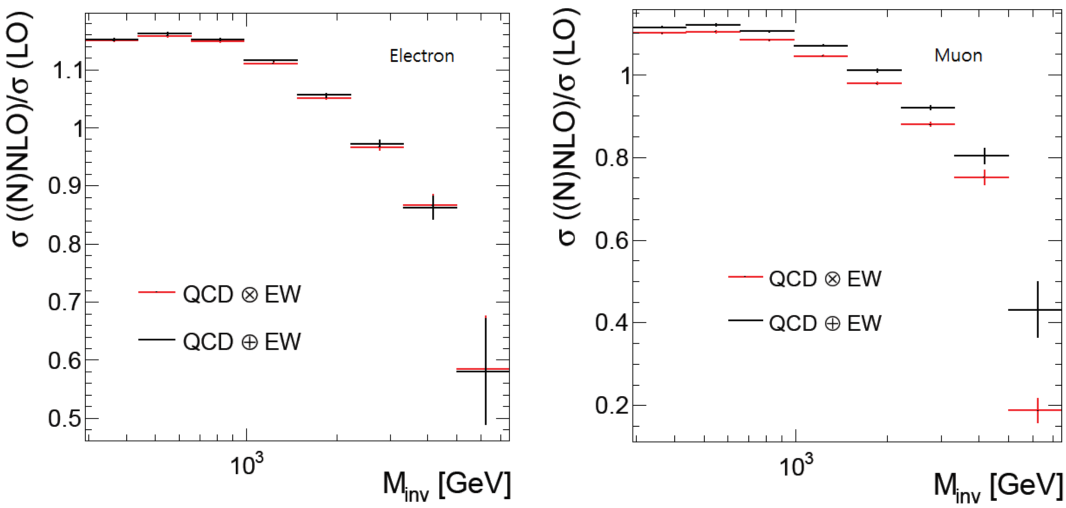

Figure 4.4: The LO and NNLO Cross section for electron (left) and muon (right) at $\sqrt{s} = 13$ TeV versus the mass of W′. There are two approaches to combine QCD and EWK corrections: additive (black) and multiplicative (red).

4.3.2 QCD multijet background from data-driven method

The misidentification of jets as leptons (more likely for electrons than for muons) is also taken into account for the possible background to this search. Most of the QCD multijet background can be efficiently rejected with the analysis selection criteria. While the contribution of QCD multijet events to the muon channel is negligible, a small contribution to the electron channel remains. Therefore the shape and normalization of the QCD multijet background used for the final results is derived from data. The sketch in Figure 4.5 shows the illustration of the "ABCD method". Different 4 regions are used to estimate the normalization and provide the QCD template data. A QCD template is produced from the events in which the electron candidate fails the isolation requirement but where all other event requirements are fulfilled. (Non-isolated electrons are expected from the multijet process) The template events are expected to be non-prompt electron.

The non-isolated electrons are scaled with normalization factors $R(p_T)$ to the expected isolated electrons. This factor is estimated in the region labeled as "QCD region", where the $p_T/E_T^{miss} > 1.5$ selection is applied. The probed phase space is specific to the analysis since the electron is the only expected object in the detector, it is also used to trigger the event.

The fake ratio is derived from the "QCD regions" C and D, where "C" region

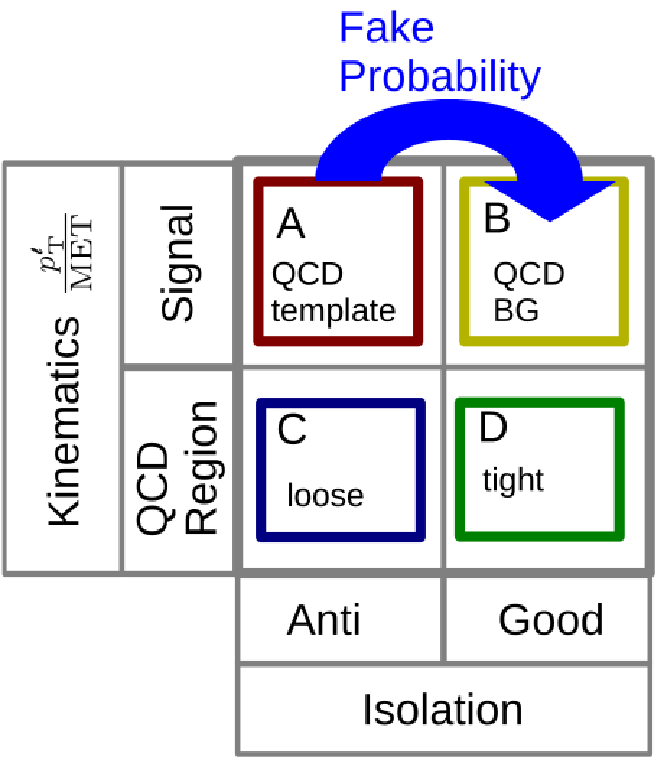

Figure 4.5: Illustration of the QCD data-driven ABCD method.

contains loose and "D" region contains tight electrons. In "C, D" regions, no requirement on p_T, E_T^{miss} or $\Delta\Phi$ have to be fulfilled. These regions are shown in Figure 4.6. The difference in number of events between data and the electro-weak background yields the number of QCD multijet events. Dividing the number of events yields the p_T dependent fake ratio $R(p_T)$. This ratio is shown in Figure 4.7. Starting at $p_T \approx 200$ GeV the ratio decreases from roughly 10 % to ≈ 1 % for high p_T. The non-isolated electrons in the "signal region" are considered as template data. These events are weighted with the p_T dependent fake ratio $R(p_T)$ and corrected for the prompt electrons using the simulated background. Based on experience with the same method in 2015, a total uncertainty of 40 % is assigned to the multijet background. In the following plots, the QCD contribution derived from data is included, labeled as "QCD DD".

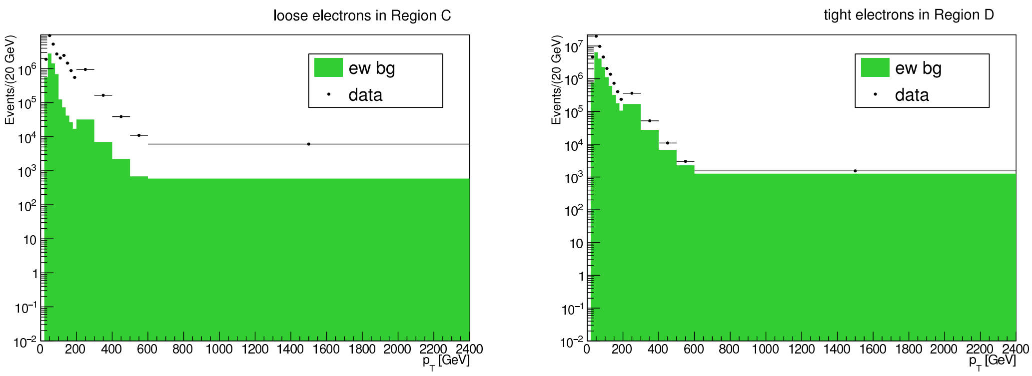

Figure 4.6: The p_T distributions are shown for loose electrons in region C (left) and for tight electrons in region D (right). The difference between the data and the electro-weak background constitutes the QCD multijet background.

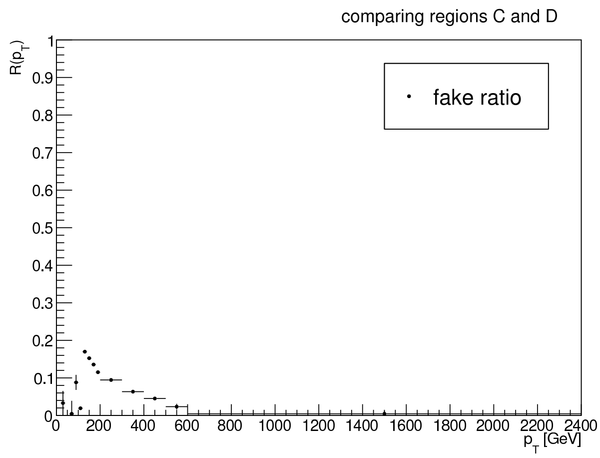

Figure 4.7: The p_T dependent fake ratio $R(p_T)$ is shown. Starting at $p_T \approx 200$ GeV the ratio decreases from roughly 10 % to $\approx$ 1 %.

Closure test for ABCD method

In order to prove whether the QCD multijet contribution obtained with the ABCD method is valid, a MC based closure test is also performed. By repeating the procedure, but instead of using the data, the combined electroweak and QCD simulated background samples are used. The QCD MC description is taken from the p_T binned PYTHIA 8 sample[5] with the p_T values ranging from 50 to 3200 GeV. The MC results are shown in Figures 4.8 and 4.9, which correspond to the Figures 4.6, 4.7 from data-driven approach. The MC-based fake ratio is applied

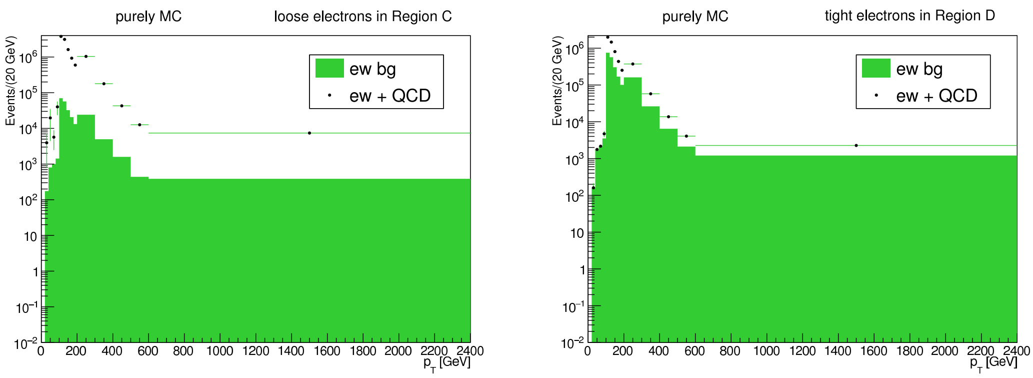

Figure 4.8: The p_T distributions are shown for loose electrons in "C" region (left) and for tight electrons in "D" region (right). The difference between the data and the electroweak backgrounds constitutes the QCD multijet background.

to the QCD template in the "A" signal region with a loose electron. The result is expected to match the QCD description in the "B" signal region with a tight electron. Checking with the distribution of E_T^{miss}, p_T and M_T as examples in Figure 4.10 from left to right, the QCD description from MC and data driven are in good agreement. It should be noted that are are slight differences in the descriptions originating in the requirement of the trigger in the data-driven method but not in the MC description. This closure test is performed to see whether the method works properly or not. The difference between the data-driven method and the MC closure test, resulting in about 40 %, is considered as systematic uncertainties. Alternatively one can vary the boundaries which define the individual regions and take the differences in the resulting QCD description as the uncertainty of the method. (Either approaches, the systematic uncertainties are within 40 %.)

[5] QCD_Pt_50to80_13TeV_P8

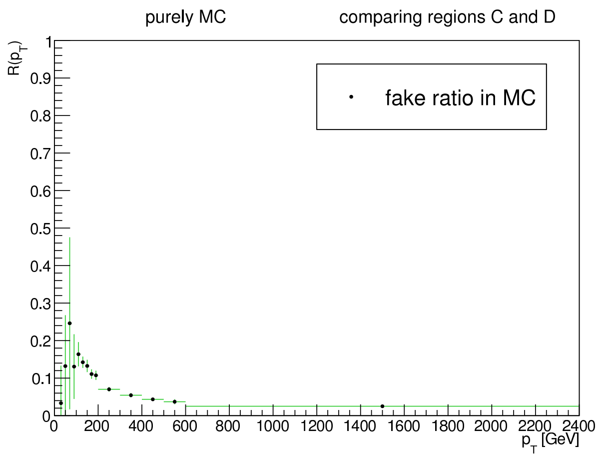

Figure 4.9: The p_T dependent fake ratio $R(p_T)$ is produced. From the $p_T \approx 200$ GeV the ratio decreases from roughly 20% to ≈ 5 %.

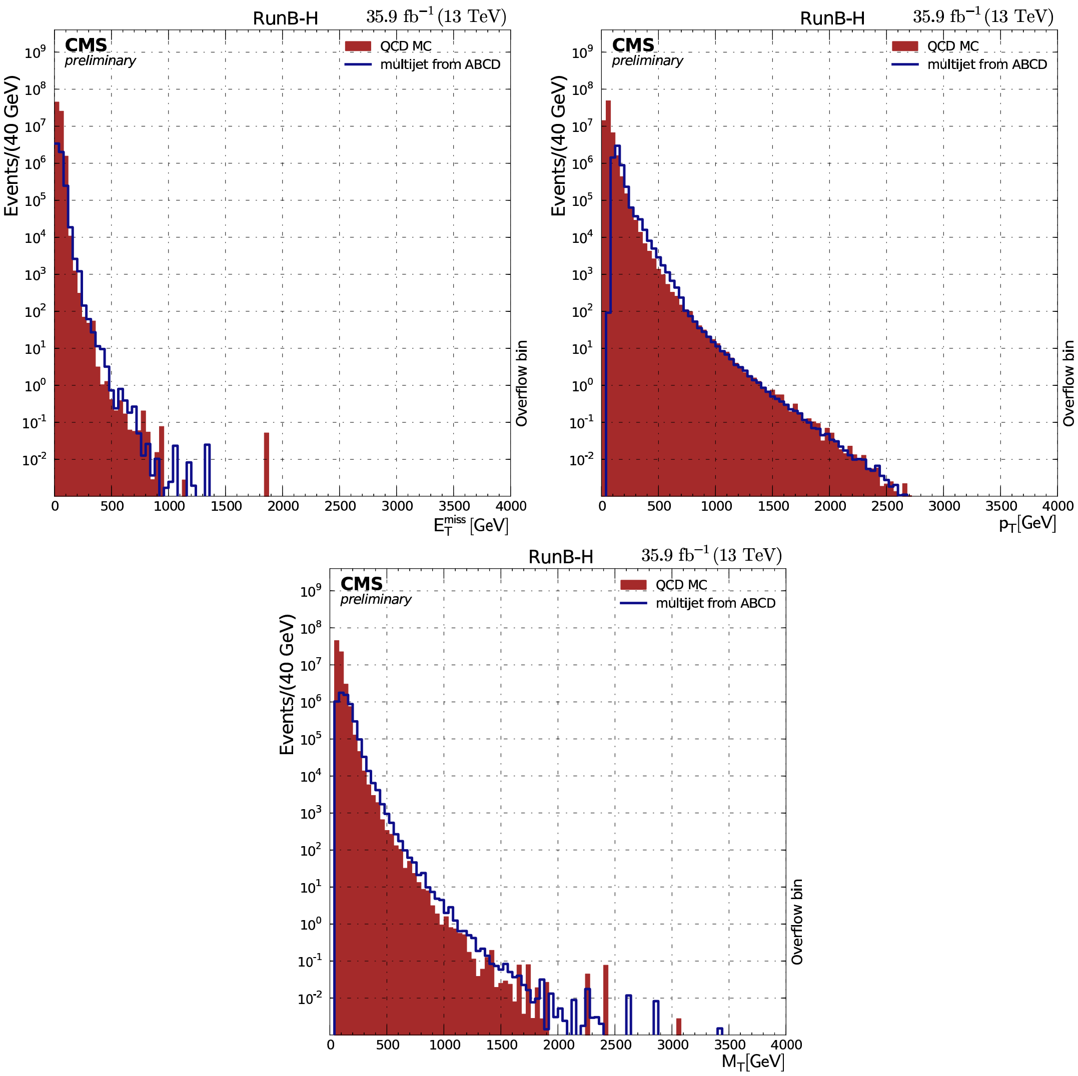

Figure 4.10: From left to right, the E_T^{miss}, p_T and M_T distributions are shown. In red the simulated QCD description, while the description extracted from the ABCD method is shown in blue. Aside from slight differences originating from the trigger being required in the ABCD method but not in the MC description, the two descriptions are in agreement.

Chapter 5

Reconstruction and Event Selection

5.1 Particle Reconstruction and Identification

In this section, the reconstruction and identification of particles related to the mono-lepton signature in the CMS detector are introduced. Reconstruction is a software process to construct physics quantities form the raw data collected in the experiment. The process can be divided into 3 steps : 1. local reconstruction within an individual detector module, 2. global reconstruction within a whole detector, and 3. combination of these to produce higher level objects.(See Figure 5.1.) The reconstruction algorithms and their procedures of electrons, muons, and missing transverse energy are presented in detail. Also the identification of high energetic leptons (electrons/muons) taken into account in this analysis is described.

5.1.1 Electron

In CMS detector, electron is reconstructed by associating a track reconstructed in the silicon tracker with a cluster of energy in the ECAL system [124, 125]. Firstly, It starts with the reconstruction of the energy deposit in the ECAL, so-called **clustering**. The energy deposits in ECAL crystals are grouped to form a cluster. The incorporation of bremsstrahlung photons is done by searching for the ECAL clusters of the latter ones and grouping their clusters together with the cluster of the primary electron to form a supercluster (a cluster of clusters). This is done by clustering algorithms. Since barrel and endcap have a different geometry and alignment, the clustering algorithms are different. For barrel electrons, the hybrid algorithm is used, while in the endcap the multi5$\times$5

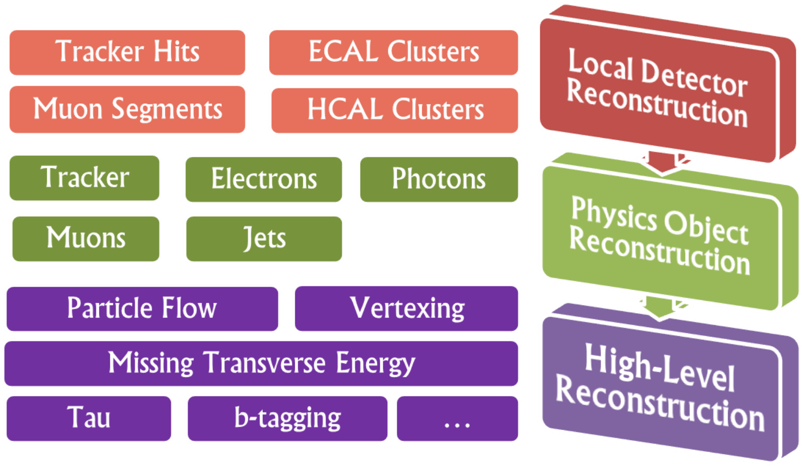

Figure 5.1: The reconstruction process can be divided into 3 steps. First in the local detector reconstruction process, the collections of independent units are made and then, each one provide a set of corresponding objects as output and lastly combination of all of these to produce higher level objects.

algorithms are applied. Both algorithms exploit magnetic field aligned along the z-axis of the detector. Therefore, the bremsstrahlung-photons will spread along the ϕ direction, while the spread in η will remain small.
The hybrid algorithm exploits features of the shower shape that is determined by collecting the energy in a small window in η and an extended window in ϕ. The seed crystal, defined as the one containing most of the energy deposited (> 1 GeV), is defined and then arrays of 5×1 crystals in $\eta \times \phi$ are added on around the seed crystal, in a range of crystals in both directions of ϕ, in case array satisfies a minimum energy threshold (>0.1 GeV). The contiguous arrays are grouped into clusters, with each distinct cluster need to satisfy a minimum energy threshold (> 0.35 GeV) of seed-array to become a final global cluster, denoted as a supercluster (SC).
In the EE, the multi5$\times$5 algorithms are used (Endcap crystals are not arranged in an $\eta \times \phi$ geometry). Similarly it also begins with the determination of seed crystal, the ones with local maximal energy (> 0.18 GeV) larger than their four closest neighbors. With starting with the largest E_T of the seed, the energy is collected in clusters of 5$\times$5 crystals (can overlap). These clusters are then grouped into an SC, in case their total E_T satisfies a minimum energy threshold (> 1 GeV) of a cluster within a range of η (±0.07) and ϕ (±0.3 rad) around each crystal. The energy-weighted positions of all grouped clusters belonging to an SC and extrapolated to the preshower detector. The reference point is determined by the position of the most energetic cluster. After reconstruction of supercluster

by clustering electron energy in ECAL, electron track is reconstructed in the tracker [126]. Electron track reconstruction begins with **seeding** step: Finding and selecting the first $2 \sim 3$ hits in the tracker from which the track can be initiated from. Track seeding is very important because its performance can highly affect the reconstruction efficiency.
For reconstructing track from the highly energetic electrons ($p_T > 10\,\mathrm{GeV}$), the ECAL based seeding procedure works better than another way of seeding. It starts with the energy and position of SC and This information used to find the trajectory of the electron in the first layers of the tracker, and then choose electron seeds among all of the reconstructed seeds. Here for ECAL based seeding, the energy-weighted position of the SC is on average to the reference point of an electron with the equal energy which didn't radiate bremsstrahlung.
Generally, in case of the low energy electron, the tracker-based seeding count on tracks which is reconstructed from the standard Kalman filter (KF) algorithms for charged particles, extrapolated to the ECAL and then matched to the SC. The track starts to be buitt with combinatorial Kalman filter (KF) method, which for each electron seed proceeds iteratively from the track parameters information from each layer, including one-by-one the information from each active layer. However, If KF tracks have a small number of hits and poor estimations of track parameter with a large χ^2 (hits and energies are largely missing when curving through tracker material due to the bremsstrahlung effect), they will be refitted using a dedicated Gaussian sum filter (GSF) algorithm [127]. Therefore the electron candidates are reconstructed from the association of a GSF track and a cluster in the ECAL in general. (this analysis is based on isolated high energetic electrons, ECAL-base seeding is of interest.) There are three main sources of electron candidates that are reconstructed with the CMS detector:
1. prompt electrons, 2. non-prompt electrons, and 3. fake electrons.
Prompt electrons come from the decays from W, Z bosons or new physics particles (like W′ boson). Non prompt electrons come from sources such as a heavy quark decaying. Fake (misidentified) electrons are not electrons.

These electrons are categorized by matching of a jet energy in the ECAL with the nearby single, high p_T track. Non-prompt and fake electrons are a background source of electrons that we want to reduce as much as possible. In this analysis, the high-energy prompt electron is the signal object what we have to find.
For high-energy electrons, the E_{sc} and p combination is mainly dominated by the energy measurement in the ECAL, thus simply the momentum estimation for high-energy electrons is using only the supercluster information in CMS. Unfortunately, due to the limitation of the detector technology, the energy deposition of enormously high-energy electrons (>∼1500 GeV in the EB, from >∼3000 GeV in the EE) bring a saturation of the front-end electronics [67]. Both the energy correction for saturated crystals and the calibration of high-energy electrons are tuned with Drell-Yan events by estimating the energy fraction ($E_1/E_{5\times5}$) between

the central crystal of a 5×5 matrix (highest energy) and rest of 24 surrounding crystals (lower energy). This energy fraction is parameterized with respect to the electron η, $E_{5\times5}$, and SC shower shape variables by using the high-mass Drell-Yan simulated events. These variables are used for identification and will be described In the following Section.

Electron Identification and Isolation

For the identification of highly energetic electrons, a dedicated set of selections is used, designed to ensure high efficiency electron Identification and isolation and a high rejection of fake electrons from QCD background. The High p_T electron group of CMS Exotica group defined and provided the identification and isolation variables with a nice package, so-called "**HEEP (High Energy Electron Pairs) ID**". The high p_T electron selection used in this analysis starts from a GSF electron on which kinematic, identification and isolation cuts are applied. The main requirements on the HEEP selection are to obtain a high efficiency > 95 % for electrons coming from the Drell-Yan process and to be p_T or pileup independent selections (for $p_T > 100$ GeV). The complete list of HEEP ID variables is in Table 5.1.1. The definition of these HEEP variable is explained

Variable	Barrel	Endcap
E_T	$E_T > 35\,\text{GeV}$	$E_T > 35\,\text{GeV}$
η_{sc} range	$\lvert\eta_{sc}\rvert < 1.4442$	$1.566 < \lvert\eta_{sc}\rvert < 2.5$
seed	isEcalDriven = True	isEcalDriven = True
$\lvert\Delta\eta_{in}^{seed}\rvert$	$\lvert\Delta\eta_{in}^{seed}\rvert < 0.004$	$\lvert\Delta\eta_{in}^{seed}\rvert < 0.006$
$\lvert\Delta\phi_{in}\rvert$	$\lvert\Delta\phi_{in}\rvert < 0.06$	$\lvert\Delta\phi_{in}\rvert < 0.06$
H/E	$H/E < 1/E + 0.05$	$H/E < 5/E + 0.05$
full 5×5 $\sigma_{i\eta i\eta}$	-	$\sigma_{i\eta i\eta} < 0.03$
$\frac{E^{1\times5}}{E^{5\times5}}, \frac{E^{2\times5}}{E^{5\times5}}$	$\frac{E^{1\times5}}{E^{5\times5}} > 0.83$ or $\frac{E^{2\times5}}{E^{5\times5}} > 0.94$	-
Inner Layer Lost Hits	Lost Hits ≤ 1	Lost Hits ≤ 1
Impact parameter, $\lvert d_{xy}\rvert$	$\lvert d_{xy}\rvert < 0.02$	$\lvert d_{xy}\rvert < 0.05$
EM+Had Depth1 Isolation, iso	$iso < 2 + 0.03E_T + 0.28\rho$	(if $E_T < 50$), $iso < 2.5 + 0.28\rho$ else if, $iso < 2.5 + 0.03(E_T - 50) + 0.28\rho$
TrackIso : Trk p_T, iso p_T	$isop_T < 5\,\text{GeV}$	$isop_T < 5\,\text{GeV}$

Table 5.1: A recent version 7.0 of the HEEP ID has been used for selecting high p_T electron. The first set is the acceptance cut, the second set is the identification cuts, and the third set is about the isolation cuts.

as below:

- E_T : Defined as the corrected electron ECAL energy $\times \sin\theta_{trk}$, where $\sin\theta_{trk}$ is the polar angle of the electron track measured at the inner track layer and then extrapolated to the interaction vertex. While for very high energy electrons, this will be the same as the supercluster energy $\times \sin(\theta_{\rm trk})$ most of the time.

- $\eta_{\rm sc}$:The pseudo-rapidity of the electron's supercluster of ECAL with respect to the center of the detector. The fiducial cuts need to be used due to detector effects and it should not be used to calculate for momentum in physics results, such as mass caculations.(η, as measured at the tracker inner layer and extrapolated to the primary vertex, should be used for calculating four momentum.)

- IsEcalDriven: A electrons can be reconstructed by ECAL-based (using EGamma techniques) or tracker-based (using particle-flow) as explained in sectionsec:electron. For high $\rm p_T$ electrons, ECAL-based performance much better than tracker-based. Therefore only electron from ECAL-based seeds is required.

- $\Delta\eta_{\rm in}^{\rm seed}$, $\Delta\phi_{\rm in}^{\rm seed}$: $\Delta\eta_{\rm in}^{\rm seed}$ ($\phi_{\rm in}$) designates the difference between the $\eta_{\rm seed}$ ($\phi_{\rm sc}$) seed cluster (supercluster)[1] and the $\eta_{\rm in}^{\rm extrap}$ ($\phi_{\rm in}^{\rm extrap}$) extrapolated from the innermost track measurement to the ECAL. This requirement checks for an acceptable matching of the electron track and the position of the seed cluster (supercluster). The constraint on $\Delta\eta_{\rm in}$ is much stronger than the constraint on $\Delta\phi_{\rm in}$, because of the larger spread of the electron's Ecal energy deposit in ϕ.

- H/E: The ratio between the energy deposited in the HCAL in a cone of $\Delta{\rm R} = \sqrt{\Delta\eta^2 + \Delta\phi^2} = 0.15$ centered on the supercluster position and the energy of supercluster. This cut provides discrimination between electrons and jets. (H/E should be small for electrons.)

- full 5×5 $\sigma_{{\rm i}\eta{\rm i}\eta}$ (EE only): The quantity $\sigma_{{\rm i}\eta{\rm i}\eta}$ is a measurement of the spread in η in units of crystals of the electrons energy in the $5{\times}5$ block centered on the seed crystal. A large spread in the energy deposition by the electron candidate indicates that the candidate is most likely a jet.

- full 5×5 $\rm E^{(1or2)\times5}/E^{5\times5}$ (EB only): Respectively the ratio between the energy of the supercluster seed and the total energy collected in the 5×5 matrix surrounding the seed and the ratio between the sum of the seed energy and the energy of the most energetic crystal adjacent to the seed and the total energy collected in the 5×5 matrix surrounding the seed.

- EM Isolation : It is defined as the transverse electromagnetic energy of all the reconstructed hits with $|{\rm E}| > 0.08\,{\rm GeV}$ in the EB ($|{\rm E}| > 0.1\,{\rm GeV}$ in the EE) in a cone of (ΔR) 0.3 radius centered on the electron's ECAL position,

[1] Instead of the supercluster η, it uses the η of the seed cluster of the supercluster which is currently a more accurate indication of the η of the original electron before bremstralung.

excluding those hits in an inner cone of 3 crystals.This variable is used only in a sum with the hadronic depth 1 isolation defined below.

- Hadronic Depth 1 Isolation: It is defined as the transverse depth hadronic energy of all the HCAL CaloTowers in a cone of 0.3 radius centered on the electron's ECAL position, excluding CaloTowers in a cone of 0.15 radius. The ρ is the average energy density per effective area originating from pileup. Becasue the pileup effect contributes to the ECAL and HCAL isolation values, ρ value is included to consider pileup effect.

- Track p_T isolation: It is defined as the sum p_T of the all tracks in a ΔR cone of radius from 0.04 to 0.3 excluding a ± 0.015 strip in eta with $p_T > 0.7$ GeV and dz_0 with ± 0.2 of the electron GsfTrack. The variable dz_0 is minimum distance in z from the point (0,0,0).

- Inner layer lost hits: The prompt electron's track starts at the beam-line and is expected to produce valid hits in the inner tracker layers. The missing Inner track layer lost hits are used to reject a conversion of photon and electron from QCD events.

- d_{xy}: It is defined as the transverse impact parameter, the minimum transverse distance of the electron track to the primary vertex. The prompt electron has a small d_{xy}, therefore it can be used to reject electrons from photon conversion or electrons from the hadronization process of a jet.

5.1.2 Muon

Muon reconstruction starts from single detector elements (i.e. pixel and strip hits in the inner tracker, or RPC hits in the muon system) or segments (reconstructed within single DT/CSC chambers), and then muon tracks are built independently in both in the inner tracker (tracker inner tracks) and in the muon system (standalone-muon tracks). These two approaches are combined into a reconstruction of a general track, Global Muon track reconstruction: Global Muon is built with the outside-in reconstruction, where starting from each standalone track, matching with nearby inner tracker tracks is found by propagating them onto the inner tracker. After both tracks candidates are geometrically matched, the Global Muon track is fitted using a Kalman-ltering technique [128], taking as input the combining hits from both tracks. The Global Muon reconstruction reduces the rate of fake tracks and gives a gain in detector length by containing the hits in the muon system. The global muon fit will give a better performance of the momentum resolution than the tracker-only fit, for high p_T muons, particularly above 200 GeV. At low p_T of the muon (< 5 GeV), the Tracker Muon reconstruction works better. Due to the high efficiency in the track reconstruction in the tracker system and segment reconstruction in the muon system, more

than 97% of the muons are reconstructed within the acceptance of the muon system,$|\eta| < 2.4$.
For the high p_T muon, as it goes through the magnet return yoke, the multiple scattering and the radiative processes can possibly change the trajectory of the muon. It means that the muon can lose large energy and also produce electromagnetic showers bringing to additional fake hits in the muon chambers, thus the estimate of the muon momentum at the production vertex can be significantly different from its real value. In order to optimize the reconstruction and especially the momentum assignment, different possibilities in terms of hits content and track fitting algorithms have been developed in CMS experiment. There are several different strategies for including information from the muon system studied by using cosmic rays [129]:

- Tracker Fit: The Tracker algorithm considers the tracker track + at least a valid muon hit, which identifies the muon.
- Tracker Plus First Muon Station (TPFMS) fit: This algorithm refits the Global Muon track not considering hits in all muon stations, except the innermost muon station containing hits (considering about reduced sensitivity to possible showering deeper in the muon system.) .
- The Picky fit: This algorithm also starts with the full hit list of the Global Muon track, but re-fits the extrapolated tracker trajectory excluding individual hits in chambers with anomalously large hit occupancy. This is done to avoid hits from potential electromagnetic showers. Hits coming from the chambers with a high probability of shower contamination (determined by the hit occupancy) are required to be compatible with the extrapolated trajectory by applying a χ^2 cut.
- The Dynamic Truncation (DYT): This algorithm starts from the Tracker track propagating outwards, to the muon stations, adding muon hits or segments only if no large energy loss has taken place. (Avoiding hits after a large energy loss in the muon system)

The combination of different algorithms provides robust and efficient muon reconstruction. To further improve the resolution at high p_T, In particular, the TuneP algorithm consists in a comparison of the performance of these several methods, choosing best track fit (TuneP) on a track-by-track basis, attending to the tail probability of the track fit χ^2/ndf and the relative p_T measurement error, $\sigma p_T/p_T$. Once TuneP high-p_T muons are reconstructed, then dedicated identication criteria are applied to ensure that the candidate is, in fact, a real muon. Analysers can set the desired balance between identification efficiency and purity by using a selection with various muon identification variables [130, 129]. In our analysis, the high-p_T ID selection is applied and detail description of muon variables are in the following Section.

Muon Identification and Isolation

For searches at the LHC having muons in the final state, it is important to remove fake muons that can occur for example in hadronic decays (decay in flight) or hadron shower remanent in the muon system that is reconstructed as a muon object (punch-trough). Fake muons are removed by applying "high-p_T muon identification" selections which rely on information from the tracker and muon system such as the number of pixel hits, the number of tracker layers with hits, the muon segments reconstructed in the muon station, as well as quality requirements on the muon track, such as the track χ^2, the number of muon chamber hits in the track fit. This selection is aimed to the best reconstruction of the muon track parameters for high p_T muons ($p_T > 200$GeV), without relying on external information in the event. In this high p_T region, the muon detectors can improve the momentum resolution of the inner tracker. To further suppress fake muons from decay in flight, Isolation cuts are used. They are applied on the muon "loose tracker relative isolation", which quantifies the energy flow of particles in proximity of the muon trajectory, computed by summing all particles in a $\Delta R = (\Delta\eta^2 + \Delta\phi^2)^{1/2}$ cone around the muon, and dividing by the muon transverse momentum. The isolation algorithm includes pile-up correction.
The high-p_T muon identification and isolation criteria are described as following:

- A good offline-reconstructed primary vertex (PV) is required to be found in the event : At least 4 tracks must be associated to the vertex and the vertex must be closed with the interaction point (IP) $|r| < 2$ cm and $|z| < 24$ cm. These PV cuts allow discarding cosmic-ray muons triggering in empty bunch-crossings, which can produce fake muons when traversing the detector near the IP and also to ensure the quality of the hadronic collisions and reject detection of particles produced between beam particles and residuals present in the defective vacuum of LHC.
- The muon must be reconstructed as a "Global" muon and a "Tracker" muon.
- The relative p_T uncertainty from the track reconstruction $\delta p_T/p_T < 0.3$ is required, to suppress muon with mis-measured muon tracks and especially ensure the quality of the p_T measurement.
- The transverse impact parameter of the muon, $|d_{xy}|$, the distance from the primary vertex, as measured by the Tracker-only fit, must be closer than 0.2 cm. A longitudinal distance parameter, $|d_z|$, of the tracker track must be less than 0.5 cm. Both parameters are defined relative to reduce background from cosmic ray muons.
- The muon must pass a relative tracker-only isolation cut, $\sum p_T$(Tracker tracks from PV)$/p_T^\mu < 0.1$: the scalar sum of the p_T of all other tracks

in a cone of $\Delta R < 0.3$ around but not including the muons tracker track must be less than 10 % of the muons p_T, also as measured by the tracker. To be used in the calculation of the tracker isolation, tracks have to be within $\Delta z = 0.2$ cm of the primary vertex with which the muon candidate is associated.

- The global muon track must have at least 6 tracker layers with hits in the fit.
- The global muon track fit must contain at least one hit from each pixel detector and the muon system.
- The tracker muon must be matched to segments in at least a muon stations. If the muon station is not on the first layer of the muon system, or if matched to one muon station on the first layer, we also required that the muon matches to more than 2 RPC layers, or that the muon is matched in at least 2 muon stations.
- To further reduce the Drell-Yan events and cosmic-ray backgrounds, the event must not have a second muon with $p_T > 25\,\mathrm{GeV}$.

The efficiencies and scale-factors of these ID and Isolation (electron and muon) using the Tag and Probe method by CMS official Muon Physics Object Group (POG) can be found in Section 5.3.

5.1.3 Missing Transverse Energy

The leptonic decays of W′-like events must contain a neutrino, which is undetectable. In CMS experiment, this neutrino is indirectly measured to so-called Missing Transverse Energy (MET). By using the conservation of the four momentum vector in the transverse plane ($\vec{p}_T^{miss}$) is defined as the transverse component of the negative vector sum of all particles as given below :

$$\vec{p}_T^{miss} = -\sum_i \vec{p}_{T,i} \tag{5.1}$$

All of stable particles in the event are reconstructed based on the Particle Flow (PF) algorithm [89, 131, 132] in CMS. The strategy of the PF algorithm is to combine the information of all CMS sub-detectors in order to reconstruct and identify all stable particles (electrons, muons, photons, charged hadrons, neutral hadrons) in an event. Based on this list of particles, the composite object like jets and $\vec{p}_T^{miss}$ are reconstructed. The PF algorithm can be divided in three steps which are briefly explained in the following.
The first step of the PF algorithm is the reconstruction of tracks from charged

particles in the tracker, clusters from energy deposits in the ECAL and HCAL as well as muon tracks from the muon system. These PF elements represent the reconstructed information from each sub-detector. Each particle will depending on its type, lead to the creation of several PF elements (e.g track and ECAL cluster in the case of an electron). For the reconstruction of the individual particles, the different PF elements have to be combined. This is done with a linking algorithm looping over pairs of PF elements and quantifying the matching between the two elements. For example, the linking of an ECAL cluster and a charged particle track is performed by extrapolating the track into the ECAL and check if the extrapolated track is within the boundaries of the cluster.

In the latter case, the track and the cluster are linked. The algorithm proceeds by grouping linked (directly or indirectly) elements into PF blocks. Since the CMS sub-detectors provide a high granularity, the PF block usually consists only out of a few elements. The key part of the PF algorithm is the identification of individual particles out of reconstructed PF blocks. This is done with an iterative approach starting with the identification of PF muons. For each time a particle is identified, the related PF block is eliminated from the collection of PF blocks and the algorithm proceeds with the reduced collection. Blocks with a muon track element from the muon detector and a charged particle track element are identified as global muon, if a global fit of both tracks leads to a reasonable χ^2 and a p_T measurement, that is compatible with the one from the charged particle track element.

The next step is to identify PF electrons. A pre-identification procedure is applied to charged particle track elements of appropriate PF blocks. For blocks passing the pre-identification, the track is refit using the GSF algorithm. The final identification is done by a boosted decision tree using a large set of track and cluster properties. (More information about the PF electron identification is given in [132].) After the application of additional quality criteria, each charged particle track linked to calorimeter clusters is treated as PF charged hadron. The particle momentum from the charged track is compared to the energy of the calorimetric clusters. In case that the calorimetric energy is significantly large, PF photons and neutral hadrons are included to compensate the energy discrepancy.

The last step of the particle identification is to identify all remaining ECAL (HCAL) clusters which are not linked to a charged particle track element as photons (neutral hadrons).

Finally, the list of particles is then exploited to reconstruct composite objects like jets and $\vec{p}_T^{miss}$.

Missing Transverse Energy Type-1 Corrections

In this analysis, type-I corrected MET value is used. The type-I $\vec{p}_T^{miss}$ corrections propagate the jet energy corrections (JEC) to the $\vec{p}_T^{miss}$. CMS uses a factorized approach for the JEC which divides the correction into different levels. Each level corrects for a different effect and is applied to the jet energy obtained after application of the precedent correction levels. The commonly applied corrections are the L1, L2 and L3 correction. L1, L2, L3 are levels of JEC. The L1 JEC is called 'offset correction' corrects for the shift of the jet energy due to the contribution of pile-up.

The L2 JEC is called 'relative jet η correction' and corrects the jet response to be at in η. The L3 JEC is the 'absolute jet p_T correction' and ensures at jet response in p_T. This and more information about JEC can be found in [133].

For the PF $\vec{p}_T^{miss}$ type-I correction, the JEC are considered for all jets with $p_T > 10\,\text{GeV}$ and a fraction of energy deposited in the ECAL smaller than 90 % of the jet energy. The formula for the raw PF $\vec{p}_T^{miss}$ given in Equation 5.5 can be expanded by dividing the sum over all PF candidates into a sum of candidates within a jet and a second with the remaining candidates. The first sum can be replaced with a sum of the uncorrected jet p_T of all jets leading to the formula given below:

$$\vec{p}_T^{\,\text{miss,uncorr.}} = -\sum_{\text{jets}} \vec{p}_{\text{T, jet}}^{\,\text{uncorr.}} - \sum_{i \notin \text{jets}} \vec{p}_{\text{T, i}} \tag{5.2}$$

The sum of jet p_T can be further divided into jets with the quantify of $\vec{p}_{\text{T,jet}}^{\,\text{L123}}$($> 10$ or $< 10\,\text{GeV}$), where $\vec{p}_{\text{T,jet}}^{\,\text{L123}}$ is the jet p_T after applying L1, L2, and L3 JEC.

$$\vec{p}_T^{\,\text{miss,uncorr.}} = -\sum_{\substack{\text{jet}\\ \vec{p}_{\text{T, jet}}^{\,\text{L123}} > 10\text{GeV}}} \vec{p}_{\text{T, jet}}^{\,\text{uncorr.}} - \sum_{\substack{\text{jet}\\ \vec{p}_{\text{T, jet}}^{\,\text{L123}} < 10\text{GeV}}} \vec{p}_{\text{T, jet}}^{\,\text{uncorr.}} - \sum_{i \notin \text{jets}} \vec{p}_{\text{T, i}} \tag{5.3}$$

The final formular for the raw PF $\vec{p}_T^{miss}$ is obtained by expanding first term.

$$\begin{aligned} \vec{p}_T^{\,\text{miss,uncorr.}} = & -\sum_{\substack{\text{jet}\\ \vec{p}_{\text{T, jet}}^{\,\text{L123}} > 10\text{GeV}}} \vec{p}_{\text{T, jet}}^{\,\text{L1}} - \sum_{\substack{\text{jet}\\ \vec{p}_{\text{T, jet}}^{\,\text{L123}} > 10\text{GeV}}} (\vec{p}_{\text{T, jet}}^{\,\text{uncorr.}} - \vec{p}_{\text{T, jet}}^{\,\text{L1}}) \\ & - \sum_{\substack{\text{jet}\\ \vec{p}_{\text{T, jet}}^{\,\text{L123}} < 10\text{GeV}}} \vec{p}_{\text{T, jet}}^{\,\text{uncorr.}} - \sum_{i \notin \text{jets}} \vec{p}_{\text{T, i}} \end{aligned} \tag{5.4}$$

The type-I correction acts on the .rst term of the formula by replacing $\vec{p}_{\text{T, jet}}^{\,\text{L1}}$ correction with $\vec{p}_{\text{T, jet}}^{\,\text{L123}}$. As a consequence, the final formular for PF type-1 corrected $\vec{p}_T^{miss}$ is :

$$\begin{aligned} \vec{p}_T^{\,\text{miss,type-I}} = & -\sum_{\substack{\text{jet}\\ \vec{p}_{\text{T, jet}}^{\,\text{L123}} > 10\text{GeV}}} \vec{p}_{\text{T, jet}}^{\,\text{L123}} - \sum_{\substack{\text{jet}\\ \vec{p}_{\text{T, jet}}^{\,\text{L123}} > 10\text{GeV}}} (\vec{p}_{\text{T, jet}}^{\,\text{uncorr.}} - \vec{p}_{\text{T, jet}}^{\,\text{L1}}) \\ & - \sum_{\substack{\text{jet}\\ \vec{p}_{\text{T, jet}}^{\,\text{L123}} < 10\text{GeV}}} \vec{p}_{\text{T, jet}}^{\,\text{uncorr.}} - \sum_{i \notin \text{jets}} \vec{p}_{\text{T, i}} \end{aligned} \tag{5.5}$$

5.2 Trigger

As introduced in Section 3.3.7, most of the events produced in LHC are not interesting processes. In order to avoid running the offline code on millions of uninteresting events, an early decision (online selection) using Trigger system is a crucial part of the CMS data flow. The High-Level Trigger takes events accepted from the Level-1 trigger and decides based on sophisticated algorithms and filters, which can determine whether an event should be kept for an offline analysis. Therefore offline analysis depends on the outcome of the HLT. Presumably, the HLT could be run in the offline reconstruction step to compute all trigger bits in order to get a complete trigger picture allowing measurement of trigger efficiency. In this analysis, the $W' \rightarrow \ell\nu$ signal signature predicts one highly energetic lepton (electron and muon). The unprescaled high p_T non-isolated single electron (muon) HLT in CMS experiment is used for the select signal-like events.

5.2.1 Electron Trigger

To select events containing a single electron with the high purity of the HLT, the reduction of the contamination from the fake electrons is crucial. It suggested that the need for calorimetry and tracker-based electron ID and isolation to keep both the E_T threshold and the HLT rate low. The selection of a good HLT electron candidate is done with several requirements (working point): a supercluster with E_T greater than a certain threshold, matching an electromagnetic L1 candidate, satisfying the electron identification parameters for Calorimeter (cluster shape and H/E), containing a hit in the pixel detector compatible with an electron's trajectory, and matching with Tracker track. The single electron trigger for selecting signal events is "`HLT_Ele115_CaloIdVT_GsfTrkIdT`" seeded by the `L1_SingleEG30-40 OR L1_SingleJet170-200 OR L1_SingleTau100er-120er` seed with various threshold values.
During data taking in Run2, we found that the trigger efficiency drops for electrons with high p_T, particularly in the barrel. To solve this problem, many efforts have been done in 2016. First for the L1 trigger, the `L1_SingleJet` and `L1_SingleTau` seed triggers has been additionally included to overall Egamma triggers so that they can mitigate the inefficiency problem of `L1_SingleEG` trigger at high E_T (TeV) electrons. This was derived from the tight H/E cuts which defined without taking saturating the ECAL Trigger towers into account : H/E < 3.125 % for the barrel and H/E < 6.25 % for endcap. The ECAL trigger towers are saturated at E_T 127.5 GeV (E_T of HCAL relatively become larger) so the high E_T electron candidates often have a large contribution of HCAL, particularly in the barrel. (Ecal saturation at 127.5 GeV means that HCAL $E_T < 4$ GeV for barrel and < 8 GeV for endcap, therefore more loose H/E cut is also implemented to `L1_SingleEG` seed from Run C period (after Run 275656).)

Despite these changes, barrel electrons above 300 GeV were still observed to be inefficient. The main reason is that the working point is uniquely sensitive to the ECAL Gain Switch problem with multifit. It has a very tight cluster shape ($\sigma_{i\eta i\eta}$) cut, particularly to barrel electrons. The dedicated study for the single electron path during PromptReco data taking period is described in Appendix 9. The most efficient and feasible solution so far was to apply another trigger path with a loose working point. Therefore, we decided to `OR` an unprescaled single photon trigger "`HLT_Photon175`" in this analysis. It can compensate for a potential efficiency loss in high p_T electron by collecting good electron candidates. This path has same L1 seeds as `HLT_Ele115_CaloIdVT_GsfTrkIdT` path but has different working points. The HLT filters and cut variables of these two signal trigger paths are described in the Table 5.2.1

HLT Filter	EB conditions	EE conditions
`HLT_Ele115_CaloIdVT_GsfTrkIdT`		
Ele115	$p_T > 115\,\text{GeV}$	$p_T > 115\,\text{GeV}$
ClusterShape	$\sigma_{i\eta i\eta} 5\times 5 < 0.01$	$\sigma_{i\eta i\eta} 5\times 5 < 0.03$
HoverE	$H/E < 0.1$	$H/E < 0.1$
GsfDeta	$\lvert\Delta\eta_{in}\rvert < 0.007$	$\lvert\Delta\eta_{in}\rvert < 0.007$
GsfDphi	$\lvert\Delta\eta_{in}\rvert < 0.06$	$\lvert\Delta\eta_{in}\rvert < 0.06$
`HLT_Photon175`		
Photon175	$p_T > 175\,\text{GeV}$	$p_T > 175\,\text{GeV}$
HoverE	$H/E < 0.15$	$H/E < 0.1$

Table 5.2: Summary of the conditions for Barrel and Endcap implemented in analysis main signal triggers.

5.2.2 Muon Trigger

The HLT muon path is consisted of two different chains: HLT muon reconstruction chain and the HLT filter logic. The reconstruction chain is common to all trigger paths having muons. The HLT muon reconstruction starts only if the L1 trigger decision for at least one of the paths having muons is positive and then it will process all muon candidates selected by initial filters on the L1 Global Muon Trigger(described in Section 3.3.7.). The main procedures of the HLT muon reconstruction are as follows (See Figure 5.2.) :

- L2 seeding : The parameters of the L1 muon candidates are converted into seeds for the standalone muon reconstruction. (known as L2 muon reconstruction)

- L2 reconstruction : Standalone muon reconstruction. Exploiting muon system information.
- L2 isolation : Calorimetric isolation for each L2 muon candidate.
- L3 reconstruction : Global muon reconstruction. The tracker reconstruction is performed in the tracker and the reconstructed track is merged with the L2 track with a global fit[2].
- L3 isolation : The tracker isolation for the L3 candidate is performed using information from neighboring tracks reconstructed only with pixel hits.

HLT Filters can be interleaved between the previous pieces of the reconstruction procedure and are specific for each muon trigger path.
During data taking in RunII, the inefficiency of L1 Muon trigger system was

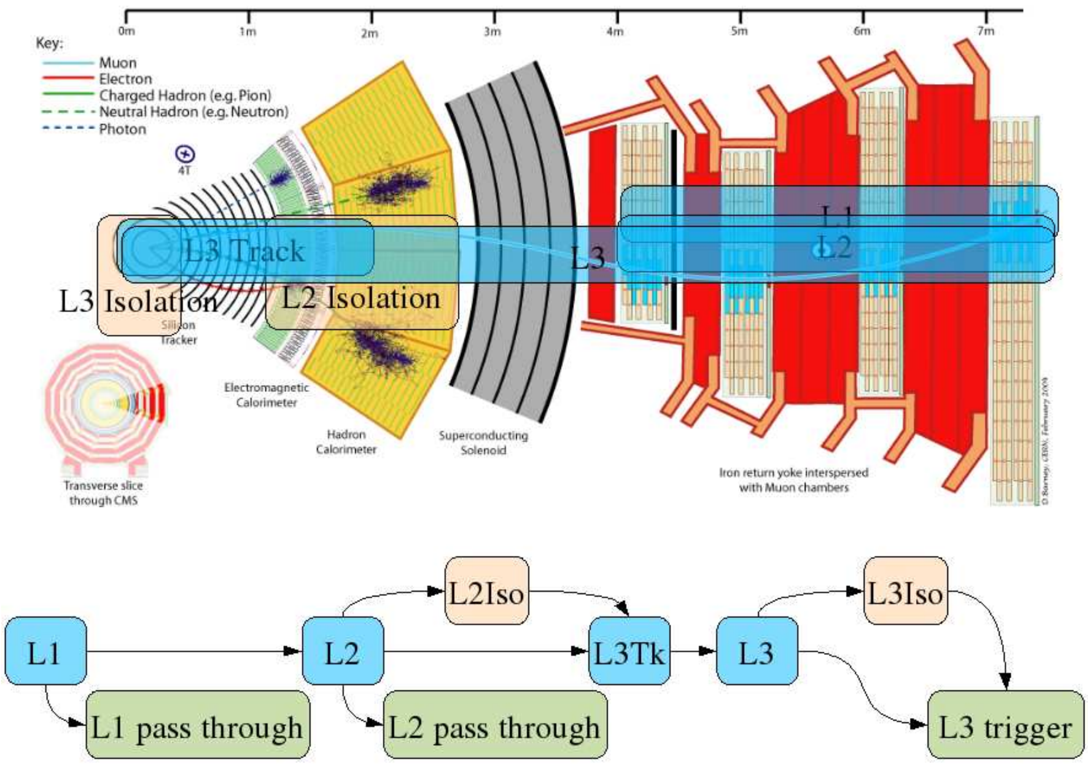

Figure 5.2: The Muon trigger workflow in CMS experiment.

observed for L1 muons. (particularly in the endcap/overlap region of the muon system.) To solve this L1 inefficiency issue, various changes happened during

[2]To save computing time, regional reconstruction in the CMS tracker is used: the pattern recognition and the track fitting are performed only in a small region of the tracker.

data taking : The L1 Barrel Muon Track Finder (BMTF) was fixed from Run 273423(B), which mitigated an inefficiency in central region $|\eta| < 0.3$ (94 pb^{-1} data collected without fix and both `HLT_Muon` and `HLT_TkMuon` paths affected). The mismatching between L2 seed and the Outer Muon Track Finder (OMTF) L1 candidate was fixed from Run 274094 (B) and only `HLT_Muon` path affected. And the major issue affecting efficiency especially for high p_T muons is a mis-configuration in the L1 Endcap Muon Tracker Finder (EMTF). It was also fixed from Run 277166(E), which corresponds to 15.4 pb^{-1}. In addition, RPC systems[3] were added at the end of the Run H, Run 282917.

In the muon analysis, the main trigger paths are `HLT_Mu50 OR HLT_TkMu50`, that select non isolated single muons with p_T above 50 GeV in the pseudorapidity range of the muon system acceptance, $|\eta| < 2.4$. These two triggers are equally seeded by `L1_SingleMu22 OR L1_SingleMu25`.
The `HLT_TkMu50` path has been newly updated since Run 274954 (after about 5.5 fb^{-1} were collected, early Run doesn't have this path). The motivation of this new path is to collect additional 1-2% more events relevant to single-muon events failing the full muon reconstruction in the trigger (due to misalignment, dead detector, and others), but passing the tracker-muon identification. In this new path, instead of producing an L2 muon and performing L3 reconstruction to produce a global muon, iterative tracking is performed in a window based on the L1 seed. Using the OR of these two trigger paths, the efficiency gets more stable and flat scale factor closer to 1. Both main triggers for leptonic channels are all fully unprescaled (every time the trigger fired the event was recorded) during the whole run range in 2016 except for new `HLT_TkMu50` path. They have a high-p_T threshold to keep the rate low without any isolation requirements. These trigger constraints are tight enough to allow the trigger to run without a prescale while still being loose enough to be very efficient at high p_T electron or muon.
During 2016 data taking period, the Muon HLT L3 reconstruction is affected by HIP problem causing a tracking inefficiency at high instantaneous luminosities. This inefficiency ls larger on single muon paths (using L3) than TkMu paths. With increasing inst. lumi (or Pileup), the inefficiency not completely recovered by ORing L3 and TkMu paths. Starting from Run 278801 a new setting of the strip APV readout chip has been deployed and it recovered the inefficiency. The effects on the APV fix measured on RunF before (Run 277932-278768) and after (Run 278802 - 278808) the fix. Figure 5.3 shows the L3 efficiency with respect to L1 as a function of instantaneous luminosity before and after the APV change.

[3] RPC system is known to measure a more precise timing than DT and CSC, but less accurate p_T assignment.

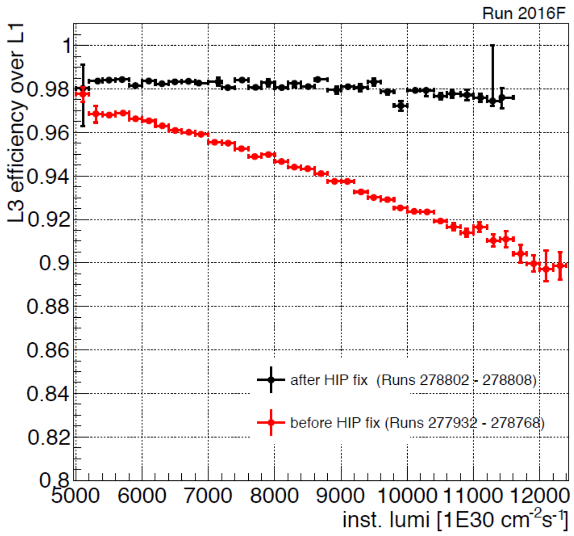

Figure 5.3: The efficiency of L3 muon reconstruction with respect to L1 (L3/L1) as a function of instantaneous luminosity before and after HIP fixed using Run 2016F dataset. This figure is provided by Muon POG [134].

5.3 Efficiencies and Scale Factors

Once the offline selections is determined by the analysis, it is essential to study how efficiently applied selections in data and MC simulation is. Particularly, it is important to estimate scale factor (SF) by comparing data and MC because they may have different efficiencies for the selections (such as reconstruction, identification, trigger, and isolation). The SF which is derived from the performance information in the data can correct MC sample: SF is defined as the data efficiency divided by the MC efficiency. Practically, when we use the offline selections to the MC sample, the efficiency of the selections (Reco, ID, ISO, Trigger, $\cdots$) must be directly measured in the same manner as the data and applied to the MC as a SF.
In following section, we will describe the efficiencies and SF of selections in this mono-lepton search analysis : HEEP ID for electrons and high-p_T ID, Loose Tracker Isolation for muons. All results are centrally produced in CMS.

Before describing the efficiencies, the most typical technique for calculating efficiencies, the Tag and Probe method, will be explained first.

5.3.1 Tag and Probe technique

To get a reliable efficiency measurement from the data, it has been a good way to take a benchmark sample well-understood Z events and measure efficiencies in this. Tag and Probe is a well-established data driven technique to extract lepton efficiencies from data, using lepton pairs (e^+e^- or $\mu^+\mu^-$) to reconstruct the Z-boson resonances. In principal this technique is to require very tight criteria on one of the two leptons (called tag) and to measure the selection efficiency on the other lepton (called probe). By determining the event selection requirement appropriately, this Z sample can be used to measure the efficiency of lepton reconstruction and selection requirements. In MC simulation, the efficiency measured in the same manner to obtain data-to-MC SFs. After well identifyied potential tag and probe pairs are selected, then separating the pairs with passing and failing probes into two different distributions (tag + passing probe and tag + failing probe). These two distributions are then fit simultaneously to the Z peak using RooFit [135], using floating parameters such as mean, width, and detector resolution. The distribution shapes are fit separately with a background and signal model, so two different functions are used to fitting for each case. An exponential is fitted to the background, and the signal can be fitted with either a voigtian function or a sum of a voigtian and a bifurcated gaussian. These functions provide a fit to a Breit-Wigner form resonance peak taking into account some changes to the shape due to factors such as detector resolution. This procedure is repeated in bins of the certain variables of the probe to compute efficiency with regards to the variable. The background is tightly removed by performing a simultaneous fit on the probes passing and failing the selection criteria. If the fitting procedure is not working properly (due to low or zero statistic in certain bins), very simple cut and count method can be also used to measure efficiency.

The Tag and Probe efficiency of the selection (i) can be calculated as follows:

$$\epsilon_{\mathrm{i}} = \frac{\mathrm{N}^{\mathrm{ipass}}_{\mathrm{probe}}}{\mathrm{N}^{\mathrm{ipass}}_{\mathrm{probe}} + \mathrm{N}^{\mathrm{ifail}}_{\mathrm{probe}}} \tag{5.6}$$

Where i can be reconstruction, identification, isolation, trigger$\cdots$ selections. The numerator is the total number of all selected signal events with probes and the denominator is the total number of selected signal events with passing probe (pass i selection). These numbers are extracted from the fit to signal or simple counting number of corresponding events. In this analysis, we use both electron and muon efficiencies from EGamma [136] and Muon POG [137] in CMS. The efficiencies and SFs generally are computed as a function of the object p_T and eta. The efficiencies and SF to match the efficiency of electron/muon reconstruction and identification in data and MC is measured and will be described.

5.3.2 Electron efficiencies and scale factors

HEEP ID and Isolation efficiency and SF

For the electron analysis, HEEP ID (isolation cut is included in HEEP ID selections) efficiencies and SFs are measured directly from the data using the "tag and probe" method. The tag electron is required to fulfill the following requirements :

- tag must be located in the barrel.
- tag must pass the HEEP ID criteria as explained in the previous section.
- tag must pass the `HLT_Ele27_eta2p1_WPTight` trigger and tag must match to the HLT electron candidate in a cone size ΔR within 0.2.
- tag must be paired with every other GSF electron (probe) in the event.

The probe electron is GSF electron with $p_T > 35$ GeV and passing probe must pass HEEP ID criteria then the efficiency is defined as the probability for a probe to pass the HEEP ID criteria. The invariant Z mass of the tag and probe pair is required to satisfy $70 < M_{ee} < 110$ GeV/c^2. If there are more than one tag and probe pairs in an event, all pairs are selected. If there are two tag electrons in a pair, both are considered to also be probes. This efficiency is measured in data and MC for barrel electron and endcap electron seperately.
For data efficiency, events are selected from `SingleElectron` dataset using the `HLT_Ele27_eta2p1_WPTight` trigger. The electron energy on data is scaled by using the recommended offline EGM scale corrections (1.0012 for EB and 1.0089 for EE) for having better data/MC agreement in Z peak region. For MC efficiency, DY, W+jets, $t\bar{t}$, single top, gamma+jet, and diboson MC samples are used which can be found in the Table 4.5 and all MC events are weighted using the `HLT_Ele27_eta2p1_WPTight` trigger SFs and pileup re-weighting(See section 5.4) is also applied to all MC. The HEEP ID efficiencies are shown as a function of electron E_T of the probe electron in Figure 5.4. Also, the data/MC SF per E_T bin and the mean value are shown in the bottom pad. For MC efficiency, to check if the contribution of Non-DY (W+jets, Top, gamma+Jet and diboson) background samples are estimated correctly, Non-DY included efficiency and Non-DY MC substracted efficiency are calculated separately, but there is no major difference between them. The systematic uncertainties of the HEEP SF are originated from non-DY background processes. The nominal value of the cross sections is varied by 50% for W+jets and 10% for $t\bar{t}$. The uncertainty of the pileup is also considered but it is negligible. Therefore the mean value of HEEP ID SFs for barrel and endcap are 0.972 ± 0.000(Stat.) ± 0.006(Syst.) and 0.983 ± 0.001(Stat.) ± 0.007(Syst.), respectively [138].

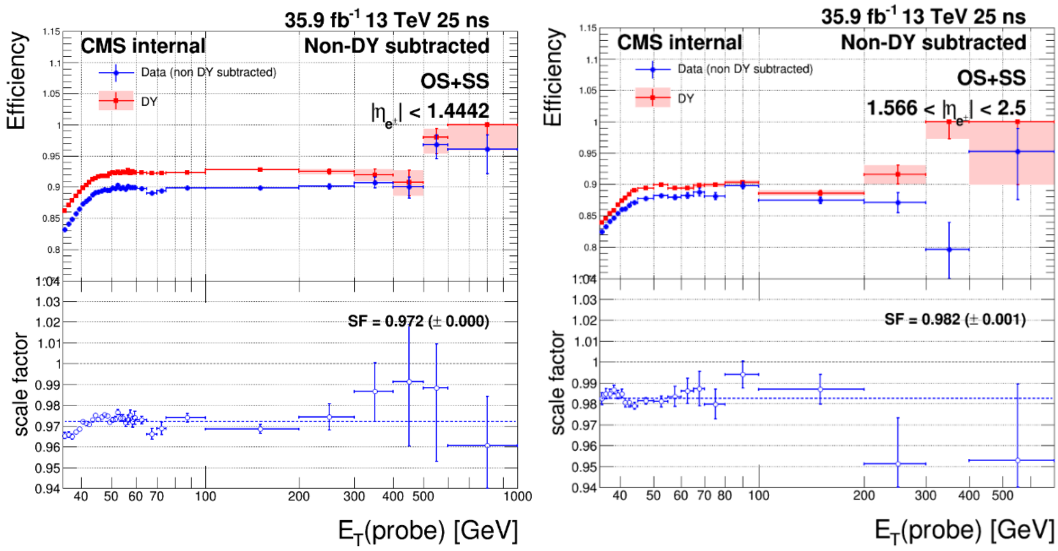

Figure 5.4: The HEEP ID efficiencies af a function of electron's E_T for 2016 full data (blue) and MC simulation (red) and scale factors are measured for each barrel (left) and endcap (right) by Tag and Probe method from EGamma POG [139, 138].

Electron Trigger efficiency and SF

For the single electron trigger efficiency, an orthogonal trigger method is used with unbiased `SingleMuon` datasets with full luminosity ($35.9\,\mathrm{fb}^{-1}$ and MC samples (Wjet and $t\bar{t}$ processes of SM) applied pileup reweighting. Events are selected firstly by orthogonal muon triggers, `HLT_Mu` OR `HLT_TkMu` to consider information independent of the single electron trigger. Trigger efficiency for an electron in barrel and endcap passing HEEP V7.0 and offline p_T cut ($> 130\,\mathrm{GeV}$) to match the reference trigger to pass trigger path is measured. There are 2 cases of efficiencies and scale factors for Barrel and Endcap. The only difference is that ORing `HLT_Photon175` applied or not.

Trigger scale factors with various p_T bins and their statistical uncertainties are summarized in Table 5.3.

We can check the former case of efficiency (ORing photon trigger applied one) is noticeably recovered in the region where p_T of the electron is more than 500 GeV by comparison with the latter case of efficiency. Each efficiency and scale factor plot is shown in figure 5.5.

electron p_T[GeV]	η	MC ϵ	Data ϵ (reMiniaod)	SF (Data/MC)
130 – 140	EB	0.965 ± 0.0046	0.956 ± 0.0025	0.991 ± 0.0040
140 – 150	EB	0.974 ± 0.0039	0.955 ± 0.0029	0.980 ± 0.0027
150 – 200	EB	0.985 ± 0.0012	0.971 ± 0.0014	0.985 ± 0.0008
200 – 300	EB	0.997 ± 0.0004	0.992 ± 0.0011	0.996 ± 0.0011
300 – 400	EB	0.983 ± 0.0119	0.995 ± 0.0024	1.012 ± 0.0121
400 – 500	EB	0.999 ± 0.0008	0.988 ± 0.0066	0.990 ± 0.0065
500 – 800	EB	1.000 ± 0.0007	0.972 ± 0.0161	0.972 ± 0.0156
800 – 2000	EB	1.000 ± 0.0002	0.857 ± 0.0935	0.857 ± 0.0791
electron p_T[GeV]	η	MC ϵ	Data ϵ (reMiniaod)	SF (Data/MC)
130 – 140	EE	0.992 ± 0.0048	0.975 ± 0.0035	0.984 ± 0.0032
140 – 150	EE	0.995 ± 0.0010	0.988 ± 0.0028	0.993 ± 0.0026
150 – 200	EE	0.994 ± 0.0007	0.991 ± 0.0015	0.997 ± 0.0014
200 – 300	EE	0.994 ± 0.0013	0.998 ± 0.0009	1.004 ± 0.0009
300 – 400	EE	0.998 ± 0.0016	1.000 ± 0.0008	1.002 ± 0.0016
400 – 500	EE	0.999 ± 0.0007	1.000 ± 0.0008	1.001 ± 0.0007
500 – 800	EE	1.000 ± 0.0012	1.000 ± 0.0008	1.000 ± 0.0014

Table 5.3: Trigger Scale factors (SF) with regards to various electron p_T bins for barrel ($0.0 < |\eta_{SC}| < 1.4442$) and endcap ($1.566 < |\eta_{SC}| < 2.5$) with statistical error. Statistical errors were dominant at high p_T region.

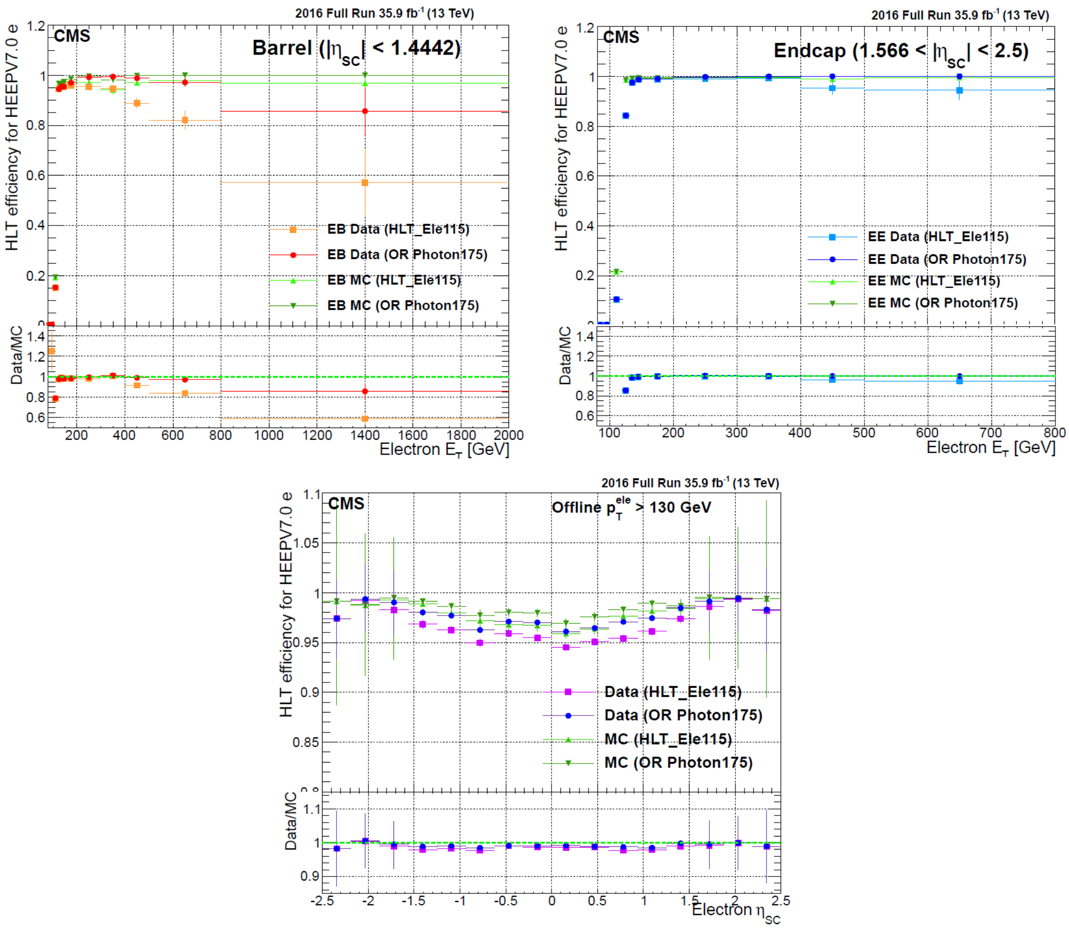

Figure 5.5: The efficiencies and scale factors of a HEEPV70 ID electron to match to the reference muon trigger to pass the signal trigger (with ORing `HLT_Photon175`) are calculated as a function of p_T for ecal barrel (left) and endcap (right). The efficiencies with respect to the η_{sc} of electron satisfying an offline $p_T > 130\,\text{GeV}$ are also calculated (bottom). An orthogonal trigger method is used with `03Feb2017 reMiniAOD SingleMuon` Data. Case1 efficiency is calculated with event passing `HLT_Ele115 OR HLT_Photon175` (red, blue circle) and Case2 efficiency is calculated with event passing a `HLT_Ele115` (orange, skyblue square).

5.3.3 Muon efficiencies and scale factors

Muon reconstruction and identification efficiency and SF

To calculate the muon efficiency, a dedicated study of the performance of the muon reconstruction and high-p_T muon identification efficiencies are determined using dimuon events from the high-p_T Z boson decays and high-mass DY pairs by high-p_T Muon POG. The efficiencies and their SFs are calculated using the counting "tag and probe" technique without high Z mass constraint (mass above 70 GeV) for securing the statistic of muons at very high momentum. Especially, This efficiency is measured as a function of muon's p_T to see the dependence of the potential differences of the muon detector performances in radiative processes of muon interactions with the detector material in simulated MC samples and `SingleMuon` dataset. For the MC efficiency, the `HLT_Mu50 OR HLT_TkMu50` trigger SFs and pileup re-weighting is applied to MC samples.
The tag muon in an event is required to satisfy high quality tracker muons with tight isolation requirements:

- tag must satisfy $p_T >53$ GeV and $|\eta| < 2.4$.
- tag must pass the `HLT_Mu50 OR HLT_TkMu50` trigger paths and tag must match to the HLT muon candidate in a cone size ΔR within 0.2.
- tag must satisfy $\delta p_T/p_T <0.5$.
- tag must pass other high-p_T muon ID criteria as described in previous section.
- tag must pass a relative tracker-only isolation $\sum p_T$(inner Tracker tracks)$/p_T^{\mu} < 0.05$ and absolute tracker-only isolation < 15 GeV.

The probe muon is Tracker muon and is required to satisfy following requirements:

- probe must satisfy $p_T >50$ GeV and $|\eta| < 2.4$.
- probe must have at least one pixel hit and at least 5 tracker layers and no lost hits of tracker track.
- probe must satisfy $|d_{xy}| < 0.2$ cm and $|d_z| < 0.5$ cm.
- probe must also satisfy $\delta p_T/p_T <0.5$.
- probe must also pass a relative tracker-only isolation $\sum p_T$(inner Tracker tracks)$/p_T^{\mu} < 0.05$ and absolute tracker-only isolation < 15 GeV.

In addition the tag and probe pairs have to satisfy several cuts: $|d_z(tag) - d_z(probe)| < 0.05$ cm, sharing a normalized vertex $\chi^2/ndf < 20$, having opposite charge and geometrical separation $\Delta R > 0.6$, and the 3-d angle between muon's momenta $< \pi$-0.02 for removing fake muon from cosmic-ray. The probe muon is used to measure the efficiency of muon reconstruction and the high-p_T muon identification. The passing probe must pass the high-p_T ID. The reconstruction and identification efficiency as a function of the muon's p is shown in Figure 5.6 in three different η ranges(left-all: $|\eta| < 2.4$, middle-barrel: $|\eta| < 1.6$[4], and right-endcap: $1.6 < |\eta| < 2.4$) and the red points represent the data and black points represent the MC. Based on this study, it is found that the standalone reconstruction and the number of standalone/global valid hit (ID variable) become less efficient at high p(orp_T) muon in forward region ($1.6 < |\eta| < 2.4$) of the detector and that MC simulation is not able to properly reproduce the observed real data trend. This efficiency decreasing trend is reasonably caused by the electromagnetic showering. The muon showering depends on the material, which is differently distributed along η. In another region ($|\eta| < 1.6$) of the detector the inefficiency measured in data with respect to MC looks linear and better as a function of muon's p and The data to MC comparisons are extrapolated above 2 TeV of momentum. According to one of the recommended recipes from Muon POG, we decided to assign only a systematic uncertainty to these effects because we already have observed SFs in this analysis. These SFs (The bottom of the Figure 5.6) are used to get a weight for each muon as a function of its momentum. This weight is divided for a reference value (weight at $p_{ref} = 100$ GeV in $|\eta| < 1.6$ and weight at $p_{ref} = 200$ GeV in $1.6 < |\eta| < 2.4$): $SF(p)/SF(p_{ref})$ per muon.

High-p_T muon ID and isolation efficiency and SF

The high-p_T muon ID and loose relative tracker muon Isolation efficiencies and SFs, which are applied in this analysis are calculated using tag and probe technique. The tag and probe muon is required to pass Global Muon and TrackerMuon with $p_T > 53$ GeV, $|\eta| < 2.4$ and relative tracker isolation < 0.1. and tag and probe pair has to pass same requirements used to measure reconstruction and identification efficiency. The tag and passing probe are required to pass high-p_T muon ID criteria. The high-p_T ID efficiency as a function of muon's p_T is shown in the top of Figure 5.7. The isolation efficiency also measured in the same way but the passing probe is required to pass both high-p_T ID and isolation criteria. The muon SF are factorised for the ID SF and the ISO SF, taking as a denominator the numerator of the former step [137]:

$$SF_{IDandISO} = SF_{ID/Tracker-Track} \cdot SF_{ISO/ID} \tag{5.7}$$

[4]eta has been merged up to 1.6, in order to get more statistic and a more reliable fit in this study.

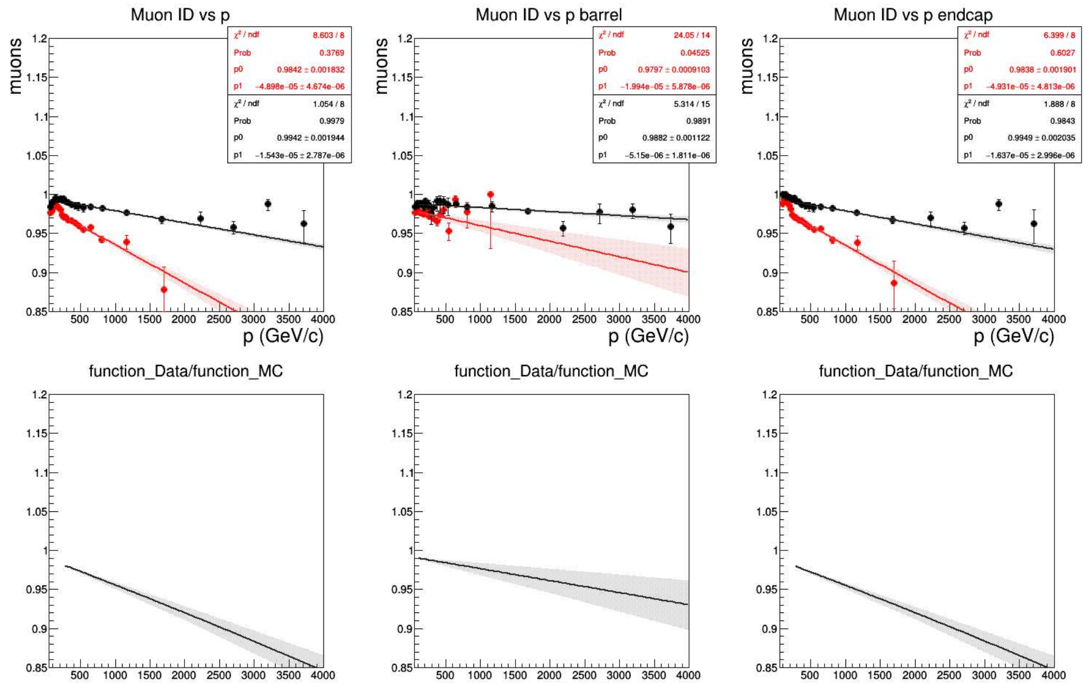

Figure 5.6: The muon reconstruction and high p_T muon identification efficiencies and scale factors for 2016 full data and MC simulation are calculated with counting Tag and Probe method. The red points represent the data and black points represent the MC. The reco + high-p_T ID efficiencies as a function of muon's p_T for different $|\eta|$ ranges (left-all: $|\eta|$ <2.4 , middle-barrel: $|\eta| < 1.6$, and right-endcap: 1.6< $|\eta|$ <2.4) are on the top. Data and MC are interpolated by a first order polynomial. The fit parameters are in the boxes. In bottom are ratio of the fits to data and mc (scale factor) used to estimate the systematic unveratinty. Error is taken from the quadratic sum. These figures are taken from Muon POG [140].

where $SF_{ID/Tracker-Track}$ is the ID SF using as denominator muon tracker tracks, and $SF_{ISO/ID}$ is the ISO SF using as denominator muon tracker tracks with the ID selection required. In addition, the Tracking reconstruction efficiencies and SFs are also calculated and applied to compensate the strip inefficiency problem (HIP) during 2016 Run data. It provided by Tracker POG, as a function of eta and number of primary vertex. The ID and Isolation results are shown in Figure 5.6 and the tracking reconstruction results are shown in Figure 5.8. The SFs of high-p_T muon ID with respect to the muon's eta has been applied, with values ranging from a minimum 0.967 (in the most forward region) to a maximum 0.994, integrated into muon's p_T. In the case of loose relative tracker muon ISO, the SFs with respect to the eta has been considered and values are close to 1. For the tracking SFs are applied in 12 bins as a function of muon's eta, integrated into muon's p_T and the number of vertices. Their values range from 0.987 up to 0.998, which also low at forward eta region.

Muon Trigger efficiency and SF

For the single muon trigger efficiency, the orthogonal method is also used with `SingleElectron` datasets and select events containing muons satisfying the offline selection criteria as in this analysis as described in Section 5.5.2. The efficiencies and scale factors for our main triggers are show in Figure 5.9 with full 2016 data and the inclusive Wjets and exclusive W mass-binned MC samples. The turn-on is very well defined around $p_T = 50$ GeV and this is used to motivate the kinematic selection of $p_T > 53$ GeV in the analysis. Beyond that value the efficiency is flat and the scale factors are independent of the p_T of the muon. The 2D-dependency of the scale factor as a function of η and p_T are also calculated, as shown in Figure 5.10. The SF dependent in muon η have been finally applied in analysis because the η dependency is stronger than the one in p_T. The values for the SF as a function of muon η range from 0.92 in the far positive endcap ($2.1 < |\eta| < 2.4$) up to 1.0 in the more central part of the CSC detectors ($1.2 < |\eta| < 1.6$), with a mean value of 0.96. In general, the main drop of the SF occur in the gaps between DT wheels, in the transition region between barrel and endcap detectors and in the highest $\eta|$ regions ($2.1 < |\eta| < 2.4$). The systematic uncertainties associated with these SF values have been obtained comparing the different methods and datasets used. More details about the uncertainties can be described in Section 6.

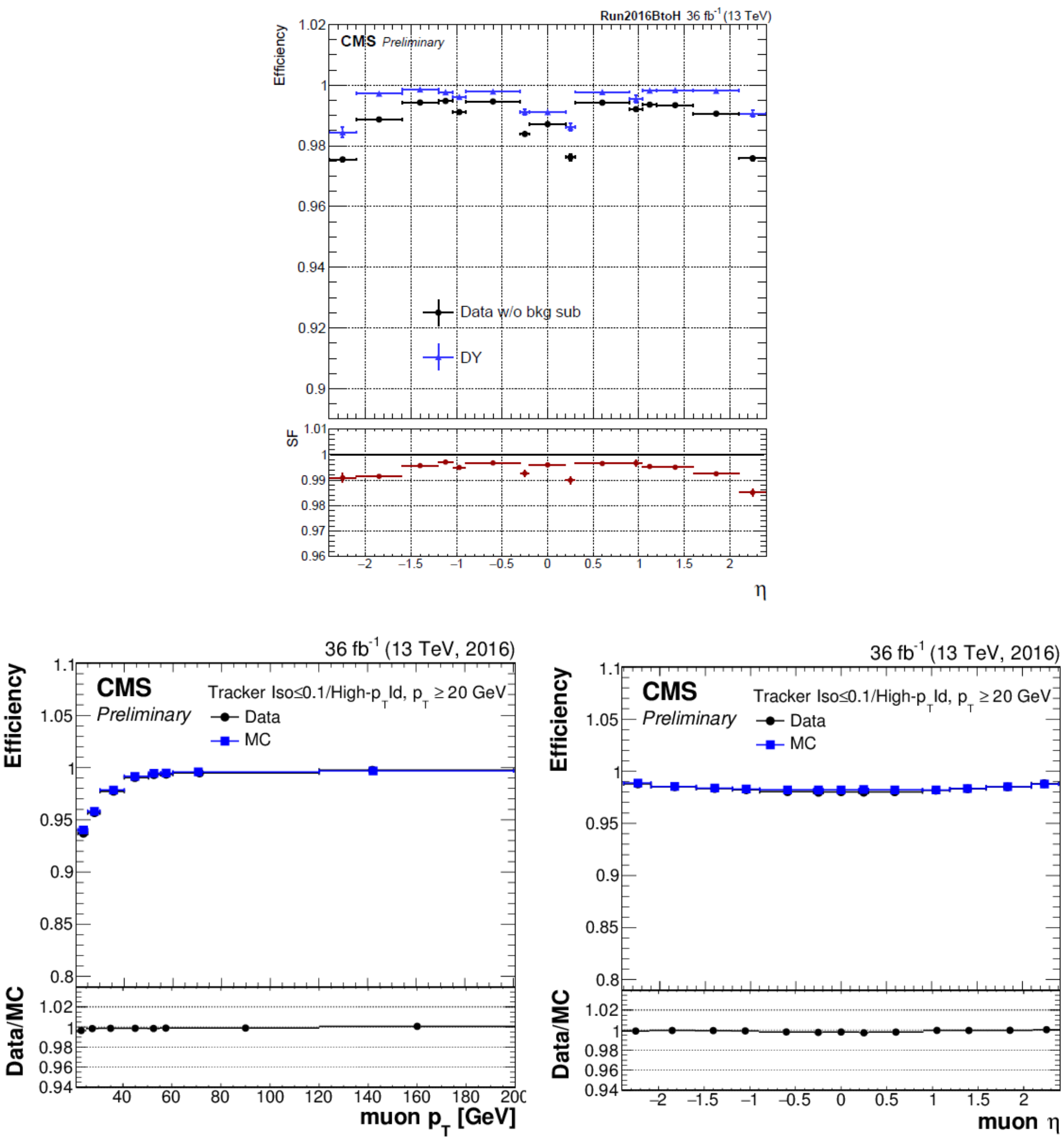

Figure 5.7: The high-p_T muon idenfication and Isolation efficiencies and scale factors for 2016 full data and MC simulation are calculated with Tag and Probe method. The muon ID efficiency as a function of muon's eta is on the top. The Loose Tracker Isolation efficiencies as a function of muon's p_T (left) and eta (right) with respect to high-p_T ID are calculated. These figures are taken from Muon POG [137, 141].

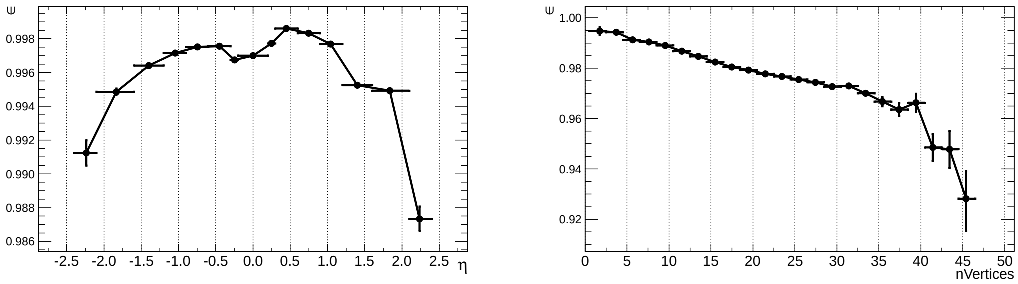

Figure 5.8: The general tracking reconstruction efficiencies for 2016 full data as a function of eta (left) and the number of primary vertex (right). This efficiency has remained close to ∼ 1 for 2015 data, but it suffers from the strip inefficiency problem, so-called HIP, that happened during data taking in 2016.

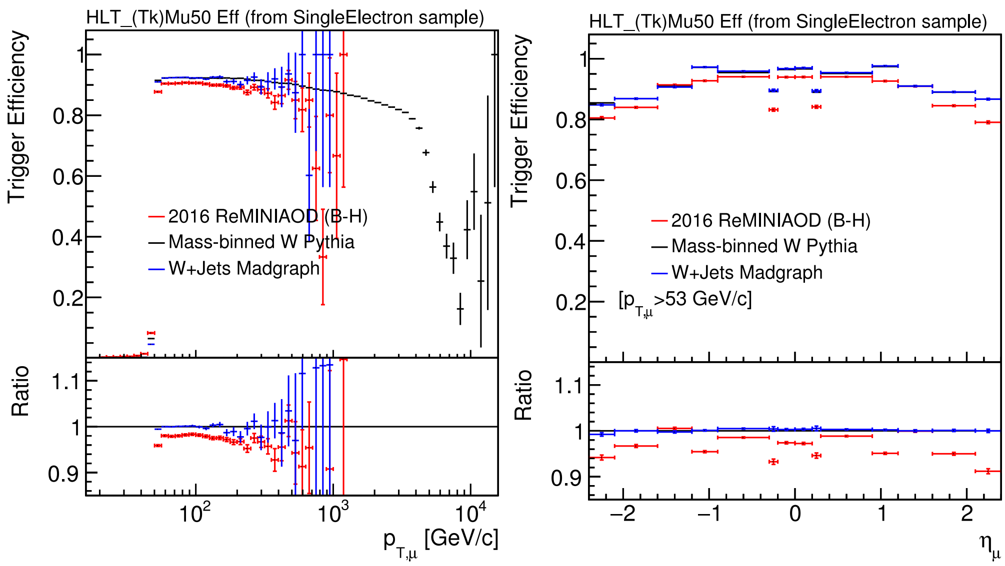

Figure 5.9: Trigger efficiency as a function of the muon p_T and η for the main trigger in the analysis, the logical OR of `HLT_Mu50` and `HLT_TkMu50` computed with the full dataset, the inclusive Madgraph Wjets sample and the mass-binned PYTHIA sample, used as a central reference. The ratio is obtained by dividing the efficiencies in data (red) and the Madgraph sample (blue) over that of the mass-binned PYTHIA sample, which contains much higher statistics.

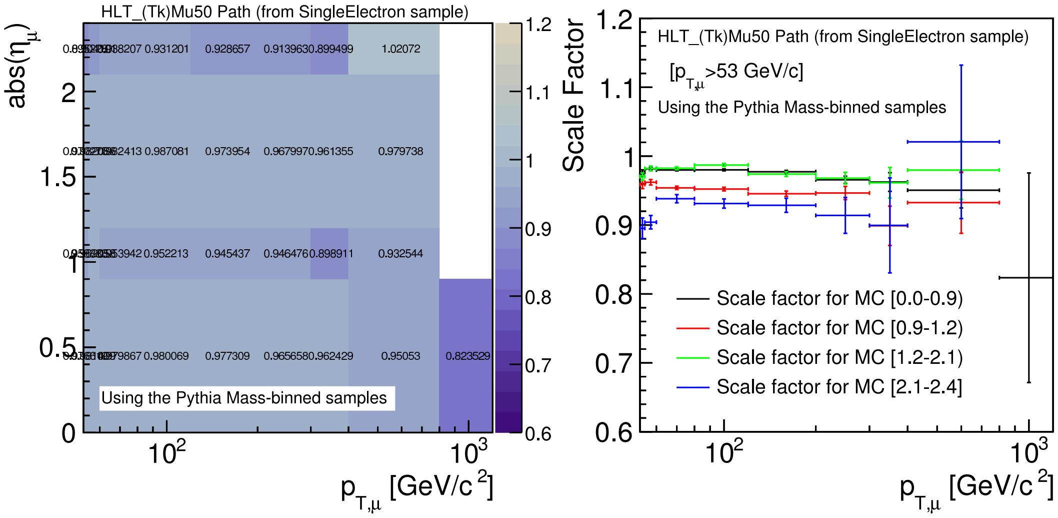

Figure 5.10: Trigger-efficiency scale factor as a function of the muon η and p_T (2D dependence) for the main trigger in the analysis, the logical OR of `HLT_Mu50` and `HLT_TkMu50`. The reference MC events are those provided by the reweighted mass-binned PYTHIA sample. On the right, the 2-D plot is shown as a function of p_T for several bins of $|\eta|$.

5.4 Pileup Reweighting

This PU reweighting procedure is necessary for any physics analysis at high luminosity LHC, since the additional interactions deposit large amounts of energy and the distributions of the additional interactions in the MC simulation are not likely identical as in the data. Therefore, in order to have the data and the MC simulated samples in the same conditions of PU, in terms of the distribution in the number of primary vertices in the collisions, PU reweighting procedure is applied to the simulation. Pileup increased over the year 2016 due to the growth of

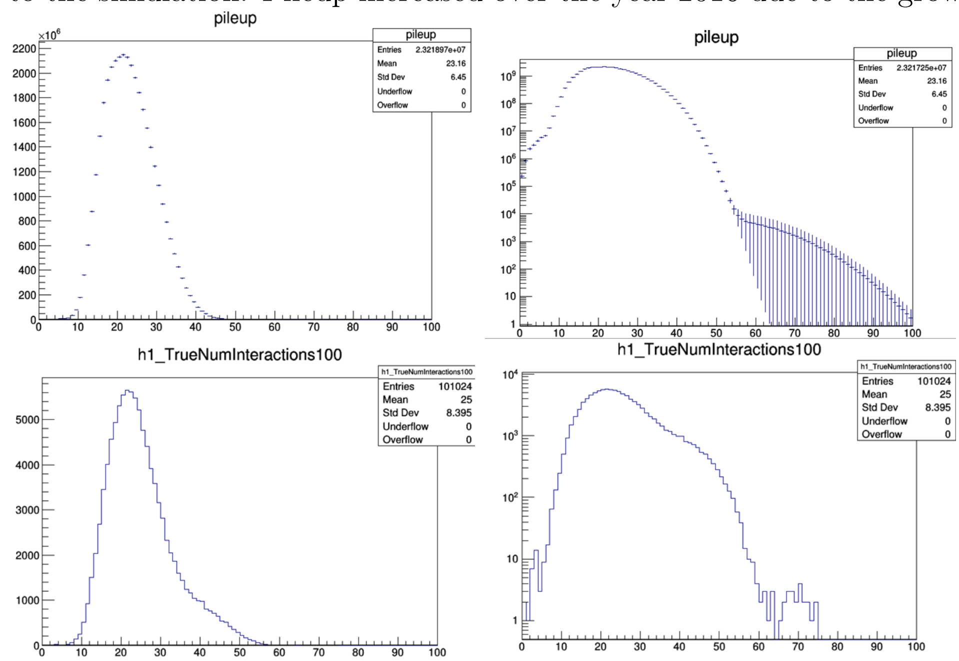

Figure 5.11: The distribution of the number of pileup in 2016 full data (top) and simulated Moriond17 MC (bottom) with different y-axis scale(left: normal, right:log scaled).

instantenous luminosity, leading to higher PU than 2015. In 2016 data running at the LHC, the average of proton-proton interactions is about 27 for each bunch crossing. The number of PU interactions in data is estimated from the measured luminosity in each bunch crossing by the total inelastic pp cross section. The CMS experiment centrally recommends using the total inelastic pp cross section of 69.2mb for 2016 data. These estimated PU information can be accessed through a JSON file which has the measured luminosity and PU information for each LimiSection. For the simulation, nevertheless the MC samples are carefully generated with the expected PU conditions in the respective data acquisition period, it is very difficult to predict because it very depends on the instantaneous luminosity recorded by the LHC and the total inelastic cross section that has an uncertainty of 5%. Therefore, the distribution of the number of vertex candidates can differ between data and simulations (See the Figure 5.11 and all the simulated sample are correctd with PU reweighting. To apply PU reweighting, the number of PU in data is compared to the known number of pileup interactions in simulations. The reweighting factors are designed in a way that only the shape will change, not the scale of the simulated distribution. The details of the official recipe of PU re-weighted in CMS are given in [142]. Figure 5.12 shows the distribution of reconstructed vertices in data and all background MC samples for muon analysis before and after applying PU reweighting. For the vertex multiplicities, the simulated statistics is not sufficient for perfect PU reweighting. However, the impact on the simple mono-lepton final state is negligible. Comparing basic quantities such as p_T of lepton in data and simulations shows excellent agreement as well as the M_T distribution. These results are presented in Section 5.5.4.

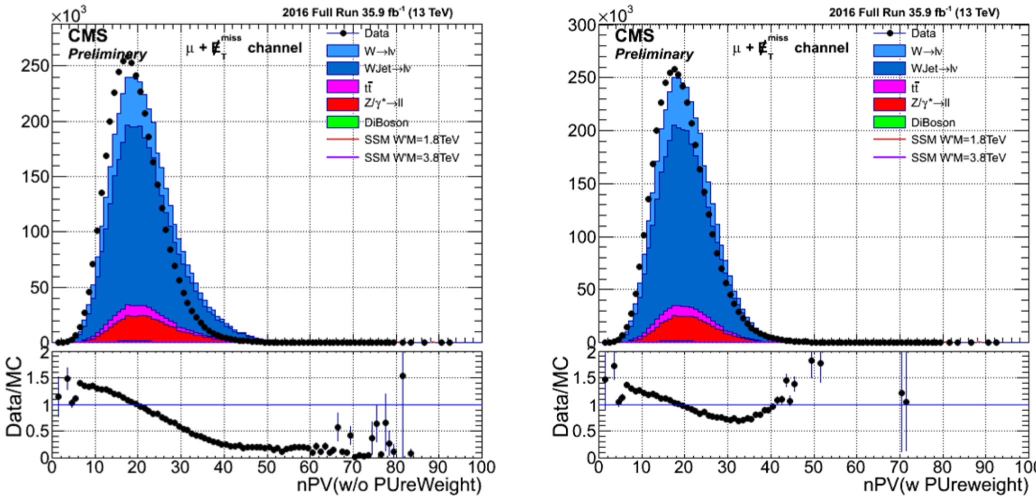

Figure 5.12: Number of primary vertices distribution for events selected by offline selection crieteria of muon analysis, before (left) and after (right) applying the pileup reweighting. The distributions in data correspond to the total 2016 luminosity.

5.5 Event Selection

5.5.1 Missing Transverse Energy Filter

A very small fraction of events could have an anomalously large MET. For example, in some cases, MET are produced from the calorimeter noise, muons from the beam or jets near non-functioning channels in the calorimeters and others. These events are rare and can be rejected efficiently in the analysis using a dedicated set of MET filters which was designed to remove these pathological events. The following recommended MET filters have been applied to the analysis. In 2016 conditions, the first six filters are available in the data and simulated sample, while the last two bad muon events filters are not and these need to be "run on the fly". In the re-reco data, the rate of high p_T fake muons is increased due to a relaxed set of tracking quality requirements introduced to mitigate the Heavy Ionizing Particle (HIP) effect. These two new filters reject out such fake muons and muon duplicates from the particle flow candidate collection. These event filters are applied at first.

- primary vertex filter : Require at least one good primary vertex in the event.
- globalTightHalo2016Filter : Reject events with beam backgrounds. Spurious signals in the detector are produced by interactions of the protons in the beam with residual gas molecules or parts of the LHC machine. These events very likely produce muons, which are in some cases detected at the experiment. Since the produced muon have a high probability to traverse the detector on a trajectory parallel to the beam direction, such events are identified by multiple calorimeter energy deposits that share the same-coordinate and CSC signals associated to these.
- HBHE noise filter : Energy deposits in the HB and HE are classified as noise by exploiting time and shape information of the measured pulses as well as geometrical structures of the signals. The identified events are rejected.
- HBHEiso noise filter : Reject events with isolated noise deposited in the HB and HE by studying energy deposits in the ECAL, HCAL and tracker information.
- EcalDeadCellTriggerPrimitiveFilter : A precise readout of the deposited energy is not possible in some ECAL towers. Instead, information from the trigger system is used to measure the deposited energy. The measurement of the trigger saturates at a certain amount of energy. Reject events that contain energy deposit in the malfunctioning/dead ECAL crystals (about 1% of the crystals) close to this threshold which lead to large energy loss.

- ee badSC noise filter (only applied to data) : Reject events where two regions of crystals in the endcap give anomalously high signals. Affected events are identified by imposing a requirement on the maximum allowed measured energy and removed if this threshold is exceeded.

- badChargedHadronFilter : Reject events where a muon has a low quality and therefore is not declared as a PF muon, and this non-PF muon makes it into the PF MET calculation as chared hadron candidate.

- badPFMuonFilter : Reject events where the muon is good enough quality to become a PF muon but is still very low quality and has large p_T.

5.5.2 Analysis Flow

The selection of new physics candidates event follows a similar strategy as RunI TeV W′ analysis [143], however, several selections are additionally considered like the top-veto in the muon channel. The analysis selections are described as below:

1. Events are triggered with a single electron[5] (muon[6]) trigger with trigger transverse momentum thresholds of 115 (50) GeV. The required offline minimum p_T has to be above the trigger turn-on. For high p_T electrons the photon175 trigger is added.

2. For offline reconstruction, electrons are required to be within the acceptance of $|\eta|$ <1.444 and 1.566< $|\eta|$ <2.5 with $p_T > 130$ GeV. Muons with $p_T >$ 53 GeV are to be reconstructed within the acceptance of $|\eta|$ <2.4.

3. Select an isolated high p_T lepton, either a HEEP v7.0 ID electron or a high p_T ID muon satisfying Loose Tracker isolation requirements. Events with a second any lepton(e,μ) with $p_T > 25$ GeV, are vetoed.

4. In the electron channel, MET (E_T^{miss}) is required to be above 150 GeV to avoid the mismodeled low MET region which is affected by jet energy corrections and electron reconstruction. Both channels use Type-1 PF MET with the 2016 MET filters as included in data and MC samples.

5. Both channel samely exploit the special feature of two-body decay kinematics in order to suppress much of backgrounds : 0.4< p_T^{ℓ}/E_T^{miss} <1.5 and $\Delta\phi(\ell,\vec{p}_T^{miss}) > 2.5$.

6. In the muon channel, additionally events containing top are rejected, so-called top-veto. In CMS, top quark related events (Single top or $t\bar{t}$) can

[5] HLT_Ele115_CaloIdVT_GsfTrkIdT OR HLT_Photon175
[6] HLT_Mu50 OR HLT_TkMu50

be confirmed by the b-tagging discriminant variable corresponding to jet multiplicity and the Combined Secondary Vertex algorithm (CSV)[7] values of jet. This top-veto is newly considered in 2016 to further reduce the contamination on the signal-like events.
To veto top events, events containing more than 5 jets or with the most energetic jet having CVS > 0.8484, which corresponds to the b-tagging medium cut according to BTV POG.

The kinematic selection for a W′ like signal provide a strong reduction of two types of events. Firstly the background contamination from di-jet events is largely reduced with the p_T^{ℓ}/E_T^{miss} selection. This ensures that the largest reconstructed object in the event is the lepton. For di-jet and Drell-Yan events, an increase with p_T^{ℓ}/E_T^{miss} is expected. On the other hand, if the p_T is small and the E_T^{miss} is large, the source of the E_T^{miss} is not the lepton. Secondly the angle between the lepton and $\vec{p}_T^{miss}$ is heavily effected by the boost of the initial heavy particle. The W boson events with high W-p_T are affected more severely by a correct QCD description. These events can have a high M_T if the $\vec{p}_T^{miss}$ is shifted by the wrongly reconstructed recoil jet. The effect of the kinematic selection is a reduction of the background by roughly 20% whereas the signal is only reduced by 5%.
In order to check the impact of each different selection, the proportions of the number of surviving events after different cuts relative to the previous cut, denoted as N-1 efficiency, are calculated in the data, MC background and two signal samples with W′ masses of 1.8 and 3.8 GeV. The resulting relative numbers are given in Table. 5.4 for electron channel and Table. 5.5 for muon channel.

	No selection	HEEP e	E_T^{miss}	Trigger	$\lvert\Delta\phi\rvert$	p_T^e/E_T^{miss}
Data	1	0.186	0.002	0.143	0.492	0.970
SM Background	1	0.051	0.002	0.182	0.498	0.974
SSM $M_{W'} = 1.8\,TeV$	1	0.798	0.968	0.995	0.977	0.982
SSM $M_{W'} = 3.8\,TeV$	1	0.765	0.927	0.991	0.985	0.988

Table 5.4: The ratio of the number of surviving events after the each different selections for searching mono-electron events with respect to selection before in data, MC backgrounds 2 signal samples, where “HEEP e” selection is requiring an HEEP electron with $p_T > 35\,GeV$(vetoing second lepton applied) and followed by low E_T^{miss} cut with threshold of 150 GeV. The trigger cut requires the electron to have a $p_T > 130\,GeV$.

With these selection requirements, the signal efficiencies for electron and muon channel are computed as the ratio of signal events satisfying all of the analysis selection critera (to kinematic cuts) to the initially generated sample within acceptance of detector. For the electron channel, the signal efficiency is 0.72±0.03 for a

[7] Top related events have to fulfill high value(close to 100%) of the CSV of leading jet.

	Trigg	2nd μ veto	high-p_T μ Id	Iso	$p_T>53$ $M_T>60$	p_T^{μ}/E_T^{miss}	$\lvert\Delta\phi\rvert$ $M_T>80$	top veto
Data	0.954	0.902	0.959	0.539	0.493	0.453	0.449	0.969
SM BG	0.954	0.883	0.984	0.940	0.717	0.738	0.693	0.970
$M_{W'}$=1.8	0.897	0.997	0.988	0.996	0.955	0.954	0.978	0.987
$M_{W'}$=3.8	0.866	0.998	0.987	0.996	0.952	0.959	0.980	0.986

Table 5.5: The ratio of the number of surviving events after the each different selection for searching mono-muon events with respect to the previous cut in data, SM predictions and 2 W′ signal samples of masses 1.8 TeV and 3.8 TeV. The initial sample contains events preselected from the SingleMuon dataset, with at least an offline muon with $p_T > 50$ GeV.

W′ boson of mass 1800 GeV and 0.68±0.03 for a W′ boson of mass 3800 GeV. For the muon channel, the signal efficiency is 0.76±0.03 for 1800 GeV and 0.71±0.03 for 3800 GeV. A plot of the efficiency for three different W′ signals can be found in Figure. 5.13. The signal efficiency (ϵ) of three SSM W′ signal samples (M(W′)= 1.8 TeV, 3.8 TeV,5.8 TeV) as a function of $p_T^{(gen)}$ and as a function of the SSM W′ mass.
To check data-MC agreement after applying selections up to kinematic selection, the distributions of the lepton p_T and E_T^{miss} in data and MC are shown in Figure 5.14 for electron (upper plots) and muon (lower plots) channels, separately. All the simulations are normalized to an equivalent luminosity 35.867 fb^{-1} as explained in Equation 4.3. These distributions show that the estimated background provides a good describtion to the data and confirm we are ready to proceed to find the best discriminate distribution to search a potential new physcis signal.

5.5.3 Discriminant variable for search

The discriminant variable needs to fulfill two important criteria. Firstly, it must have high separating power between signal and backgrounds. Secondly, in case of the positive signal, it needs to be able to give information about the nature of the signal. Owing to the two-body resonant nature of the W′ signal, a natural candidate would be the lepton-neutrino invariant mass that is directly sensitive to the pole mass and width of the resonance. Unfortunately, in the W′ search, the invariant mass cannot be reconstructed since the missing transverse momentum component along the beam axis, $\vec{p}_z^{miss}$, cannot be measured experimentally. Instead, the transverse mass, M_T, defined only with quantities measured in the transverse plane is used. Thus the main discriminant variable used in the search is the transverse invariant mass distribution, M_T, defined from the lepton p_T, the

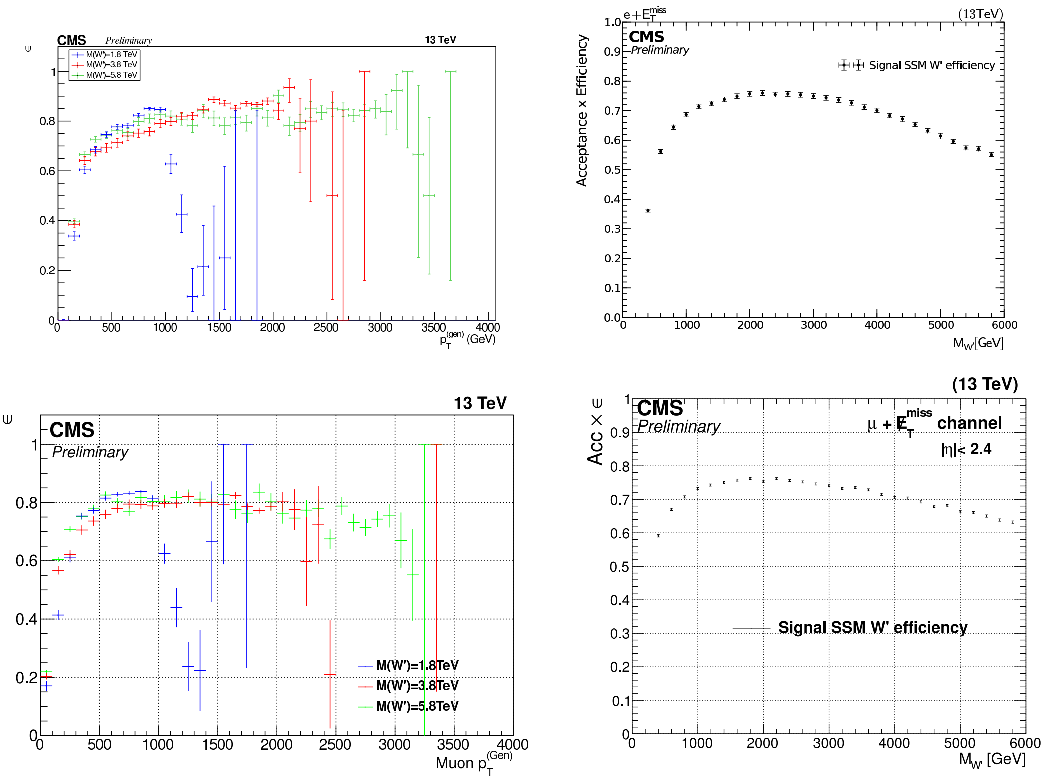

Figure 5.13: Signal acceptance×efficiency for SSM W′ in the electron channel (top) and muon channel (bottom) for three different W′ masses (M(W′)=1.8, 3.8, and 5.8 TeV, left) and as a function of the W′ masses (right).

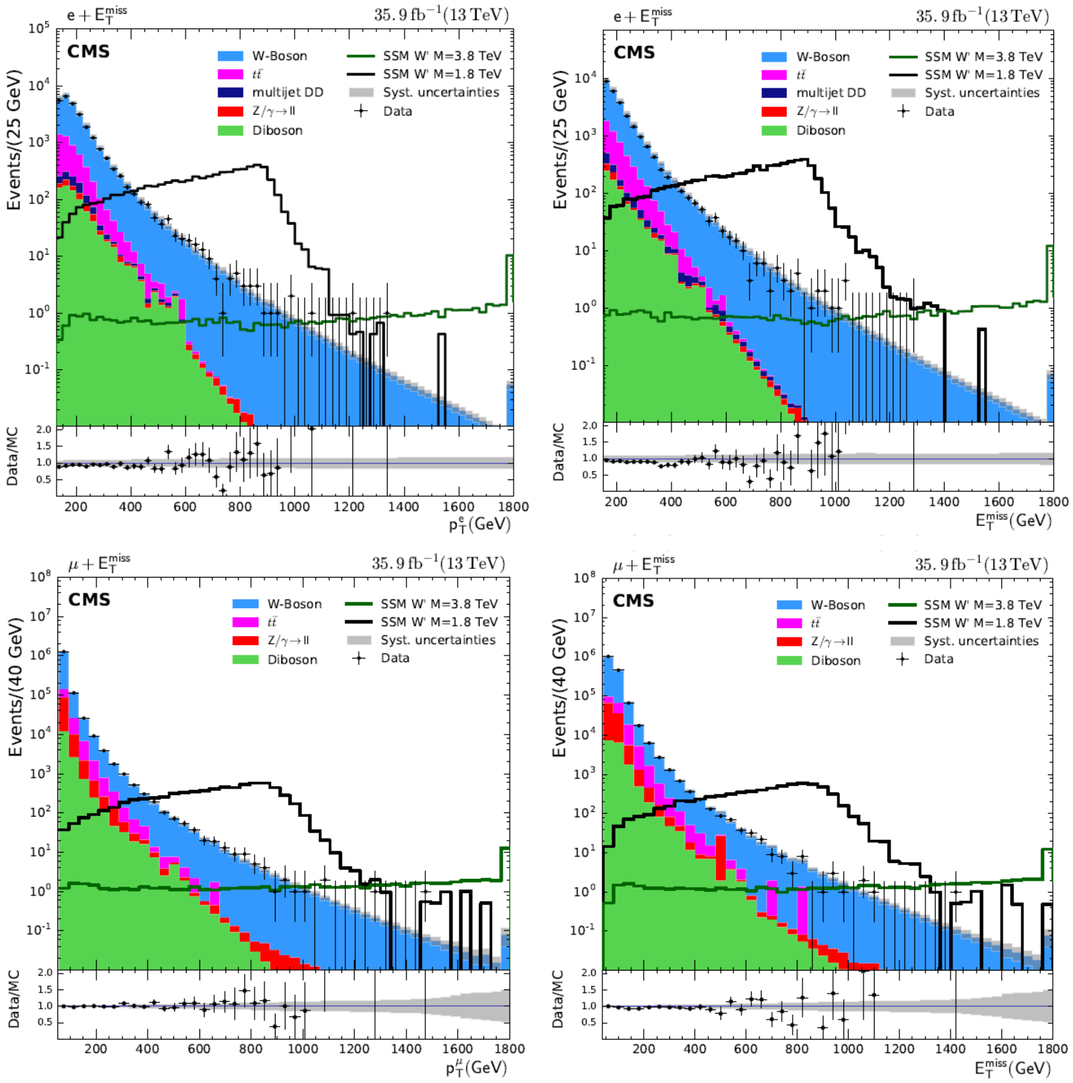

Figure 5.14: Distributions of electron p_T (left) and E_T^{miss} (right) after applying all selections up to kinematic selection for data (poiints) and expected SM backgrounds (coloured filled histogram) for the electron channel. The QCD multijet background in the electron channel is derived from data. The Diboson background includes WW, ZZ and WZ contributions. Also shown are SSM W′ signal examples for the two indicated masses, 1.8 and 3.8 TeV. The last bin shows the total overflow.

MET (E_T^{miss}) in the event, and the difference in the azimutal angle $\Delta\phi(\ell,\vec{p}_T^{miss})$.

$$M_T = \sqrt{2p_T^{\ell}E_T^{miss}(1-\cos[\Delta\phi(\ell,\vec{p}_T^{miss})])} \quad (5.8)$$

where the shape of the distribution is taken into account to perform the statistical analysis of the data. The shape of the transverse mass of a resonance has an end-point at the original mass: $M_T < M_{W'}$. Potential W′ signal events are expected to appear at high M_T values, while the different background contributions and particularly the SM W boson decays, appear as a tail as the transverse mass increases. In next section, M_T distribution and objects variable plots for each channel described.

5.5.4 Final Transverse mass distribution

Electron results

The key distributions for the electron channel after application of all the event selection steps are shown in Figure 5.15 which depicts the resulting transverse mass M_T. With the statistics of 35.9 fb^{-1}, the data are below the SM background prediction. The events with high transverse mass have been inspected and all look reasonable. The number of interesting mono-electron events for a selected set of M_T thresholds of 0.5 TeV, 1 TeV, 1.5 TeV and 2 TeV are listed in Table 5.5.4. We can compare the number of surviving events from data and total SM backgrounds and four signal examples with different W′ masses of 1.8 TeV, 2.4 TeV, 3.8 TeV and 4.2 TeV, respectively. There is no significant access of a W′ like signal in data.

	M_T >0.5 TeV	M_T >1	M_T >2	M_T >3	M_T >4
Electron Data	4400	200	2.0	0.0	0.0
Sum of SM BG	4790 ± 510	213 ± 28	5.00 ± 0.96	0.260 ± 0.077	0.016 ± 0.008
SSM $M_{W'}$=1.8 TeV	6320 ± 900	5040 ± 770	25.9 ± 5.8	0.43 ± 0.44	0 ± 0
SSM $M_{W'}$=2.4 TeV	1360 ± 220	1180 ± 200	560 ± 100	1.14 ± 0.44	0 ± 0
SSM $M_{W'}$=3.8 TeV	61 ± 14	53 ± 13	40 ± 11	23.9 ± 8.4	0.44 ± 0.25
SSM $M_{W'}$=4.2 TeV	27.6 ± 7.8	23.3 ± 7.3	17.6 ± 6.5	11.8 ± 5.4	3.4 ± 2.2

Table 5.6: Expected and observed number of data, signal and background events in the electron channel for corresponding selected set of M_T integrated above each M_T thresholds for 35.9 fb^{-1} of integrated luminosity. The signal yield is using NNLO cross sections.

An event display for one of the electron events with the high M_T of over 2 TeV is displayed in Fig. 5.16.

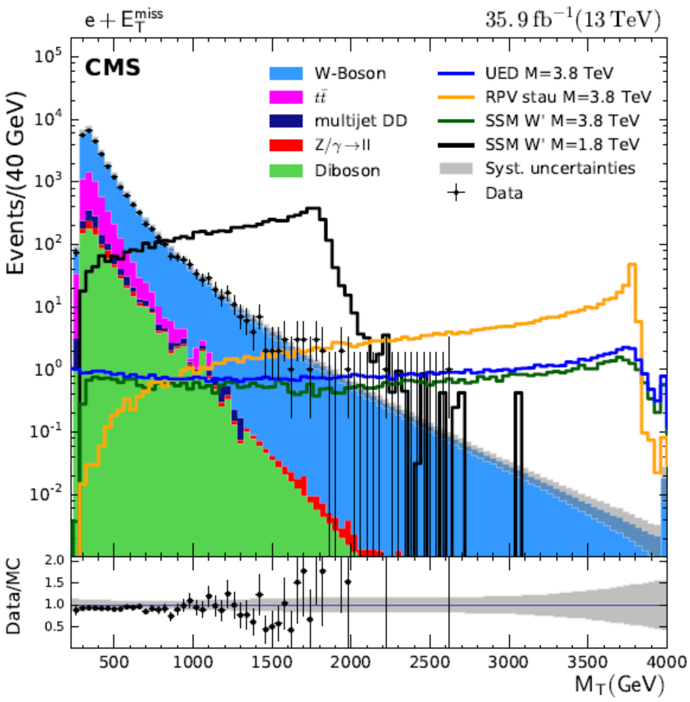

Figure 5.15: Distributions of the transverse mass M_T after all event selections for data and expected SM backgrounds in the electron channel. Signal examples for SSM W′ masses of 1.8 and 3.8 TeV, including detector simulations. Also signal exmaples for split-UED and RPV SUSY are depicted. The bottom panels show the ratio of data to SM prediction with systematic uncertainty band.

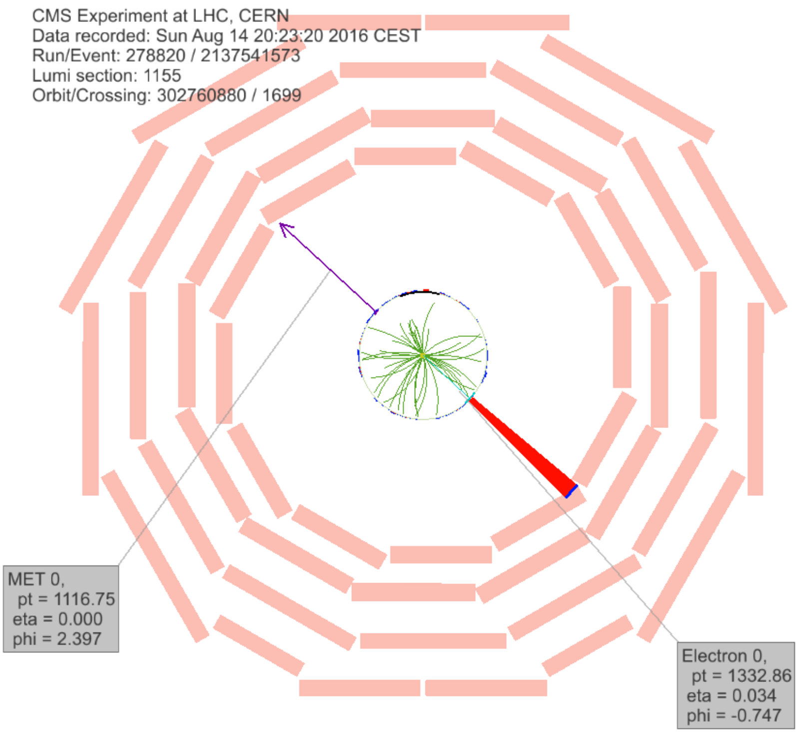

Figure 5.16: Event display for one of the events with maximum M_T in data for e $+E_T^{miss}$ channel. The M_T is about 2.4 TeV derived from a 1.3 TeV electron and 1.1 TeV E_T^{miss}. The event is shown on MiniAOD level before JEC is applied, which causes the E_T^{miss} to be recalculated.

Muon results

According to the M_T distribution after all event selections, the agreement between the expected and observed number of events is very reasonable. Expected and observed number of events for a selected set of M_T with the corresponding specific M_T threshold are shown in Table 5.7.

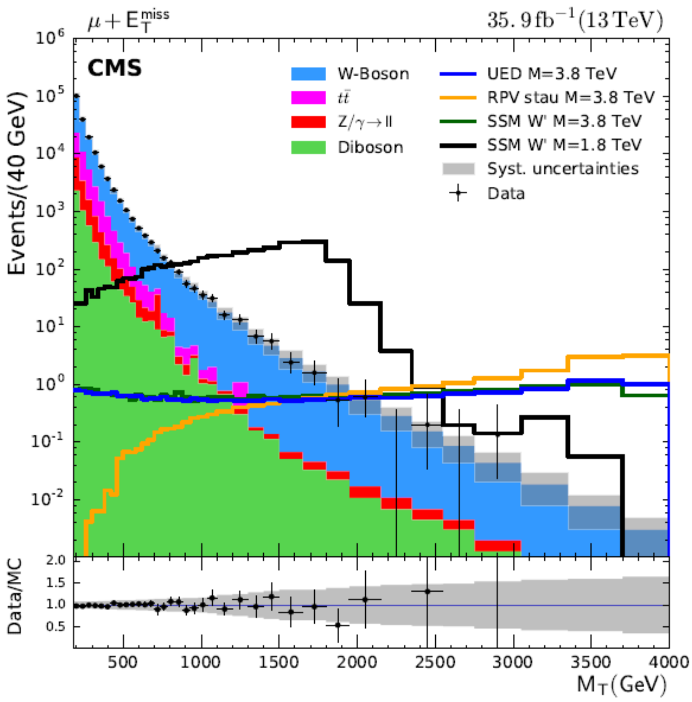

Figure 5.17: Distributions of the transverse mass M_T after all event selections for data and expected SM backgrounds in the muon channel. Signal examples for SSM W′ masses of 1.8 and 3.8 TeV, including detector simulations. Also signal exmaples for split-UED and RPV SUSY are depicted. The bottom panels show the ratio of data to SM prediction with systematic uncertainty band.

An example of an event display in the $\mu + E_T^{miss}$ channel is presented in Figure 5.18. The event contains a muon with $p_T = 1461.6$ GeV, according to TuneP, and a $E_T^{miss} = 1430.5$ GeV, clearly dictated by the muon p_T. The transverse mass, $M_T = 2891.7$ GeV.

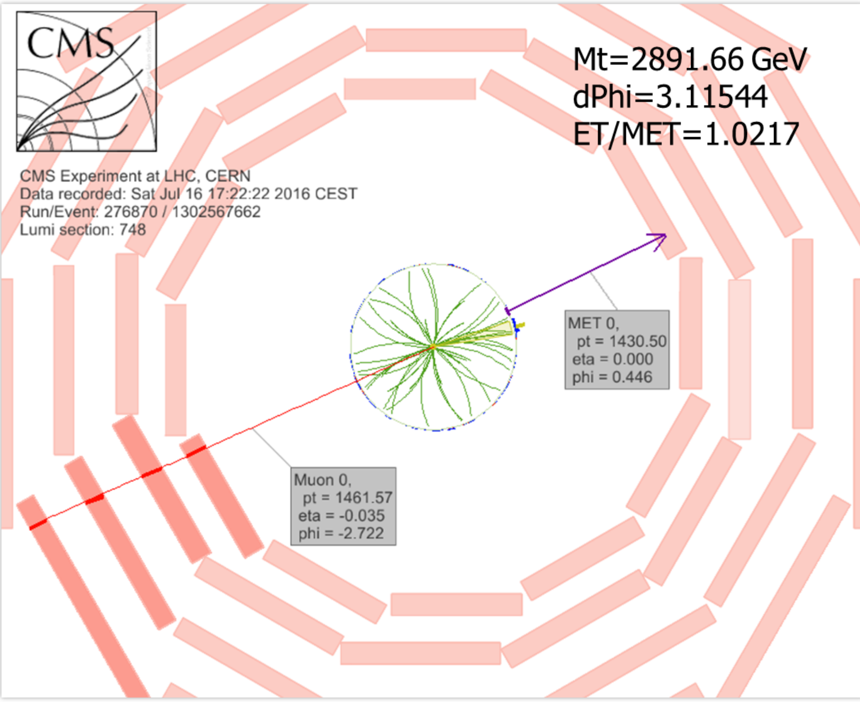

Figure 5.18: Event display in the $\mu + E_{\mathrm{T}}^{\mathrm{miss}}$ channel for the maximum $\mathrm{M_T}$ of the events($> 2\,\mathrm{TeV}$) in data.

	$M_T > 1$ TeV	$M_T > 2$	$M_T > 3$	$M_T > 4$
Muon Data	208	4	0	0
Sum of SM BG	216.7 ± 20	6.0 ± 1.2	0.27 ± 0.21	0.02 ± 0.02
SSM $M_{W'}$= 1.8 TeV	5345 ± 530	96 ± 14	2.5 ± 1.2	0 ±
SSM $M_{W'}$= 2.4 TeV	1282 ± 120	577 ± 85	2.4 ± 1.2	0.1 ± 0.05
SSM $M_{W'}$= 3.8 TeV	57 ± 6	42 ± 6	24 ± 12	2 ± 1
SSM $M_{W'}$= 4.2 TeV	25 ± 3	19 ± 3	12 ± 6	3.6 ± 1.8

Table 5.7: Expected and observed number of data, signal and background events in the muon channel for corresponding selected set of M_T integrated above each M_T thresholds for 35.9 fb^{-1} of integrated luminosity. The signal yield is using NNLO cross sections.

Chapter 6

Systematic Uncertainties

Every measurement in experiment suffers from the imperfect knowledge of input quantities. Mismeasurement of lepton energy or momentum, resulting from both detector resolution and imperfect scale calibration, can result in a smearing of the M_T spectrum. Therefore a study the related effects on the measurement must be done and evaluated the systematic uncertainties. In this analysis, a number of sources of systematic uncertainties that affect the result of the limit calculation are taken into account. For each source of systematic uncertainty, shifts of $\pm 1\sigma$ are considered, the kinematic of the signature particles (e, μ, E_T^{miss}) are recalculated as well as M_T distribution, and all selection are samely reapplied. Each source of uncertainty is described in the following.

The most relevant systematic uncertainties in both channels derived from the modeling of the SM background, which is used to compare our data, searching for a significant difference the potential existence of a new particle or effect. Systematic uncertainties from the Modeling of SM background, Luminosity, Pileup reweighting, and MET commonly occured and must be considered in both channels.
Firstly, each source of systematic uncertainty for both channels is explained in following :

- Luminosity : The luminosity is an essential ingredient for the calculation of the normalization of the MC simulations. It has been determined by recording relative changes in the instantaneous luminosity with the cluster counting method in the silicon pixel detector. The absolute scale of the luminosity has been derived with Van der Meer scans [76, 144]. A larger/smaller luminosity would lead to a constant upward/downward shift of the SM background expectation, however, it will not change the shape of the M_T distribution. Officially provided the luminosity systematic uncertainty of 2.5 % is considered, thus being 35.9± 0.9 the equivalent luminosity used for the analysis.

- Pileup :
The uncertainty due to the pileup reweighting is considered as ±5% (±3.5 mb) is assigned on the inelastic pp cross section of 69.2 mb used in the pileup reweighting procedure. The reweighting method used to determine the number of collision events per bunch crossing needs the total inelastic pp cross section as an input. The uncertainty is propagated to the analysis by studying the change of the M_T distribution of each channel when the total inelastic cross section used in the pileup reweighting procedure is increased and decreased by one standard deviation.

- PDF :
In modeling procedure, the dominant uncertainties arise from the PDFs uncertainties and signal/background K-factor. The PDFs uncertainty is related to the choice of PDF set. CT14 [145, 146], MMHT14 [147] and NNPDF3.0 [113] are included and combined with a Hessian [148] approach with 30 eigenvectors. More detailed is described in end of this Chapter.

- K-Factor :
The uncertainties from these K-factors account for a ±5 % uncertainty on the (N)NLO cross sections used to derive them and, in addition, the difference between the additive and multiplicative approach when combining EWK and QCD corrections.

- MET scale :
For the MET uncertainty, we followed the recommendation from JETMet group. All physics objects are entering into the MET calculation so their specific uncertainties should be taken into account. For every event, the momentum of each particle type (muon, electron, jet, unclustered energy and tau) is shifted within its uncertainties upward or downward, and the MET is recalculated using those shifted momenta. Beside the muons or electrons, which are already considered, the other uncertainties seem to have a negligible effect. In addition, there is a 10 % uncertainty on the MET scale and the resolution of the unclustered energy. Unclustered energy describes jets with a transverse momentum below 10 GeV together with all the tracks that are not associated with jets or other objects. The x and y component of this unclustered energy are getting scaled and smeared and a smeared M_T distribution is obtained.

With the exception of the luminosity, each systematic uncertainty can change the normalization as well as the shape of the transverse mass spectrum. The difference to the nominal value is taken as uncertainties. These uncertainties are so called shape uncertainties. For each shape uncertainty in this chapter, the quantity in question is varied according to its uncertainty and the M_T spectrum is recalculated. The shifted M_T distribution will be fitted and compared to the unshifted fit. Other objects dependent systematics are explained in following section.

Systematic Uncertainty for electron channel

In electron channel, typically the mismeasurements of the electron energy scale and resolution are small enough in CMS experiment. (They don't change the M_T shape in a sizeable way.) The sources of systematic uncertainty considered in electron channel are explained below:

- Electron energy scale/resolution :
  The systematic uncertainty on the electron energy scale and resolution are centrally produced by EGamma POG. The uncertainty in the electron energy scale is estimated to be 0.4 % and 0.8 % in the barrel and endcaps, respectively For the electron energy resolution uncertainty, an additional Gaussian smearing of 1.2 % and 2.4 % in the barrel and endcap is applied to the MC simulation (detailed information can be found in [149]).
- HEEP ID :
  The uncertainties on the HEEP SF are 0.6 % and 0.7 % for barrel and endcaps. The main source of uncertainty on the SF comes from varied cross sections of non-DY processes, 10 % for $t\bar{t}$ and 50 % for W+jets MC processes. Also the uncertainty of the pileup reweighting is considered but it is negligible.(See Section 5.3.2.)
- QCD multijet data-driven method:
  The difference between the data-driven approach and the MC closure test is taken as systematic uncertainties, resulting in about 40 % (As described in previous Section 4.3.2).

Each source of uncertainty is shifted by $\pm 1\sigma$ and the resulting M_T distributions are recalculated. The difference with respect to the nominal distribution is used to estimate the uncertainty in the expected number of events.

Systematic Uncertainty for muon channel

In muon channel, the most important systematic uncertainty is associated with the muon p_T measurement (and consequently with the E_T^{miss} as stated in Chapter 5.1.3), in the form of a bias on the p_T scale or a worsening of the p_T resolution.

Sources of smaller uncertainty come from the lepton and trigger scale factors, used to adequate the simulated samples to the data. The sources of systematic uncertainty contribute to muon channel are explained below:

- Muon p_T scale :
  For the muon p_T scale, the generalized endpoint method is used, relating the uncertainty in p_T to that in measuring the transverse curvature of muon tracks (κ), defined as $\kappa = q/p_T$. The study is performed using high p_T muons, as a function of η and ϕ, by comparing cosmic muons data and dimuon events from high-p_T Z boson decays in collisions, together with the corresponding simulation MC samples A bias is injected in simulated events in order to describe the κ distribution in data and the value that minimizes the difference in a given bin in η and ϕ is taken as the bias. It has been revealed that in the central barrel region ($|\eta|$ <1.2), the amplitude of the bias is very small, consistent with zero, within the uncertainty of 0.025/ TeV. In the forward region (especially in $1.2 < |\eta| < 2.1$, and in particular muon ϕ zones, values of the scale bias different from zero are found. The average value of the modification in the simulated p_T coming from these scale biases is used as uncertainty for $p_T > 200$GeV. (Reaching values of up to 24 (40) % for the most forward (backward) bins ($|\eta| > 2.1$) and in a given ϕ region.) This uncertainty is propagated to E_T^{miss} and M_T. The uncertainty of the muon p_T measurement relates to the smallness of curvature of tracks for high-p_T muons.[1]

- Muon p_T resolution :
  The p_T resolution at high-p_T values is studies using cosmic muon data and simulated samples, which allow testing the barrel region, and boosted dimuon events for the endcaps, have concluded that simulated samples reproduced quite well the resolution observed in data. An uncertainties of ± 1 % in the barrel 2 % in the endcap are assigned to the measured p_T and no additional smearing is implemented.

- Trigger :
  For trigger scale factors we use as systematic uncertainty the difference between the values derived in our analysis, using the measurement on the orthogonal data sets (Section 5.3.3) and the "official" ones available within the Muon POG, which have been obtained using the Tag&Probe method. These two sets of results are consistent within 2 % of the SF values, in all the muon η bins considered, for muon $p_T < 300$ GeV.

- Tracking and Isolation :
  For the tracking and muon isolation, the values provided by the studies in

[1]but the energy of the electrons is measured in the crystal calorimeter so uncertainties is very small.

the Muon POG are applied, as a function of muon η (and integrated in p_T and number of vertices). The uncertainties have been checked not to vary significantly in the high p_T region. Uncertainties of ±0.05% for the tracking SF and muon isolation, independently, have been used.

- high-p_T Muon ID :
  As described in previous Section 5.3.3, the reconstruction and high-p_T identification efficiencies for very energetic muons are determined using dimuon events in data and simulated samples. These SFs have an effect as a function of $p_T$andη and are used to assign an systematic source on the reconstruction and muon identification. The systematic uncertainty is differently estimated for the barrel ($|\eta| < 1.6$) and for the endcap (1.6< $|\eta|$ <2.4), with downward uncertainties dependent on muon momentum, which amount to 3 % for the barrel and up to 20 % for the endcap for muon p_T of 5 TeV.

All of the systematics uncertainties are summarized in the Table 6.1.

Channel	Systematic uncertainty	Value
Both	Luminosity	2.5 %
	Pileup	±5 % of MinBias cross section
	Background PDF	function of M_T (1 % at 300 GeV, 20 % at 3.2 TeV)
	k-factor on W-BG 4.3.1	±5 %
	MET scale	10 % of unclustered energy
Electron	QCD (data-driven)	40 %
	Electron energy scale	0.4 % (barrel), 0.8 % (endcap)
	Electron energy resolution	1.2 % (barrel), 2.4 % (endcap)
	HEEP SF	0.6 % (barrel), 0.7 % (endcap)
Muon	Muon p_T scale	0.05 (barrel), 24 % / 40 %(forward / backward)
	Muon p_T resolution	±1 (barrel), 2 % (endcap)
	Trigger SF	2 %
	tracking and isolation SF	±0.05%
	high-p_T Muon Id SF	3 % for p_T= 5 TeV (barrel)
		20 % for p_T= 5 TeV (endcap)

Table 6.1: Systematic uncertainties in electron and muon channel.

Parton Density Functions (PDF) and α_s Uncertainty of signal

In this section, more detailed methods used for calculating the PDF uncertainty are given. The Parton Distribution Function (PDF) is dominant factor to expect the produced event rate for physics processes and its uncertainties is the major source of systematics on the theoretical cross section calculation. Therefore the accurate determination of PDFs and their corresponding uncertainties is important. In order to progress in the determination of PDFs, many groups have constantly provided updates of their PDFs with the inclusion of LHC data and various methodological developments. Although various new PDF sets are released by different groups based on similar data sets, there are still variations in both the ensuing central values and uncertainties of each PDF group. This suggests that use of the PDFs from only one of groups might underestimate the true uncertainties, and a combination of individual PDF sets is required for a robust estimation of uncertainty in theoretical production cross-sections.

During Run II at LHC, PDF4LHC Working group proposed to use PDF4LHC15 combined PDFs [150] which are based on a statistical combination of 3 representative PDF sets (CT14 [145, 146], MMHT2014 [147] and NNPDF3.0 [113]), before that the traditional envelope method [151] is usually applied. These new combined NNLO PDF sets are described in Table 6.2 and all these samples are available in LHAPDF6 [152].

According to the new method [150], two different representations of PDF4LHC15 uncertainties are being used : the MC representation [153, 154], in which the probability distribution of PDFs is given as an ensemble of replicas, whose mean and standard deviation provide respectively central value and uncertainty, and the Hessian representation [148], in which a central PDF is given, along with error sets, each of which corresponds to an eigenvector of the covariance matrix in the parameter space. The general guidance to use PDF4LHC15 combined sets according to the specific phenomenological applications is provided, we use for specifically the new physics search with massive exotic particles.

Table 6.2: Summary of the new combined NNLO PDF4LHC15 sets with n_f^{max}=5 (Remind that N_{mem} is the number of error sets and all PDF sets has zeroth member(best-fit value) in LHAPDF6, so the total number of PDF members is N_{mem}+1).

ErrorType	PDF set name	application to LHC	N_{mem}	$\alpha_s(M_Z^2)$
MC replicas	PDF4LHC15_nnlo_mc	BSM search(massive particle)	100	0.118
Hessian	PDF4LHC15_nnlo_100	Precision measurement	100	0.118
	PDF4LHC15_nnlo_30	limited Num. of err PDFs	30	0.118
-	PDF4LHC15_nnlo_asvar		1	(0) 0.1165 (1) 0.1195

Calculation of PDF+α_s uncertainties

The PDF uncertainty on the signal or background production cross section is estimated by using PDF reweighting method comparing the new NNLO PDF4LHC15 combined sets with reference LO PDF set[2], NNPDF2.3 [113]. The

[2]MC for RunII are generated with full simulation using CUETP8M1 condition based on

cross section for each PDF set is estimated by multipling the weighting factor (R) to the reference cross section.

$$\sigma^{P} = \sigma^{ref} \times \frac{1}{N}\sum_{i=1}^{N} w_i(x_1, x_2, Q) \equiv \sigma^{ref} \times R \qquad (6.1)$$

where, N is the number of events in the generated sample. The weight $w_i(x_1, x_2, Q)$ of the i^{th} event for PDF set (P) is calculated by the following formula,

$$w_i(x_1, x_2, Q) = \frac{f_1^{(P)}(x_1, Q) \times f_2^{(P)}(x_2, Q)}{f_1^{(ref)}(x_1, Q) \times f_2^{(ref)}(x_2, Q)} \qquad (6.2)$$

where,

P = PDF4LHC15_mc_nnlo(MC),
PDF4LHC15_30_nnlo, PDF4LHC15_100_nnlo(Hessian)

ref = NNPDF2.3_lo_as_0130_qed PDF for RunII

x_I = Bjorken's x for parton I (I=1,2)

Q = factorization scale

$f_I^{(J)}(x_I, Q)$ = PDF value for I^{th} parton and PDF set J, calculated using LHAPDF package

The uncertainty for cross section is estimated by the variation of R.

The PDF and combined PDF+α_s uncertainties for each PDF4LHC15 sets are computed from 68 % C.L. as recommended by PDF4LHC group. Hessian and MC set have different ways for estimating PDF uncertainties.
For Hessian sets(PDF4LHC15_100, PDF4LHC15_30), the master formula to evaluate the PDF uncertainty is as follow

$$\delta^{PDF}R = \sqrt{\sum_{k=1}^{N_{mem}} (R^{(k)} - R^{(0)})^2} \qquad (6.3)$$

where, $R^{(k)}$ (Equation 6.1) for the PDF set with mem = k. $R^{(0)}$ is the best fit value of Hessian sets.
For MC set (PDF4LHC15_mc), PDF uncertainties can be calculated with two different methods. one is the standard deviation of the distribution

$$\delta^{PDF}R = \sqrt{\frac{1}{N_{mem}-1}\sum_{k=1}^{N_{mem}} (R^{(k)} - \langle R \rangle)^2} \qquad (6.4)$$

Monash tune in PYTHIA8.2 with reference NNPDF23LO_QED($\alpha_s = 0.130$) PDF set.

where the mean value of R is give by

$$< \mathrm{R} >= \frac{1}{\mathrm{N_{mem}}} \sum_{\mathrm{k}=1}^{\mathrm{N_{mem}}} \mathrm{R}^{(\mathrm{k})} \tag{6.5}$$

the other way is to compute 68 % CL interval for each bin, by reordering the $\mathrm{N_{mem}}$=100 for R values in ascending order

$$\begin{aligned} \mathrm{R}^{(1)} \leq \mathrm{R}^{(2)} \leq \cdots \leq \mathrm{R}^{(\mathrm{N_{mem}}-1)} \leq \mathrm{R}^{(\mathrm{N_{mem}})}, \\ \delta^{\mathrm{PDF}}\mathrm{R} = \frac{\mathrm{R}^{(84)} - \mathrm{R}^{(16)}}{2} \end{aligned} \tag{6.6}$$

In addition, in the non-Gaussian case midpoint of the 68 % CL interval is recommended to use central value.

$$\bar{R} = \frac{R^{(84)} + R^{(16)}}{2} \tag{6.7}$$

For computation of the combined PDF+α_s uncertainties, The central values for α_s value is 0.118 and $\delta\alpha_\mathrm{s}$ is 0.0015 at the 68 % confidence level and combined PDF+α_s uncertainties are obtained adding the two uncertainties in quadrature:

$$\begin{aligned} \delta^{\alpha_\mathrm{s}}\mathrm{R} = \frac{\mathrm{R}^{(\alpha_\mathrm{s}=0.1195)} - \mathrm{R}^{(\alpha_\mathrm{s}=0.1165)}}{2} \\ \delta^{\mathrm{PDF}+\alpha_\mathrm{s}}\mathrm{R} = \sqrt{(\delta^{\mathrm{PDF}}\mathrm{R})^2 + (\delta^{\alpha_\mathrm{s}}\mathrm{R})^2} \end{aligned} \tag{6.8}$$

For the BSM case of MC set, We can obtaine two combined PDF+α_s uncertianties by following the official recommendation. Total PDF+α_s uncertainty values for all different cases are summarized in Figure 6.1 and Table 6.3.

The total PDF+α_s uncertainty for signal ranges from 1.734 % to 13.44 % and is raised to about $\mathrm{m_{W'}}$=4.8 TeV and then decreased due to the large contribution of off-shell mass tail in high mass W′ events.

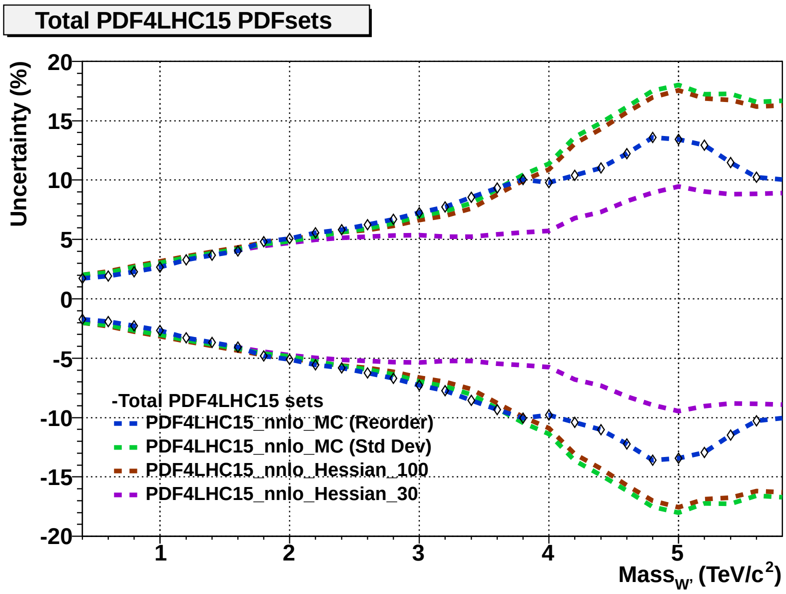

Figure 6.1: The combined PDF+α_s uncertainties for Hessian PDF sets (PDF4LHC15_100 and PDF4LHC15_30) and MC PDF set(PDF4LHC15_mc) for two different methods (standard deviation and re-ordering methods) for the W′ signal cross section.

Table 6.3: The cross section times branching fraction for W′ boson. Both LO and NNLO cross section are calculated by FEWZ. The K-Factor is defined as the ratio of NNLO and LO cross section. In accordance with the PDF4LHC RunII recommendations in new physics analysis, final combined PDF+α_s uncertainties for PDF4LHC15_mc set is estimated by using reordering method.

W′ Mass (TeV/c^2)	13TeV LO (fb)	13TeV NNLO (fb)	K-Factor	PDF+α_s Uncertainty (±%)
0.4	84153	111394	1.324	1.734
0.6	19225	25718	1.338	1.906
0.8	6494	8717	1.342	2.279
1.0	2699	3623	1.346	2.679
1.2	1276	1709	1.340	3.284
1.4	657.3	877.2	1.335	3.669
1.6	360.2	478.2	1.328	4.046
1.8	206.5	272.4	1.319	4.801
2.0	122.6	160.4	1.309	5.088
2.2	74.73	96.96	1.298	5.562
2.4	46.59	59.81	1.284	5.825
2.6	29.56	37.51	1.269	6.238
2.8	19.03	23.85	1.253	6.684
3.0	12.41	15.35	1.237	7.268
3.2	8.195	9.984	1.218	7.743
3.4	5.467	6.568	1.201	8.547
3.6	3.687	4.371	1.186	9.326
3.8	2.516	2.943	1.170	10.05
4.0	1.734	2.009	1.159	9.782
4.2	1.211	1.393	1.150	10.40
4.4	8.565×10^{-1}	9.819×10^{-1}	1.146	11.01
4.6	6.148×10^{-1}	7.062×10^{-1}	1.149	12.24
4.8	4.487×10^{-1}	5.189×10^{-1}	1.156	13.60
5.0	3.323×10^{-1}	3.893×10^{-1}	1.172	13.44
5.2	2.515×10^{-1}	2.983×10^{-1}	1.186	12.95
5.4	1.930×10^{-1}	2.337×10^{-1}	1.211	11.47
5.6	1.513×10^{-1}	1.866×10^{-1}	1.233	10.26
5.8	1.203×10^{-1}	1.515×10^{-1}	1.259	10.05

Chapter 7

Limit Calculation

The discriminating variable in this search is the transverse mass, M_T. The fully binned distribution obtained after the complete event selection, considering shape and normalization, is applied. Signal events are expected to reside at very high M_T where the SM background expectation is below one event. The final M_T distributions are presented in Figure 5.15 and Figure 5.17 for electron and muon decaying channel, respectively.

For each electron and muon, the detailed systematic uncertainties (See Section 6) are applied when calculating the limit. As no significant deviation from the expectation is observed in either channel, exclusion limits on the production cross section are calculated. Most recent results of W′ in 2015 data can be found in [12, 15] and W′ masses below 3.6 TeV and 3.9 TeV were excluded in the electron and muon channel analysis, respectively. When combining both channels, the limit extended up to 4.1 TeV.

Upper limits on the SSM W′ production cross section times branching fraction $\sigma_{W'} \times \mathcal{B}(W' \rightarrow \ell\nu)$, with $\ell = $ e or μ, are determined by using Bayesian approach with a uniform positive prior probability distribution for the signal cross section. Furthermore, results are interpreted in terms of the variety of models described in Section 2.3 such as split-UED and RPV SUSY. Less model-dependent is the determination of a generic cross section limit and a study of the coupling strength.

7.1 Statistical Analysis

As no significant deviation from the expectation is observed, exclusion limits on the production cross section for a number of models interpretations are calculated. For this analysis, the parameter of interest is the signal the cross section. In practice, the limits are derived using the Higgs *combine* tool [155], using as input the binned M_T distributions, for the background and signals, normalized to MC cross sections including K-factors (up to NNLO for signal, NNLO/NLO for

background). The correlation between common systematic uncertainty sources is taken into account, that is, luminosity, PU weighting, PDFs, k-factor and the common part of MET uncertainty.
For the limit setting is done with a Bayesian approach [21] using a uniform positive prior probability distribution for the signal cross section. Systematic uncertainties on the expected signal and background yields are included via nuisance parameters with log-normal prior distributions.

$$\mathrm{P(theory|data)} \propto \mathrm{P(data|theory)} \cdot \mathrm{P(theory)} \tag{7.1}$$

where P(data|theory) is called likelihood (L). It is basically the probability of observing N events in data, given the expectation of b background events and s signal events from theory. P(theory) is the prior probability of the theory. It represents the initial degree of belief on the signal model under test. P(theory|data) is the posterior probability. The anticipated signal, which is being searched for, is represented by a parameter of interest, POI, corresponding to the number of expected signal events (s), if the theory is valid. The likelihood is a function of the POI and nuisance parameters (ν), which are used to model systematic uncertainties, and distributed as a Poisson fuction. The likelihood function and the prior function can be used to calculate the posterior probability P.

$$\mathrm{P(s|N)} = \frac{\mathrm{L(N|s)}\pi\mathrm{(s)}}{\int \mathrm{L(N|s)}\pi\mathrm{(s)ds}} \tag{7.2}$$

To eliminate the dependence on the nuisance parameters (ν), the posterior probability has to be integrated over ν.

$$P(s|N) = \int P(s,\nu|N)d\nu \tag{7.3}$$

The integration is not analytically solvable because of the high number of dimension $\nu = (\nu_1, \nu_2, \cdots, \nu_\mathrm{n})$ the Markov-Chain Monte Carlo (MCMC) method is used. Based on the posterior probability, an upper limit on the number of signal events($\mathrm{s_{up}}$) can be computed at a confidence level of $1-\alpha = 95\%$ by

$$1 - \alpha = 0.95 = \int_{-\infty}^{\mathrm{s_{up}}} \mathrm{P(s|N)} \tag{7.4}$$

The cross section limits are calculated with two different methods. First, for the limits on the SSM W′ and split-UED models, the entire $\mathrm{M_T}$ spectrum in Figure 5.15, 5.17 with $\mathrm{M_T} > 220$ GeV selection is considered to take the shape of the distribution into account using a binned likelihood, so-called multi-bin approach. The other one is a model independent upper limit on the cross section times branching fraction using single-bin counting approach. To determine a model independent limit, all events above a threshold $\mathrm{M_T^{min}}$ are summed. The resulting limit can be reinterpreted for other models with a lepton and MET final state. The limits on specific RPV SUSY process are derived by applying the model independent limit approach. These two limit setting approaches are more explained below.

7.1.1 Single-bin counting approach

This single-bin counting approarch is simply based on comparing the number of expected events with the number of observed events Since the existence of a SSM W′ would lead to an excess of events at high M_T above the exponentially falling SM background, it used the set a lower M_T threshold (M_T^{min}) and the number of events above this M_T^{min} threshold. This will improve the signal to background ratio and increase the exclusion power of the method. The optimal value for M_T^{min} will in general depend on the signal shape and cross section. In this approach, all bins above M_T^{min} are merged into a single bin. Therefore, this method we called single-bin method. The formula for calculation of N and the corresponding likelihood function is given:

$$N_{exp} = \mathcal{A}(\mathcal{L}, \epsilon) \cdot \sigma_s + b \tag{7.5}$$

$$\mathrm{L} = \frac{(\mathrm{N_{exp}})^{\mathrm{N_{obs}}}}{\mathrm{N_{obs}}!} \cdot \mathrm{e}^{-\mathrm{N_{exp}}} = \frac{(\mathcal{A} \cdot \sigma_\mathrm{s} + \mathrm{b})^{\mathrm{N_{obs}}}}{\mathrm{N_{obs}}!} \cdot \mathrm{e}^{-(\mathcal{A} \cdot \sigma_\mathrm{s} + \mathrm{b})} \tag{7.6}$$

Here $\mathcal{A}$ is the signal acceptance, σ_s is the signal cross section, the expected number of background events (b) and observed data events (N_{obs}) in the bin. The signal acceptance is defined to be a product of the integrated luminosity and efficiency times geometrical acceptance ϵ for the chosen M_T^{min}. The signal cross section σ_s is the parameter of interest on which a upper limit is to be set. $\mathcal{L}, \epsilon$ and b are treated as nuisance parameters. Systematic uncertainties on the nuisance parameteres are incorporated by multiplying the likelihood with the prior functions of the nuisance parameters. the log-normal functions are used as priors. The posterior pdf for the σ_s is given as follows:

$$\prod(\sigma_\mathrm{s}|\mathrm{N_{obs}}) = \int \mathrm{d}\mathcal{L}\mathrm{d}\epsilon\mathrm{d}\mathrm{b}\,\pi(\sigma_\mathrm{s})\pi(\mathcal{L}) \cdot \frac{(\pi(\epsilon) \cdot \mathcal{A} \cdot \sigma_\mathrm{s} + \pi(\mathrm{b}) \cdot \mathrm{b})^{\mathrm{N_{obs}}}}{\mathrm{N_{obs}}!} \cdot \mathrm{e}^{-(\pi(\epsilon) \cdot \mathcal{A} \cdot \sigma_\mathrm{s} + \pi(\mathrm{b}) \cdot \mathrm{b})} \tag{7.7}$$

Where $\pi(\mathcal{L}), \pi(\epsilon)$ and $\pi(b)$ represnet the priors for the nuisance parameters and $\pi(\sigma_s)$ the prior for POI. For σ_s a uniform prior is taken into account. The upper limits on the σ_s can be calculated with Equation 7.4. To quantify the expected exclusion limit and possible variations due to statistical and systematic uncertainties, pseudo experiments are use. To quantify the spread of the expected limit a 1σ (2σ) band is determined by taking the range centered around the median which contains 68.2% (95.4%) of all the limits from pseudo experiments.

The lower M_T threshold is chosen by optimizing it for the best expected limit. For each mass point the expected exclusion limit is calcualted using thresholds between 250 GeV and 4000 GeV.

7.1.2 Model-independent cross section limit

A model-independent cross section limit is determined using a single-bin approach. No assumptions on the shape of the signal M_T distribution have to be made following the quite flat acceptance × efficiency as a function of W′ mass. In order to determine any limit for a specific model from the model-independent limit, only the model -dependent part of the efficiency must be taken into account. The experimental efficiencies for the signal are already considered, including the effect of the kinematic selections (p_T^ℓ/E_T^{miss} and $\Delta\phi(\ell, \vec{p}_T^{miss})$ cuts), geometrical acceptance (η) and trigger threshold. The effect of the threshold M_T^{min} on the signal is determined by counting the events with $M_T > M_T^{min}$ and dividing it by the number of generated events (f_{M_T}), as illustrated in Figure 7.1. For $M_T > 400$

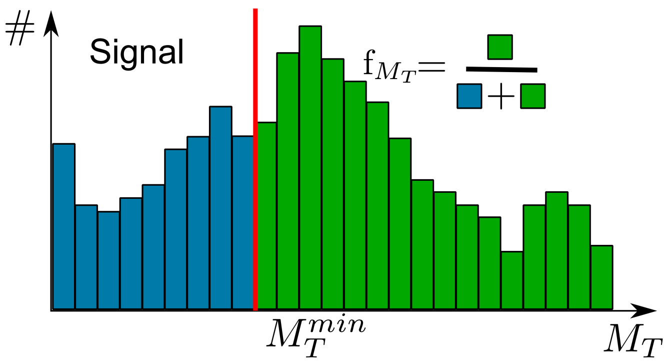

Figure 7.1: Illustration of the model-independent cross section limit determined. A series of single bins is determined by the threshold on M_T denoted as M_T^{min}.

GeV the reconstruction efficiency is nearly cosntant, therefore f_{M_T} can evaluate at generator level. A limit on the production cross secion times branching fraction $(\sigma \times \mathcal{B} \times \mathcal{A} \times \epsilon)_{excl}$ given in Figure 7.2 by applying the fraction $f_{M_T}(M_T^{min})$:

$$(\sigma \times \mathcal{B} \times \mathcal{A} \times \epsilon)_{excl} = \frac{(\sigma \times \mathcal{B} \times \mathcal{A} \times \epsilon)_{MI}(M_T^{min})}{f_{M_T}(M_T^{min})}.$$

Models with a theoretical cross section $(\sigma \times B)_{theo}$ larger than $(\sigma \times B)_{excl}$ can be excluded. The procedure described here can be applied to any model that has back-to-back kinematic properties similar to those of a generic W′, and thus a

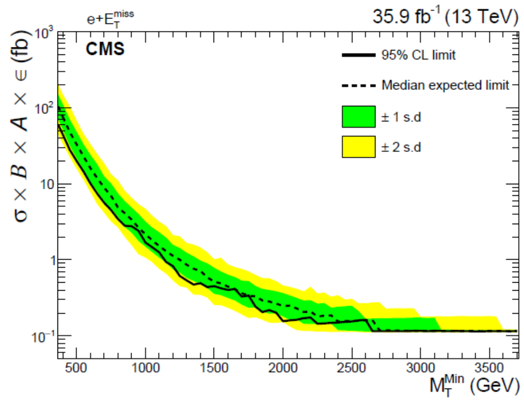

Figure 7.2: The expected (dashed line) and observed (solid line) 95% CL on the model-independent limits ($\sigma(\mathrm{W}') \times B(\mathrm{W}' \to \ell\nu) \times \mathcal{A} \times \epsilon$) abovea threshold $\mathrm{M}_\mathrm{T}^\mathrm{min}$ for the individual electron (left) and muon channels (right). The shaded bands represent the 1σ and 2σ uncertainty bands.

similar signal efficiency, which is a reasonable assumption for a two-body decay of a massive state. If the kinematic properties are very different, the fraction of events $\mathrm{f}_{\mathrm{M_T}}(\mathrm{M}_\mathrm{T}^\mathrm{min})$ needs to be taken into consideration. The result for the electron, muon channel is shown seperately in Figure 7.2. It is a strong fuction of the threshold $\mathrm{M}_\mathrm{T}^\mathrm{min}$. In either channel, cross section balues $\sigma \times B$ between 40 to 50 fb for $\mathrm{M}_\mathrm{T}^\mathrm{min} > 400\,\mathrm{GeV}$ and 0.1 fb for $\mathrm{M}_\mathrm{T}^\mathrm{min} > 3\,\mathrm{TeV}$ are excluded for the given $\mathrm{M}_\mathrm{T}^\mathrm{min}$ thresholds.
To verify the application of the model-independent limit, it was applied to an SSM W′ of 5 TeV corresponding to the present limit.(in next SSM W′ limit section in Figure 8.2) The simulated signal distributions yield a fraction $\mathrm{f}_{\mathrm{M_T}}$ ranging from 0.61 at $\mathrm{M}_\mathrm{T}^\mathrm{min} = 2025$ GeV to 0.99 at $\mathrm{M}_\mathrm{T}^\mathrm{min} = 300$ GeV. The exclusion limit on $(\sigma \times B)_\mathrm{excl}$ as a function of $\mathrm{M}_\mathrm{T}^\mathrm{min}$ is then calculated by dividing the model-independent limit $(\sigma \times B)_\mathrm{MI}$ by the corresponding $\mathrm{f}_{\mathrm{M_T}}$, resulting in a maximum excluded cross section of 0.1 fb at a $\mathrm{M}_\mathrm{T}^\mathrm{min}$ above 4 TeV for this particular signal sample. Given a theoretical cross section $(\sigma \times B)_\mathrm{theo} \approx 0.39$ fb this signal is excluded. It should be noted that this approach corresponds to a single-bin limit which is expected to differ slightly from a dedicated analysis exploiting the full $\mathrm{M_T}$ shape.

7.1.3 Multi-bin approach

The single-bin approach uses only a small amount of the available information. During the optimization procedure, expected upper cross section limits are calculated for a large set of different $\mathrm{M_T}$ thresholds. Since the bins above $\mathrm{M}_\mathrm{T}^\mathrm{min}$

are merged in single-bin method, all information about the distribution of the events is lost. Therefore the single-bin approach is not really sensitive to the shape of the signal. Once the optimization is done, the information about the $\mathrm{M_T}$ spectrum below $\mathrm{M_T^{min}}$ has no impact on the limit. Especially the information about the measured data below $\mathrm{M_T^{min}}$ and the distribution of the data points above $\mathrm{M_T^{min}}$ is not used at all, since the optimization is done based solely on simulations. A multi-bin approach can be used which is a generalization of the single-bin method. Instead of using one large bin starting at $\mathrm{M_T^{min}}$, the whole $\mathrm{M_T}$ range is used divided into multiple bins. For each bin a Poisson counting experiment is performed similar to the single-bin method. The combination of all the bins is done by multiplying the single-bin likelihoods as follows,

$$\mathrm{L} = \prod_{\mathrm{k}=1}^{\mathrm{n}} \frac{(\mathrm{N_{exp}^k})^{\mathrm{N_{obs}^k}}}{\mathrm{N_{obs}^k}!} \cdot \mathrm{e}^{\mathrm{N_{exp}^k}} = \prod_{\mathrm{k}=1}^{\mathrm{n}} \frac{(\mathcal{A}^\mathrm{k} \cdot \sigma_\mathrm{s} + \mathrm{b^k})^{\mathrm{N_{obs}^k}}}{\mathrm{N_{obs}^k}!} \cdot e^{-(\mathcal{A}^\mathrm{k} \cdot \sigma_\mathrm{s} + \mathrm{b^k})} \tag{7.8}$$

The product loops over all bins which are used for the limit calculation. Similar to Equation 7.7, $\mathcal{A}^\mathrm{k}$ and $\mathrm{b^k}$ are the signal acceptance and Standard Model expectation in kth bin. For the treatment of systematic uncertainties the distinction between normalization and shape uncertainties is made as already explained in Chapter 6. Since the multi-bin method uses the full $\mathrm{M_T}$ range, it is sensitive to the distributions of the events as a function of $\mathrm{M_T}$ and thus sensitive to the shape of the signal. Multiple bins can be considered into the limit calculation by multiplying the different probabilities in Equation 7.4, resulting in,

$$0.95 = \int_{-\infty}^{\mathrm{S_{up}}} \prod_{\mathrm{i}} \mathrm{P_i}(\mathrm{s}|\mathrm{N}) \tag{7.9}$$

Chapter 8

Results and Interpretations

8.1 Exclusion limit on an SSM W′ boson

The search for an SSM W′ boson yields limits on the cross section times branching fraction for the electron and muon channels. The multi-bin method is used for determinating the 95% CL upper cross section limits, as shown Figure 8.1 as a function of W′ mass. The PDF uncertainties are shown as a thin band around the NNLO cross section. The central value of the theoretical cross section times branching fraction is used for deriving the mass limit. With the 35.9 fb^{-1} of 2016 data, W′ masses below 4.9 TeV (expected limit is 5.0 TeV) and 4.9 TeV (expected 4.9 TeV) are now excluded in the electron and muon channel, respectively.
After combining both electron and muon channels, which corresponds to doubling the statistics, the exclusion limit increases to 5.2 TeV (expected 5.2 TeV), as shown in Figure 8.2 (left). This result is a significant improvement over the 2015 result of 3.6 TeV and 3.9 TeV in the electron and muon channels, respectively [12]. For high masses (around 5 TeV and beyond), the limit becomes less stringent because of the increasing fraction of off-shell production and also of the lack of data gives dominant effect in the exclusion reach. The one and two sigma bands in the electron channel represent the systematic uncertainties as described in Section6. Also shown in Figure 8.1 are theoretical cross sections for a number of interpretations. For the benchmark SSM W′, the displayed NNLO theoretical cross section represents the specific channel (including the Branching fraction to electron or muon) with the corresponding PDF uncertainty (shaded) band. In addition, the LO cross section for the SSM model is shown. For the split-UED model NNLO cross sections are displayed for two two extreme values of the bulk mass parameter μ corresponding to a minimal μ=0.05 TeV (boson mass limit of 2.4 TeV) and a maximal μ=10 TeV) (boson mass limit of 5.6 TeV).

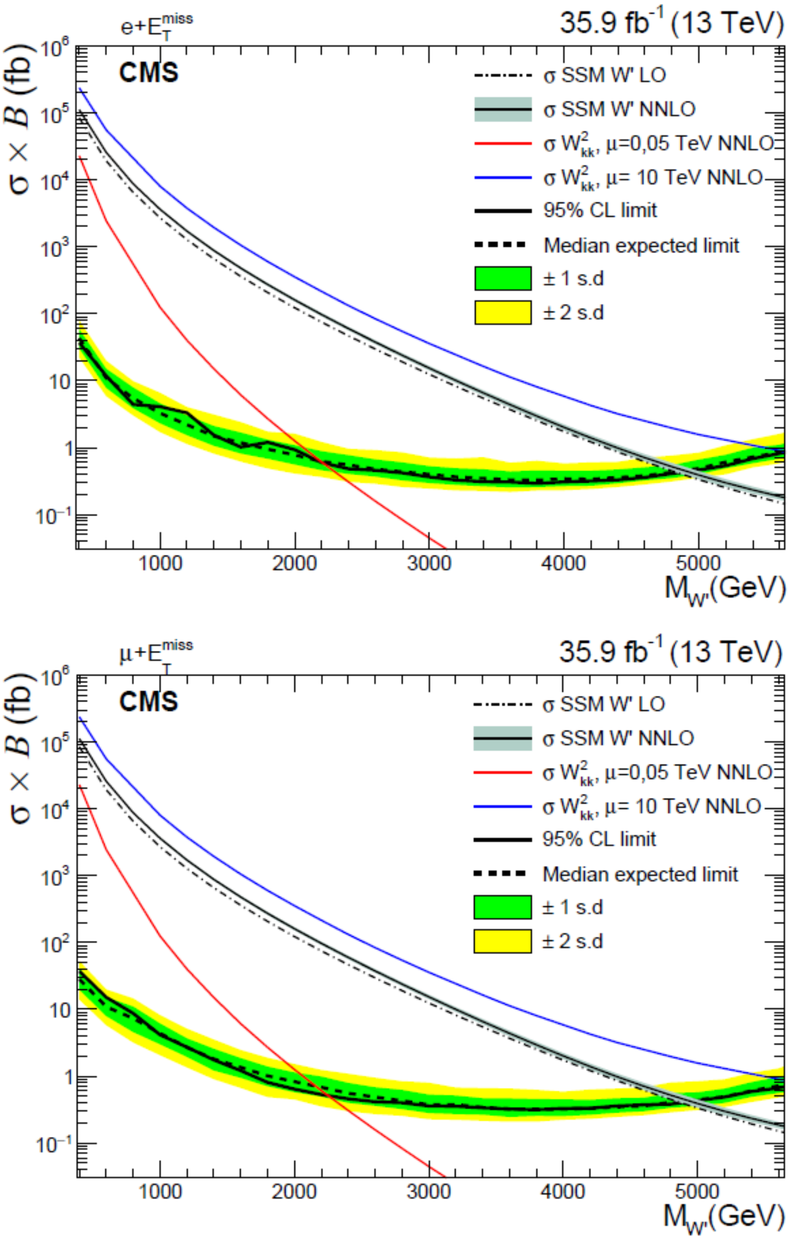

Figure 8.1: Expected (dashed line) and observed (solid line) 95% CL limits in the SSM W′ interpretation for the electron (top) and muon (bottom) channels. The shaded bands indicate the 1σ and 2σ uncertainty bands. Also shown are theoretical cross sections for the SSM benchmark model (black with grey band for the PDF uncertainties) and the split-UED (red and blue solid lines) interpretations.

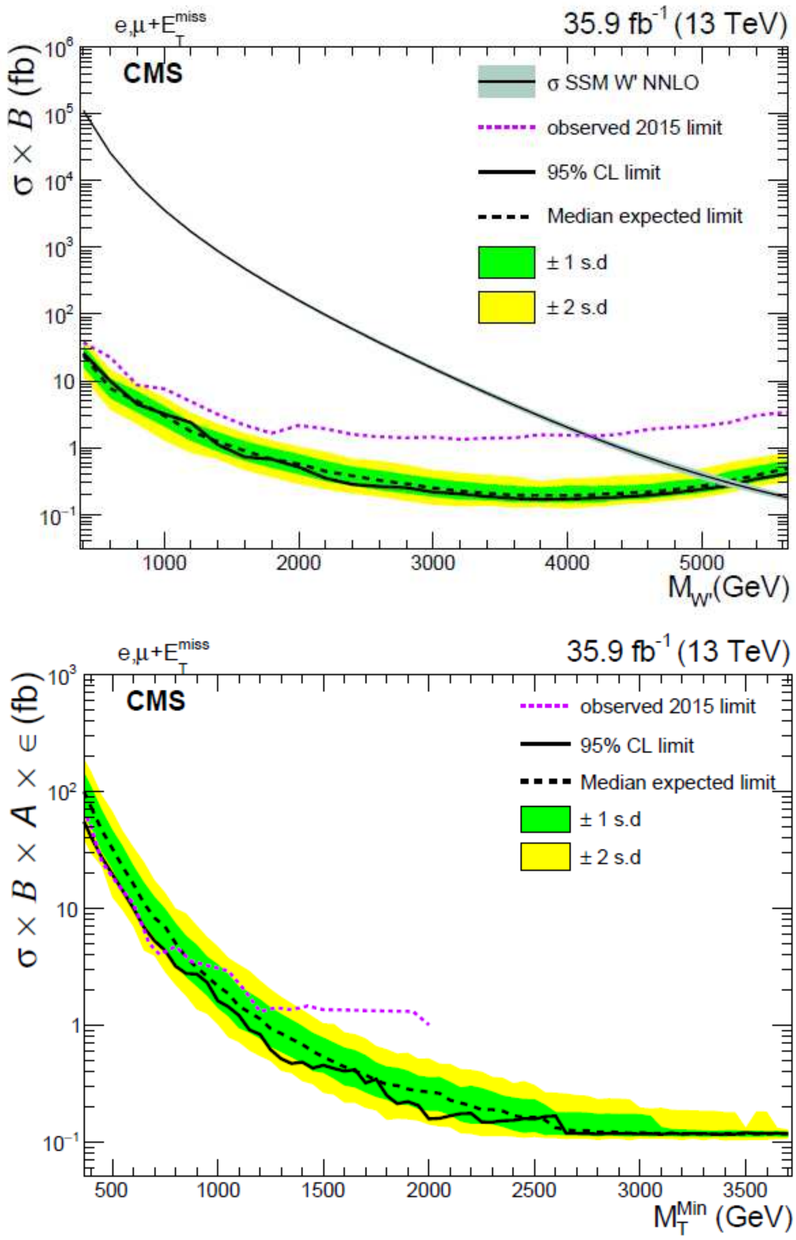

Figure 8.2: Combination of electron and muon channels in comparison to the previous exclusion limit from the analysis in 2015 [12]. The latter is shown as a dotted line for the regions in W′ mass and in cross section which were inverstigted in 2015. Expected (dashed line) and observed (solid line) limits for the 2016 result are at 95% CL and shaded bands represent the 1 and 2σ uncertainty bands. The SSM W′ interpretation result is on the top and bottom is the model-independent cross section limit. A significant gain is achieved for high masses.

8.2 Limits on coupling strength

The limit on the cross section depends on both the position of a potential excess and the width. Due to the relation between the coupling of a particle to its width, a limit can also be set on the coupling strength. As previously described in Section 4.2, the width is connected to the coupling constant as given in Equation 4.1. In order to compute the limit for different couplings, $g_{W'}/g_W \neq 1$, reweighted samples are used which take into account the proper signal width and differences in reconstructed M_T shape. For $g_{W'}/g_W = 1$ the theoretical LO cross sections from Tab. 4.4 apply. For $g_{W'}/g_W \neq 1$ the theoretical cross sections scale with the coupling strength based on the reweighted samples resulting in the blue curve in Figure 8.3. For a given mass the cross section limit as a function of the coupling strength $g_{W'}/g_W$ is determined. This is shown exemplary for the mass of 4.8 TeV in Figure 8.3. A cross section limit as a function of the coupling

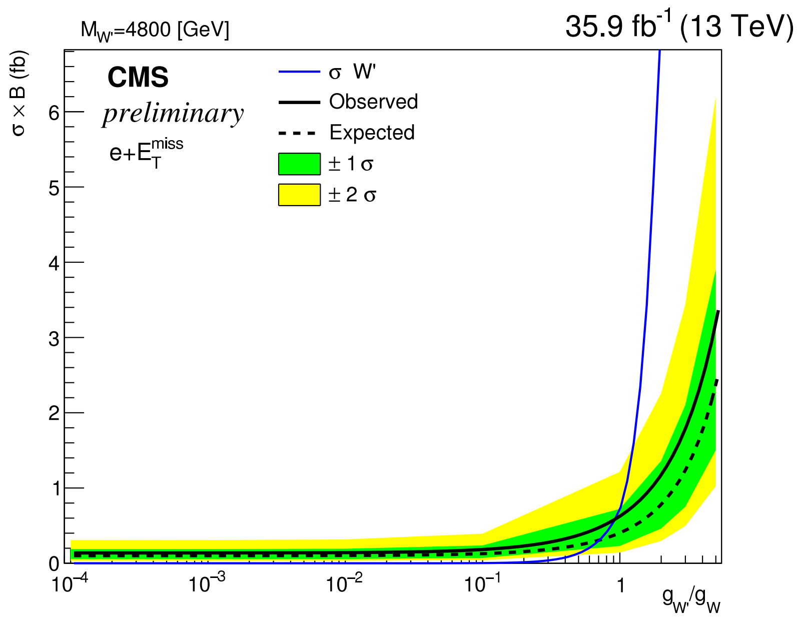

Figure 8.3: For the example of a W′ boson with 4.8 TeV, which corresponds to the single channel SSM limit, the 95% CL limits on the cross section as a function of the coupling strength for the electron channel is shown. The dashed and solid lines corresponds to the expected and observed limits respectively while the solid blue line corresponds to the cross section of the W′ boson for 4.8 TeV and the shaded bands represent the one- and two-sigma uncertainty bands.

is determined for each mass point. The experimental input derives from the final M_T distribution in Figure 8.1. The procedure is repeated for the full range of W′ masses and the corresponding intersection points provide the input for exclusion

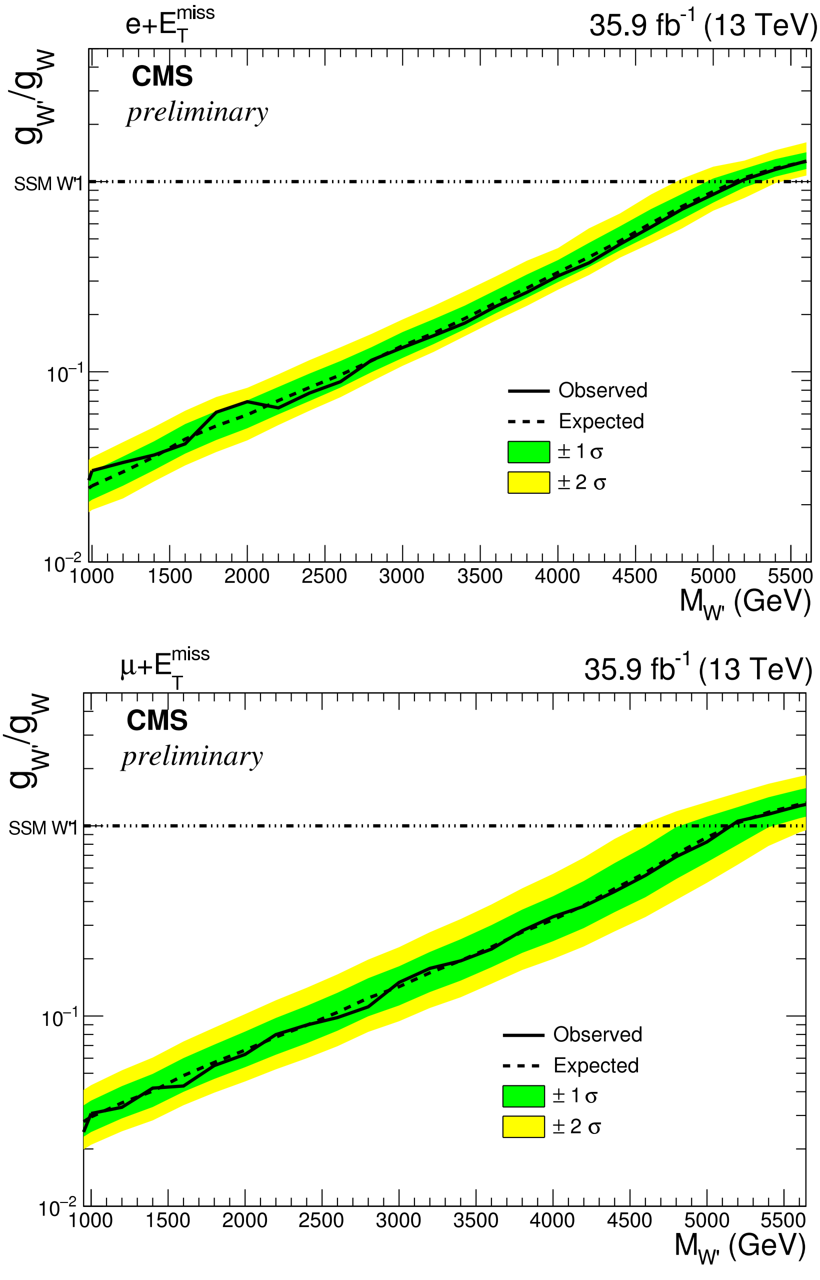

Figure 8.4: Expected (dashed line) and observed (solid line) 95% CL limits on the coupling strength $g_{W'}/g_W$ as a function of the $m_{W'}$, for the electron (top) and muon (bottom) channels. The shaded bands represent the one- and two-sigma uncertainty bands.

limit on coupling strength $g_{W'}/g_W$ as a function of the W′ masses. The excluded cross section is determined from the intersection of the theoretical cross section curve with the observed (still expected) cross section limit. For the example in Figure 8.3 this intersection is by construction around $g_{W'}/g_W = 1$.
For the limit setting procedure covering the full range of coupling strengths, the cross section limit is approximated using a second-degree polynomial, while the theoretical cross section is interpolated linearly on a logarithmic x scale. The procedure described above for the 4.8 TeV mass is repeated for the full range of W′ masses and the corresponding intersection points provide the input for exclusion limit on the coupling strength $g_{W'}/g_W$ as a function of the W′ mass, $M_{W'}$, as shown in Figure 9.1. Everything above the experimental limit is excluded. For low masses, weak couplings up to nearly 10^{-2} can be excluded.

8.3 Split-UED limits

The UED model is parameterized by the quantities R and μ, which are the radius of the extra dimension and the bulk mass parameter of the fermion field in five dimensions. The lower limits on the mass for n = 2 can be directly translated from the SSM W′ limit into bounds on the split-UED parameter space $(1/R, \mu)$, as the signal shape (see Figure 4.2) and signal efficiency are identical to the SSM W′ signal. The split-UED limits are displayed in Figure 8.5, separately for either channel as well as combined. The observed experimental limits on the radius of the extra dimension R are 2.8 TeV (electron channel) and 2.75 TeV (muons) at $\mu \approx 10$ TeV. The value of 2.9 TeV holds when combining both channels but already at $\mu \approx 4$ TeV Also here, the combination does not provide a real sensitivity gain and stays at 2.9 TeV.

In 8 TeV result [11], the observed limit on 1/R based on the combination of electron and muon channels corresponds to 1.8 TeV, being increased to 2.9 TeV in this analysis.

8.4 Limits on RPV SUSY

Another interpretation assumes a scalar tau as a mediator, with two couplings at the production and decay vertex, as detailed in Section 2.3.3. The couplings are defined in Figure 2.2. While λ'_{3xx} is common to either decay channel, the coupling at the decay is either λ_{231} (for $e+\nu_\mu$) or λ_{132} (for $\mu + \nu_e$). As shown in Figure 4.2 this signal has a slightly different shape, a sharper Jacobian peak and essentially no off-shell part at high mediator masses affecting the signal efficiency. In particular, at low masses the stau signal efficiency is higher. Applying the procedure from model independent approach, the fraction of events f_{M_T} is

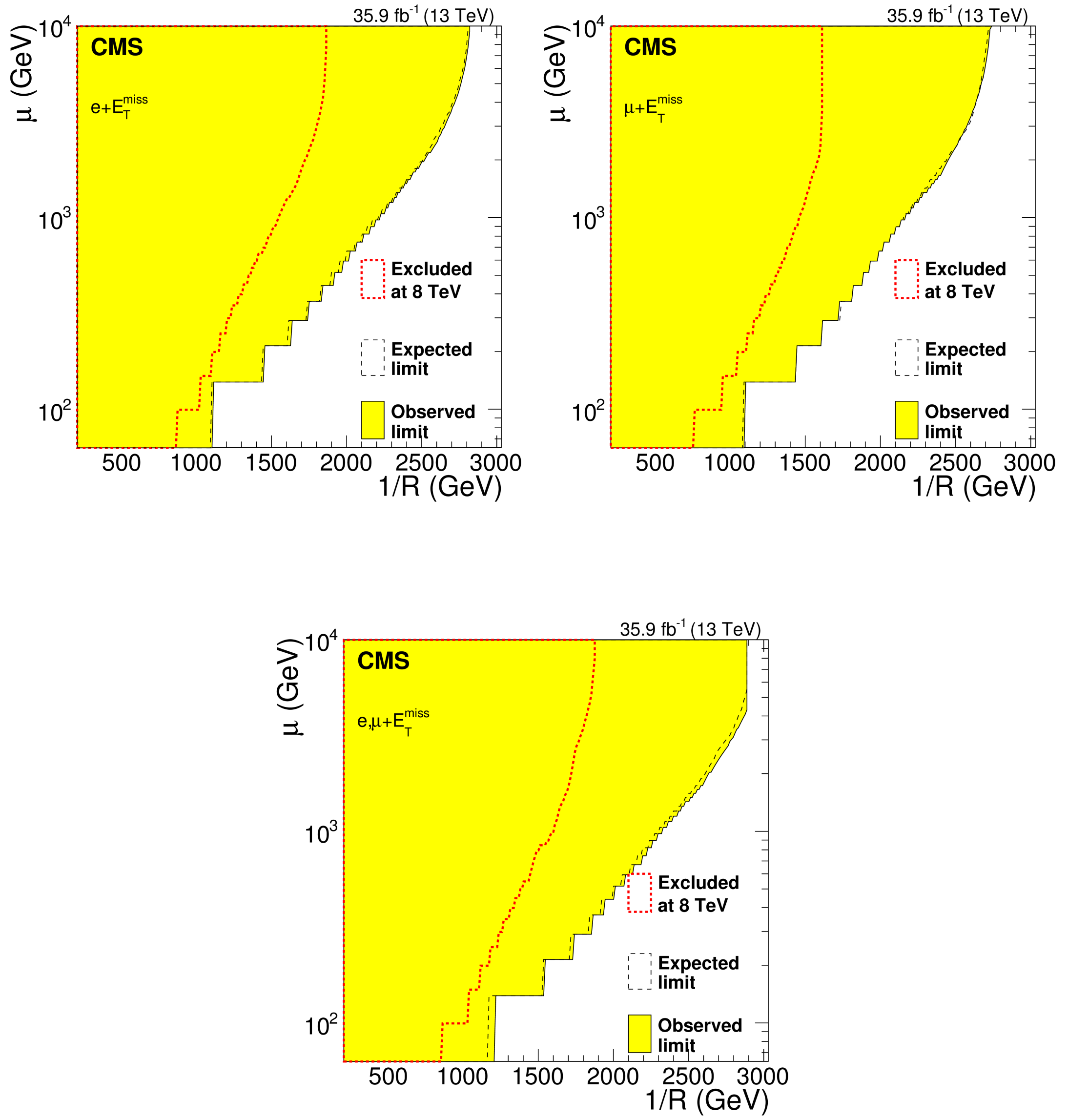

Figure 8.5: Exclusion limit in the split-UED interpretation for the n=2 case in the electron (top-left) and muon (top-right) channels, respectively. On the bottom, the combination of both channels in comparison to our Run I 8 TeV result [11]. As usual, the expected limit is depicted as a dashed line and the experimentally excluded region as a solid black line (filled as a yellow area).

determined for the stau model at generator level and a correction with respect to the SSM W′ applied. For a stau-mass of 3.6 TeV,as a function of M_T^{min}, the value for f_{M_T} is 0.99 (M_T^{min} <750 GeV), 0.90 (M_T^{min} = 1650 GeV) and 0.82 (M_T^{min} = 2100 GeV). Observed exclusion limit contour in the mediator mass and product coupling ($M_{stau} - \lambda'_{3xx}$) parameter plane as a function of a given fixed value $\lambda^{fix}_{231/132}$ are shown in Figure 8.6.

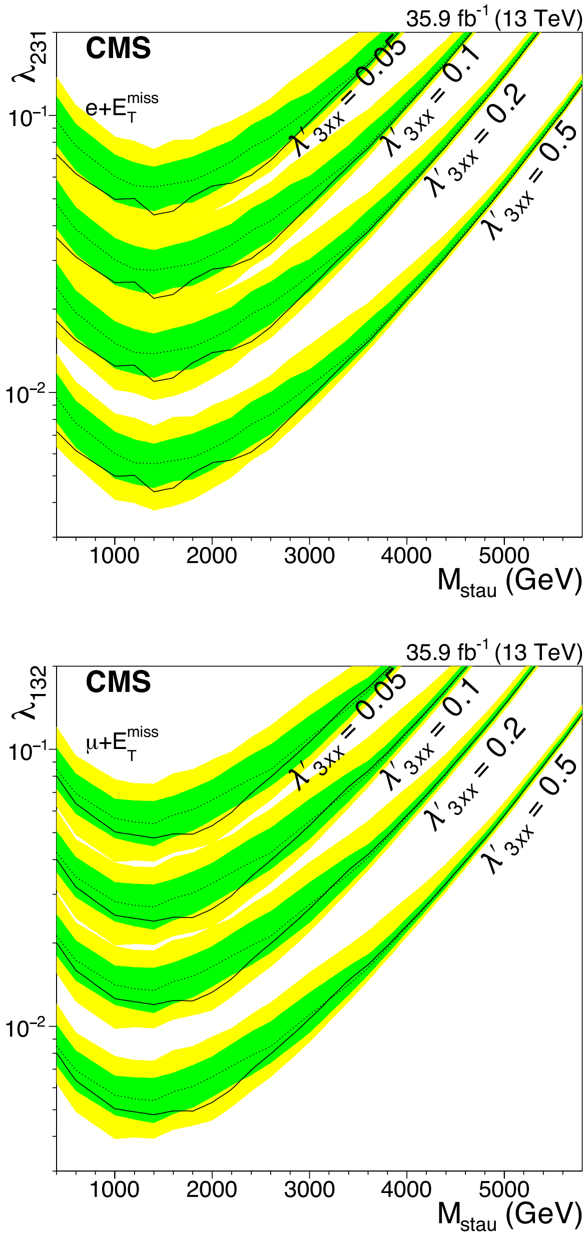

Figure 8.6: Observed exclusion limits for different couplings in the model with a scalar tau as a mediator, shown as a function of the mediator mass. The observed (expected) limit is displayed as a solid (dotted) line and the one-sigma uncertainty band in green. The couplings λ'_{3xx}, λ_{231} and λ_{132} are defined in Figure 2.2. Results are shown for the final state consisting of $e{+}\nu_{\mu}$ on the top and $\mu + \nu_e$ on the bottom.

Chapter 9

Conclusion

A search for new physics in the lepton + MET final state was performed using the full statistics of $35.9\,\mathrm{fb}^{-1}$ accumulated in 2016. Detector conditions are very similar and center of mass is identical to the data collected in 2015. The integrated luminosity has increased by about one order of magnitude with respect to 2015 and yields an increased sensitivity for high masses. No evidence for a W′ boson or other signs of new physics is observed when examining the transverse mass distributions in the electron and muon channels. Subsequently, the exclusion limits for a SSM-like W′ increased from 3.6 (3.9) TeV in 2015 to 4.9 (4.8) TeV with the 2016 statistics in the individual electron(muon) channels. A combination of both channels increases the limit further to 5.2 TeV.
Also the coupling strength is examined which has a direct impact on the cross section. For W′ masses around 1 TeV couplings down to nearly 10^{-2} are excluded. Interpretations in a number of other models is performed. The split UED model is parametrized by the bulk mass parameter μ and the radius of the extra dimension R. The latter can constrainted by this analysis to be above 2.9 TeV. In a SUSY model with R-parity violation, a scalar tau could act as a mediator and decay flavor violating into either $\mathrm{e}+\nu_{\mu}$ or $\mu+\nu_{\mathrm{e}}$. For different coupling strengths of $\lambda'_{3\mathrm{xx}}$ at the production vertex, limits on the coupling strengths at the decay vertex as a function of the mediator mass can derived. All results are summarized in Table 9.1.
The LHC experiment is expected to work continuously for next decades so-called HL-LHC and CMS detector will be able to handle the challenges imposed by a further HL-LHC run with $\sqrt{\mathrm{s}} = 14$ TeV, corresponding integrated luminosity 3000 fb^{-1}. An overview of LHC and CMS upgrade plan is summarized in the Figure ??. It is crucial to prepare accurate preictions about the future sensitivity of the experiment for the new physics. More data, high luminosity era of the LHC will substantially improve the discovery range for all of these BSM models in this mono leptonic channels. For examples SSM W′ can be searched with masses greater than rougly 7 TeV. The high luminosity also gives a better

sensitivity to low-mass small coupling W′ bosons and also for many other new physics models. The HL-LHC program is very useful to exploring new physics with high energetic Mono-lepton final states and this allows CMS experiments to reaching a new frontier. If a new physics with the TeV scale of particle exists, it may be possible to clarify and discover it by the HL-LHC era.

Category	Parameter	Result (previous result)
SSM W′	$M_{W'}$ ($g_{W'} = g_W$)	$M_{W'} \leq 5.2\,\mathrm{TeV}(4.2\,\mathrm{TeV})$
SSM W′ with various $g_{W'}$	$M_{W'} \sim 1\,\mathrm{TeV}$ ($g_{W'}/g_W \neq 1,$)	$g_{W'}/g_W \geq 0.01$
split-UED W^2_{KK}	$\mu \sim 0.05$ TeV 1/R	$M_{W'} \leq 2.4\,\mathrm{TeV}$ $1/R \leq 1.4\,\mathrm{TeV}$
split-UED W^2_{KK}	$\mu \sim$ (max)10 TeV 1/R	$M_{W'} \leq 5.6\,\mathrm{TeV}$ $1/R \leq 2.9\,\mathrm{TeV}(1.8\,\mathrm{TeV})$
RPV SUSY stau	λ'_{3xx} =0.05, λ_{decay} $M_{stau} \sim 1.5\,\mathrm{TeV}$	$\lambda_{decay} \geq 0.05$
RPV SUSY stau	λ'_{3xx} =0.5, λ_{decay} $M_{stau} \sim 1.5\,\mathrm{TeV}$	$\lambda_{decay} \geq 0.005$

Table 9.1: Summary of the limit result with various model interpretations.

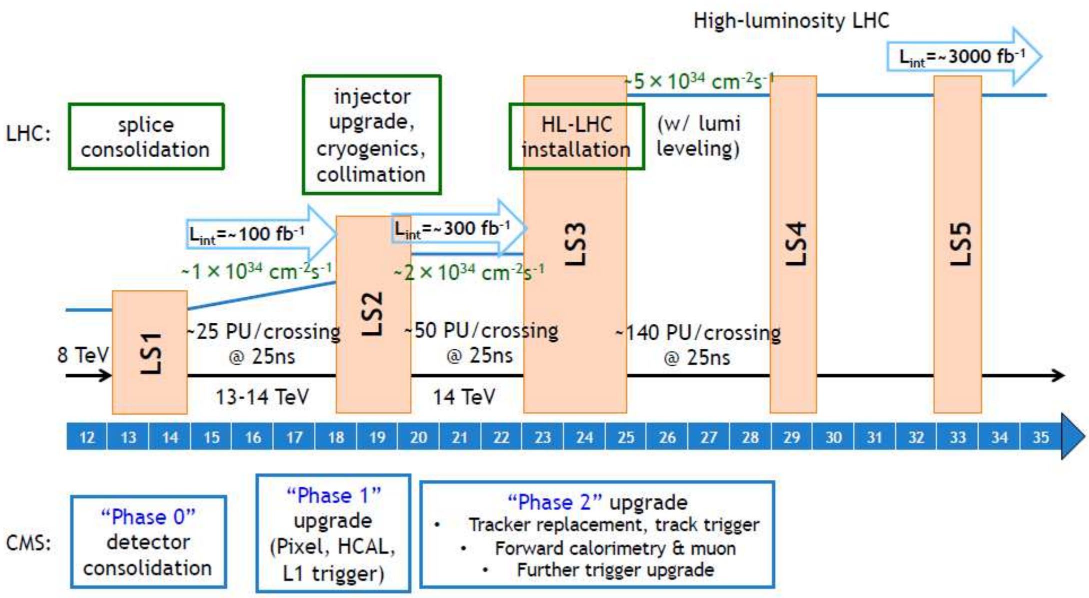

Figure 9.1: An overview of LHC and CMS upgrade plan.

Appendix A : ECAL Slew Rate Issue

In the CMS electron/photon reconstruction, the energy of certain high energy crystals was misreconstructed. This is called the "Gain Switch Issue" or the "ECAL Slew Rate Issue" and effects on high-p_T electrons/photons in data. For every crystal in the ECAL, 10 samples are read for every 25 ns and fitted their pulse to obtain the in-time energy deposit in each crystal. (See Figure 2.)

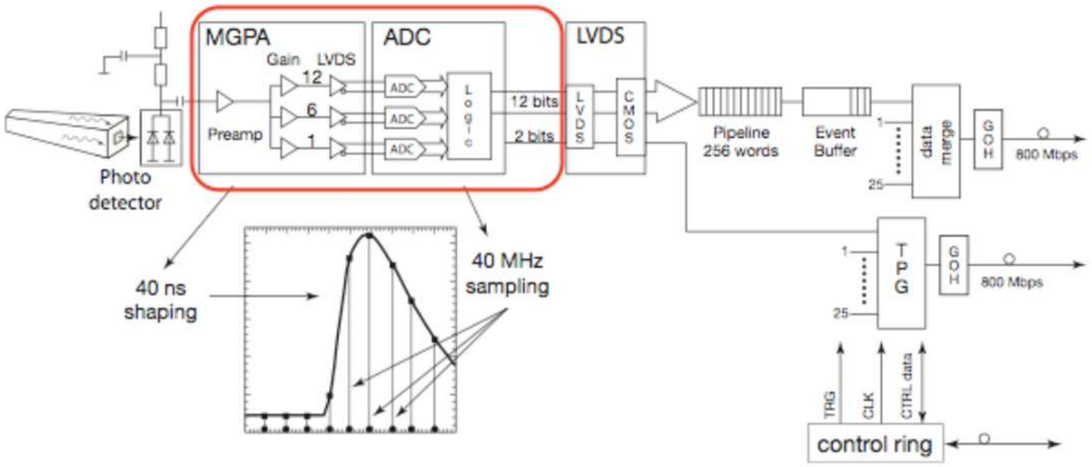

Figure 2: This grapic shows the ECAL electronics in CMS. There are three different gains (Gx12, Gx6, and Gx1) and three independent digitizations to select input with highest non saturated signal.

There are three different gains : Gx12 (0-150 GeV), Gx6 (150-300 GeV), and Gx1 (300-1890 GeV). The barrel ECAL electronics have a non-linearity at the end of a gain range (Gx1) and this causes a distortion of the pulse shape when there is the ADC switches gain during the ECAL pulse. The Multifit, new RunII algorithm for reconstructing the amplitude of the pulse, does not handle this correctly and reports a reduced energy. A gain switch from sample 4 to sample 5 reconstruct the amplitude of the pulse shape lower than it should be. This is typically up to 10% lower but for Gx12 to Gx1 switches, multifit can split the energy between different bunch crossings, with a loss of around 50%. This ECAL slew rate is not simulated in the MC and only interacts poorly with multifit in the ECAL barrel. Therefore only barrel electrons/photon having energies of a couple hundred GeV in data with a gain switch are effected (with Gx1 switches being the most problematic.).

The fixes are only intended to apply to barrel electrons/photons and crystals only replaced if they are gain switched barrel crystals. The weight method from RunI is immune to the issue so we reconstruct EcalRecHits collection where the weight reco-ed hits replace the multifit reco-ed hits. The supercluster of all barrel e/γ is reclustered from these new rec-hit collection, however, the energy and showershape of a electron/photon is only recomputed if there is gain switched crystal in the 5x5 area centred on the seed crystal.

Appendix B : Single Electron Trigger Study

Trigger condition has changed several times in 2016 data taking periods. In this appendix, to check the performance of high-p_T single electron trigger during 2016 RunII, the efficiencies have been measured from early `PromptReco` Data and early MC samples. According to 3 different conditions in electron Trigger, we divided 3 parts (Period B, Period C to F and Period G) to check the performance. The detail of changes in EG Trigger environment is covered in Table 9. In Period B, (this is the baseline for the early trigger condition) there is inefficiency in high p_T electrons. In Period C-F, lower E_T SingleJet seeding and new SingleTau seeding are implemented and H/E cut is relaxed. These fixes resolve a loss of L1 EG efficiency at high p_T arising out of tight H/E criteria which was caused by saturation of ECAL trigger tower at ET 127.5 GeV but there is an another issue of strip dynamic inefficiency so-called 'HIP (Heavy Ionizing Particle) effect' which affected tracking efficiency. In Period G, the HIP problem is also solved.

we estimate data trigger efficiency using an orthogonal (unbiased) SingleMuon PromptReco data. The trigger efficiency for a HEEP passed isolated electron having fired the reference paths(HLT_Mu or HLT_TkMu) to pass the signal HLT for barrel and endcap are measured for each of the three periods 3. We check that the inefficiencies in high p_T electron mitigated as the problems are fixed. The MC trigger efficiency is measured by ZToEE re-HLT Spring16 MC samples. The re-HLT MC is emulated L1+HLT menu which is compatible with Period B (Run 274954) setup. One finds the efficiency in Figure 4 which indicates L1 trigger efficiency lose about 5% in the p_T region between 0.5 and 2TeV and also the HLT efficiency is about 10% reduced for p_T higher than 0.5TeV. The measured efficiencies in each period are listed in Table 3. These efficiencies are applied to the simulated background samples in the analysis of the electron channel.

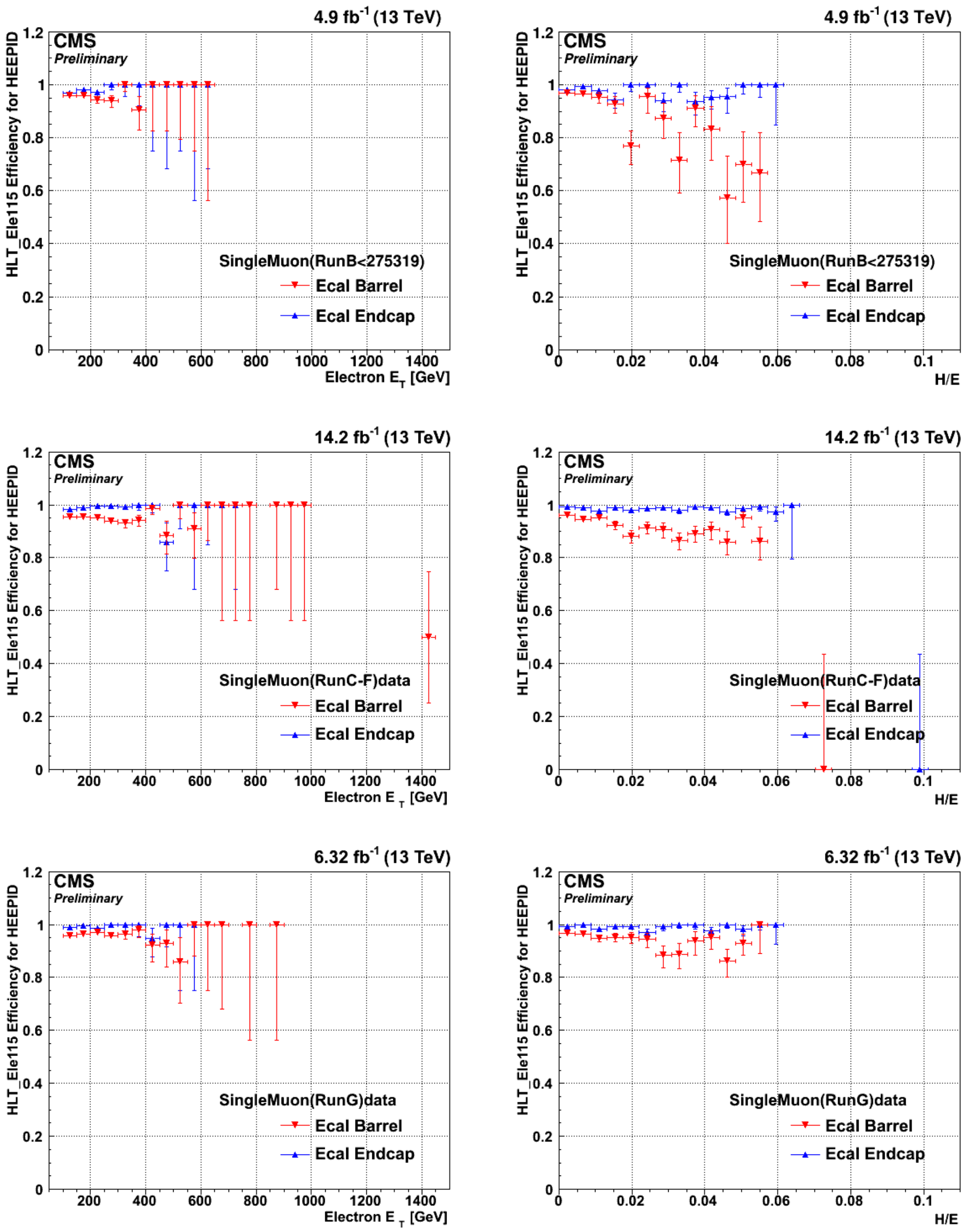

Figure 3: The data trigger efficiency of a HEEP passing electron as a function of p_T(Left) and H/E(Right) for each period. From top, middle to bottom the used periods are RunB $<$ 275319, RunC-F and RunG (PromptReco). The red points indicate ecal barrel and blue points indicates endcap.

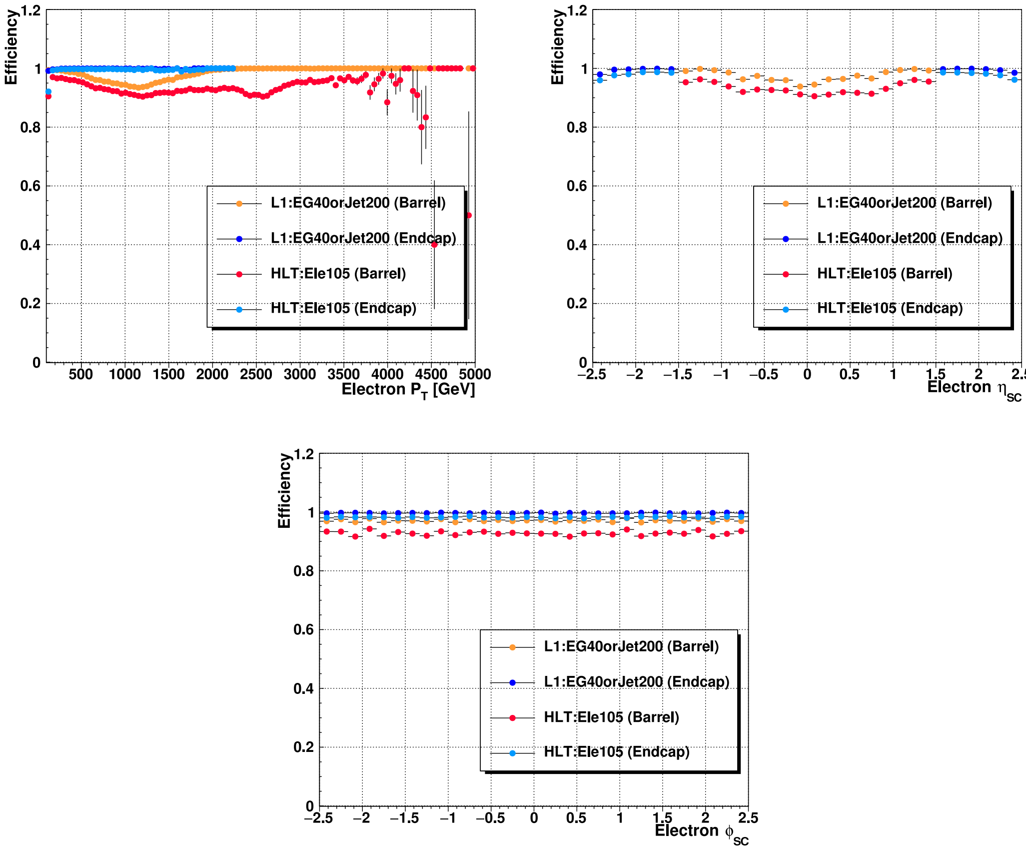

Figure 4: The efficiency for a generated electron passing HEEP and passing L1 Filter (L1_SingleEG40 OR L1_SingleJet200, Orange) and also for passing our HLT path (HLT_Ele105(or 115)_CaloIdVT_GsfTrkIdT, Red) as a function of p_T (top left plot), η_{SC}(top right plot) and ϕ_{SC} (bottom plot). The HLT efficiencies with regards to different p_T bins for ecal barrel and endcap are described in the Table 3.

Run Period	Run range	Average PU	Description (HLT version)
B	273158-274442	PU 19	Baseline (v1)
	274954-275066	PU 19	Tracking change, updates H/E cut in pixel match, reHLT MC (v2)
	275067-275311	PU 20	Increase maxEt for jet seeding(v3)
C,D	275319-276834	PU 21	Tracking updates, Reduce minEt for jet seeding, Add tau seeding(v4)
E	276870-278240	PU 24	Seed addition, Re-enabling back EE angular cuts (v5)
F,G	278273-280385	PU 24	New tunes for WP, HIP mitigation updates (v6)
H	281613	PU 25	(v7)
	281639-283059	PU 25	Method2 H/E, bugfix H/E rhoCorr, tracking change

Table 2: Trigger condition has changed many times in 2016 data taking periods. The detail of updates in EG Trigger environment is described with corresponding run time periods. Note that, trigger menu version in reHLT MC generation is v2.

electron E_T range(GeV)	Barrel(abs(η_{SC}) < 1.4442) MC(reHLT)	Period 1(Run B)	Period 2(RunC-F)	Period 3(RunG)
100-200	0.947 ± 0.003	$0.960^{+0.004}_{-0.005}$	0.953 ± 0.002	0.961 ± 0.003
200-300	0.967 ± 0.001	$0.943^{+0.010}_{-0.011}$	$0.947^{+0.004}_{-0.005}$	0.966 ± 0.005
300-400	0.962 ± 0.001	$0.970^{+0.017}_{-0.026}$	$0.934^{+0.012}_{-0.013}$	$0.968^{+0.011}_{-0.015}$
400-500	0.958 ± 0.001	1 ± 0.099	$0.957^{+0.018}_{-0.025}$	$0.925^{+0.035}_{-0.049}$
500-600	0.949 ± 0.001	1 ± 0.134	$0.969^{+0.022}_{-0.043}$	$0.933^{+0.047}_{-0.085}$
600-700	0.935 ± 0.001	1 ± 0.437	1 ± 0.120	1 ± 0.249
700-800	0.932 ± 0.001		1.000 ± 0.318	1.000 ± 0.437
800-900	0.925 ± 0.001		1.000 ± 0.318	1.000 ± 0.437
900-1000	0.918 ± 0.002		1.000 ± 0.437	
1000-1100	0.915 ± 0.002		1.000 ± 0.437	
1100-1500	0.909 ± 0.002		0.500 ± 0.248	
Global bin	0.928 ± 0.001	0.958 ± 0.019	0.952 ± 0.008	0.962 ± 0.012
E_T range(GeV)	Endcap (1.566 <abs(η_{SC}) < 2.5)			
100-200	0.964 ± 0.002	$0.976^{+0.005}_{-0.006}$	0.986 ± 0.002	0.993 ± 0.002
200-300	0.996 ± 0.001	$0.980^{+0.009}_{-0.012}$	0.996 ± 0.002	$0.991^{+0.003}_{-0.005}$
300-400	0.997 ± 0.000	1 ± 0.030	$0.995^{+0.004}_{-0.008}$	1 ± 0.015
400-500	0.998 ± 0.000	1 ± 0.174	$0.959^{+0.023}_{-0.036}$	$0.968^{+0.023}_{-0.045}$
500-600	0.997 ± 0.000	1 ± 0.205	1 ± 0.079	1 ± 0.151
600-700	0.997 ± 0.000	1 ± 0.318	1 ± 0.134	
700-800	0.997 ± 0.001		1.000 ± 0.318	
800-900	0.998 ± 0.000			
900-1000	0.997 ± 0.001			
1000-1100	0.997 ± 0.001			
1100-1500	0.996 ± 0.001			
Global bin	0.982 ± 0.003	0.978 ± 0.030	0.988 ± 0.014	0.992 ± 0.020

Table 3: HLT_Ele115_CaloIdVT_GsfTrkIdT efficiency for a HEEP ID passed electron calculated with regards to different run periods and various p_T bins for barrel and endcap.

Bibliography

[1] G. Arnison et al. Experimental Observation of Isolated Large Transverse Energy Electrons with Associated Missing Energy at s**(1/2) = 540-GeV. *Physics Letters B*, 122:103–116, 1983. url https://doi.org/10.1016/0370-2693(83)91177-2.

[2] G. Arnison et al. Experimental Observation of Lepton Pairs of Invariant Mass Around 95-GeV/c**2 at the CERN SPS Collider. *Physics Letters B*, 126:398–410, 1983. url https://doi.org/10.1016/0370-2693(83)90188-0.

[3] F. Abe et al. Observation of top quark production in $\bar{p}p$ collisions. *Phys. Rev. Lett.*, 74:2626–2631, 1995. url https://link.aps.org/doi/10.1103/PhysRevLett.74.2626.

[4] S. Abachi et al. Observation of the top quark. *Phys. Rev. Lett.*, 74:2632–2637, 1995. url https://link.aps.org/doi/10.1103/PhysRevLett.74.2626.

[5] K. Kodama et al. Observation of tau neutrino interactions. *Physics Letters B*, 504(3):218 – 224, 2001. url http://www.sciencedirect.com/science/article/pii/S0370269301003070.

[6] S. Chatrchyan et al. Observation of a new boson at a mass of 125 gev with the cms experiment at the lhc. *Physics Letters B*, 716(1):30 – 61, 2012. url http://www.sciencedirect.com/science/article/pii/S0370269312008581.

[7] G. Aad et al. Observation of a new particle in the search for the standard model higgs boson with the atlas detector at the lhc. *Physics Letters B*, 716(1):1 – 29, 2012. url http://www.sciencedirect.com/science/article/pii/S037026931200857X.

[8] V. M. Abazov et al. Search for w′ bosons decaying to an electron and a neutrino with the d0 detector. *Phys. Rev. Lett.*, 100:031804, Jan 2008. url https://link.aps.org/doi/10.1103/PhysRevLett.100.031804.

[9] T. Aaltonen et al. Search for a new heavy gauge boson w′ with event signature electron+missing transverse energy in $p\bar{p}$ collisions at $\sqrt{s} = 1.96$TeV. *Phys. Rev. D*, 83:031102, Feb 2011. url https://link.aps.org/doi/10.1103/PhysRevD.83.031102.

[10] S. Chatrchyan et al. Search for leptonic decays of w′ bosons in pp collisions at $\sqrt{s} = 7$ TeV. *Journal of High Energy Physics*, 2012(8):23, Aug 2012. url https://doi.org/10.1007/JHEP08(2012)023.

[11] Vardan Khachatryan et al. Search for physics beyond the standard model in final states with a lepton and missing transverse energy in proton-proton collisions at $\sqrt{s} = 8$TeV. *Phys. Rev.*, D91(9):092005, 2015. url https://doi.org/10.1103/PhysRevD.91.092005.

[12] Search for heavy gauge w′ bosons in events with an energetic lepton and large missing transverse momentum at $\sqrt{s}$=13 TeV. *Physics Letters B*, 770(Supplement C):278 – 301, 2017. url http://www.sciencedirect.com/science/article/pii/S0370269317303179.

[13] J. Bouchami et al. Atlas search for a heavy gauge boson decaying to a charged lepton and a neutrino in pp collisions at $\sqrt{s} = 7$ tev. *The European Physical Journal C*, 72(12):2241, Dec 2012. url https://doi.org/10.1140/epjc/s10052-012-2241-5.

[14] Georges Aad et al. Search for new particles in events with one lepton and missing transverse momentum in *pp* collisions at $\sqrt{s} = 8$ TeV with the ATLAS detector. *Journal of High Energy Physics*, 2014(9):37, Sep 2014. url https://doi.org/10.1007/JHEP09(2014)037.

[15] Morad Aaboud et al. Search for a new heavy gauge boson resonance decaying into a lepton and missing transverse momentum in 36 fb^{-1} of *pp* collisions at $\sqrt{s} = 13$ TeV with the ATLAS experiment. 2017. url https://arxiv.org/abs/1706.04786.

[16] Sheldon L. Glashow. Partial-symmetries of weak interactions. *Nuclear Physics*, 22(4):579 – 588, 1961. url http://www.sciencedirect.com/science/article/pii/0029558261904692.

[17] A. Salam and J. C. Ward. Electromagnetic and weak interactions. *Physics Letters*, 13:168–171, November 1964. url http://doi.org/10.1016/0031-9163(64)90711-5.

[18] Steven Weinberg. A model of leptons. *Phys. Rev. Lett.*, 19:1264–1266, Nov 1967. url https://link.aps.org/doi/10.1103/PhysRevLett.19.1264.

[19] S. L. Glashow, J. Iliopoulos, and L. Maiani. Weak Interactions with Lepton-Hadron Symmetry. *Physics Review D*, 2:1285–1292, 1970. url http://doi.org/10.1103/PhysRevD.2.1285.

[20] F. Halzen and A. D. Martin. *Quarks and leptons : an introductory course in modern particle physics*. 1984. url http://adsabs.harvard.edu/abs/1984qlic.book.....H.

[21] C. Patrignani et al. Review of Particle Physics. *Chin. Phys.*, C40(10):100001, 2016. url https://doi.org/10.1088/1674-1137/40/10/100001.

[22] A. Einstein. ber einen die erzeugung und verwandlung des lichtes betreffenden heuristischen gesichtspunkt. *Annalen der Physik*, 322(6):132–148, 1905. url http://dx.doi.org/10.1002/andp.19053220607.

[23] C. Berger et al. Evidence for gluon bremsstrahlung in e^+e^- annihilations at high energies. *Physics Letters B*, 86:418–425, October 1979. url http://adsabs.harvard.edu/abs/1979PhLB...86..418B.

[24] C. Berger et al. Discovery of Three-Jet Events and a Test of Quantum Chromodynamics at PETRA. *Physical Review Letters*, 43:830–833, September 1979. url http://adsabs.harvard.edu/abs/1979PhRvL..43..830B.

[25] Timo van Ritbergen and Robin G. Stuart. On the precise determination of the fermi coupling constant from the muon lifetime. *Nuclear Physics B*, 564(3):343 – 390, 2000. url http://www.sciencedirect.com/science/article/pii/S0550321399005726.

[26] Georges Aad et al. Combined measurement of the higgs boson mass in pp collisions at $\sqrt{s} = 7$ and 8 tev with the atlas and cms experiments. *Phys. Rev. Lett.*, 114:191803, 2015. url https://journals.aps.org/prl/pdf/10.1103/PhysRevLett.114.191803.

[27] Csaba Csaki and Philip Tanedo. Beyond the Standard Model. In *Proceedings, 2013 European School of High-Energy Physics (ESHEP 2013): Paradfurdo, Hungary, June 5-18, 2013*, pages 169–268, 2015. url https://inspirehep.net/record/1422131/files/arXiv:1602.04228.pdf.

[28] R. Rosenfeld. Physics Beyond the Standard Model. In *Proceedings, 8th CERN?Latin-American School of High-Energy Physics (CLASHEP2015): Ibarra, Ecuador, March 05-17, 2015*, pages 159–164, 2016. url https://inspirehep.net/record/1614174/files/arXiv:1708.00800.pdf.

[29] Freeman Dyson. Is a graviton detectable? *Int. J. Mod. Phys.*, A28:1330041, 2013. url http://www.worldscientific.com/doi/abs/10.1142/S0217751X1330041X.

[30] S.R Choudhury et al. Probing large distance higher dimensional gravity from lensing data. *Astroparticle Physics*, 21(5):559 – 563, 2004. url http://www.sciencedirect.com/science/article/pii/S0927650504000696.

[31] B. P. Abbott et al. Observation of Gravitational Waves from a Binary Black Hole Merger. *Phys. Rev. Lett.*, 116(6):061102, 2016. url https://inspirehep.net/record/1421100/files/openaccess_PhysRevLett.116.061102.pdf.

[32] Gianfranco Bertone, Dan Hooper, and Joseph Silk. Particle dark matter: evidence, candidates and constraints. *Physics Reports*, 405(5):279 – 390, 2005. url http://www.sciencedirect.com/science/article/pii/S0370157304003515.

[33] N. Aghanim P. A. R. Ade et al. Planck 2015 results - xiii. cosmological parameters. *Astronomy Astrophysics*, 594(A13), 2015. url https://www.aanda.org/articles/aa/pdf/2016/10/aa25830-15.pdf.

[34] Q. R. Ahmad et al. Measurement of the rate of $\nu_e + d \rightarrow p + p + e^-$ interactions produced by ^8b solar neutrinos at the sudbury neutrino observatory. *Phys. Rev. Lett.*, 87:071301, Jul 2001. url https://link.aps.org/doi/10.1103/PhysRevLett.87.071301.

[35] Y. Fukuda, T. Hayakawa, et al. Evidence for oscillation of atmospheric neutrinos. *Phys. Rev. Lett.*, 81:1562–1567, Aug 1998. url https://link.aps.org/doi/10.1103/PhysRevLett.81.1562.

[36] J. K. Ahn et al. Observation of reactor electron antineutrinos disappearance in the reno experiment. *Phys. Rev. Lett.*, 108:191802, May 2012. url https://link.aps.org/doi/10.1103/PhysRevLett.108.191802.

[37] F. P. An et al. Observation of electron-antineutrino disappearance at daya bay. *Phys. Rev. Lett.*, 108:171803, Apr 2012. url https://link.aps.org/doi/10.1103/PhysRevLett.108.171803.

[38] N. Agafonova et al. Observation of a first tau neutrino candidate event in the opera experiment in the cngs beam. *Physics Letters B*, 691(3):138 – 145, 2010. url http://www.sciencedirect.com/science/article/pii/S0370269310007537.

[39] Randolf Pohl et al. Muonic hydrogen and the proton radius puzzle. *Annual Review of Nuclear and Particle Science*, 63(1):175–204, 2013. url https://doi.org/10.1146/annurev-nucl-102212-170627.

[40] Carl E. Carlson. The proton radius puzzle. *Progress in Particle and Nuclear Physics*, 82:59 – 77, 2015. url http://www.sciencedirect.com/science/article/pii/S0146641015000034.

[41] Thomas Blum et al. The Muon (g-2) Theory Value: Present and Future. 2013. url https://arxiv.org/abs/1311.2198.

[42] D. Giusti et al. Strange and charm HVP contributions to the muon $(g-2)$ including QED corrections with twisted-mass fermions. 2017. url https://arxiv.org/abs/1707.03019.

[43] Ken Hsieh et al. Global Analysis of General SU(2) x SU(2) x U(1) Models with Precision Data. *Phys. Rev.*, D82:035011, 2010. url https://doi.org/10.1103/PhysRevD.82.035011.

[44] Tommi Alanne et al. LHC Data and Aspects of New Physics. *JHEP*, 01:041, 2014. url https://doi.org/10.1007/JHEP01(2014)041.

[45] Qing-Hong Cao et al. Discovery and Identification of W' and Z' in SU(2) x SU(2) x U(1) Models at the LHC. *Phys. Rev.*, D86:095010, 2012. url https://doi.org/10.1103/PhysRevD.86.095010.

[46] R. N. Mohapatra and J. C. Pati. "natural" left-right symmetry. *Phys. Rev. D*, 11:2558–2561, May 1975. url https://link.aps.org/doi/10.1103/PhysRevD.11.2558.

[47] Rabindra N. Mohapatra and Jogesh C. Pati. Left-right gauge symmetry and an "isoconjugate" model of CP violation. *Phys. Rev. D*, 11:566–571, Feb 1975. url https://link.aps.org/doi/10.1103/PhysRevD.11.566.

[48] Rabindra N. Mohapatra et al. Neutrino masses and mixings in gauge models with spontaneous parity violation. *Phys. Rev. D*, 23:165–180, Jan 1981. url https://link.aps.org/doi/10.1103/PhysRevD.23.165.

[49] Jogesh C. Pati and Abdus Salam. Is baryon number conserved? *Phys. Rev. Lett.*, 31:661–664, Sep 1973. url https://link.aps.org/doi/10.1103/PhysRevLett.31.661.

[50] V. Barger, W. Y. Keung, and Ernest Ma. Gauge model with light w and z bosons. *Phys. Rev. D*, 22:727–737, Aug 1980. url https://link.aps.org/doi/10.1103/PhysRevD.22.727.

[51] V. Barger, W. Y. Keung, and Ernest Ma. Doubling of weak gauge bosons in an extension of the standard model. *Phys. Rev. Lett.*, 44:1169–1172, May 1980. url https://link.aps.org/doi/10.1103/PhysRevLett.44.1169.

[52] R. Sekhar Chivukula et al. A three site higgsless model. *Phys. Rev. D*, 74:075011, Oct 2006. url https://link.aps.org/doi/10.1103/PhysRevD.74.075011.

[53] Howard Georgi et al. The un-unified standard model. *Nuclear Physics B*, 331(3):541 – 555, 1990. url http://www.sciencedirect.com/science/article/pii/055032139090083P.

[54] Xiao-yuan Li and Ernest Ma. Gauge model of generation nonuniversality. *Phys. Rev. Lett.*, 47:1788–1791, Dec 1981. url https://link.aps.org/doi/10.1103/PhysRevLett.47.1788.

[55] Ehab Malkawi, Tim Tait, and C.-P. Yuan. A model of strong flavor dynamics for the top quark. *Physics Letters B*, 385(1):304 – 310, 1996. url http://www.sciencedirect.com/science/article/pii/0370269396008593.

[56] G. Altarelli et al. Searching for new heavy vector bosons in $p\bar{p}$ colliders. *Zeitschrift für Physik C Particles and Fields*, 45(1):109–121, Mar 1989. url https://doi.org/10.1007/BF01556677.

[57] Seong Chan Park et al. Dark matter and collider phenomenology of split-ued. *Journal of High Energy Physics*, 2009(09):078, 2009. url http://stacks.iop.org/1126-6708/2009/i=09/a=078.

[58] Kyoungchul Kong, Seong Chan Park, and Thomas G. Rizzo. Collider Phenomenology with Split-UED. *JHEP*, 04:081, 2010. url https://doi.org/10.1007/JHEP04(2010)081.

[59] Thomas Appelquist et al. Bounds on universal extra dimensions. *Phys. Rev.*, D64:035002, 2001. url https://link.aps.org/doi/10.1103/PhysRevD.64.035002.

[60] I. Antoniadis. A possible new dimension at a few tev. *Physics Letters B*, 246(3):377 – 384, 1990. url http://www.sciencedirect.com/science/article/pii/037026939090617F.

[61] DongHee Kim, Youngdo Oh, and Seong Chan Park. w' at the lhc with $\sqrt{s}$ = 14 tev: Split universal extra dimension model. *Journal of the Korean Physical Society*, 67(7):1137–1141, Oct 2015. url https://doi.org/10.3938/jkps.67.1137.

[62] H. K. Dreiner and T. Stefaniak. Bounds on r-parity violation from resonant slepton production at the lhc. *Phys. Rev. D*, 86:055010, Sep 2012. url https://link.aps.org/doi/10.1103/PhysRevD.86.055010.

[63] R. Barbier, , et al. R-parity-violating supersymmetry. *Physics Reports*, 420(1):1 – 195, 2005. url http://www.sciencedirect.com/science/article/pii/S0370157305003327.

[64] Lyndon Evans and Philip Bryant. Lhc machine. *Journal of Instrumentation*, 3(08):S08001, 2008. url http://stacks.iop.org/1748-0221/3/i=08/a=S08001.

[65] Oliver S. Bruning et al. LHC Design Report Vol.1: The LHC Main Ring. 2004.

[66] LEP Design Report: Vol.2. The LEP Main Ring. 1984.

[67] The CMS Collaboration. The cms experiment at the cern lhc. *Journal of Instrumentation*, 3(08):S08004, 2008. url http://stacks.iop.org/1748-0221/3/i=08/a=S08004.

[68] The ATLAS Collaboration. The atlas experiment at the cern large hadron collider. *Journal of Instrumentation*, 3(08):S08003, 2008. url http://stacks.iop.org/1748-0221/3/i=08/a=S08003.

[69] The LHCb Collaboration. The lhcb detector at the lhc. *Journal of Instrumentation*, 3(08):S08005, 2008. url http://stacks.iop.org/1748-0221/3/i=08/a=S08005.

[70] The ALICE Collaboration. The alice experiment at the cern lhc. *Journal of Instrumentation*, 3(08):S08002, 2008. url http://stacks.iop.org/1748-0221/3/i=08/a=S08002.

[71] The LHCf Collaboration. The lhcf detector at the cern large hadron collider. *Journal of Instrumentation*, 3(08):S08006, 2008. url http://stacks.iop.org/1748-0221/3/i=08/a=S08006.

[72] The TOTEM Collaboration. The totem experiment at the cern large hadron collider. *Journal of Instrumentation*, 3(08):S08007, 2008. url http://stacks.iop.org/1748-0221/3/i=08/a=S08007.

[73] James Pinfold et al. Technical Design Report of the MoEDAL Experiment. 2009.

[74] Long term lhc schedule. url https://lhc-commissioning.web.cern.ch/lhc-commissioning/schedule/LHC-long-term.htm.

[75] Lhc programme coordination (lpc) website. url https://lpc.web.cern.ch/lumi2.html.

[76] CMS Collaboration. CMS Luminosity Measurements for the 2016 Data Taking Period. Technical Report CMS-PAS-LUM-17-001, CERN, Geneva, 2017. url https://cds.cern.ch/record/2257069.

[77] Thomas Mc Cauley. Collisions recorded by the CMS detector on 14 Oct 2016 during the high pile-up fill. url https://cds.cern.ch/record/2231915, Nov 2016.

[78] A. D. Martin et al. Parton distributions for the lhc. *The European Physical Journal C*, 63(2):189–285, Sep 2009. url https://doi.org/10.1140/epjc/s10052-009-1072-5.

[79] Altarelli G, , et al. Qcd evolution equation for parton densities. *Scholarpedia*, 4(1):7124, 2009. url http://www.scholarpedia.org/article/QCD_evolution_equations_for_parton_densities.

[80] Peter Skands, Stefano Carrazza, and Juan Rojo. Tuning PYTHIA 8.1: the Monash 2013 Tune. *Eur. Phys. J.*, C74(8):3024, 2014. url https://doi.org/10.1140/epjc/s10052-014-3024-y.

[81] Vardan Khachatryan et al. Event generator tunes obtained from underlying event and multiparton scattering measurements. *Eur. Phys. J.*, C76(3):155, 2016. url https://doi.org/10.1140/epjc/s10052-016-3988-x.

[82] Tai Sakuma and Thomas McCauley. Detector and Event Visualization with SketchUp at the CMS Experiment. *J. Phys. Conf. Ser.*, 513:022032, 2014. url http://stacks.iop.org/1742-6596/513/i=2/a=022032.

[83] Serguei Chatrchyan et al. Description and performance of track and primary-vertex reconstruction with the CMS tracker. *JINST*, 9(10):P10009, 2014. url https:/doi.org/10.1088/1748-0221/9/10/P10009.

[84] Serguei Chatrchyan et al. CMS Tracking Performance Results from Early LHC Operation. *Eur. Phys. J.*, C70:1165–1192, 2010. url https://doi.org/10.1140/epjc/s10052-010-1491-3.

[85] Serguei Chatrchyan et al. Alignment of the CMS tracker with LHC and cosmic ray data. *JINST*, 9:P06009, 2014. url https://doi.org/10.1088/1748-0221/9/06/P06009.

[86] David Aaron Matzner Dominguez et al. CMS Technical Design Report for the Pixel Detector Upgrade. 2012.

[87] M. Lipinski. The Phase-1 upgrade of the CMS pixel detector. *JINST*, 12(07):C07009, 2017. url https://doi.org/10.1088/1748-0221/12/07/C07009.

[88] Emilio Meschi et al. Electron Reconstruction in the CMS Electromagnetic Calorimeter. Technical Report CMS-NOTE-2001-034, CERN, Geneva, Jun 2001. url http://cds.cern.ch/record/687345.

[89] Particle-Flow Event Reconstruction in CMS and Performance for Jets, Taus, and MET. 2009.

[90] P Adzic. Energy resolution of the barrel of the cms electromagnetic calorimeter. *Journal of Instrumentation*, 2(04):P04004, 2007. url http://stacks.iop.org/1748-0221/2/i=04/a=P04004.

[91] J Mans, , et al. CMS Technical Design Report for the Phase 1 Upgrade of the Hadron Calorimeter. Technical Report CERN-LHCC-2012-015. CMS-TDR-10, Sep 2012. url http://cds.cern.ch/record/1481837.

[92] S Chatrchyan, V Khachatryan, et al. Performance of the CMS Hadron Calorimeter with Cosmic Ray Muons and LHC Beam Data. *JINST*, 5(arXiv:0911.4991. CMS-CFT-09-009):T03012 . 35 p, Nov 2009. url http://cds.cern.ch/record/1223950.

[93] Giovanni Abbiendi. The CMS muon system in Run2: preparation, status and first results. *PoS*, EPS-HEP2015:237, 2015.

[94] Andres Cabrera-Mora. Status and performance of the CMS muon system in Run2. *PoS*, ICHEP2016:733, 2016.

[95] Serguei Chatrchyan et al. The performance of the CMS muon detector in proton-proton collisions at sqrt(s) = 7 TeV at the LHC. *JINST*, 8:P11002, 2013. url https://doi.org/10.1088/1748-0221/8/11/P11002.

[96] Serguei Chatrchyan et al. Performance of CMS muon reconstruction in pp collision events at $\sqrt{s} = 7$ TeV. *JINST*, 7:P10002, 2012. url https://doi.org/10.1088/1748-0221/7/10/P10002.

[97] A Tapper and Darin Acosta. CMS Technical Design Report for the Level-1 Trigger Upgrade. Technical Report CERN-LHCC-2013-011. CMS-TDR-12, Jun 2013. url https://cds.cern.ch/record/1556311.

[98] G L Bayatyan, N Grigorian, , et al. *CMS TriDAS project: Technical Design Report, Volume 1: The Trigger Systems*. Technical Design Report CMS. 2000. url https://cds.cern.ch/record/706847.

[99] M Baber, M Blake, et al. Development and testing of an upgrade to the cms level-1 calorimeter trigger. *Journal of Instrumentation*, 9(01):C01006, 2014. url http://stacks.iop.org/1748-0221/9/i=01/a=C01006.

[100] A. Zabi, F. Beaudette, et al. The cms level-1 calorimeter trigger for the lhc run ii. *Journal of Instrumentation*, 12(01):C01065, 2017. url http://stacks.iop.org/1748-0221/12/i=01/a=C01065.

[101] K Compton, S Dasu, et al. The mp7 and ctp-6: multi-hundred gbps processing boards for calorimeter trigger upgrades at cms. *Journal of Instrumentation*, 7(12):C12024, 2012. url http://stacks.iop.org/1748-0221/7/i=12/a=C12024.

[102] Imperial College London. User guide for the master processor, virtex7 mp7. url http://www.hep.ph.ic.ac.uk/mp7/documents/UserGuideForTheMP7.latest.pdf.

[103] CMS L1 Calorimeter Trigger performance in 2016 data. Jul 2016. url https://cds.cern.ch/record/2202966.

[104] A. Zabi, F. Beaudette, et al. Triggering on electrons, jets and tau leptons with the cms upgraded calorimeter trigger for the lhc run ii. *Journal of Instrumentation*, 11(02):C02008, 2016. url http://stacks.iop.org/1748-0221/11/i=02/a=C02008.

[105] M. Jeitler et al. Upgrade of the cms global muon trigger. *IEEE Transactions on Nuclear Science*, 62(3):1104–1109, June 2015. url https://doi.org/10.1109/TNS.2015.2435060.

[106] J. Fulcher et al. The new global muon trigger of the cms experiment. *IEEE Transactions on Nuclear Science*, 64(6):1467–1473, June 2017. url https://doi.org/10.1109/TNS.2017.2663442.

[107] D Acosta, G Brown, et al. The cms modular track finder boards, mtf6 and mtf7. *Journal of Instrumentation*, 8(12):C12034, 2013. url http://stacks.iop.org/1748-0221/8/i=12/a=C12034.

[108] J. Wittmann et al. The upgrade of the cms global trigger. *Journal of Instrumentation*, 11(02):C02029, 2016. url http://stacks.iop.org/1748-0221/11/i=02/a=C02029.

[109] P. Bortignon. Design and performance of the upgrade of the CMS L1 muon trigger. *Nucl. Instrum. Meth.*, A824:256–257, 2016. url https://doi.org/10.1016/j.nima.2015.11.065.

[110] L1 muon trigger performance - ICHEP16 dataset. Jul 2016. url http://cds.cern.ch/record/2202986.

[111] T. Bawej et al. The new cms daq system for run-2 of the lhc. In *2014 19th IEEE-NPSS Real Time Conference*, pages 1–1, May 2014. url https://doi.org/10.1109/RTC.2014.7097437.

[112] Torbjrn Sjstrand et al. An Introduction to PYTHIA 8.2. *Comput. Phys. Commun.*, 191:159–177, 2015. url https://doi.org/10.1016/j.cpc.2015.01.024.

[113] Richard D. Ball et al. Parton distributions with LHC data. *Nucl. Phys.*, B867:244–289, 2013. url https://doi.org/10.1016/j.nuclphysb.2012.10.003.

[114] Johan Alwall et al. MadGraph 5 : Going Beyond. *JHEP*, 06:128, 2011. url https://doi.org/10.1007/JHEP06(2011)128.

[115] Seth Quackenbush et al. W physics at the lhc with fewz 2.1. *Computer Physics Communications*, 184(1):209 – 214, 2013. url http://www.sciencedirect.com/science/article/pii/S0010465512002913.

[116] J. Alwall, , et al. The automated computation of tree-level and next-to-leading order differential cross sections, and their matching to parton shower simulations. *JHEP*, 07:079, 2014. url https://doi.org/10.1007/JHEP07(2014)079.

[117] Paolo Nason. A New method for combining NLO QCD with shower Monte Carlo algorithms. *JHEP*, 11:040, 2004. url https://doi.org/10.1088/1126-6708/2004/11/040.

[118] Stefano Frixione et al. Matching NLO QCD computations with Parton Shower simulations: the POWHEG method. *JHEP*, 11:070, 2007. url https://doi.org/10.1088/1126-6708/2007/11/070.

[119] Simone Alioli et al. A general framework for implementing NLO calculations in shower Monte Carlo programs: the POWHEG BOX. *JHEP*, 06:043, 2010. url https://doi.org/10.1007/JHEP06(2010)043.

[120] J. Alwall et al. Comparative study of various algorithms for the merging of parton showers and matrix elements in hadronic collisions. *The European Physical Journal C*, 53(3):473–500, Feb 2008. url https://doi.org/10.1140/epjc/s10052-007-0490-5.

[121] Denis Perret-Gallix. Computational particle physics for event generators and data analysis. *Journal of Physics: Conference Series*, 454(1):012051, 2013. url http://stacks.iop.org/1742-6596/454/i=1/a=012051.

[122] Sergey G. Bondarenko and Andrey A. Sapronov. NLO EW and QCD proton-proton cross section calculations with mcsanc-v1.01. *Comput. Phys. Commun.*, 184:2343–2350, 2013. url https://doi.org/10.1016/j.cpc.2013.05.010.

[123] Jon Butterworth et al. PDF4LHC recommendations for LHC Run II. *J. Phys.*, G43:023001, 2016. url https://doi.org/10.1088/0954-3899/43/2/023001.

[124] S. Baffioni et al. Electron reconstruction in CMS. *Eur. Phys. J.*, C49:1099–1116, 2007. url https://doi.org/10.1140/epjc/s10052-006-0175-5.

[125] Vardan Khachatryan et al. Performance of Electron Reconstruction and Selection with the CMS Detector in Proton-Proton Collisions at s = 8 TeV. *JINST*, 10(06):P06005, 2015. url http://stacks.iop.org/1748-0221/10/i=06/a=P06005.

[126] The CMS Collaboration. Description and performance of track and primary-vertex reconstruction with the cms tracker. *Journal of Instrumentation*, 9(10):P10009, 2014. url http://stacks.iop.org/1748-0221/9/i=10/a=P10009.

[127] Wolfgang Adam et al. Reconstruction of Electrons with the Gaussian-Sum Filter in the CMS Tracker at the LHC. 2005.

[128] R. Fruhwirth. Application of Kalman filtering to track and vertex fitting. *Nucl. Instrum. Meth.*, A262:444–450, 1987. url https://doi.org/10.1016/0168-9002(87)90887-4.

[129] CMS Collaboration. Performance of cms muon reconstruction in cosmic-ray events. *Journal of Instrumentation*, 5(03):T03022, 2010. url http://stacks.iop.org/1748-0221/5/i=03/a=T03022.

[130] Serguei Chatrchyan et al. Performance of CMS muon reconstruction in pp collision events at $\sqrt{s} = 7$ TeV. *JINST*, 7:P10002, 2012. url https://doi.org/10.1088/1748-0221/7/10/P10002.

[131] Florian Beaudette. The CMS Particle Flow Algorithm. In *Proceedings, International Conference on Calorimetry for the High Energy Frontier (CHEF 2013): Paris, France, April 22-25, 2013*, pages 295–304, 2013. url https://inspirehep.net/record/1279774/files/arXiv:1401.8155.pdf.

[132] A. M. Sirunyan et al. Particle-flow reconstruction and global event description with the cms detector. *JINST*, 12:P10003, 2017. url https://doi.org/10.1088/1748-0221/12/10/P10003.

[133] The CMS collaboration. Determination of jet energy calibration and transverse momentum resolution in cms. *Journal of Instrumentation*, 6(11):P11002, 2011. url http://stacks.iop.org/1748-0221/6/i=11/a=P11002.

[134] Muon POG. Impact of the APV fix on muon reconstruction. Aug 2016. url https://indico.cern.ch/event/546903/contributions/2218492/subcontributions/199641/attachments/1326428/1991426/Muon_TSG24Aug.pdf.

[135] W Verkerke and D Kirkby. The RooFit toolkit for data modeling. Technical Report physics/0306116, SLAC, Stanford, CA, Jun 2003. url https://cds.cern.ch/record/622147.

[136] Electron and photon performance in CMS with the full 2016 data sample. Mar 2017. url https://cds.cern.ch/record/2255497.

[137] Muon POG. Muon Identification and Isolation efficiency on full 2016 dataset. Mar 2017. url http://cds.cern.ch/record/2257968.

[138] EGM POG. Electron Efficiencies and scale factors. url https://twiki.cern.ch/twiki/bin/view/CMS/EgammaIDRecipesRun2#Electron_efficiencies_and_scale.

[139] EGM POG. HEEPv7.0 scale factor. 2 2017. url https://indico.cern.ch/event/604912/contributions/2490008/attachments/1418885/2173433/HEEP7_Moriond_GSFix_final_RW_v3.pdf.

[140] Muon POG. Status of muon efficiencies studies at high momentum. url https://indico.cern.ch/event/674258/contributions/2758840/attachments/1543279/2425639/2017.10.18_MuonEfficienciesHighP_MuonPOG_v2.pdf.

[141] Muon POG. High-pT Muon ID Efficiency and SF for Z' analysis. Oct 2017. url https://indico.cern.ch/event/667435/contributions/2740678/subcontributions/239465/attachments/1535351/2404957/IDEff_SF_NonHad_Min_20171004_v7.pdf.

[142] CMS Collaboration. Utilities for accessing pileup information for data. url https://twiki.cern.ch/twiki/bin/Viewauth/CMS/PileupJSONFileforData.

[143] Vardan Khachatryan et al. Search for heavy gauge W' boson in events with an energetic lepton and large missing transverse momentum at $\sqrt{s} = 13$ TeV. *Phys. Lett.*, B770:278–301, 2017. url https://doi.org/10.1016/j.physletb.2017.04.043.

[144] CMS Collaboration. CMS Luminosity Based on Pixel Cluster Counting - Summer 2013 Update. Technical Report CMS-PAS-LUM-13-001, CERN, Geneva, 2013.

[145] Sayipjamal Dulat et al. New parton distribution functions from a global analysis of quantum chromodynamics. *Phys. Rev.*, D93(3):033006, 2016. url https://doi.org/10.1103/PhysRevD.93.033006.

[146] Sayipjamal Dulat et al. The ct14 global analysis of quantum chromodynamics. 06 2015.

[147] L. A. Harland-Lang et al. Parton distributions in the LHC era: MMHT 2014 PDFs. *Eur. Phys. J.*, C75(5):204, 2015. url https://doi.org/10.1140/epjc/s10052-015-3397-6.

[148] J. Pumplin and others. Uncertainties of predictions from parton distribution functions. 2. The Hessian method. *Phys. Rev.*, D65:014013, 2001. url https://doi.org/10.1103/PhysRevD.65.014013.

[149] The CMS Collaboration. Energy calibration and resolution of the cms electromagnetic calorimeter in pp collisions at $\sqrt{s} = 7$ tev. *Journal of Instrumentation*, 8(09):P09009, 2013. url http://stacks.iop.org/1748-0221/8/i=09/a=P09009.

[150] Sergey Alekhin et al. The PDF4LHC Working Group Interim Report. 2011.

[151] Michiel Botje et al. The PDF4LHC Working Group Interim Recommendations. 2011.

[152] Andy Buckley et al. LHAPDF6: parton density access in the LHC precision era. *Eur. Phys. J.*, C75:132, 2015. url https://doi.org/10.1140/epjc/s10052-015-3318-8.

[153] Richard D. Ball et al. A Determination of parton distributions with faithful uncertainty estimation. *Nucl. Phys.*, B809:1–63, 2009. [Erratum: Nucl. Phys.B816,293(2009)] url https://doi.org/10.1016/j.nuclphysb.2009.02.027.

[154] Jun Gao and Pavel Nadolsky. A meta-analysis of parton distribution functions. *JHEP*, 07:035, 2014. url https://doi.org/10.1007/JHEP07(2014)035.

[155] Procedure for the LHC Higgs boson search combination in summer 2011. 2011.

List of Publications

"Search for heavy gauge W' boson in events with an energetic lepton and large missing transverse momentum at $\sqrt{s} = 13$ TeV", CMS Collaboration(J. Lee et al.), Phys. Lett. B770 (2017) 278-301 arXiv:1612.09274 [hep-ex] CMS-EXO-15-006, CERN-EP-2016-281 doi.org/10.1016/j.physletb.2017.04.043.

"Lepton MET Early Analysis Run 2", CMS Collaboration(J. Lee et al.), CMS-PAS-EXO-15-006, CERN 2016.

"Search for high-mass resonances in lepton plus MET final state with 2016 data", CMS Collaboration(J. Lee et al.), CMS-PAS-EXO-16-033, Target Journal JHEP CERN 2017.

"PDF Uncertainties and K-factor for the W' Search at 8 TeV Collisions", CMS Collaboration(J. Lee et al.), CMS-AN-2012/172, CERN 2012.

"PDF Uncertainties and K-factor Calculations for the SSM W' at 13 TeV Collisions", CMS Collaboration(J. Lee et al.), CMS-AN-2014/240, CERN 2014.

"Calculation of PDF and α_S uncertainties for the SSM W' search for RunII using 2015 PDF4LHC recipe", CMS Collaboration(J. Lee et al.), CMS-AN-2016/047, CERN 2016.

Acknowledgements

First of all, I would like to express my sincere gratitude to my supervisor Prof. DongHee Kim who gave me the continuous support, encouragement, the opportunity to study this wonderful research on the New physics search at CERN. It was truly a special experience for me.

I am also very grateful to Prof. Youngdo Oh for his many advice and guidance. Particularly his continuous help in commenting on my thesis as well as his many words of physics concept were very helpful.
I also would like to express my gratitude to the rest of my thesis committee members Prof. Chang-Seong Moon, Prof. Un-ki Yang, and Prof. Minsuk Kim for their time, insightful comments, and suggestions to this thesis, but also for the hard question which incented me to widen my research from various perspectives.

I am also grateful to our KNU members Dr. Yuchul Yang, Dr. Daejung Kong, Dr. Jieun Kim and Dr. Sunghyun Chang for their support and encouragement for providing helpful advice on analysis.
I owe special thanks to Yuchul for leading me to work on the CMS data analysis as well as teaching me a lot not only about particle physics, but also about technical details such as grid computing, programming, and bash scripting.

I had an invaluable experience to work with CMS Lepton+MET (W′) Analysis Group at CERN. Special thanks to the conveners: Dr. Kerstin Hoepfner, Dr. Begoña De La Cruz for their great support, help, and providing me very useful comments on all my reports and talks. Also many thanks to all members of W′ group: Oscar Gonzalez Lopez, Klaas Padeken, Alberto Escalante Del Valle, Sebastian Wiedenbeck, Fabian Bispinck, Viktor Kutzner, and Marcel Materok for helping me a lot.

I am very grateful to the CMS EXOTICA group-especially the conveners of EXO, Non-hadronic and Z′ group: Dr. Slava Valouev, Dr. Ivan Mikulec, Dr. Daniele Del Re, Dr. Francesco Pandolfi, Dr. Eva Halkiadakis, and Dr. Sam James Harper for the providing continuous exchange of information and helpful comments.

Also, the working on EXO Trigger group was a great opportunity for me and I am very grateful to the conveners of the group: Dr. Nadir Daci, Dr. Bingxuan Liu, Dr. Bhawna Gomber, and Dr. Swagata Mukherjee for giving me great feedback with helpful advice and comments.

During Offline and Computing project, I am very grateful to the Reconstruction Core Monitoring and Development group, Slava and Carl, for giving me great opportunity to learn about how to develop CMSSW and usage of Git.

I thank all my friends and colleagues, especially to 208 lab family, Jaeyun Choi, Namgyun Jeong, Adil Khan for the stimulating and inspiring discussions, sleepless nights, and for all the fun we have had in the last four years.

Last but not the least, I would like to express my sincerest thanks to my family : my father Weonsik Lee and my mother Weon You who raised me with a love of science and fully supported me, and my two sisters Jungshin, Jungmin and my brother Beyongjun and Jungshin's family for supporting me spiritually throughout writing this thesis and my life. Thank you.

질량중심에너지 13 TeV의 양성자-양성자 충돌실험에서 높은 에너지의 모노-렙톤 (전자 또는 뮤온)으로 붕괴하는 모드를 통한 새로운 물리 현상 탐색

이 정 은

경북대학교 대학원 물리학과 입자물리학 전공
(지도교수 김 동 희)

(초 록)

높은 에너지의 모노-렙톤 (전자 또는 뮤온과 중성미자)으로 붕괴하는 새로운 물리 현상들을 탐색하였다. 질량 중심 에너지가 13 TeV인 LHC 양성자-양성자 충돌 실험에서 CMS 검출기로 2016년 동안 획득한 총 35.9 fb^{-1}의 데이터를 분석한 결과, 표준모형에서 예측된 배경사건 이외에 새로운 물리에 대한 실험적 증거는 발견되지 않았다. 이 결과로부터 표준모형의 W 보존입자와 동일한 결합상수를 갖는 Sequential 표준모형의 W' 보존입자 질량에 대한 하한선을 95% 유의 수준으로 5.1 TeV/c^2로 설정하였고, 일반적인 결합상수에 대한 한계도 구하였다. Split-UED 이론에서는 매개변수 μ= 4 TeV 인 경우 여분차원의 크기인 R 반경의 하한선을 95% 유의 수준으로 2.9 TeV/c^2 로 설정하였다. 또한 초대칭성이론이 예측하는 스칼라 타우입자가 R 패러티가 깨어지면서 모노-렙톤으로 붕괴하는 현상을 분석하여 생성 및 붕괴 결합상수 (λ‘, λ)에 따른 스칼라 타우입자의 질량 하한치를 95%의 유의 수준으로 설정하였다.